UNIVERSITAT DE BARCELONA

# Optical control of endogenous receptors and cellular excitability with light

Aida Garrido Charles

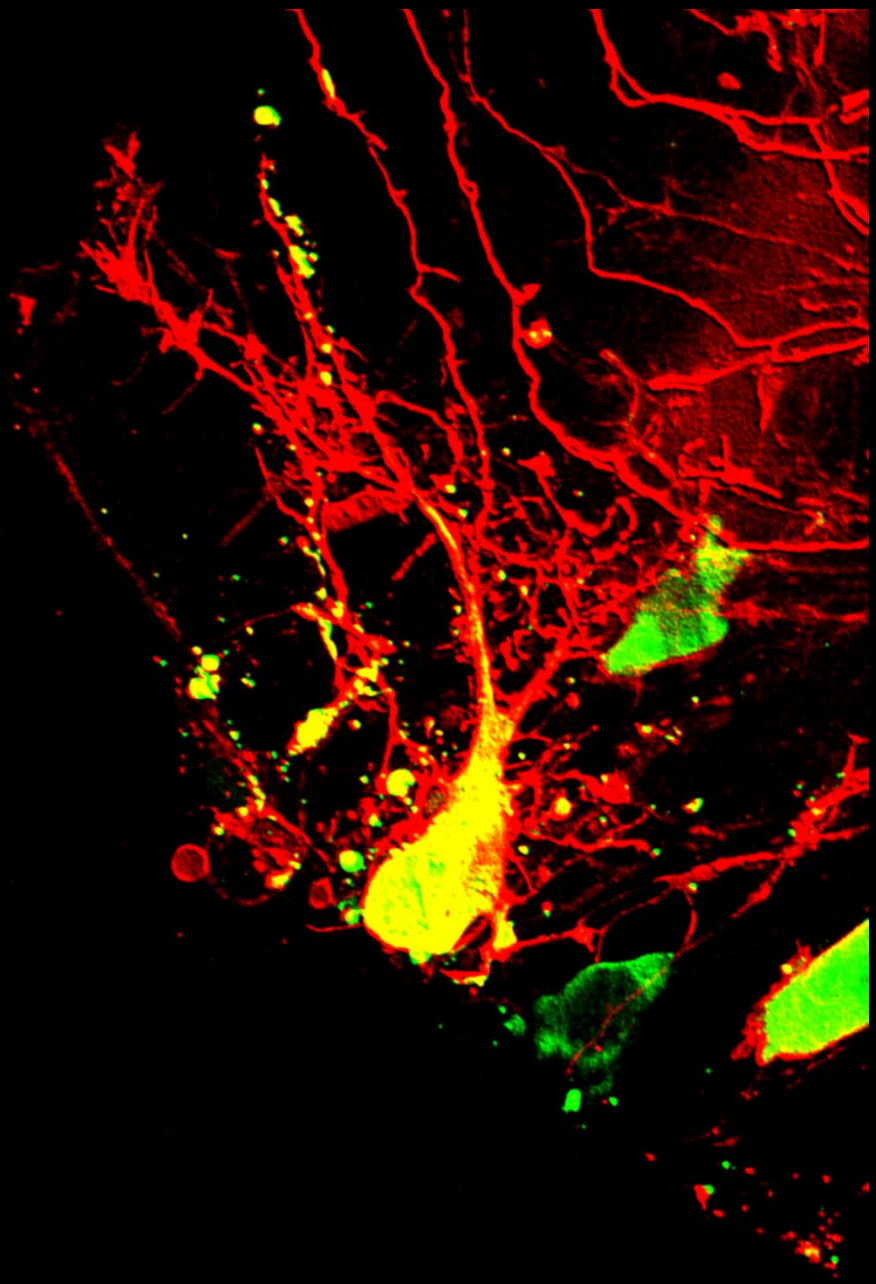

# Optical control of endogenous receptors and cellular excitability with light

**Aida Garrido Charles**

UNIVERSITAT DE BARCELONA

FACULTAT DE FARMÀCIA I CIÈNCIES DE L'ALIMENTACIÓ

Prof. Pau Gorostiza Langa

# Optical control of endogenous receptors and cellular excitability with light

Aida Garrido Charles, 2019

UNIVERSITAT DE BARCELONA

FACULTAT DE FARMÀCIA I CIÈNCIES DE L'ALIMENTACIÓ

Programa de Doctorat en Biomedicina

2014-2019

# Optical control of endogenous receptors and cellular excitability with light

Memòria presentada per Aida Garrido Charles per optar al títol de doctor per la Universitat de Barcelona.


Director: Prof. Pau Gorostiza Langa

ICREA Researcher professor at
Nanoprobes and Nanoswitches Group
Institute for Bioengineering of Catalonia

Doctorand: Aida Garrido Charles

Nanoprobes and Nanoswitches Group
Institute for Bioengineering of Catalonia


Barcelona, September 2019

# CERCANT LA VERITAT

He anat fins més enllà de les muntanyes,
pels confins dels oceans m'he endinsat
he forfollat, de la terra, les entranyes
tan obstinat, que exànime m'he quedat.

Tots els dies, per boscos i pinedes;
a tota au que canta o vola, he preguntat;
a prats, rius, herba, marges i voreres
interpel·lo: On puc trobar la veritat?

La busco dins de mi, no és fàcil cosa,
la necessito per acabar el meu neguit,
en llibres, en l'aire, en els records, en una rosa
tot és fosc, no hi veig res prou definit.

M'afaiçona una veu, molt dolça i fina
que m'omple de tristesa i pietat,
diu que el món, és tot una ruïna
i que ningú no em pot dir què és la veritat.

I, m'impressiona tant i tant l'indefinit
que em sento com vaixell desarborat,
ja no pregunto, puix em sento avergonyit
com un adolescent amb rostre sufocat.

Vaig preguntar a un home, que era molt gran
que de tant vellet, ja caminava tot corbat.
"Si estimes com m'has dit, i estimes tant"
va dir..."Has trobat la vertadera veritat".

Francesc Charles

A la família.

Imagina’t...

## TABLE OF CONTENTS

**PREFACE**

The fine control of neural communications defines us as human beings. Humans are only beaten in number of neurons and synapses in the brain by African elephants. But taking into account that we do not weight tons and measure around 3 meters, our brain is one of the most compacted, organized and specialized of its kind. So far, we only understand a small percentage of the function of brain. Over the years, we anatomically discerned specialized regions that control different functions of our body. The development of microscopic techniques and staining procedures by Golgi and Ramón y Cajal gave a lower scale view of the components of the complex machinery of each region. However, this "end point" studies in fixed tissues did not bring light about how these specialized – compartmentalized cells communicate and function together. Functional studies started with Hodgkin and Huxley recordings in giant nerve of squid. The fathers of neuro-electrophysiology demonstrated that neurons communicate with each other by electric pulses, and that with the appropriate equipment we can record and control different characteristics of the neurons to study the communication mechanism involved. They defined the importance of ion concentration, which is the key for neural communication. Differences in ion concentration between intracellular and extracellular compartments defines a difference in electrochemical potential that enables the neuron to be prepared to receive and communicate neural signals. How is this difference maintained? How can it be changed?

The cell membrane of neurons isolates the intracellular environment from the extracellular media. It acts as a capacitor keeping negative charges internally and positive charges externally. But these compartments are not sealed. Membrane anchored proteins act as communicating channels between the two compartments. Molecular biology and high-resolution techniques helped us to better understand the function of such proteins, and so neurons, by overexpression and cloning methods for the physiological and molecular structure study of specific proteins, subunits or peptides.

The fine regulation of all these proteins evokes or inhibits neural communication. Selective pharmacology to control subtypes of proteins involved in neurotransmission also facilitated the study of neural function. And finally, the relationship between morphology and activity was optimized by all-optical non-invasive approaches, which were highly expected for *in vivo* applications.

Now light became a key new player in the game.

A convergence of tools to study the limits of imagination.

## CHAPTER 1 | INTRODUCTION

### The basis of Neurotransmission

Among different animal species, there is a huge diversity in nervous system traits in terms of size, morphology, specialized regions, types of cells or complexity of the circuits, among others. But if we look into the minimal unit that constitutes the simplest nervous system, we all agree that it is a neuron (Figure 1). The diversity of cells in the nervous system is astronomical, not only in morphology but also at the molecular level and during development. However, all neurons share common features that differentiate them from cells of other tissues: (1) neurons are usually polarized; (2) neural functions are compartmentalized to optimize the process of electrical signals; (3) they can be excited by variations of electric membrane potential; (4) their specialization bestow the ability to receive, process and communicate electrical signals.

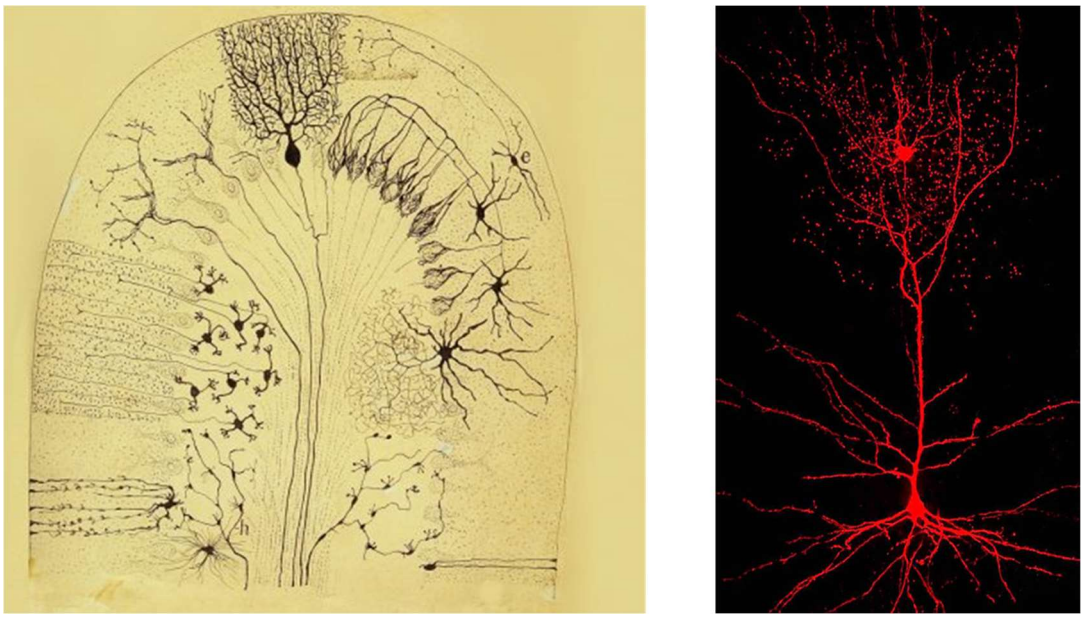

**Figure 1.** (Left) Cerebellar cortex drawing by Santiago Ramón y Cajal in 1904. Property of *Ministerio de Ciencia, Innovación y Universidades.* (Right) Confocal fluorescence image showing a roseship neuron forming its axonal cloud in the tuft of the apical dendrite of the layer 2/3 pyramidal cell. Adapted from (Boldog *et al.*, 2018).

Principal differentiated compartments include soma, dendrites, axons and terminals. The soma is the cell body which contain the nucleus and all the organelles responsible for RNA and protein synthesis. Dendrites and axon emerge from the soma and constitute around the 90% of the total volume of the neuron. Dendrites are numerous fine ramified prolongations that receive information from other neurons. On the other side, usually only one single axon emerges from the soma and transmit electrical signals to other neurons or target organs through its neural terminals. In that way neurons have two different poles, the basal with the dendrites and the apical with the axon(Kandel, Eric R., Schwartz, James H., Jessell, 2000).

Cytosol of the neuron is separated from the extracellular media by a lipidic bilayer, as described in other cell types. This hydrophobic barrier is the responsible of the maintenance of a differential membrane potential by keeping differential charges between intracellular and

extracellular media. The stable membrane potential of the neuron when it is not excited is called resting potential. The difference in charge between intra- and extracellular compartments is defined by the difference in ion concentration given by the ion flux across ionic channels anchored in the membrane. There are two types of ion channels, resting (always open) and regulated (closed in resting conditions). Resting ion channels are responsible of keeping a negative charge inside the neuron compared with a positive charge of the extracellular media. The resting potential of a neuron is usually between -60 and -70 mV. Resting ion channels of neurons are permeable to $K^+$, $Na^+$ and $Cl^-$(Xu, 2013; Agez *et al.*, 2017). Organic anions like proteins and amino acids are negatively charged and also contribute to the difference in potential but they cannot cross the cell membrane. Since $Na^+$ is highly concentrated extracellularly it passively diffuses to intracellular compartments. And the same for $K^+$, which is more concentrated intracellularly and diffuses to extracellular media. Thus, ion flux depends on the electrochemical dragging force, but also on the conductance of the membrane for a specific ion. A neuron has relatively few $Na^+$ resting channels, so in resting potential the conductance for $Na^+$ is very low and the entry of $Na^+$ is limited. But flux of $K^+$ is relatively big because the number of $K^+$ resting channels is bigger. Then, passive diffusion of $K^+$ balance $Na^+$ influx. However, this passive flux of ions has to be compensated to maintain the ionic gradient of $Na^+$ and $K^+$. This balance is maintained by energy-consuming $Na^+/K^+$ ion pumps. By hydrolysis of one molecule of ATP, $Na^+/K^+$ ion pumps can internalize two ions of $K^+$ and extract 3 ions of $Na^+$, creating an efflux of positive charge(Kandel, Eric R., Schwartz, James H., Jessell, 2000).

A change in resting potential such as a reduction of the different polarization, so less negative membrane potential is called depolarization. An increase of negative potential is called hyperpolarization. When the depolarization is big enough to surpass the threshold, the neuron responds actively with the aperture of voltage-gated ionic channels and then an action potential (AP) is produced(Bean, 2007).

Thus, neurons are specialized and compartmentalized cells, but they are not isolated, neurons communicate with each other by a structure called synapse.

## The neuronal functional unit: the synapse

A synapse is a dynamic structure that allows to pass a signal from a neuron to another one (Figure 2a). There are two basic types of synapses: electrical and chemical. Electric synapses are the most direct and simple way of transmission between neurons. Depolarizing signals are transduced from the presynaptic to the postsynaptic neuron via *gap junctions*, without affecting inhibitory signaling or long-term synaptic regulation at the postsynaptic cell. This kind of neurotransmission is instantaneous and direct, all the electrical signals are transduced even when they do not evoke an action potential. These kinds of synapses are important for the rapid communication (fast escape responses), coordinated responses of a population of neurons and transmission of metabolic signals(Nagy, Pereda and Rash, 2018).

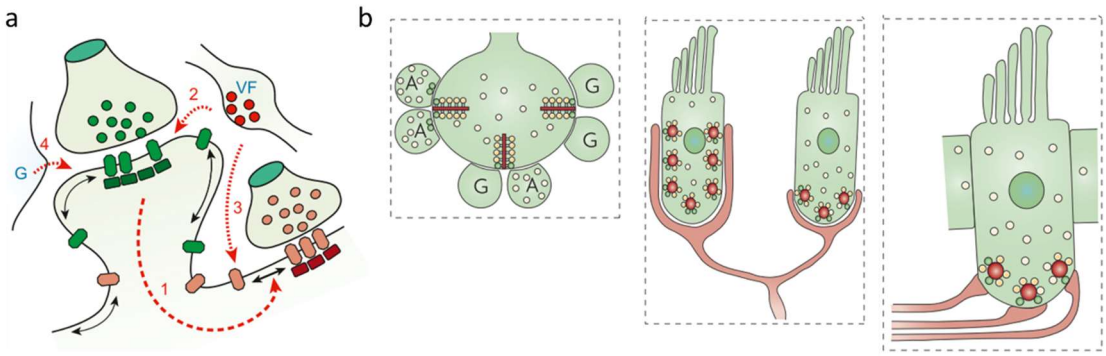


**Figure 2. Synapses are plastic structures.** a) Extrinsic tuning of receptor diffusion-trap: Excitatory events may tune inhibitory receptor lateral diffusion (1). Volume-transmitted molecules may tune the synaptic trapping of excitatory (2) and inhibitory (3) receptors as well as glial-cell-derived factors (4). Adapted from (Choquet and Triller, 2013). b) Diversity of ultrafast specialized ribbon synapses (Sterling and Matthews, 2005).

On the other hand, chemical synapses may not be as fast as electrical synapses, but they have the property to amplify the signal. Structurally, chemical synapses are separated by 20-40 nm from the presynaptic terminal to the postsynaptic. This gap is called the *synaptic cleft*. At the presynaptic terminal, synaptic vesicles filled with neurotransmitters accumulate in the active zone, ready to be released upon a depolarizing signal (Figure 2b). Presynaptic action potential induces the entry of $Ca^{2+}$ via voltage-gated $Ca^{2+}$ channels. The increase in intracellular calcium induces the fusion of vesicles with presynaptic plasma membrane and the subsequent neurotransmitter release. This process is called *exocytosis*.

The trigger for AP firing is at the presynaptic site. $Na^{+}$ and $K^{+}$ ions are important in the depolarization process of the presynaptic neuron but not crucial for neurotransmitter release. In presence of TTX and TEA (blockers of $Na^{+}$ and $K^{+}$ channels, respectively), upon induced depolarization of the presynaptic neuron, we can observe postsynaptic depolarization (AP). However, a reduction in extracellular concentration of $Ca^{2+}$ decrease synaptic transmission or even is blocked. Progressive depolarization of the presynaptic neuron induces the gradual entry of $Ca^{2+}$ and subsequent neurotransmitter release. This entry is gradual because $Ca^{2+}$ channels are voltage dependent that keep open during depolarization. Even though, the close proximity from neurotransmitter release site solve the problem of slower opening of the channel, being able to release the transmitters in 0.2 ms. When Ca-channels are closed, $Ca^{2+}$ concentration sharply decrease (1 ms). There are several types of calcium channels, with different biophysical and pharmacological properties(Bean, 2007).

There is a huge variety of chemical transducers to precisely control or modify the postsynaptic neuron producing excitatory or inhibitory signals in a range from milliseconds to several minutes. The nature of the neurotransmitters released and their capacity to bind and activate postsynaptic receptors would evoke the opening or closing of postsynaptic channels. Consequently, conductance, membrane potential and synaptic structure of postsynaptic neuron is modified.

## Postsynaptic receptors. Structure and general activation process

Basically, postsynaptic receptors are membrane anchored proteins with an extracellular region to recognize and transduce neurotransmitter signaling. These receptors influence the aperture or closing of postsynaptic ionic channels directly (ionotropic receptors) or indirectly (metabotropic receptors).

In the central nervous system, there are two kind of synapses, excitatory or inhibitory, usually glutamatergic or gabaergic, respectively. Among glutamatergic receptors there are two big families, ionotropic (ionic channels directly activated by glutamate, iGluRs) and metabotropic (indirect activation by second messengers, excitatory or inhibitory, mGluRs). And in ionotropic glutamate receptors there are three main subtypes depending on their structural homology and pharmacology: AMPA, NMDA and Kainate. A fourth family of ionotropic δ receptors has been described whose function is still unknown. These receptors are integral membrane proteins organized in tetramers to form an ion channel pore. In each of the subunits in the tetramer can be distinguished four domains: amino-terminal (NTD) and ligand-binding domain (LBD) in the extracellular region, transmembrane domain (TMD), and intracellular carboxyl-terminal domain (CTD) (Figure 3).

Recently published kainate and AMPARs structure (Mayer, 2005; Meyerson *et al.*, 2016; Herguedas *et al.*, 2019; Zhao *et al.*, 2019) better describe the relationship between structure and function of iGluRs (revised in(Zhu and Gouaux, 2017)). Beyond the tetrameric organization of the TMD, subunits conformationally arrange as A/C and B/D subunit pairs, and each one interact differentially to ion channel pore having distinguishable gating implications. The first step in the assembly of iGluRs is the formation of dimers of dimers with NTD interactions. Final tetramerization occurs by interactions of the LBDs and TMDs. There are clear differences between NTD and LBD arrangements. NTD layer is arranged as local dimers between A/B and C/D subunits, whereas in the LBD layer dimers are formed by A/D and B/C subunits.

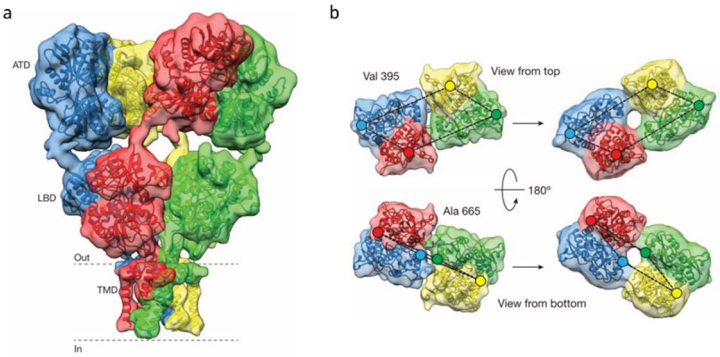


**Figure 3. Isosurface representation of the GluA2 closed state cryo-EM structure at 10Å resolution segmented.** a) Distal AC (green and blue) and proximal BD (red and yellow) subunits of GluA2 crystal structure (PDB 3KG2) coordinates for the ATD, LBD and transmembrane regions fit separately as rigid bodies; the dashed lines highlight putative membrane boundaries. b) Isosurface views of LBD tetramer region density maps fit with LBD dimers in closed (left) and active (right) states. Coloured dots identify the locations of αC atoms for Val 395 (upper lobe) and Ala 665 (lower lobe). Adapted from (Meyerson *et al.*, 2014).

The NTD of all glutamate receptors has been described to be involved in regulatory processes of the receptor such as targeting the receptors to the membrane, influence open probability,

deactivation, desensitization, and regulation of subunit-specific assembly. NTD also contains binding sites for divalent cations ($Zn^{2+}$), negative allosteric modulators or extracellular proteins. Glycosylation sites at the NTD are also important for differences in ligand affinities, trafficking and molecular weights of native receptors, affecting desensitization and maximal currents(Traynelis *et al.*, 2010).

The LBD is a clamshell-like structure formed by polypeptide structures S1 and S2. It is a highly conserved amino acid sequence within different glutamate receptor classes, including metabotropic. Agonists like glutamate, glycine or aspartate, and their analogs, contain α-amino and α-carboxyl groups that interact with conserved residues, and variations lead to agonist discrimination.

Before agonist binds to the LBD, the receptor is in a resting, nonconducting state (closed) (Figure 3b). Upon agonist interaction, LBD changes its conformation from an open clamshell to closed clamshell conformation. This cleft closure involves a change in 2-fold symmetry that triggers ion channel opening at the TMD(Twomey and Sobolevsky, 2018). Depending on subunit occupancy, and so agonist concentration, this conformational change that give rise to a pre-active state can be followed by a fully open conducting state or an active but not conducting state (desensitized). This subunit occupancy and difference of conductance states can be observed in single-channel currents where agonist type and concentration induce multiple pore opening conductance levels(Robert and Howe, 2003; Reiner and Isacoff, 2014).

The mechanisms that describe receptor gating by agonist binding depends on the LBD subunits available. In general, upon agonist binding, there is a conformational change in the LBD that closes the clamshell structure preventing agonist dissociation. Subsequently, another conformational change in the ion channel activates the receptor(Zhao *et al.*, 2019). Structural differences also may explain differential activation kinetics.

The diversity in gating kinetics of each receptor subtype defines the time course of synaptic currents and their implication in synaptic physiology and plasticity. The fastest activation and deactivation rates with strong desensitization are characteristics of AMPARs, evoking a single excitatory postsynaptic current in the rage of millisecond time scale. After, kainate receptors have relatively fast gating kinetics and strong desensitization. In the last position, NMDARs show much slower gating kinetics (ms), deactivation (s), with weak or no desensitization(Traynelis *et al.*, 2010).

On the other side, inhibition of ion pore opening is achieved when antagonists interact with the LBD. Most commonly used AMPA and Kainate antagonists are quinoxalinediones. Among them, NBQX seems to be more selective for AMPA receptors. Surprisingly, the presence of TARPs converts CNQX and DNQX, but not NBQX, from antagonist to weak partial agonists because both CNQX and DNQX induce partial domain closure in these conditions. In the case of NMDARs the most used competitive antagonist is AP5 and its analogs. AP5 interacts with GluN2 subunit and has been widely used to distinguish NMDAR activity from AMPA and kainate receptor activity(Traynelis *et al.*, 2010).

Additionally, allosteric modulators that modify desensitization kinetics interact in a binding site within the dimer interface between the ligand binding domains. For example, cyclothiazide (CTZ) has two binding sites to slow the onset of desensitization and indirectly slow the channel closure rate by increasing agonist potency (PDB 5WEO)(Twomey *et al.*, 2017). More precisely, CTZ attenuates desensitization by stabilizing the dimer assembly. The effect of CTZ on AMPARs is reversible, instead, Concanavalin A (Con A) irreversibly potentiates agonist-evoked currents

specifically for kainate receptors by keeping the activated channel in the open state(Partin *et al.*, 1993). However, Con A does not alter synaptic kainate receptor currents and only weakly potentiates whole-cell currents from cultured hippocampal neurons.

Below the LBD and anchored into the membrane there is the TMD, which is arranged in a 4-fold axis symmetry of subunits to form an ion channel. Each subunit has 4 transmembrane helices (M1-M4). M2 loop lines the inner cavity of the pore and contain the editing QRN site. M3 lines the outer cavity and M1 is exterior to M2 and M3. M4 is associated with ion channel core of an adjacent subunit.

The TMD is the one responsible for ion pore formation. Residues in the lining pore determine ion permeability and conductance. Specifically, QRN site of the re-entrant M2 loop is a key determinant of single channel conductance, $Ca^{2+}$ permeability, channel block by polyamines, $Mg^{2+}$ sensitivity, channel block by organic compounds, and assembly into heteromeric complexes(Traynelis *et al.*, 2010).

The current carried through most glutamate receptor channels is a mixture of monovalent cations ($K^+$ and $Na^+$) plus $Ca^{2+}$. The flux of $Ca^{2+}$ through NMDA and $Ca^{2+}$ permeable AMPARs channels is a key factor contributing to various forms of synaptic plasticity, gene regulation, neuropathology and fast transmitter release. Importantly though, NMDARs are 3 to 4 times more permeable to $Ca^{2+}$ than calcium permeable AMPA or kainate receptors.

And finally, intracellular CTD is the most variable domain of glutamate receptors about sequence and length. Its basic function is regulatory. By docking motifs with intracellular proteins and phosphorylation sites, it modifies membrane trafficking, stabilization, post-transcriptional modifications and targeting for degradation. It can also interact directly with signaling proteins such as PKC, CamKII, and adaptor or scaffolding proteins(Henley, 2003; Traynelis *et al.*, 2010). These interactions allow local signaling with spatial and temporal specificity to receptor regulation. Post-translational modifications of glutamate receptors such as phosphorylation, glycosylation, palmitoylation and SUMOylation can regulate trafficking, surface expression, endocytosis, receptor-protein interactions, and so synaptic plasticity(Choquet and Triller, 2013).

## Ionotropic glutamate receptors

### NMDA receptors

N-methyl-D-aspartate (NMDA) receptors are ionotropic glutamate receptors that respond specifically to N-methyl-D-aspartate. They form heteromers of combinations of subunits NR1 (with eight different splicing isoforms), NR2A-D, and NR3A-B. Early in development NR2B, NR2D, and NR3A are abundant and during maturation they are substituted by NR2A and NR2C. This subunit predominance is also region and neuron specific. Functional NMDARs always contain NR1 combined with one or two subunits of NR2 or NR3, and different variant combinations affect functional characteristics of the receptor like kinetics, conductance, $Ca^{2+}$ permeability, and $Mg^{2+}$ and $Zn^{2+}$ sensitivity.

NMDA receptors are slightly different from the other ionotropic glutamate receptors: 1) its channel has high conductance, being permeable to $Na^+$, $K^+$ and $Ca^{2+}$; 2) glycine interaction at GluN1 or GluN3 subunit is needed as a cofactor to activate the channel; 3) its opening depends on membrane voltage and ligand binding (glutamate at GluN2 subunit). When cell membrane is at resting potential (-65 mV), extracellular $Mg^{2+}$ binds strongly to NMDARs blocking its pore.

Almost all central synapses contain NMDA and AMPA receptors to form the functional synaptic unit. In that way, presynaptic release of glutamate coactivates both NMDA and AMPA receptors. But glutamate by itself cannot activate NMDARs. When the membrane is depolarized by fast AMPAR-mediated response, $Mg^{2+}$ is displaced and other cations can flow through the channel. Compared to AMPA receptors, the excitatory postsynaptic potential that NMDARs evoke is slow in rise and decay. The activation of NMDARs induces the entry of $Ca^{2+}$, which can activate intracellular $Ca^{2+}$ dependent processes. Downstream signaling pathways such as CaMKII, PKC, and PKA are thought to be involved in induction of long-term potentiation (LTP). These long-lasting modifications depend on synaptic activity and are important for processes like memory and learning(Gereau and Swanson, 2008).

The subsequent increase in intracellular $Ca^{2+}$ triggers a long-lasting change in AMPA receptor-mediated synaptic transmission. The study of AMPA and NMDA receptor currents in synaptic plasticity in silent synapses (synapses that contain functional NMDARs but lack functional AMPARs) give rise to a model of synaptic plasticity where upon LTP-induction, NMDA activation and subsequent $Ca^{2+}$ entry trigger the insertion of AMPARs into the postsynaptic density(Choquet and Triller, 2013). A mis-regulation in $Ca^{2+}$ entry can induce an excitotoxic effect in the neuron due to an activation of calcium dependent signaling cascades and enzymes that produce toxic free radicals.

**AMPA receptors**

Early in the development, most of the synapses contains mostly NMDARs. In the synaptotopic model of dendrite growth, it is described that initial contact of the branches are done by adhesive mechanism. As synapses mature, the content of iGluRs changes and active synapses receiving sufficient afferent glutamatergic inputs mobilize AMPARs, induce activation of intracellular calcium signaling pathways and cytoskeleton stabilization (Haas, Li and Cline, 2006).

AMPARs stands for α-Amino-3-hydroxy-5-methyl-4-isoxazolepropionic acid receptors, which are ionotropic glutamate receptors specifically activated by this agonist. AMPARs mediate the vast majority of fast excitatory glutamatergic transmission. AMPAR family are formed by 4 different subunits, GluA1-A4, whose expression is developmentally regulated, region and cell-type specific, and activity-dependent. Within the adult forebrain principal neurons, including hippocampus and cortex, the predominant subtype comprises GluA1 and GluA2 with a secondary minor role of GluA2/3, usually forming heteromers. Their expression is also extended over the animal kingdom in organisms as rodents, honeybees, nematode worms, and humans. They are essential for brain correct function and are also involved in the expression of long-term and short-term synaptic plasticity, related to memory and learning, development and certain neurologic diseases, such as Alzheimer or stroke(Gereau and Swanson, 2008).

The kinetics and amplitude of the excitatory synaptic response are determined by the biophysical properties of the receptor subunit combination and the density of receptor expression, convolved with the time course of glutamate release and uptake. AMPARs have a relatively small single-channel conductance and fast kinetics, and they rapidly inactivate and desensitize in the presence of agonist. The affinity for glutamate is relatively low compared to NMDARs ($EC_{50}$ =0.5 mM)(Traynelis *et al.*, 2010). The mean single-channel conductance is also proportional to the concentration of the agonist(Robert and Howe, 2003). Each subunit is thought to bind its ligand independently, and as more agonist molecules are bound to the

receptor complex, the predominant subconductance state increases(Gereau and Swanson, 2008; Twomey *et al.*, 2017).

One particularity of AMPARs is their $Ca^{2+}$ permeability, as previously denoted important for synapse maturation and circuit development. Calcium permeability is controlled by QRN editing site. GluA2 subunits contain a specific 10-nucleotides at the intron sequence before the exon encoding the QRN editing site which control the change from Gln to Arg at the tip of the reentrant pore loop. GluA2 containing channels are impermeable to $Ca^{2+}$ and have a linear current-voltage relationship, whereas those lacking GluA2 subunit are permeable to $Ca^{2+}$ and show inward rectification due to a voltage-dependent block by endogenous polyamines. This change affects also trafficking and favor heteromeric assembly. Additionally, alternative splicing of the AMPA receptor subunits generates two isoforms of the LBD termed flip and flop, which control desensitization and deactivation as well as sensitivity to allosteric modulators(Traynelis *et al.*, 2010).

Regarding their role in synaptic plasticity, two main factors are important: AMPA receptor expression, which is a dynamic and highly regulated process; and membrane distribution, which is highly regulated by postsynaptic proteins such as PSD-95(Choquet and Triller, 2013). Rapid lateral movement of AMPARs in the membrane of neurons from extrasynaptic sites to synaptic sites has an important role for regulation of diffusion within the plasma membrane for example upon induction of LTP processes(Bosch *et al.*, 2014).

**Kainate receptors**

Unlike AMPA and NMDA receptors, kainate receptors can play a role at both pre- and postsynaptic sites. At presynaptic locations KARs might regulate transmitter release at excitatory and inhibitory synapses. At the postsynaptic site, they collaborate with AMPARs and NMDARs in the synaptic response. In addition to their role as ionotropic receptors, kainate receptors also signal via G-protein coupled second-messenger cascades to downstream effectors, with a main implication in the control of transmitter release(Petrovic *et al.*, 2017).

The study of KARs has been hampered by the lack of specific agonists and antagonists that do not interact with AMPARs and well performing antibodies. KARs show strong developmental and regional regulation. Looking at subunit specific expression it is described that GluK1 is expressed in hippocampal and cortical interneurons, dorsal root ganglion neurons, Purkinje cells and sensory neurons; GluK2 is mostly expressed by principal cells like pyramidal and granular cells of hippocampus, cerebellar granular cells, and cortical pyramidal cells; GluK3 is expressed in the neocortex and dentate gyrus in the hippocampus; GluK4 is present in CA3 pyramidal neurons, dentate gyrus, neocortex and Purkinje cells; and GluK5 is widely expressed in the brain. The best-studied site of kainate receptor-mediated synaptic transmission is at the mossy fiber-CA3 pyramidal cell synapse. There, heterotetramers formed by GluK2 and GluK5 are found postsynaptically, whereas receptors formed from combinations of GluK1 to GluK3 are located presynaptically. At mossy fiber, kainate receptors act in a concerted manner to amplify synaptic integration and frequency-dependent spike transmission. Another example of target-specific localization of glutamate receptors is the absence of kainate receptors at associational/commissural synapses onto CA3 pyramidal cells or the predominance of GluK2 on local circuit inhibitory interneurons. Differential localization can influence in different manner transmitter release, such as in the case of GABA. Presynaptic KARs might diminish inhibition and somatodendritic KARs increase the activity of GABA interneurons(Gereau and Swanson, 2008).

During development for example, motility of axons during maturation is regulated by KARs activity. Also, there is an activity-dependent switch from kainate to AMPA receptors, as a developmental form of LTP (Kidd and Isaac, 1999; Petrovic *et al.*, 2017). KARs are also involved in synaptic plasticity form of LTD (Park *et al.*, 2006).

Synaptic kainate receptors often possess a slower time course and smaller excitatory postsynaptic currents compared to AMPAR- mediated EPSCs(Castillo, Malenka and Nicoll, 1997; Frerking, Malenka and Nicoll, 1998; Vignes, M. *et al.*, 1998). This feature can be accounted by the presence of specific KAR auxiliary subunits (Neto1 and Neto2). Their role influencing KAR function implies an alteration of gating properties of KARs: slowdown of desensitization onset and faster recovery from desensitized state. This implies an increase in time of steady currents in presence of agonist.

Studies of the molecular structure of GluK1 and GluK2 LBD show that residues interacting with glutamate in their binding pockets differ, making the GluK2 binding pocket bigger than that of GluK1. These differences also contribute to explain the higher glutamate $EC_{50}$ for GluK1 (47 µM) than for GluK2 (9 µM)(Mayer, 2005; Traynelis *et al.*, 2010). Comparing with AMPA receptors, GluK1 and GluK2 agonist binding pockets are larger than that of GluA2, allowing kainate receptors to accommodate larger ligands such as KAR selective agonist SYM2081(Mayer, 2005). Thus, steric occlusion and interdomain interactions might explain differential selectivity for agonist and antagonist between subtypes and the unique kinetic of deactivation and recovery from desensitization (Weston *et al.*, 2006).

Another regulatory function of KARs is the inhibition of the slow afterhyperpolarization current generated by voltage-sensitive calcium-dependent $K^+$ channels. This inhibition prevents spike adaptation and increase neuronal excitability. Their role in the control of transmission of information and excitability indicate that they might have an important role in epilepsy, by inhibition of GABA release and overactivation of aberrant synapses. Studies in dorsal root ganglion neurons also show a possible contribution of KARs in pain and fear memory(Ko *et al.*, 2005).

**Therapeutic potential**

As described below, ionotropic glutamate receptors are key players in excitatory neurotransmission. An impairment in the correct function or a dysregulation of excitatory-inhibitory balance are responsible of a plethora of neurological disorders. Huge efforts are put in the study of such diseases and in the development of specific drugs to treat or improve symptoms and life quality of the patients. One recent pioneer example is the work done by Dr Altafaj and co-workers (Soto *et al.*, 2019) in the treatment of pediatric encephalopathy caused by a mutation in NMDAR subunit GluN2B.

In more general terms, NMDA receptor antagonists have been studied in the treatment of major depression, Parkinson's disease and neuropathic pain, among other diseases (reviewed in (Paoletti, Bellone and Zhou, 2013)).

On the other hand, AMPA receptor potentiators (ampakines) are studied for the improvement of recognition memory performance and attention in Alzheimer's disease, schizophrenia, attention deficit hyperactivity disorder and depression (Gereau and Swanson, 2008). NMDA and AMPA receptors antagonists might present partial neuroprotective effect against stroke but also induced a lot of side effects.

As well, kainate receptors are involved in mood disorders like schizophrenia and biopolar disorders, mental retardation, Huntington disease, epilepsy and pain. Inhibitors of GluK1 (highly expressed in DRG neurons) may have therapeutic analgesic activity and also seem useful in the treatment of epilepsy and neuropsychiatric conditions(Lerma and Marques, 2013).

## Spatiotemporal control of neurotransmission

The importance of excitatory neurotransmission in diseases like Alzheimer, seizures or stroke, highlights the necessity of tools to control the actors involved in the scene, neurotransmitters and receptors. Classical pharmacology is based in the development of diffusible drugs with high affinity for a subtype of receptor. However, chemical design has limitations, and selectivity cannot reach the desired 100%, so side effects are usual(Casey, 1997; Berger and Iyengar, 2011).

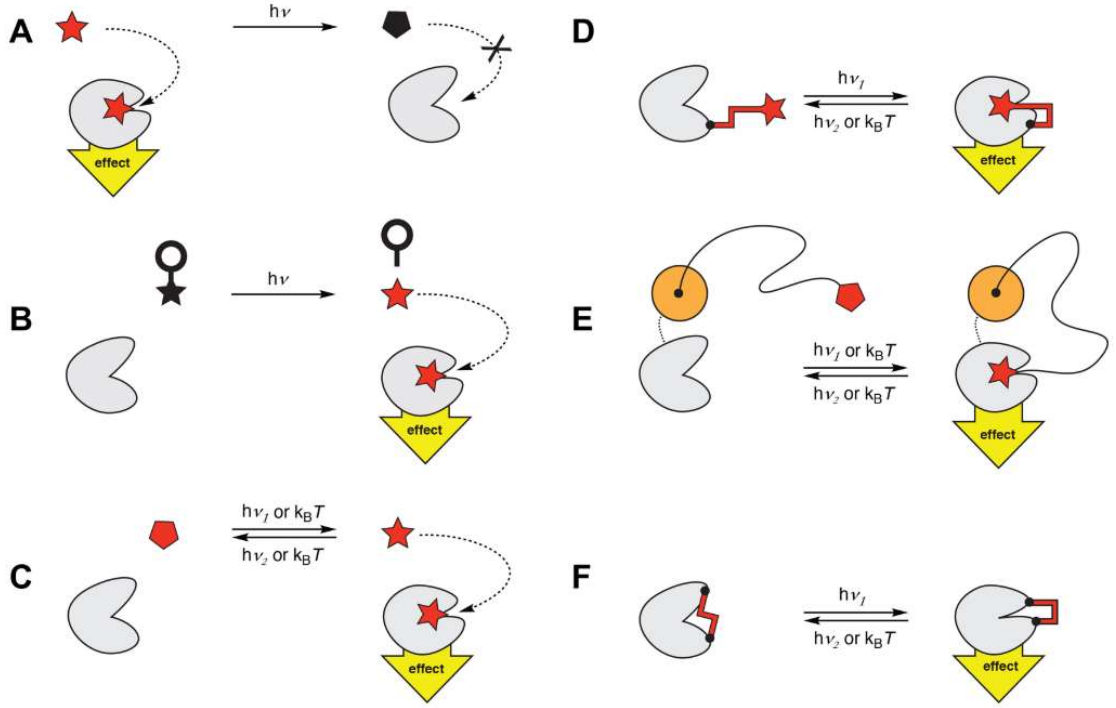


**Figure 4. Modalities of photopharmacology.** a) Irreversible photoinactivation. b) Irreversible photoactivation (photo-uncaging). c) Reversible photoactivation/inactivation using a photochromic ligand (PCL) that toggles between an inactive (pentagon) and active (star) form. d) Photoswitchable (closely) tethered ligand (PTL). e) Photoswitchable orthogonal remotely tethered ligand (PORTL). f) Photoswitchable cross-linker. Extracted from(Hüll, Morstein and Trauner, 2018).

The synthesis of photochemical ligands started already in the '70s with the aim to confer light sensitivity on endogenous receptors without genetic modifications. Photosensitive ligands include caged compounds (Figure 4a-b), photoswitches (Figure 4c-e) and photolabels (Figure 4f). Caged compounds are ligands protected by a light-sensitive group. They are the most widely used in neuroscience due to their properties: 1) inactive before photolysis; 2) rate of uncaging is fast; 3) use of biocompatible wavelengths for uncaging, also two-photon sensitive (Ellis-Davies, 2019); 4) by-products of photolysis are usually non-toxic; 5) downstream effects are not influenced by upstream signaling, a very useful feature in the recognition of connectivity maps (Callaway and Katzt, 1993; Shepherd, 2012). General neurotransmitters like glutamate, GABA, dopamine and serotonin have been caged, but also more specific agonists like NMDA, kainate, or nicotinic and glycine receptor agonists, and agonists and antagonist of neuropeptide

receptors(Ellis-Davies, 2007). However, they also are limited to be a one-way reaction, photo-uncaging is irreversible; they diffuse so a high concentration is needed to be useful; and under these conditions their specificity is poorer (unintended effects are observed on GABA receptors and GluN1 subunit of NMDARs (Maier *et al.*, 2005; Olson *et al.*, 2013)).

The second group of photochemical ligands is photoswitchable or photochromic ligands (PCLs). Compared to caged-compounds, PCLs contain a light sensitive group that isomerizes reversibly upon illumination with two different wavelengths of light. Usually, one of the isomers displays higher activity than the other, and illumination reversibly control the activation of target proteins. The most widely used photoswitchable light sensitive group is azobenzene. The thermally relaxed isoform of azobenzene is the *trans* configuration. Near-UV light stimulation changes azobenzene configuration to *cis* isomer, which is less stable and shorter (5.5Å) than *trans* (<10 Å). Back isomerization *cis-trans* can be achieved by blue-green light stimulation or by thermal relaxation in the dark at lifetimes ranging from milliseconds to days depending on the substituents of the core. Some examples of PCLs include channel blockers for voltage-gated $K^+$ channels, $Na^+$ channels and $Ca^{2+}$ channels; activators of G-protein coupled inwardly rectifying potassium (GIRK) channels; modulators of delayed rectifier $K^+$ channels, ATP-sensitive $K^+$ channels and two-pore domain $K^+$ channels; activators of transient receptor potential V1 (TRPV1) channels; agonist and antagonists of ionotropic receptors (iGluRs)(Volgraf *et al.*, 2007); agonists and pore blockers of nicotinic acetylcholine receptors (nAChRs); an agonist of adenosine receptors; an antagonist of GABAaRs; and allosteric modulators of metabotropic glutamate receptors (mGluRs)(Pittolo *et al.*, 2014; Rovira *et al.*, 2016), muscarinic receptor agonists(Riefolo *et al.*, 2019), and of $GABA_A$Rs(Gomila *et al.*, 2019; Maleeva *et al.*, 2019) (extended revision in (Paoletti, Ellis-Davies and Mourot, 2019) and (Bautista-Barrufet, Izquierdo-Serra and Gorostiza, 2014)).

Another more recently used photoswitchable group is cyclic azobenzene or "bridged-azobenzene". This closed carbon-disubstituted azobenzene is characterized to have a more stable *cis* isomer than *trans* isomer. This feature allows the administration of inert *cis* isomer that can be photoactivated with visible light. Thus, overcoming the usual intrinsic activity of PCLs like GluAzo where *trans*-isomer is the active one. Recent examples include the work of Ellis-Davies in the development of LAB-Glu to control extracellular NMDA receptors and LAB-QA to block intracellularly voltage-gated potassium channels (Thapaliya, Zhao and Ellis-Davies, 2019). Our group also described two bridged-Azos able to control iGluRs and induce selective neuronal firing (Gisela Cabré *et al.*, 2019). And recently Trauner and co-workers described potassium channel blockers and openers with cyclic azobenzenes(Trads *et al.*, 2019).

These interesting features of *cis*-isomer stability can also be observed in the case of stilbenes. Compared to bridged-azobenzene, stilbene cannot photoisomerize between *trans-cis*, and *cis-trans* isomerization is possible but irreversible. Thus, both isomers must be separately synthesized. In this way, *cis*-stilbene behaves like a non-destructive caged compound that does not create side products of the uncaging, a concept developed by our collaborators at the organic chemistry department of UAB as "Non-destructive caged ligands".

But in the case of freely diffusible ligands the main problem is the diffusion resulting in low effective concentration. To solve this issue, another chemical design emerged from the idea to keep the ligand placed closely to the binding pocket and control its interaction with light. These new compounds were called photoswitchable tethered ligands (PTLs). The structure of PTLs is tri-modular: with a pharmacologically active head (agonist, antagonist or blocker), switch moiety (azobenzene), and a reactive group, usually an electrophilic group that reacts with nucleophilic

amino acids (e.g. maleimide with cysteine). Anchoring of the PTL by the cysteine residue is rapid, selective and irreversible. In this way, effective concentration near the LBD is high enough to be able to activate the receptor and *trans-cis* biological activity is clearly distinguished. First approach was the modification of the voltage-gated potassium channel Shaker (SPARK), which has been used to silence neurons (Banghart M, Borges K, Isacoff E, Trauner D, 2004; Banghart *et al.*, 2009). Another important approach was the modification of GluK2 LBD to attach a "maleimide-azobenze-glutamate" (MAG) to a genetically engineered cysteine in the position 439. This new light activatable receptor called LiGluR (Volgraf *et al.*, 2006) is able to depolarize the cell membrane and induce neuronal activation (Szobota *et al.*, 2007). More recently, MAG-derivatives have been proved effective with 2-photon stimulation (Izquierdo-Serra *et al.*, 2014; Carroll *et al.*, 2015) and so new possibilities emerge for the application of PTLs in vivo (G. Cabré *et al.*, 2019).

Subsequent sequence studies in other receptors and single point mutations give rise to other types of light activatable receptors(Hüll, Morstein and Trauner, 2018): acetylcholine receptor control with LinAChR (Tochitsky *et al.*, 2012); LiGABARs (Lin *et al.*, 2014); LimGluRs (Levitz *et al.*, 2013); LiGluNs, photo-agonist or -antagonist of NMDARs (Berlin *et al.*, 2016). Other PTLs include the control of two-pore domain $K^+$ channels and purinergic P2X receptors(Lemoine *et al.*, 2013) and dopamine receptors (Donthamsetti *et al.*, 2017). Extended revision in (Paoletti, Ellis-Davies and Mourot, 2019) and (Bautista-Barrufet, Izquierdo-Serra and Gorostiza, 2014).

Using the same strategy for anchoring, it is also possible to bi-anchor chemical photoswitches to two cysteines from different subunits or different membrane proteins to evoke mechanical forces controlled by light stimulation. These photoswitches in particular are called nanotweezers or optotweezers. Their design and application in the control of pore opening and ion flux was focused on P2X receptors and acid-sensing ion channels (ASICs)(Browne *et al.*, 2014; Habermacher *et al.*, 2016).

Another approach is the use of photoswitchable orthogonal remotely tethered ligands (PORTLs), which are conjugated to larger protein tags (SNAP-tag). With this strategy the objective is to avoid the disadvantages of maleimide reactivity with water (hydrolysis of maleimide) or other non-desired nucleophiles. The change in conformation of the chromophore affects ligand efficacy as it does in PCLs. As a proof of concept, Trauner and co-workers fused a SNAP-tag to metabotropic glutamate receptor 2 (mGlu2) and photosensitized it by benzylguanine chemistry to an azobenzene photoswitch (Broichhagen *et al.*, 2015). More recently, Isacoff and Trauner describe membrane anchored PORTLs for genetically-targeted optical control of an endogenous G protein-coupled receptor (Donthamsetti *et al.*, 2019).

However, genetic modification and protein overexpression is needed in the case of classical PTLs. Expression of the mutated subunits for PTL anchoring could be performed by viral transduction or transgenesis in knock-in mice. Both methods have their advantages and disadvantages. Transgenesis is better in terms of stable protein expression and localization, but it is an expensive and arduous method. On the other hand, viral transduction is rapid and can be circuit-specific targeted (e.g. affecting only postsynaptic neurons), but expression levels may not be as stable(Paoletti, Ellis-Davies and Mourot, 2019).

For these reasons, our group designed a new family of PTLs capable to attach to an endogenous receptor without requiring gene-engineering. The chemical design was similar to MAG but modifying the reactive group we were able to attach the photoswitch to endogenous native glutamate receptors. Due to the mechanism of covalent conjugation of the photoswitch to the

receptor, which targets the ligand binding site, we called them "targeted covalent photoswitches" (TCPs)(Izquierdo-Serra *et al.*, 2016).

## Intrinsically light sensitive proteins: Optogenetics

In the last 10-15 years, great effort has been put in neurobiology to selectively activate a region of the brain, one specific neuron or even a single spine. This level of accuracy has only been reached with the discovery of light sensitive proteins that actually form an ion pore. Upon light stimulation, the pore is opened and lets ions flow through, thereby depolarizing the neuron of interest. This important discovery was described firstly in 2002 by Nagel et al and first applied to depolarize neurons in 2005 (Boyden). That was the rise of optogenetics.

Optogenetics comprises the use of genetic manipulations with a family of opsins including ion channels and pumps. Naturally, bacteriorhodopsins and halorhodopsins are proton and chloride pumps, respectively, that have an inhibitory effect when overexpressed in neural systems. On the contrary, channelrhodopsins (ChRs) have an excitatory effect by inducing neural depolarization letting positively charged ions flow through (Figure 5).

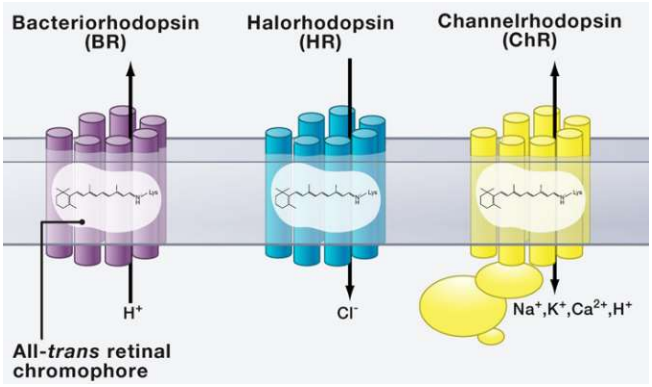


**Figure 5. Microbial opsins as tools in optogenetics**. Adapted from (Zhang *et al.*, 2011).

The first described ChRs revolutionized the field of neuroscience, but this first generation presented some biological limitations (Lin, 2010). Improvements in optogenetics are based on the discovery of new opsins in nature or characterization of point mutations in opsins already described which tune speed, fidelity, cation-anion conductance (inhibitory ChR), and bi-stability increasing $\tau_{off}$ to obtain step function opsins (no need of continuous illumination) (reviewed in (Deisseroth and Hegemann, 2017)).

All these adaptations led optogenetics to be used in many fields, for example in the study of neural circuits (Förster *et al.*, 2017), restoration of blindness (Yue *et al.*, 2016), in vivo studies in *Caenorhabditis elegans* nematodes(Tsukada and Mori, 2015), olfactory bulb (Braubach *et al.*, 2018), hearing restoration (Keppeler *et al.*, 2018; Mager *et al.*, 2018), pain (Iyer *et al.*, 2016), and many others.

## Applications and future challenges

The use of optical sensitive proteins and light-regulated drugs transformed the study of neurotransmission processes. The use of excitatory and inhibitory overexpression of opsins helped in the dual study of neural circuits. And the improvement of all optical approaches to

track neural function, i.e. calcium imaging by genetically encoded calcium indicators(Dana *et al.*, 2016; Yang and Yuste, 2017) or the development of new fluorescent voltage sensors(Gong *et al.*, 2015; Kost *et al.*, 2019), collaborate in the same direction in a less invasive experimental setup for in vivo studies.

Still, overexpression of exogenous proteins that control neural excitability may interfere in physiological cell behavior and gene therapy is, despite great advances, not a generally accepted procedure. As a complement, photopharmacology aims to selectively control drug activity in time and space, and if possible, on endogenous receptors. With this final goal, possible therapeutic scenarios have been proposed, for example in order to improve pain management(Mourot *et al.*, 2012), in vision restoration(Tochitsky, Ivan; Kramer, 2015), or more recently as photo-activatable antitumoral treatment (Matera *et al.*, 2018). This is an unstoppable emergent new field that day after day keeps surprising us.

## Objectives

The general aim of the present work is to obtain new photoswitchable ligands capable of photosensitizing endogenous non-modified neural receptors and to use them to optically control neural activity.

In order to achieve that aim, the thesis has been structured in three main objectives, which are developed in the corresponding parts:

**Part I. Engineering the reactive properties of photoswitchable tethered ligands (PTLs):**

**Chapter 2:** the following objectives are developed:

- To devise a strategy to target and chemically attaching photoswitches to native excitatory glutamate receptors, and to characterize the photocontrol enabled by such targeted covalent photoswitches (TCPs).
- Use of TCPs as tools to photocontrol neural activity in organotypic hippocampal slices at the level of single cell and single spine.
- Application of TCPs to photoregulate neural activity in vivo and influence nerve regeneration using as in vivo model the olfactory nerve of *Xenopus tropicalis* tadpoles.

**Chapter 3:** is focused on this objective:

- Developing a strategy to spatiotemporally control PTL conjugation using photolabile groups.

**Part II. Engineering the optical properties of photoswitchable tethered ligands (PTLs):**

**Chapter 4:** the following objectives are developed:

- Development of a TCP with high-frequency operation using visible light. Characterization of optical, pharmacological, and physiological responses in vitro of receptor photoregulation.
- Application of high-frequency TCPs to photoactivate the neurons of the auditory nerve and brainstem.

**Chapter 5:** is focused on this objective:

- Rational development of photoswitches with enhanced multiphoton sensitivity.

**Chapter 6:** is focused on this objective:

- Development of a "light harvesting" strategy to tune the action spectrum characteristics and sensitivity of photoswitches via chemical conjugation of fluorophores, photosensitization, and energy transfer.

**Part III. Engineering the optical properties of diffusible photochromic ligands (PCLs):**

**Chapter 7:** is focused on this objective:

- Design and characterization of irreversibly and non-destructively activated PCLs based on stilbene to prevent the photogeneration of undesired uncaging products.

**Chapter 8:** is focused on this objective:

- Design and characterization of inverted switching PCLs based on bridged azobenzenes.

## Part I. Engineering the reactive properties of photoswitchable tethered ligands (PTLs)

# CHAPTER 2| Photoswitches targeting functional endogenous glutamate receptors allow the non-genetic light-control of single synapses and single neurons in vivo.

Aida Garrido-Charles[1,2*], Miquel Bosch[1,2,*,#], Hyojung Lee[1,2], Xavier Rovira[1,2,&], Silvia Pittolo[1,2,^], Artur Llobet[3], Ana Trapero[1,4], Amadeu Llebaria[4], Eduardo Soriano[5,6], Maria V. Sanchez-Vives[7,8], Christine E. Holt[9], Pau Gorostiza[1,2,8]

1 Institute for Bioengineering of Catalonia (IBEC), Barcelona Institute for Science and Technology (BIST), Carrer de Baldiri Reixac 15-21, 08028 Barcelona, Spain

2 Network Biomedical Research Center in Bioengineering, Biomaterials, and Nanomedicine (CIBER-BBN), 28029 Madrid, Spain

3 Laboratory of Neurobiology, Neuroscience Program, Bellvitge Biomedical Research Institute (IDIBELL), L'Hospitalet de Llobregat; Department of Pathology and Experimental Therapy, School of Medicine, University of Barcelona, L'Hospitalet de Llobregat; Institute of Neurosciences, University of Barcelona, L'Hospitalet de Llobregat

4 Institute of Advanced Chemistry of Catalonia, Consejo Superior de Investigaciones Científicas (IQAC-CSIC), 08034 Barcelona, Spain.

5 Department of Cell Biology, Physiology, and Immunology, University of Barcelona (UB), 08028 Barcelona, Spain.

6 Network Center of Biomedical Research in Neurodegenerative Diseases (CIBERNED), 28031 Madrid, Spain.

7 Institut d'Investigacions Biomèdiques August Pi i Sunyer (IDIBAPS), Barcelona, Spain.

8 Catalan Institution for Research and Advanced Studies (ICREA), 08010 Barcelona, Spain

9 Department of Physiology, Development and Neuroscience, University of Cambridge, Cambridge, UK

[*] These two authors made an equivalent contribution to this work.

# Present address: Institut d'Investigacions Biomèdiques August Pi i Sunyer (IDIBAPS), Barcelona, Spain.

& Present address: Universitat de Vic, Barcelona, Spain.

^ Present address: University of California, San Francisco, USA.

Keywords: glutamate receptors, photopharmacology, photoswitches, recycling, trafficking, AMPAR, Kainate, dendritic spines, synapse organization and dynamics, plasticity, long term depression, hippocampus, Xenopus laevis, rat.

## ABSTRACT

Glutamate receptors (GluRs) play key roles in electrochemical transmission in excitatory synapses and in the regulation of synaptic plasticity. We have recently developed a targeted covalently attached photoswitch (TCP) that allows the remote control of endogenous iGluRs using light. We combined this photopharmacological effector with genetic and chemical calcium sensors to achieve an all-optical reversible control of iGluRs at multiple levels of spatial resolution in the brain: from single neurons to single synapses in rat hippocampal slices and in intact *Xenopus laevis* olfactory bulb *in vivo*. We found this probe to selectively target the AMPA and kainate receptors. Labeled receptors were functional for long periods of time (>8 hours), which allowed us to longitudinally track receptor dynamics during events of synaptic plasticity. In particular, we induced long-term depression (LTD) and monitored the internalization of functional endogenous AMPA/KA receptors in hippocampal neurons. TCPs are therefore a unique optical tool to label, photo-control and functionally track endogenous receptors at multiple levels of spatial and temporal resolution in brain tissue without genetic manipulation.

## INTRODUCTION

Models of receptor dynamics at the synapse have been developed and refined for many years, mainly using electrophysiological and biochemical tools to elucidate glutamate receptor (GluR) dynamics and modifications during events of plasticity, in dissociated neurons, in slices or in vivo[1,2]. The recent development of optical and photochemical tools has contributed to improve this model. Fluorescently tagged GluRs (e.g. with EGFP or SEP) can be tracked with time lapse two-photon (2P) or confocal microscopy [3]. Many of these techniques, however, suffer from substantial limitations. Some of them involve the genetic manipulation of GluRs, either to attach an electrophysiological tag or fluorescent tags or immunoreactive labels [4–7], and usually involve the need of exogenous overexpression. The dynamics of endogenous GluRs have been monitored in populations at different time points [8] but not longitudinally over time or functionally.

GluRs play an essential role in neuronal physiology. They are responsible for the transmission of the electrochemical signal in excitatory synapses and also for the regulation of the plastic properties of these synapses [9–11]. There exist different types of glutamate receptors classified in two main groups: ionotropic and metabotropic. Ionotropic receptors are cation-permeable ion channels that open upon binding of glutamate and contribute to the depolarization of the postsynaptic neuron. Among these receptors, there are the AMPA-type (AMPAR), the kainate-type (KAR) and the NMDA-type (NMDAR). AMPAR and KAR are $Na^+/K^+/Ca^{2+}$ channels and are the main contributors of the synaptic transmission [12]. Their concentration in the post-synaptic density (PSD) determine the strength of that synapse. The NMDAR are $Ca^{2+}$ channels mainly responsible to modulate the plasticity of the synapse. The entry of $Ca^{2+}$ through NMDAR triggers the cascade of events that ends up potentiating (LTP) or depressing the synapse on the long-term (LTD) [13]. On the other hand, metabotropic glutamate receptors (mGluR) respond to glutamate binding by triggering intracellular G protein-coupled signaling. These receptors modulate synaptic transmission and plasticity [10].

External manipulation of cell physiology has been usually performed by drug administration, both for fundamental research and therapeutic purposes. But classic pharmacology has some disadvantages like low spatial and temporal control of drug action, which causes side effects and reduces efficacy. The development of light-regulated tools has transformed the manipulation of cellular physiology and has been especially used to control neuronal activity. Nowadays, there are two basic approaches to light control biological processes: optogenetics[14], based on the over-expression of intrinsically light-sensitive proteins; and photopharmacology[15], enabled by the chemical design of light-sensitive drugs that can be activated or inactivated depending on their configuration. Inside the family of light-regulated drugs there are two types of photoswitches available: diffusible photochromic ligands (PCLs) and photoswitchable tethered ligands (PTLs) [16]. The main difference between them resides in the local concentration that they can reach. PCLs diffuse freely in the media and PTLs are covalently attached to their target receptor, allowing a high local concentration and in consequence rapid functional responses.

Conventional optogenetics and tethered photopharmacology require gene therapy to overexpress exogenous proteins into the system of interest, often altering cellular physiology. An alternative is now offered by Targeted Covalent Photoswitches (TCPs) [17], PORTLs[18–20] or maPORTLs[21] that can operate on endogenous receptors without genetic manipulation. In particular, TCPs are azobenzene-derived photoswitches that can be covalently attached to GluRs and that specifically can activate and reversible inactivate them with millisecond temporal precision [17]. They have been used to control neuronal activity in neurons in vitro and have also

been applied to photosensitize retinal cells. Even so, photoswitches are not only used to control biological processes but also to understand them. As example, the work of Reiner and Isacoff that use tethered ligands to study glutamate receptor desensitization and occupancy[22]; or the use of optogenetic tools to control endocytosis in active synapses that reveal roles of LTD in motor learning[23]. Here, we push forward the application of these tools to achieve the maximum precision in temporal and spatial resolution to photocontrol neuronal activity at multiple levels of resolution and to monitor the dynamics of functional endogenous GluRs in events of synaptic plasticity (during induction of LTD).

TCPs were designed to specifically target endogenous GluRs in order to regulate their function using light. By modulating GluRs one can potentially control the activity of synapses, neurons, neuronal circuits and whole brain regions at will, in a remote way, and at any desired temporal and spatial pattern. Our goal here was precisely to test the feasibility of all these possibilities. TCP was initially tested in cultured cells and dorsal root ganglion neurons and applied to restore photoresponses in ex vivo retinas[17]. Here, we explored the boundaries of the spatial and temporal resolution achievable with TCP in different experimental approaches: 1) in vitro dissociated rat hippocampal neuronal cell cultures (**Figure 1, S1-S2**), 2) *ex vivo* rat hippocampal organotypic slices (**Figures 2-5**), and 3) in vivo *Xenopus laevis* olfactory bulb (**Figures 6-7, S4**). We finally applied TCP in one of these approaches to study the dynamics of glutamate receptors during events of synaptic plasticity such as long-term depression (LTD) of hippocampal Schaffer collateral synaptic transmission (**Figure 5**).

In conclusion, we achieve the reversible photocontrol of activation and deactivation of a population of neurons in rat hippocampal slices and in the intact brain of a complete organism (*Xenopus* tadpoles). We further achieve the modulation of single neurons and also single dendritic spines just by application of TCPs.

## RESULTS

### Targeted covalent photoswitches (TCPs) for endogenous receptors

The first description of a PTL able to conjugate to an endogenous, genetically non-modified receptor is detailed in Izquierdo-Serra et al., 2016. The characterization of a library of compounds gives rise to Targeted Covalent Photoswitches (TCPs) able to bio-conjugate and light-activate the ionotropic glutamate receptor GluK1. By introduction of a highly reactive NHS ester group (red in **Figure 1a**), TCPs can anchor through an affinity labeling process to native receptors, thus avoiding genetic modifications. In this process, first the glutamate group of TCP binds to the high affinity ligand binding site at the LBD, thereby producing a high local effective concentration of the NHS ester group of TCP around neighboring lysine residues, and then one (or a few) of them react preferentially to the photoswitch, attaching it covalently to the protein. The light-sensitive azobenzene moiety (green in **Figure 1a**) can be isomerized to the *cis* form by UV or violet light (360-420 nm) and back isomerized to the *trans* thermally stable form by green light (450-550 nm). In the *cis* isoform, ligand moiety (blue in **Figure 1a**) from TCP can interact with the ligand binding pocket of GluR, induce the opening of the channel and trigger an ionic current flow (**Figure 1b**). In the *trans* isoform, ligand part of TCP cannot reach the ligand binding pocket and the receptor can change its conformation allowing the channel to close. Among a combinatorial library of compounds of different length, TCP9 and TCP10 displayed the best photoresponses when isomerized reversibly with illumination of wavelength between 380 nm (active *cis* isomer) and 500 nm (inactive *trans* isomer).

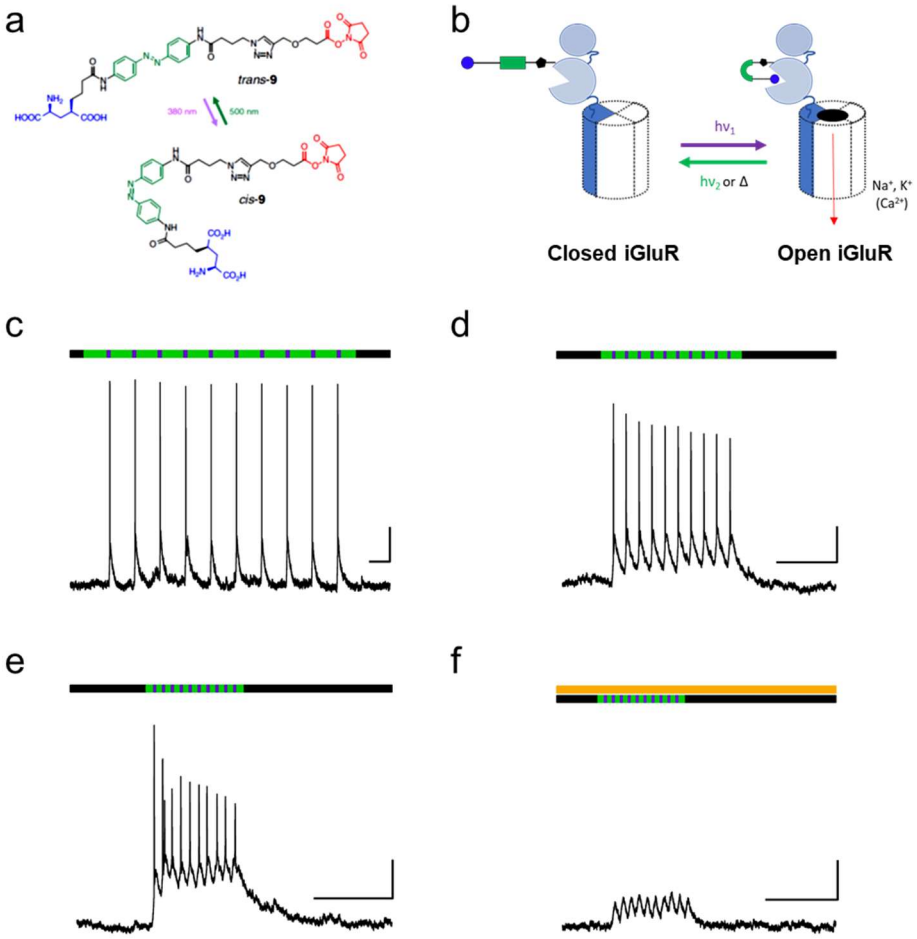


**Figure 1. Targeted covalent photoswitches (TCP) allow the bidirectional control of endogenous glutamate receptors in 2D hippocampal neural cultures.** a) Example of full TCP9 chemical structure showing the photoisomerization between the *trans* (green light, λ=500 nm) and *cis* configurations (violet light, λ=380 nm). Adapted from [17]. b) Operational mode of TCP9 on iGluR receptors. An agonist (blue) is tethered to an LBD through a reactive NHS ester group (red in panel A) via linkers (black). In *trans* state of the switch (azobenzene, green), the ligand cannot reach the binding pocket, whereas in *cis* state, the ligand docks and stabilizes the activated (closed) conformation of the LBD. Thus, channel pore opens allowing the influx of $Na^+$, $Ca^{2+}$ and $K^+$. This effect can be reversed by light stimulation between 380 – 500 nm. c) Current clamp recording from hippocampal neurons after 11 days in culture treated with TCP9 (12.4 µM for 2 min at pH9) and exposed to alternating 500 nm-light (green) and 380 nm-light (purple), membrane potential = -70 mV. Violet light pulses of 40 ms at 1 Hz (c), 5 Hz (d) and 10 Hz (e). (f) Current clamp recording to 1 mM DNQX (AMPA/kainate receptor competitive antagonist, yellow bars) perfusion on the same neuron and with the same illumination sequence. Reversible responses to DNQX indicate covalent TCP9 conjugation and reveal a high local effective TCP9 concentration under violet light. Scale bar 10 mV, 10 s.

We previously confirmed this regulation of inward currents in GluK1-transfected cells and in dorsal root ganglion (DRG) neurons [17]. Here, we further test the temporal resolution of TCP9 at controlling action potential firing while activating endogenous receptors in dissociated hippocampal neurons in culture without genetic manipulation. After TCP9 conjugation and washout, we can control robustly and reversibly action potential firing in patch-clamp recordings

at high time resolution by applying flashes of 40 ms of violet light (380 nm) at different frequencies: 1 Hz (**Figure 1c**), 5 Hz (**Figure 1d**) and 10 Hz (**Figure 1e**).

As previously described in GluK1, *cis* is the active isomer, obtained with UV light illumination, has slow thermal relaxation time (around 80 min) and acts as a full agonist. Pharmacological characterization of TCP9 in hippocampal neural cultures indicates that these photoresponses were dependent on the presence of endogenous AMPA and/or KA receptors, as they were blocked by the broad AMPA/KA receptor inhibitor NBQX (**Figure 1f** and **Figure S1a**). TCP9 does not conjugate to NMDA receptors, because the presence of AP5 (100 µM, NMDARs antagonist) does not alter photoresponses (**Figure S1a**). We also demonstrate the photostability of TCP9 once conjugated and that photoresponses depend on light intensity (**Figure S2**), as increasing the light power results in a faster and bigger response.

In GluK1 it was pharmacologically demonstrated that the conjugation mechanism follows an affinity labeling process. In principle, the reactive electrophilic group of TCP (red in **Figure 1a**) can bind to any nucleophilic (amino and hydroxyl) group on the cell surface, but it preferentially conjugates to lysine residues of glutamate receptors through the intrinsic affinity of the glutamate moiety (blue in **Figure 1a**) to the LBD of these receptors [24]. We checked whether this affinity-driven selective conjugation takes place in endogenous receptors of intact neurons. We incubated cultured neurons with TCP9 in the absence or presence of NBQX and then we measured light-induced currents in the absence of any inhibitor. Currents were reduced by 86 % in cells conjugated under NBQX (**Figure S2b**), suggesting that this inhibitor prevented affinity binding and covalent conjugation of TCP. These results show that TCP can efficiently photosensitize endogenous glutamate receptors in hippocampal neurons and allow the efficient photocontrol of neuronal firing activity with millisecond precision.

The ligand cavity of GluK1 (PDB 1TXF)[25] is bigger and more permissive than that of GluK2 (PDB 1TT1) [25] and AMPA (PDB 6QKC)[26] receptors. Even though we can precisely control neural firing, GluK1 is not the main ionotropic glutamate receptor expressed on hippocampal neurons. Thus, we considered the possibility that TCP9 could also photo-activate AMPA receptors. In order to test this idea, we transiently transfected HEK cells to overexpress GluA1 homotetramers and incubated them with TCP9. Electrophysiological recordings show inward currents upon illumination with UV light that can be reversed with visible light illumination (**Figure S3**). Steady state photocurrents can be recorded in presence of cyclothiazide (CTZ). Local perfusion of saturating concentration of glutamate induces the full opening of the whole population of channels on the cell membrane. DNQX local perfusion antagonizes photocurrents as a demonstration of pharmacologically specific labeling of TCP9 to GluA1. Photocurrents are still present at the end of the recording after several washout cycles, indicating covalent conjugation of TCP9 to the receptor.

## Targeted covalent photoswitches (TCPs) for endogenous receptors in hippocampal organotypic slices

We next aimed at studying the capabilities of TCP at their maximum temporal and spatial resolution in a developed brain tissue with natural 3D complexity in physiological conditions. To this end we used rat hippocampal organotypic slices, where neurons and synapses show similar morphology and physiology as in the intact brain [4]. We longitudinally monitored neuronal and synaptic activity using calcium imaging in a fluorescence confocal microscope. This all-optical approach allowed us to combine optical effectors (TCP) to control neuronal activity with optical

sensors (genetically encoded calcium indicators) to monitor multiple cells simultaneously. We biolistically transfected neurons with plasmids expressing the calcium sensor GCaMP6s together with DsRed2 (**Figure 2a**). We used DsRed2 as a cell filler used to locate neurons and spines and as calcium-independent fluorescence signal as ratiometric control. We incubated transfected slices with TCP9 to allow its conjugation to GluRs and washed it before imaging. We tested the viability of this approach by raster-illuminating the entire field of view with the violet light laser (405 nm) for 1 min. About half of the transfected neurons (~48%) were efficiently photoswitched, i.e. they increased their activity after violet light-induced *cis*-isomerization of TCP9 (**Figure 2b-d**). We back *trans*-isomerized TCP9 by green light laser (514 nm) for another minute. Almost all cells (~95%) ceased their activity after green light exposure. Cells responded to TCP9 activation with an average of ~2-fold increase in fluorescence signal (**Figure 2c-d**). Given the thickness of the slice, we were initially concerned that TCP could react with the slice surface and could not conjugate with cells in deeper layers. However, we found cells responding to violet light at depths down to ~100 µm, indicating that TCP9 efficiently penetrated deep into the tissue.

Also, photoactivation capacity is maintained over time (**Figure 2e**) without any photobleaching or photo- fatigue effect on the TCP9 or decrease of neural response during several hours. This persistence allowed performing pharmacological characterization, which require long imaging recordings.

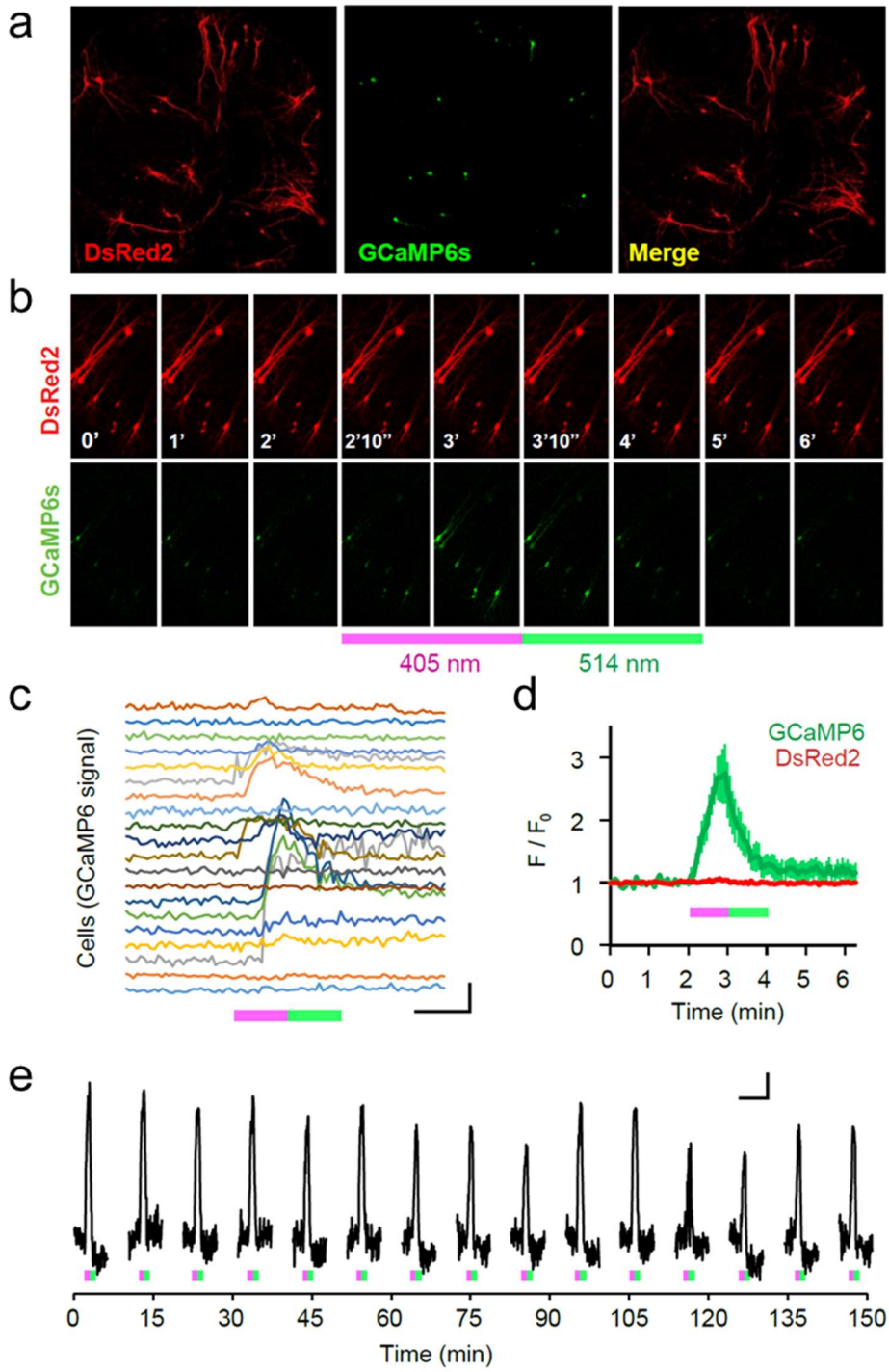


**Figure 2. TCP9 allows the bidirectional control of endogenous glutamate receptors in 3D hippocampal slices as observed using an all-optical approach.** a) Microphotograph of an organotypic hippocampal slice expressing GCaMP6s (green) and DsRed2 (red). b) Time-lapse images of GCaMP6s and DsRed2 fluorescence of TCP9 evoked photoresponses. c) GCaMP6s signal from single cells in the field of view after illumination with a 405 nm raster scanning laser, followed by 514 nm light stimulation (scanning laser) (n= 20). Scale bar two-fold increase ($dF/F_0$), 1 min. d) Average fluorescence response of normalized GCaMP6s and DsRed2 signal upon light stimulation (405 and 514 nm) (n= 10). e) Time-lapse $Ca^{2+}$ photoresponses in rat organotypic slices incubated with TCP9 are maintained over time. Scale bar 0.3 $dF/F_0$, 5 min. 1P stimulation was performed at 405 nm (purple bar, 0.81 mW $\mu m^{-2}$) and 514 nm (green bar, 0.35 mW $\mu m^{-2}$).

We took advantage of the ability to control simultaneous activation of different neurons by whole field of view stimulation, in order to pharmacologically characterize TCP9-evoked photoresponses (**Figure 3**) in organotypic hippocampal slices. In comparison to control conditions (**Figure 3a**), bath perfusion of TTX ($Na^+$ channel blocker, **Figure 3b**) or AP5 (NMDAR antagonist, **Figure 3c**) does not affect photoresponse amplitude. Instead, photoresponses can only be pharmacologically antagonized by NBQX or CNQX (AMPA and Kainate antagonists) (**Figure 3d-e**), as observed before in dissociated hippocampal neuron cultures. The same light stimulation protocol in absence of TCP9 do not elicit any calcium response (**Figure 3f**). Taking into account all these results (**Figure 3g**), we can conclude that TCP9 photoactivation in organotypic slices is pharmacologically specific to AMPA/kainate receptors.

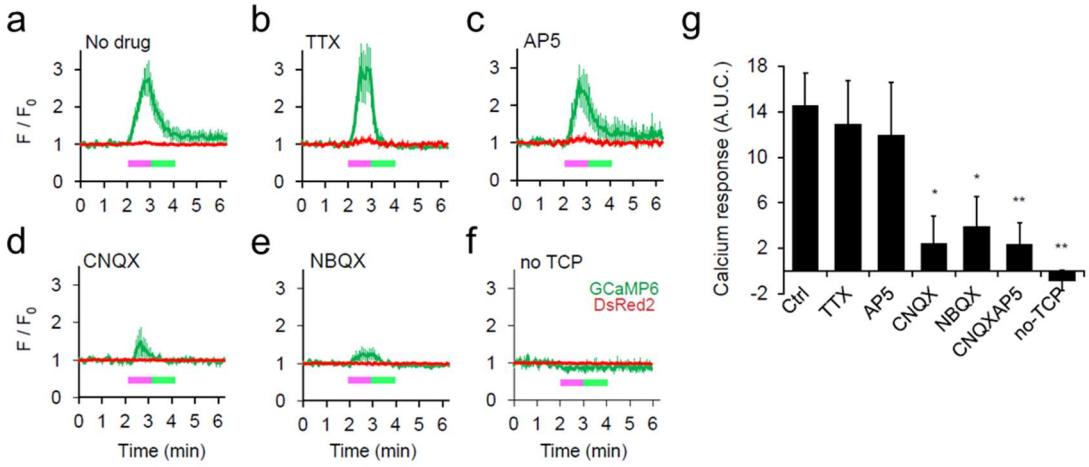


**Figure 3. TCP9 photocontrol neuronal activity by preferentially targeting endogenous AMPAR and KA receptors.** a-f) Average fluorescence response of GCaMP6s (green) and DsRed2 (red) signal upon light stimulation (405 and 514 nm). g) Quantification of calcium photoresponses as area under the curve (AUC). Data are represented as mean ±SEM of: No drug, n=15; CNQX, n= 6; AP5, n=6; NBQX, n=15; TTX, n=5; no TCP9, n=5. * $p < 0.05$, ** $p < 0.01$ with respect to Control (ANOVA).

## Functional tracking of endogenous AMPA receptors

Internalization of AMPARs induces a depression of synaptic transmission[27]. We use TCP9 long lasting (~4-8 h) and stable photo-activation effect as a readout of synaptic transmission to describe for the first time the dynamics of functional endogenous AMPARs in the plasticity process of LTD.

After induction of NMDAR-dependent LTD by brief bath application of NMDA[28], TCP9-evoked photoresponse amplitude clearly decrease (**Figure 4**). Peak distribution over time, before and after NMDA application, also demonstrate the decrease in light-induced neural activation in the majority of cells in the slice 80 min after LTD induction (**Figure 4b**). Long-lasting depression of synaptic transmission, >20% of reduction of photoresponses with respect to baseline, can be observed up to 120 min after LTD induction (**Figure 4c**).

Here, we proved that TCP9 modification on the endogenous receptors does not affect natural receptor endocytosis, which strengthens its potential to study plasticity processes (LTP and LTD). Both constitute cellular substrates of learning and memory, achieved during the consolidation

phases of LTP and LTD. TCP9 allows then to study the dynamics of AMPAR/KAR over time during physiological events of plasticity without the need of any genetic intervention (avoiding overexpression or introduction of exogenous proteins that could interfere with endogenous protein dynamics). TCP9 also reveals the receptors that are functional, i.e. those responding to (light-induced) glutamate binding, by opening the channel and letting $Ca^{2+}$ ions to flow. This tool, therefore, can be further applied to study other forms of plasticity, such as LTP, or late phases of LTD and LTP, and homeostatic plasticity[1].

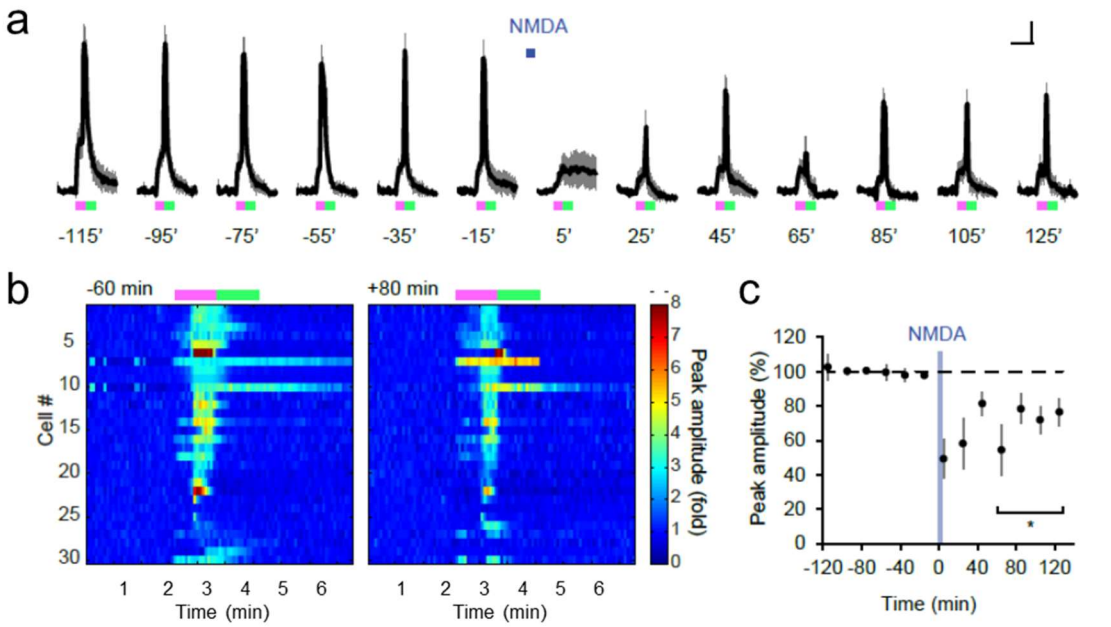


**Figure 4. Tracking functional endogenous AMPAR/KAR during events of synaptic plasticity.** a) Cycles of photoactivation of TCP-labeled cells in hippocampal slices are repeated every 20 min. GCaMP6s signal traces show a stable photoresponse for 2 hours (baseline). NMDAR-dependent LTD induction by bath application of 20 µM NMDA for 3 min reduces the magnitude of photoresponses for the long term (>120 min). Traces are the mean ±SEM of n=30 cells from one representative experiment. Scale bar: 2 min, 0.3-fold ($F/F_0$). b) Raster plot showing individual cell responses over time (color-coded GCaMP6s intensity peak amplitude) during stimulation 60 min before LTD induction compared to 80 min after LTD induction. c) GCaMP6s peak amplitude photoresponses normalized (to baseline) over time shows a long-term decrease of photoresponse intensity (by 25%; mean ±SEM of n=4 independent experiments). *p < 0.05 comparing the last 60 min period (85'-125') with the 60 min baseline period before application of NMDA (Student's paired t-test).

## TCP9 can optically activate single neurons and single spines

We next tested the spatial resolution of TCP9-control of neuronal activity provided by a laser beam. We focused the violet laser (405 nm) to the soma of a single pyramidal neuron of the CA1-CA3 regions and illuminated it with flashes of 10 s (**Figure 5a**). We achieved the specific activation of single neurons with a similar efficiency as when illuminating of the entire field, suggesting that TCP9 conjugation was sufficiently high to produce responses in approximately half of the cells. Most of the responding neurons (92%) could be reliably activated and inactivated in a bidirectional way with flashes of violet light. Only 8 % of neurons did not respond to subsequent rounds of activation, either by non-increasing GCaMP6s signal or by non-decreasing a saturated GCaMP6s signal, probably due to photobleaching or photodamage

effects. Photoregulation of single neuron activation is highly selective as only one of the non-irradiated neighboring cells also responded to light (**Figure 5b-c**) and with a delay of seconds, indicative of an indirect activation due to a putative synaptic connectivity between them.

A unique feature of TCP9 is that it tags covalently endogenous receptors naturally located at synapses. Thus, TCP9 offers an opportunity to optically control neural activity at the level of a single spine using the minimum spatial resolution achievable with the laser (spot stimulation of pixel size). By focusing on DsRed2 fluorescence signal to optimally visualize dendritic spines, we can precisely induce sizable photoresponses, as GCaMP6s signal increase, at the level of a single spine by light pulse duration as short as 1 ms (**Figure 5d-g**). DsRed2 fluorescence signal is not disturbed by 405 nm light pulse illumination (**Figure 5e**), also indicative of absence of photodamage due to focused light stimulation.

In these experiments we also explored the spatial confinement of TCP9 activation by studying GCaMP6s fluorescence at the adjacent dendrite. As shown in **Figure 5f**, TCP9 activation is spatially controlled and do not activate the closely located dendrite. Remarkably, photoactivation of the spine can be achieved repeatedly over time (**Figure 5g**).

The long-lasting and stable effect of TCP9 photoswitching of endogenous AMPAR/KAR recorded in organotypic slices demonstrates the reversible effect, in contrast to caged compounds, and the high local concentration that provides a PTL. Thermal stability of *cis* isomers also allows shortening illumination pulses and reducing light power required, thus reducing phototoxicity. The robust calcium photoresponses obtained are representative of physiological receptor dynamics since no anti-desensitization treatment or genetic modification was applied to the neurons. Preservation of receptor kinetics is advantageous also since physiological receptor desensitization limits calcium influx and its possible cytotoxic side-effects.

The efficiency and spatiotemporal control of TCP9 photoswitching in organotypic brain slices show the potential of TCPs as photopharmacological tools to study neural plasticity processes.

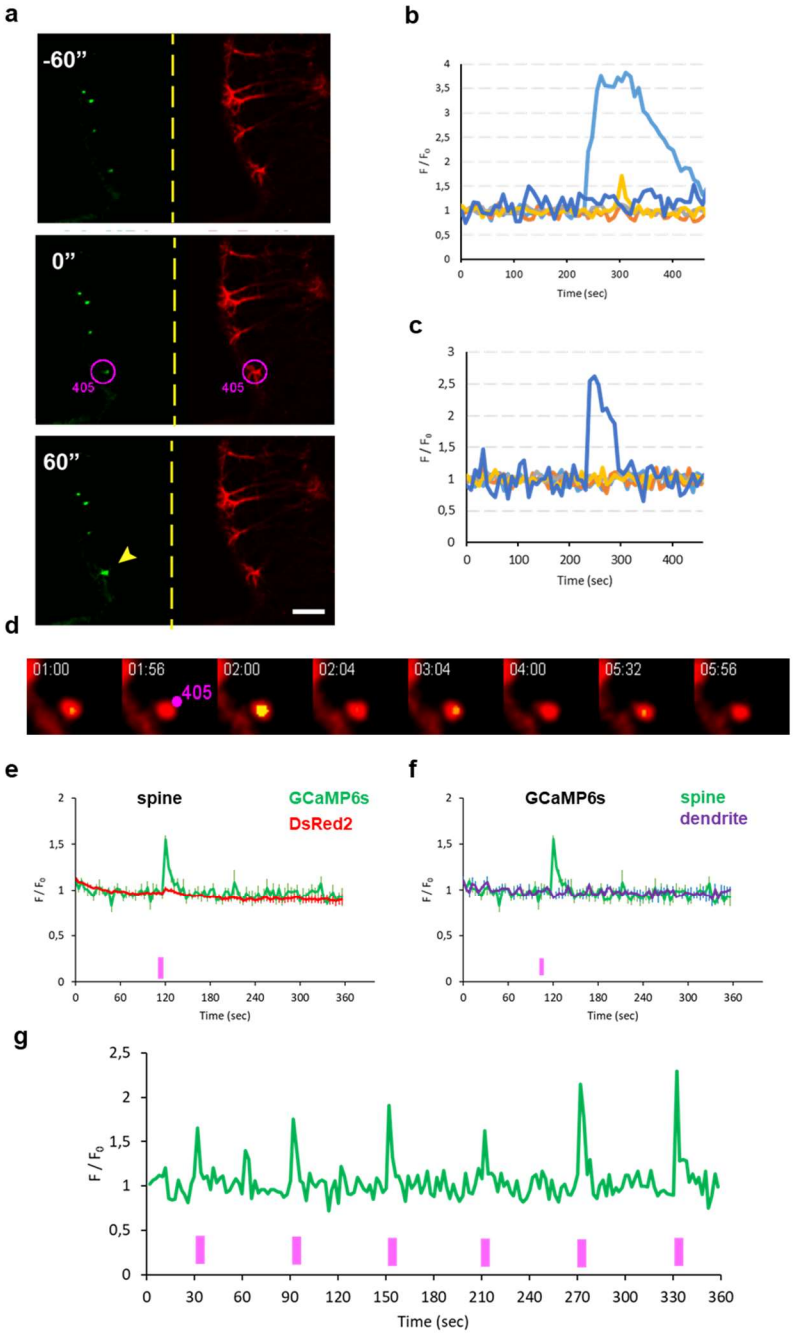


**Figure 5. TCP9 control of neuronal activity allows high spatial and temporal resolution.** a) Time-lapse images of GCaMP6s (green) and DsRed2 (red) fluorescence of TCP9 evoked photoresponses on a single neuron. Scale bar 50 µm. b) GCaMP6s signal from single cells in the field of view in (a) after illumination with a spotlight at 405 nm. d) Time-lapse images of merge fluorescence signal from GCaMP6s (green) and DsRed2 (red) of TCP9 evoked photoresponses on a single spine. e) Average fluorescence response of normalized GCaMP6s and DsRed2 signal upon light stimulation of a single spine (n= 4). f) Average fluorescence response from spine (green) and dendrite (purple) of normalized GCaMP6s signal upon light stimulation of a single spine (n= 4). g) Time-lapse $Ca^{2+}$ photoresponses of normalized GCaMP6s signal after repetitive light stimulation of a single spine. Violet bars indicate spotlight illumination with 405 nm laser with FRAP module.

**TCP9 photocontrols neural activity in vivo in *Xenopus* larvae**

The strong ability to control neural activity in a 3D tissue encouraged us to move on to one step further and try to optically induce neural activity in vivo. Previously, we tested TCP9 in rat hippocampal neurons but for a proof of concept of TCP9 in vivo, mammalians pose several complications. A very flexible and advantageous alternative is offered by amphibians like *Xenopus* larvae. Their nervous system is simplified but it shows significant structural and functional homology to the human central nervous system; they have transparent skin; availability of high number of individuals; easy manipulation for imaging recordings[29]. All together bestow to *Xenopus* model the optimal characteristics for the study of synaptogenesis and dendrite development.

Although iGluR receptors are quite conserved between animal kingdoms, we wanted to be sure that we could photoactivate iGluRs from the amphibian *Xenopus* so we started testing TCP9 with preparations of brain slices of *Xenopus tropicalis.* In order to perform calcium imaging experiments in *X. tropicalis* telencephalon slices [30], we set up a method by incubation of a chemical calcium indicator (OGB-1-AM). This chemical labeling is precise enough to distinguish spontaneous cell activity (**Figure S4a**) and TCP9 induced calcium waves (**Figure S4b,f**) similar to glutamate perfusion responses (**Figure S4c**). Light stimulation of non-treated slices does not evoke sizable calcium responses (**Figure S4d**) and green light stimulation does not induce TCP9 photo-activation (**Figure S4e**).

Next, to perform in vivo one-photon $Ca^{2+}$ recordings, bolus injection of OGB-1AM and TCP9 [31] showed a weaker labeling. Spontaneous activity and glutamate evoked calcium waves could be occasionally recorded but TCP9-induced photoresponses are hardly observed. Our preliminary conclusions were that the calcium indicator labeling was inadequate or TCP9 could not be correctly conjugated by direct bolus injection (Data not shown).

In order to overcome these problems of labeling resolution, we in vivo electroporate in *Xenopus laevis* embryos with a combination of a genetic calcium indicator (GCaMP6s) and a morphological marker (mRFP) (ratio of 2:1 respectively) (**Figure 6a-c,f**) (for details see Methods and Appendix protocols)[32,33]. Co-electroporation and expression of two plasmids in the same cell is less efficient, but in comparison with our previous results with bolus injection of chemical calcium indicators, now we can record spontaneous neural activity in single neurons (**Figure 6d**). In presence of TCP9, we can control neural activity with whole field stimulation (**Figure 6e**). As we can see, incubation of TCP9 does not interfere with the natural behavior of neurons (spontaneous activity is not inhibited) (**Figure 6d**). As done with hippocampal organotypic slices, similar results are obtained when we optically stimulate one single neuron from the field of view (**Figure 6f-g**). The graph plot of time lapse recordings during three consecutive light stimulation demonstrates that it is possible to precisely activate one single neuron without influencing the activity of neighboring neurons (**Figure 6g**).

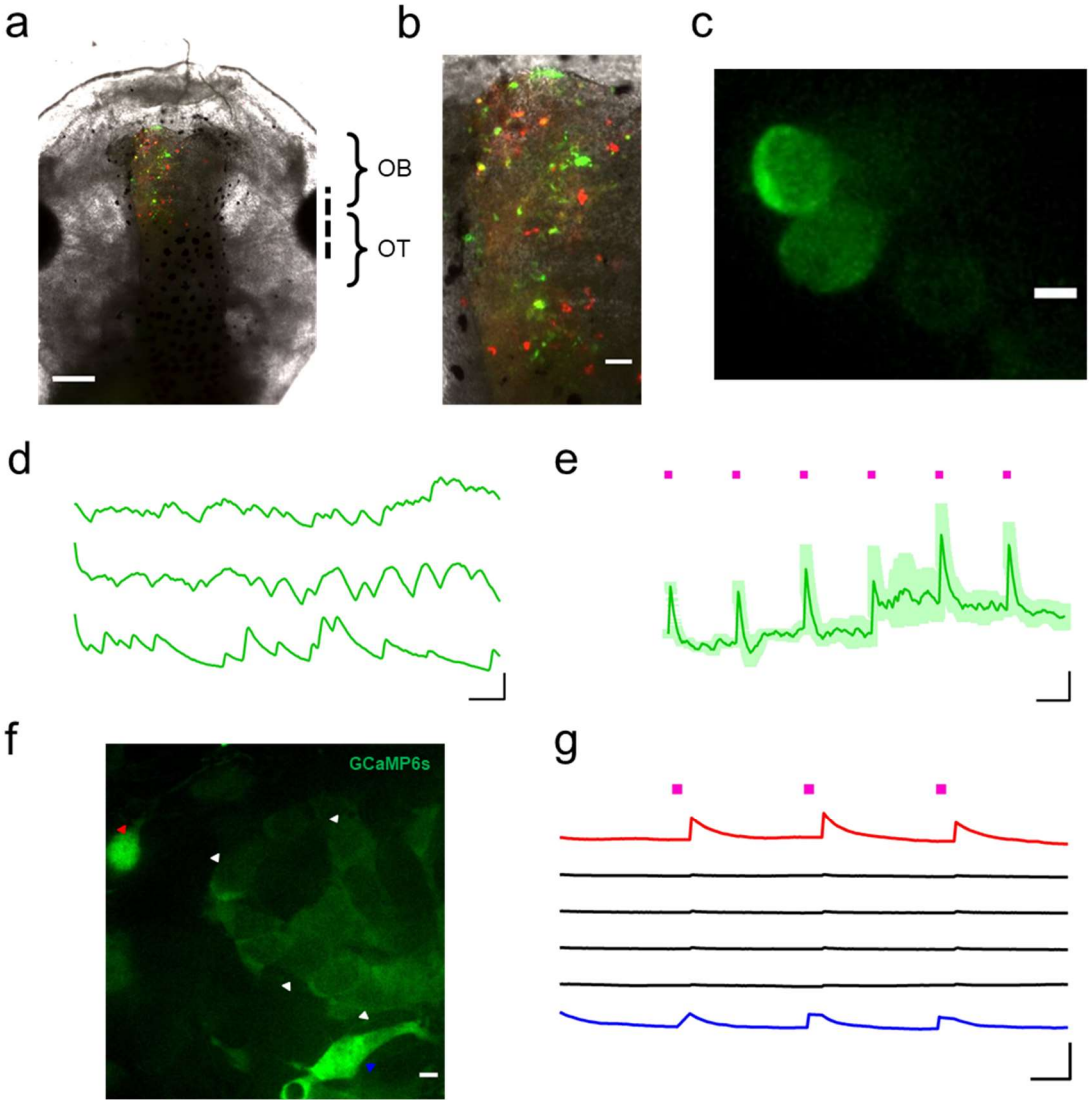


**Figure 6. Neural activity photo induced by TCP9 in *Xenopus* larvae in vivo.** a,b) Olfactory bulb neurons electroporated with GCaMP6s:mRFP (2:1) at stage 28-30. a) OB, olfactory bulbs; OT, optic tectum. Dashed line indicates an eye. Scale bar (a) 100 µm and (b) 20 µm. c) Basal GCaMP6s fluorescence of electroporated olfactory bulb neurons. Scale bar 5 µm. d) Spontaneous activity recorded in cells shown in (c) after TCP9 incubation (250 µM, 15 min in 1X MBS with 0.1mg/ml MS222). Scale bar 10 s, 0.1-fold ($F/F_0$). e) Time course average of neural GCaMP6s fluorescence as a readout of neural activation photo induced by TCP9 after 405 nm laser stimulation (purple squares, 10% laser power for 50 ms). Scale bar 10 s, 0.1-fold ($F/F_0$). f) Basal GCaMP6s fluorescence of electroporated olfactory bulb neurons. Scale bar 5 µm. g) Single cell time course of calcium signal. Single cell stimulation by TCP9 after repetitive (x3) single light spot at 405 nm (1% power, purple squares) induce cell-specific fluorescence increase. Traces correspond to cells pointed in (f) with colored arrows (black traces correspond to white arrows). Scale bar 5 s, 0.5-fold ($F/F_0$).

Interestingly, the olfactory bulb is the only region described with spiny neurons in *Xenopus* [29]. Most of the cell types electroporated show a neuron-like shape without spines on their dendrites, but in some cases, we can observe some spiny neurons (**Figure 7a**). To avoid as much as possible photobleaching and scattered light that can stimulate the dendrite, laser power and exposition time were optimized. One single light pulse of stimulation triggers calcium influx in single spines (**Figure 7a-b**). Recovery occurs in few seconds and photostimulation is reproducible after several pulses (**Figure 7c**). TCP9 photoactivation is specific as we demonstrated that light

stimulation without TCP9 does not elicit comparable calcium signal increase, even at higher light power (**Figure S5**).

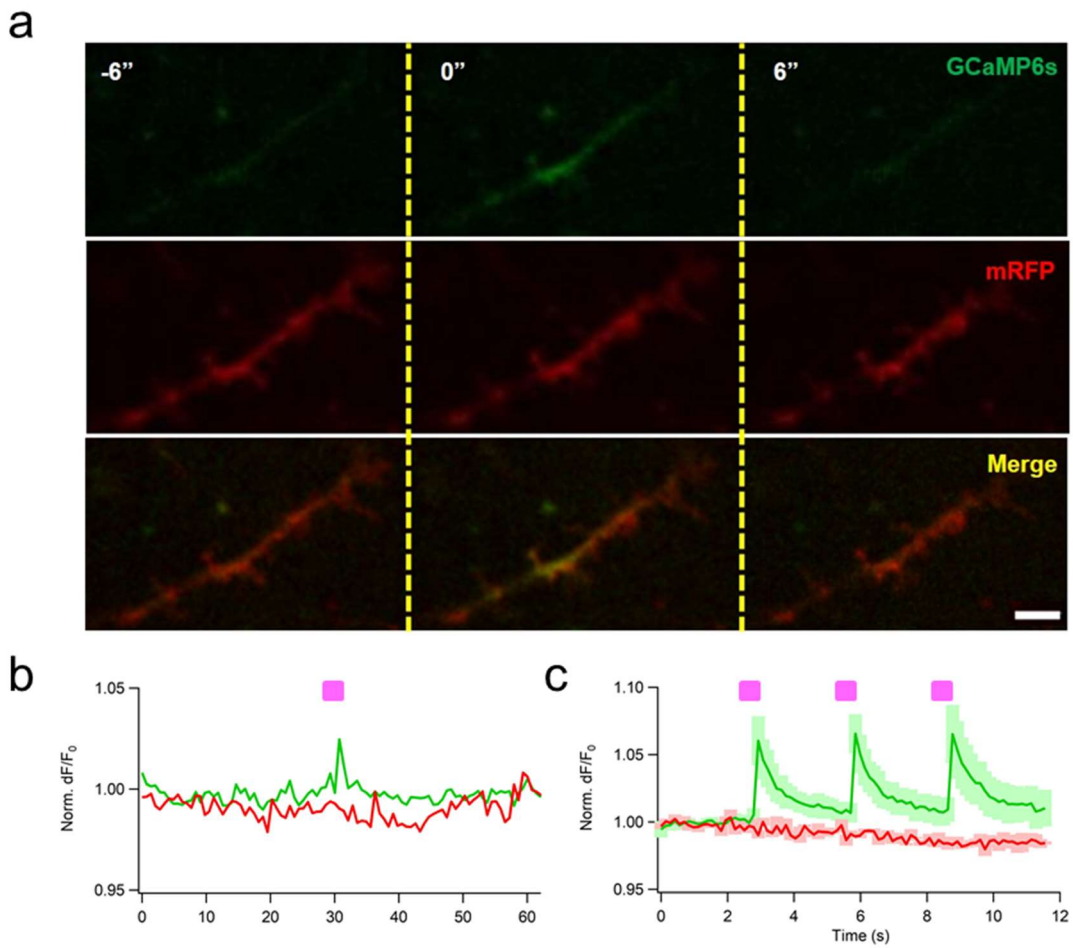


**Figure 7. Photocontrolled activation of single synapses in vivo using TCP9.** a) Time-lapse images of an olfactory bulb neuron electroporated with GCaMP6s:mRFP (2:1) at stage 28-30. Tadpole was incubated with TCP9 (250 µM, 15 min in 1X MBS with 0.1 mg/ml MS222). Scale bar 6 µm. b) Time course of calcium signal from single spine stimulated by single spotlight at 405 nm (1% power). Stimulation was performed with FRAP module Volocity (PerkinElmer). c) Time course average of single spine photo-activation after 3 stimulations (405 nm 1% power). GCaMP6s trace (green) is the average of 6 recordings from 3 different spines from 3 different tadpoles. mRFP trace (red) is the average of 3 recordings from 2 different spines from 2 different tadpoles. Traces are mean ±SEM.

In general, TCP9 photoresponses evoked in vivo are comparable to light-evoked neural activation in hippocampal organotypic slices in terms of reproducibility, recovery time, light pulse reliability, specificity and time resolution.

## DISCUSSION AND CONCLUSIONS

As described in Izquierdo et.al, 2016[17], it is possible to covalently attach PTLs to endogenous glutamate receptors by substitution of the reactive group maleimide by an NHS ester. These new PTLs, called Targeted Covalent Photoswitches (TCPs), demonstrated their capacity to conjugate and photocontrol GluK1[17], and GluA1 homotetramers (this chapter) over-expressed

in a cell line (tsA201 HEK293 cells). Pharmacological inhibition of TCP9 induced photoresponses in primary cultures of dissociated hippocampal neurons corroborate that TCP9 conjugates to endogenous receptors an allows controlling their activity without altering their normal behavior; we can control temporally and spatially the activation of a neuron; and its effect is reversible and can be repeated for hours.

Since genetic engineering is not required to photocontrol neural firing with TCPs, they are ideal for further tests in intact neural circuits in organotypic slices of rat hippocampus and *in vivo* using as a model *Xenopus* larva. Spatial resolution of photoactivation of TCP9 in organotypic hippocampal slices demonstrate the potential of functional tracking endogenous receptors at the level of single spines. Such kind of tools are of special interest for the study of plastic processes, with the advantage that TCP9 does not need special genetic modifications to be operative.
In particular in vivo, we initially tried to photomodulate nerve regeneration in a model of *Xenopus tropicalis* tadpoles (Supplementary results), where we did not observe an improvement of axonal regeneration with TCP9 and LED illumination. However, better labeling, resolution of calcium indicators, and imaging system proved the ability of TCP9 to photomodulate neural activity in *X.laevis* larvae in vivo in real time at single spine level of stimulation. Moreover, with an increment in resolution and sensitivity we could test our molecules at higher stimulation rates to be comparable to the physiological neural activity. *Xenopus* larvae have several advantages as a model to study axonal growth and development[34,35]. In combination with spatiotemporal resolution of TCP9 specific activation of AMPARs we envisage an experimental approach to study the role of native AMPARs in the refinement of retinal ganglion cell axon arbors. AMPARs are described to be involved in axon branch stabilization[36]. Thus, we hypothesize that an over-activation of AMPARs will result in more complex axonal arbors with more mature and stable branches, maybe similar effect as antagonizing NMDARs[37].

In conclusion, here we performed a comprehensive exploration of the different functionalities of covalently attached photoswitches, we have successfully achieved the desired properties on endogenous receptors, and we have demonstrated several new applications in intact brain tissue and in vivo.

**ACKNOWLEDGEMENTS**

We are grateful to members of Gorostiza lab (Dra Nuria Camarero), Soriano lab (Dr Antoni Parcerisas and Dr Ashraf Muhaisen), Llobet lab (Beatrice Terni), Ciruela lab, Holt lab (Dr Hovy Wong), Sanchez-Vives lab (Alessandra Camassa) and Advanced microscopy facility (IRB) (Anna Lladó and Lidia Bardia).

**AUTHOR CONTRIBUTION**

Pau Gorostiza conceived and supervised the project. Miquel Bosch designed and supervised experiments in brain slices. Ana Trapero performed the chemical synthesis at the laboratory of Amadeu Llebaria (IQAC-CID) under his supervision. Aida Garrido-Charles performed in vitro characterization and in vivo experiments. In vivo experiments were supervised by Hovy Wong

and Christine Holt (Cambridge, UK). Organotypic hippocampal slices were performed by Miquel Bosch and Hyojung Lee at the laboratory of Eduardo Soriano (UB). Aida Garrido-Charles assisted to imaging sessions of organotypic slices. Aida Garrido-Charles, Miquel Bosch and Pau Gorostiza wrote the manuscript.

**SUPPLEMENTARY FIGURES**

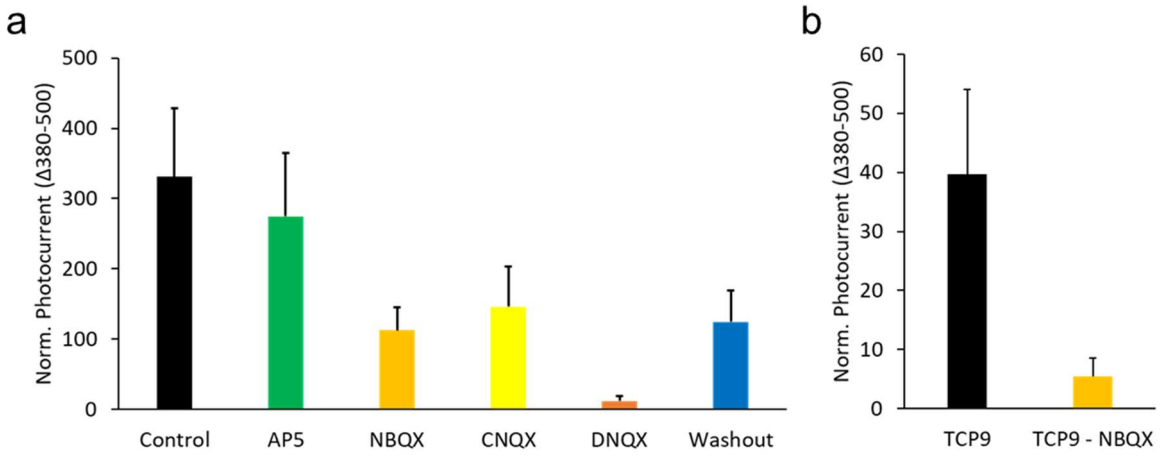


**Figure S1. TCP9 targets preferentially AMPAR and KAR by affinity labelling in rat hippocampal neurons.** a) Quantification of normalized photocurrent difference after incubation of TCP9 (25 µM for 2 min at pH9, control n=9) and bath application of: AP5 (100 µM, n=10); NBQX (10 µM, n=10); CNQX (10 µM, n=4); DNQX (100 µM, n=2); and after washout recovery (n=11). b) Quantification of normalized photocurrent difference after incubation of TCP9 (2.5 µM for 10 min at pH8) in competition with 100 µM NBQX (orange, n=5; black is control, n=9). Error bars are mean ±SEM.

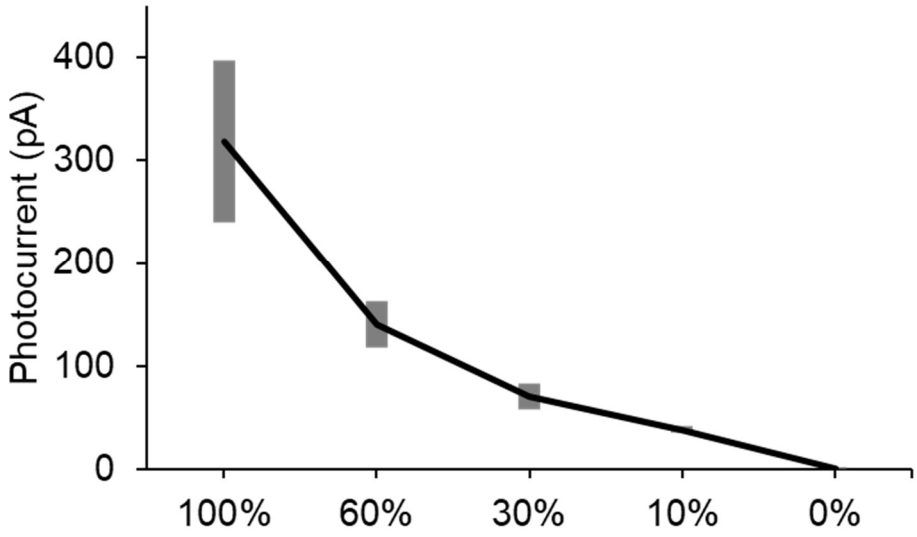


**Figure S2. Light intensity dependence of TCP9 activation in rat hippocampal neural cultures.** Photosensitivity of TCP9 was determined from the dependence of light-induced photocurrent in hippocampal neurons with light intensity. Error bars are mean ±SEM, n=11 photocurrent for 0% intensity, n=15 photocurrents for 10-30-60-100% intensity.

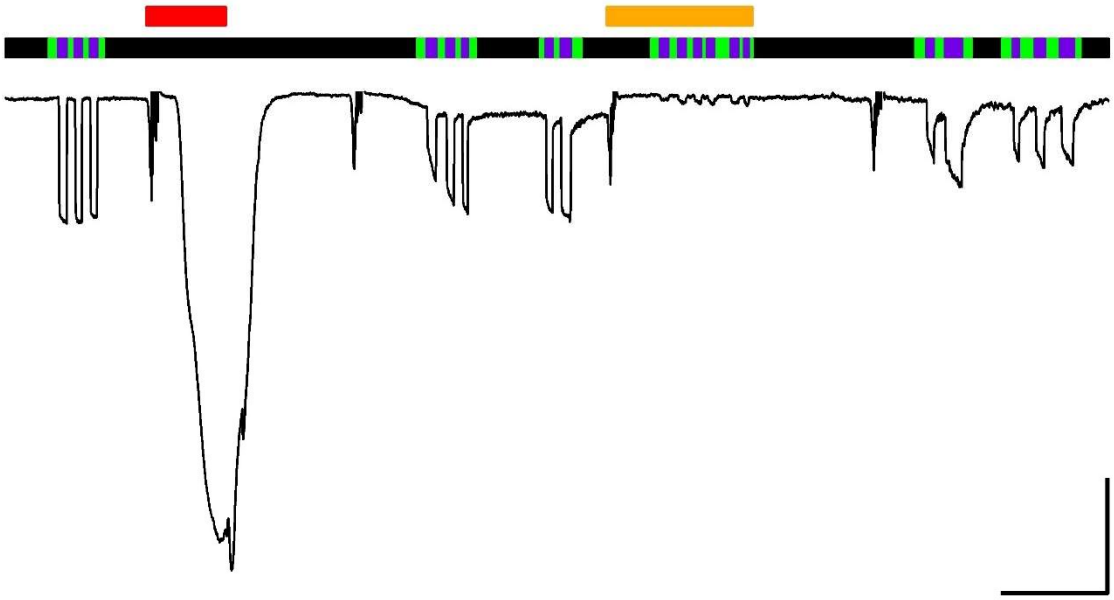

**Figure S3. Current whole-cell voltage clamp recording in HEK239 tsA201 cells expressing GluA1 incubated with TCP9 (25 µM for 2 min at pH9).** Light pulses are indicated in green (500 nm) and purple (380 nm) and are done in presence of CTZ (25 µM). Absence of light is colored in dark. Addition of 500 µM of glutamate is indicated in red and 50 µM of DNQX is in orange. Scale bar 50 s, 500 pA.

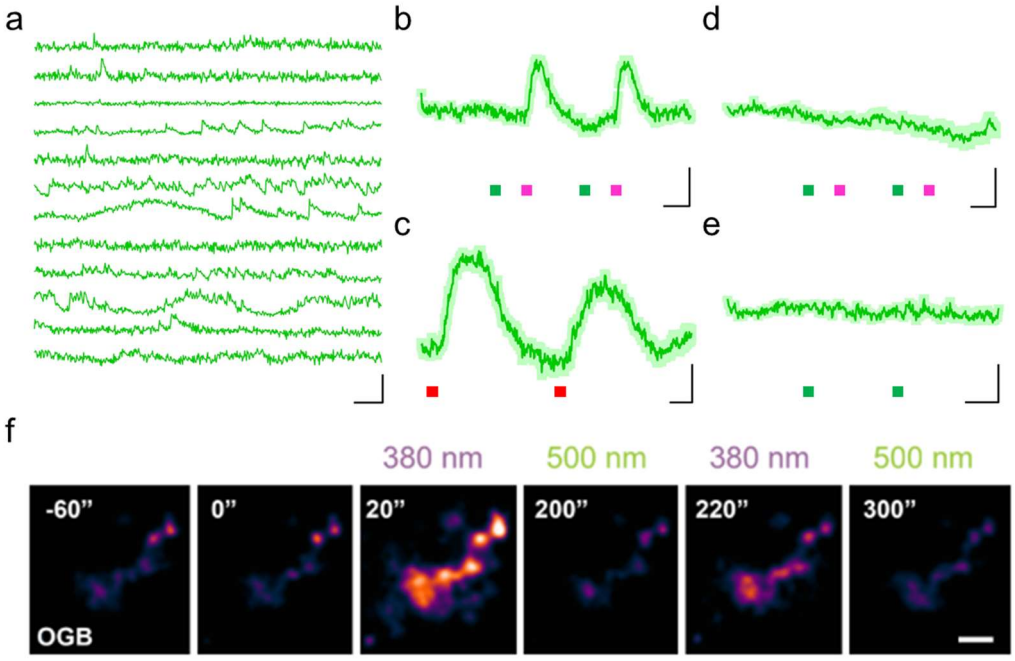


**Figures S4. Calcium imaging in *Xenopus tropicalis* olfactory bulb slices incubated with TCP9 and OGB1-AM.** a) Real time spontaneous activity of single cells recorded from a *X.tropicalis* brain slice incubated with OGB1-AM (20 µM, 30 min) followed by incubation of TCP9 (250 µM, 20 min). Scale bar 50 s, 0.5 $dF/F_0$. b) TCP9 induced photo-activation by pulses of 380 and 500 nm (purple and green, respectively). c) Physiological calcium signal increase upon bath perfusion of glutamate (1 mM). d) Brain slices not incubated with TCP9 do not respond to light. e) Brain slices incubated with TCP9 do not respond to 500 nm light. Thus, discarding light or TCP9 unspecific effects. b-e) Scale bar 50 s, 0.05 $dF/F_0$. f) Time-lapse images of OGB1-AM fluorescence. Scale bar 20 µm.

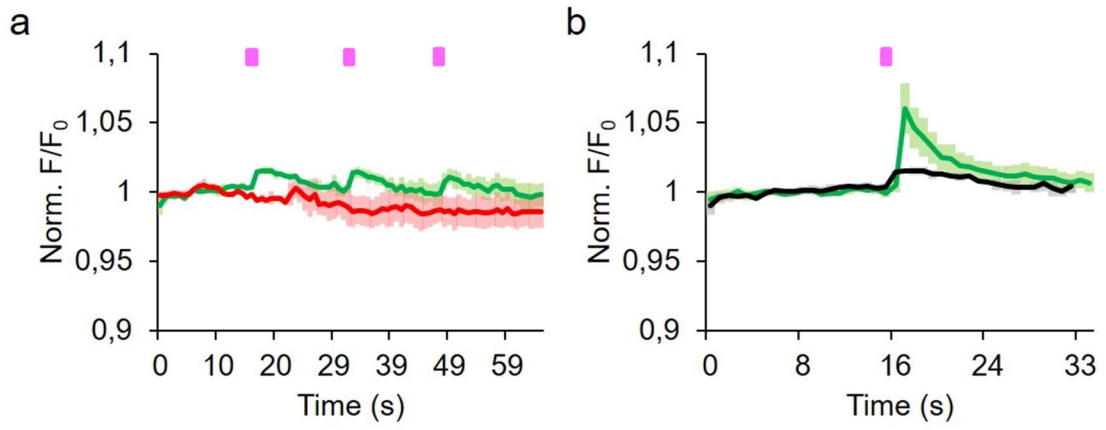


**Figure S5. Light stimulation of spines in non-treated TCP9 tadpoles do not respond to light at higher light power.** a) Time course average of single spine evoked fluorescence after 3 consecutive stimulations (405 nm 5%). GCaMP6s trace (green) and mRFP trace (red) are the average from 3 different spines from the same tadpole. b) Comparison of single pulse average between TCP9 incubated tadpoles stimulated with 405 nm at 1% (green trace) and TCP9 non-treated tadpole stimulated with 405 nm at 5% (black trace).

## METHODS

**Cell line and transfection**. HEK293 tsA201 cell line (SV40-transformed, Human Embryonic Kidney 293 cells) was maintained at 37 °C in a 5% $CO_2$ humid incubator with Dulbecco's Modified Eagle Medium/Nutrient Mixture F-12 media (DMEM) (1:1, Invitrogen) supplemented with 10% Fetal Bovine Serum (FBS) and 1% Penicillin/Streptomycin. Cells transiently expressed the receptor subunit GluA1. The expression plasmid of GluA1 was kindly provided by David Soto (University of Barcelona). DNA–X-tremGENE 9 Transfection Reagent (Roche) mix was used following manufacturer's instructions with a Reagent:DNA ratio of 3:1. GluA1 plasmid was co-transfected with eGFP with a Transfection Reagent:GluA1:eGPF ratio of 3:1:0.1. The mix was incubated for 20 min at room temperature, meanwhile cells were detached and freshly plated into a 12-mulltiwell plate at a density of $3 \times 10^5$ cells before the DNA-Transfection Reagent mix was added dropwise into each well. Experiments were performed after 48–72 h, and the day before the experiment cells were plated at low density on 16-mm coverslips (Fisher Scientific) treated with collagen (Sigma-Aldrich) to allow cell adhesion.

**Electrophysiology.** Whole-cell voltage-clamp recordings were done using an EPC-10 amplifier and data at 10 kHz was acquired with amplifier's software Patch Master (HEKA). Bath solution was composed of (in mM): 140 NaCl, 1 $MgCl_2$, 2.5 KCl, 10 HEPES, 2.5 $CaCl_2$ and 10–20 glucose to fix osmolarity to 310 mOsm·$kg^{-1}$, while pH 7.42 was adjusted with NaOH. Borosilicate glass pipettes were pulled with a typical resistance of 4–6 MΩ for HEK293 cells. Pipette solution contained (in mM): 120 cesium methanosulfonate, 10 TEA-Cl, 5 $MgCl_2$, 3 $Na_2ATP$, 1 $Na_2GTP$, 20 HEPES, 0.5 EGTA; osmolarity was 290 mOsm·$kg^{-1}$ and pH 7.2 was adjusted with CsOH.

Before starting the recording, cells were incubated with TCP9 at a concentration of 25 µM (<1% DMSO) for 2 min, in the absence of light and in pH 9 bath solution composed by (in mM): 100 NaCl, 1 $MgCl_2$, 2.5 KCl, 2.5 $CaCl_2$, 10 glucose and 50 sodiumcarbonate/sodiumbicarbonate, 310mOsm$kg^{-1}$, pH 9 adjusted with NaOH.

Light stimulation was done by illumination of the entire focused field using a Polychrome V monochromator (TILL Photonics) connected through the back port of an IX71 inverted microscope (Olympus) with a CP- ACHROMAT x40/0.65 objective (Zeiss) or XLUMPLFLN 20XW x20/1 water immersion objective (Olympus). For automatically controlling wavelength, the monochromator was connected to the EPC-10 amplifier via Photochromic Manual Control (TILL Photonics) and controlled with the photometry module of Patch Master. Light power density measured with a Newport 1916-C light meter after the objective was 22.0 µW $mm^{-2}$ for 380 nm, 45.9 µW $mm^{-2}$ for 460 nm and 47.4 µW $mm^{-2}$ for 500 nm.

**Rat hippocampal neural primary culture**. All procedures were conducted in accordance with the European guidelines for animal care and use in research, and were approved by the Animal Experimentation Ethics Committee at the University of Barcelona (Spain). Low-density primary hippocampal cultures were prepared from newborn P0-P3 pups from Sprague Dawley rat and maintained in cell culture for 1-2 weeks in coverslips coated with poly-L-lysine (Sigma-Aldrich), as previously described [38–40]. Cells were cultured with complete medium (Neurobasal A, B-27 5%, GlutaMax (0.5x), glucose 15 mM, penicillin (5 U $ml^{-1}$) and streptomycin (5 µg $ml^{-1}$)). Within 48-72 h an anti-mitotic treatment with AraC 5 µM is done to avoid fibroblast and astrocyte proliferation. Half of the medium in each well was changed every 3-4 days.

**Electrophysiology recording conditions for rat hippocampal neurons.** Voltage and current-clamp recordings under whole-cell configuration were done using an EPC- 10 amplifier and data at 10 kHz was acquired with amplifier's software Patch Master (HEKA). Bath solution was

composed of (in mM): 140 NaCl, 2 $MgCl_2$, 2.5 KCl, 10 HEPES, 0.2 $CaCl_2$ and 10–20 mM glucose to fix osmolarity to 310 mOsm·$kg^{-1}$, pH 7.42 adjusted with NaOH. Borosilicate glass pipettes were pulled with a typical resistance of 6–8 MΩ for neurons. Pipette solution contained (in mM): 130 KCl, 5 $MgCl_2$, 3 $Na_2ATP$, 1 $Na_2GTP$, 20 HEPES, 0.5 EGTA. Osmolarity is adjusted at 289 mOsm·$kg^{-1}$ and pH 7.2 adjusted with KOH. During recordings, neurons were maintained at room temperature (r.t., 25-27 °C) in a continuous perfusion of bath solution.

Before starting the recording, neurons were incubated with TCP9 at a concentration between 12 and 25 µM (1% DMSO) for 2min, in the absence of light and in pH 9 bath solution composed by (in mM): 100 NaCl, 1 $MgCl_2$, 2.5 KCl, 2.5 $CaCl_2$, 10 glucose and 50 sodiumcarbonate/sodiumbicarbonate, 310mOsm$kg^{-1}$, pH 9 adjusted with NaOH. Incubation conditions for affinity labelling are the following: 2.5 µM of TCP9, 1% DMSO in pH 8 bath solution alone or in competition with 100 µM NBQX for 10 min (**Figure S2b**). Composition of pH 8 bath solution is the same as the bath solution used for recordings, with pH adjusted at 8 with NaOH. Before placing the coverslip to the recording chamber, cells were washed again with fresh bath solution.

Light stimulation was done by illumination of the entire focused field using a Polychrome V monochromator (TILL Photonics) connected through the back port of an IX71 inverted microscope (Olympus) with a CP- ACHROMAT x40/0.65 objective (Zeiss). For automatically controlling wavelength, the monochromator was connected to the EPC-10 amplifier via Photochromic Manual Control (TILL Photonics) and controlled with the photometry module of Patch Master. Light power density measured with a Newport 1916-C light meter after the objective was 1.6 mW $mm^{-2}$ for 425 nm, 0.8 mW $mm^{-2}$ for 380 nm and 1.8 mW $mm^{-2}$ for 500 nm.

**Rat organotypic hippocampal slice culture and gene transfection.** All procedures were conducted in accordance with the European guidelines for animal care and use in research, and were approved by the Animal Experimentation Ethics Committee at the University of Barcelona (Spain). Hippocampal organotypic slice cultures were prepared from postnatal day 6-7 rats as described [41]. Slices were cultured at 35 °C on interface membranes (Millipore) and fed with MEM media containing 20% horse serum, 27 mM D-glucose, 6 mM $NaHCO_3$, 2 mM CaCl2, 2 mM $MgSO_4$, 30 mM HEPES, 0.01 % ascorbic acid and 1 µg/ml insulin. pH was adjusted to 7.3 and osmolality to 300-320 mOsm $kg^{-1}$. Slices were biolistically transfected (BioRad) after 5-7 DIV with GCaMP6s (Addgene) under CMV promoter and DsRed2 under CAG promoter as described [4,8].

**TCP9 conjugation in hippocampal slice culture.** For hippocampal organotypic slice cultures, TCP9 was incubated at 250 µM in a 12-multiwell plate in artificial cerebrospinal fluid (ACSF) containing: 119 mM NaCl, 2.5 mM KCl, 3 mM $CaCl_2$, 0.2 mM $MgCl_2$, 26.2 mM $NaHCO_3$, 1 mM $NaH_2PO_4$ and 11 mM glucose, equilibrated with 5% $CO_2$/95% $O_2$. Three different steps of washout with fresh ACSF were done in different wells of the same plate, lasting 1 min, 5 min and 5 min. Afterwards, slices were placed on the recording chamber. Slices were maintained at room temperature (r.t., 25-27 °C) in a continuous perfusion of ACSF.

**Calcium imaging with 1P stimulation.** Time-lapse fluorescence imaging was carried out in the Advanced Digital Microscopy Core Facility of IRB Barcelona with a SP5 spectral confocal multiphoton microscope (Leica) equipped with a 405 nm cw diode laser, an Argon laser (488 and 514 nm). We used a 40x/1.25-0.75-NA Oil objective (HCX PL APO, Leica). Imaging was performed at 8-15 DIV in pyramidal neurons co-expressing GCaMP6s and DsRed2 in a single focused plane. Selected neurons presented healthy morphology and no signs of fluorescent aggregates. Green and red fluorescent proteins were simultaneously excited at 488 nm for 343 ms, using bidirectional laser scanning at 400 Hz. Images were recorded with a resolution of 512x512, and

with an imaging interval of 4 s. Green and red fluorescence were recorded with two different HyD detectors with a detection range from 500 to 550 nm and from 569 to 648 nm, respectively. Pinhole aperture was set at maximum (600 µm). Whole field photostimulation flashes were fit to keep imaging interval, and periods lasted in total for 1 min. Photostimulation was done at 256x256 resolution with bidirectional laser scan. One-photon photostimulation was done at 405 nm (0.81 mW $\mu m^{-2}$), and back-photoisomerization was achieved at 514 nm (0.35 mW $\mu m^{-2}$). Inter-stimulus imaging periods lasted 1.5 min. Single cell and single spine photostimulation were performed using a Flymode FRAP module. Intensity and duration of the photostimulation intervals were adjusted to obtain the optimal photoresponse and reproducibility. At the end of each experiment we reconfirmed that the neuron kept its healthy morphology.

***Xenopus laevis* embryos maintenance.** *Xenopus laevis* embryos obtained from in vitro fertilization were raised in 0.1X Modified Barth's saline (MBS; 8.8 mM NaCl, 0.1 mM KCl, 82 µM $MgSO_4$, 0.24 mM $NaHCO_3$, 0.1 mM HEPES, 33 µM $Ca(NO_3)_2$, 41 µM $CaCl_2$) at 14-22°C, and staged according to the table of Nieuwkoop and Faber (Nieuwkoop and Faber, 1967). This research has been regulated under the Animals (Scientific Procedures) Act 1986 Amendment Regulations 2012 following ethical review by the University of Cambridge Animal Welfare and Ethical Review Body (AWERB).

**In vivo electroporation.** Olfactory bulb electroporation procedure was modified from [32,33]. Stage 28 embryos were anesthetized in 0.4 mg/ml MS222 in 1X MBS. The central ventricle between olfactory bulbs was injected with electroporation mixture (1 µg/µl of GCaMP6s:mRFP; 2:1), followed by 8 squared electric pulses of 50 ms duration at 1000 ms intervals, delivered at 18 V. The embryos were recovered and raised in 0.1X MBS until the desired embryonic stage for experiment.

**In vivo calcium imaging.** Embryos were lightly anaesthetized with 0.4mg/ml MS222 in 1X MBS. The surface of the brain was exposed by removal of the overlying epidermis [42,43]. Embryos were mounted in an oxygenated chamber created with Permanox slides (Sigma-Aldrich) and Gene Frame (ThermoFisher) and bathed in 1X MBS with 0.1 mg/ml MS222, for visualization with fluorescence microscopy. Real time calcium imaging was performed using 60X UPLSAPO objective (NA 1.3) with a PerkinElmer Spinning Disk UltraVIEW ERS, Olympus IX81 inverted spinning disk confocal microscope. Imaging of electroporated cell distribution in the olfactory bulb was performed with Plan Fluor 20X (NA 0.5) using a Nikon Eclipse TE2000-U inverted microscope. Z stack intervals of 1-2 µm were employed for acquiring images with Volocity (PerkinElmer).

**Data analysis and statistics**. Amplitude of photocurrents were analyzed using IgorPro (Wavemetrics). Displayed whole-cell current traces have been filtered using the infinite impulse response digital filter from IgorPro (low-pass filter with cutoff of 50 Hz). The drift in current observed during light spectra recordings was corrected where appropriate with the IgorPro (WaveMetrics) software using a custom-made macro for drift correction.

Organotypic hippocampal slices calcium images were acquired with the acquisition software LAS AF (version 2.4.1 + Matrix HCS-A). These images were analyzed with ImageJ and the mean fluorescence value for each cell profile was calculated using the same software. The fluorescence signals were treated to obtain ΔF/F values according to:

$$\frac{\Delta F}{F} = \frac{F\text{-}F_0}{F_0} \quad (1)$$

where $F_0$ is each cell's average signal for the experiment's baseline and F is the fluorescence signal upon stimulation. The resulting fluorescence ratios were analyzed in Microsoft Excel (Microsoft).

To obtain cell-averaged calcium imaging graphs, ΔF/F (also represented as $dF/F_0$) values were first normalized with respect to the average ΔF/F values from the baseline period (images recorded before any light stimulation).

## SUPPLEMENTARY RESULTS

### Nerve regeneration animal model of Xenopus tropicalis

Further applications of TCP9 were explored as to photocontrol nerve regeneration in our model in transgenic *Xenopus tropicalis.* Our hypothesis is that increased activity (evoked by TCP9 and light) in the targeted neurons to be reconnected, would induce differences in the regeneration rate and the thickness of the regenerated nerve. After degeneration of the olfactory nerve, TCP was injected in the olfactory bulb. To photoactivate TCP, tadpoles were kept in separated tanks with an illumination pattern of: (1) 1 Hz alternating 380 nm and 500 nm light; and (2) 375 nm light on for 10 sec every 2 min. We observed that in control animals the regeneration is completed in four days, as in wild type non-treated animals. But, regeneration in TCP-treated group with illumination pattern (1) is 1 day slower than in controls (**Figure S6a**). Illumination pattern (2) do not evoke significant changes in the regeneration process of the degenerated olfactory nerve (**Figure S6b**). For details in protocol and analysis see Appendix protocols.

Nerve regeneration in amphibians is a finely tuned process characterized to be activity dependent[43,44]. If we alter neural activity in the olfactory bulb with TCP light stimulation, we alter the whole homeostasis of the process. One possible explanation of the delay observed under illumination pattern (1) might be that TCP targets ionotropic glutamate receptors (kainate and AMPA) from external tufted cells at the granular layer of the olfactory bulb. The overactivation of these cells inhibits spontaneous and odor-evoked neural activity transduced to mitral/tufted cells[45]. However, TCP administration and conjugation are not specifically directed to one single cell type of the olfactory bulb and so with the current approximation we can only conclude that proper input signals and circuitry homeostasis is essential in the correct nerve regeneration process.

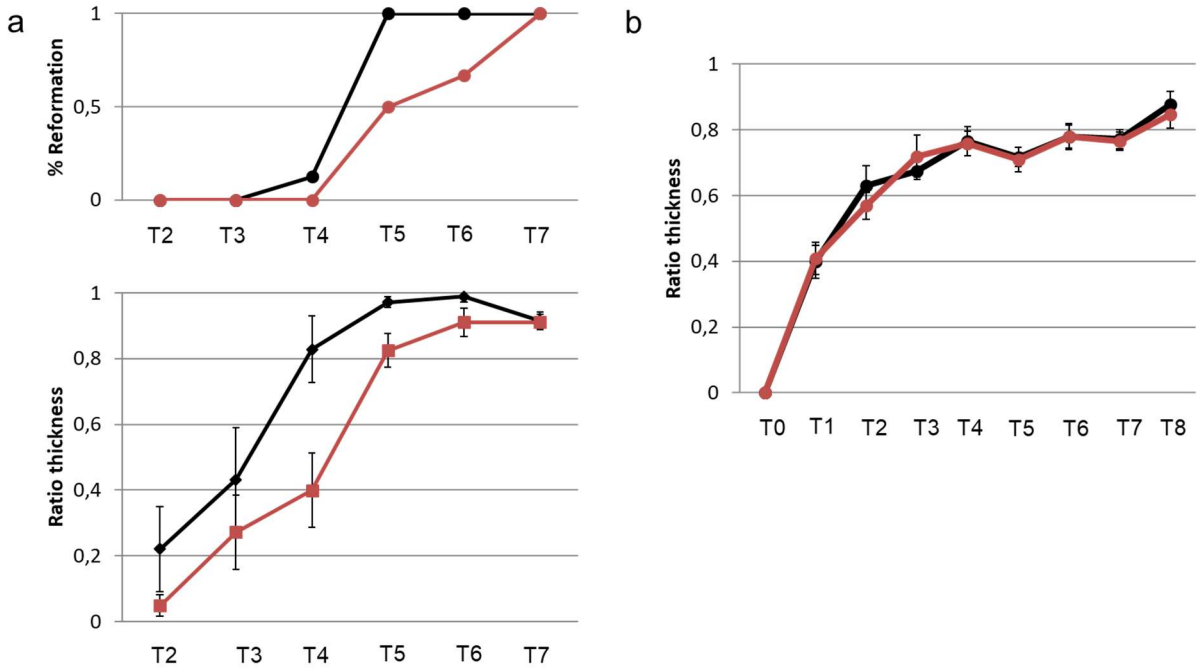


**Figure S6. Time-course of olfactory nerve reformation.** Top a) shows the percentage of successful reconnection to the olfactory bulb and the relative increase in olfactory nerve width as a function of time (down) obtained after TCP9 treatment with illumination pattern 1. b) Relative increase in olfactory nerve thickness after TCP9 treatment with illumination pattern 2. Data points are displayed as mean ±SEM.

**REFERENCES**


1. Choquet, D. & Triller, A. The dynamic synapse. *Neuron* **80**, 691–703 (2013).
2. Sharpee, T. O. *et al.* 25th Annual Computational Neuroscience Meeting: CNS-2016. *BMC Neurosci.* **17**, 1–112 (2016).
3. Malinow, R. & Malenka, R. C. Ampa Receptor Trafficking and Synaptic Plasticity. *Annu. Rev. Neurosci.* **25**, 103–126 (2002).
4. Bosch, M., Castro, J., Sur, M. & Hayashi, Y. Photomarking Relocalization Technique for Correlated Two-Photon and Electron Microcopy Imaging of Single Stimulated Synapses. in *Synapse Development: Methods and Protocols* (ed. Poulopoulos, A.) 185–214 (Springer New York, 2017). doi:10.1007/978-1-4939-6688-2_14
5. Groc, L. *et al.* Surface trafficking of neurotransmitter receptor: Comparison between single-molecule/quantum dot strategies. *J. Neurosci.* **27**, 12433–12437 (2007).
6. Alcor, D., Gouzer, G. & Triller, A. Single-particle tracking methods for the study of membrane receptors dynamics. *Eur. J. Neurosci.* **30**, 987–997 (2009).
7. Okamoto, K., Bosch, M. & Hayashi, Y. The roles of CaMKII and F-Actin in the structural plasticity of dendritic Spines: A potential molecular identity of a synaptic tag? *Physiology* **24**, 357–366 (2009).
8. Bosch, M. *et al.* Structural and molecular remodeling of dendritic spine substructures during long-term potentiation. *Neuron* **86**, 3279–3288 (2014).
9. Willard, S. S. & Koochekpour, S. Glutamate , Glutamate Receptors , and Downstream Signaling Pathways. *Int. J. Biol. Sci.* **9**, 948–959 (2013).
10. *The Glutamate Receptors*. (Humana Press, 2008).
11. Scheefhals, N. & MacGillavry, H. D. Functional organization of postsynaptic glutamate receptors. *Mol. Cell. Neurosci.* **91**, 82–94 (2018).
12. Traynelis, S. F. *et al.* Glutamate Receptor Ion Channels : Structure , Regulation , and Function. *Pharmacol. Rev.* **62**, 405–496 (2010).
13. Luscher, C. & Malenka, R. C. NMDA Receptor-Dependent Long-Term Potentiation and Long-Term Depression (LTP/LTD). *Cold Spring Harb. Perspect. Biol.* **4**, a005710–a005710 (2012).
14. Rost, B. R., Schneider-Warme, F., Schmitz, D. & Hegemann, P. Optogenetic Tools for Subcellular Applications in Neuroscience. *Neuron* **96**, 572–603 (2017).
15. Paoletti, P., Ellis-Davies, G. C. R. & Mourot, A. Optical control of neuronal ion channels and receptors. *Nat. Rev. Neurosci.* (2019). doi:10.1038/s41583-019-0197-2
16. Kienzler, M. A. & Isacoff, E. Y. Precise modulation of neuronal activity with synthetic photoswitchable ligands. *Curr. Opin. Neurobiol.* (2017). doi:10.1016/j.conb.2017.05.021
17. Izquierdo-Serra, M. *et al.* Optical control of endogenous receptors and cellular excitability using targeted covalent photoswitches. *Nat. Commun.* **7**, 12221 (2016).
18. Farrants, H. *et al.* SNAP-Tagged Nanobodies Enable Reversible Optical Control of a G Protein-Coupled Receptor via a Remotely Tethered Photoswitchable Ligand. *ACS Chem. Biol.* **13**, 2682–2688 (2018).

19. Broichhagen, J. *et al.* Orthogonal optical control of a G protein-coupled receptor with a SNAP-tethered photochromic ligand. *ACS Cent. Sci.* **1**, 383–393 (2015).

20. Levitz, J. *et al.* Dual optical control and mechanistic insights into photoswitchable group II and III metabotropic glutamate receptors. *Proc. Natl. Acad. Sci. U. S. A.* **114**, E3546–E3554 (2017).

21. Donthamsetti, P. C. *et al.* Genetically-targeted optical control of an endogenous G protein-coupled receptor. *J. Am. Chem. Soc.* (2019). doi:10.1021/jacs.9b02895

22. Reiner, A. & Isacoff, E. Y. Tethered ligands reveal glutamate receptor desensitization depends on subunit occupancy. *Nat. Chem. Biol.* 1–10 (2014). doi:10.1038/nchembio.1458

23. Kakegawa, W. *et al.* Optogenetic Control of Synaptic AMPA Receptor Endocytosis Reveals Roles of LTD in Motor Learning. *Neuron* **99**, 985-998.e6 (2018).

24. Bayley, H. & Knowles, J. R. Affinity labeling. in *Methods in Enzymology* (ed. William, M. W. & Jakoby, B. . 69) 69–114 (Academic Press, 1977).

25. Mayer, M. L. Crystal Structures of the GluR5 and GluR6 Ligand Binding Cores : Molecular Mechanisms Underlying Kainate Receptor Selectivity. *Neuron* **45**, 539–552 (2005).

26. Herguedas, B. *et al.* Architecture of the heteromeric GluA1/2 AMPA receptor in complex with the auxiliary subunit TARP γ8. *Science (80-. ).* eaav9011 (2019). doi:10.1126/science.aav9011

27. Ehlers, M. D. Reinsertion or degradation of AMPA receptors determined by activity-dependent endocytic sorting. *Neuron* **28**, 511–525 (2000).

28. Lee, H. K., Kameyama, K., Huganir, R. L. & Bear, M. F. NMDA induces long-term synaptic depression and dephosphorylation of the GluR1 subunit of AMPA receptors in hippocampus. *Neuron* **21**, 1151–1162 (1998).

29. Huang, Y.-B., Hu, C.-R., Zhang, L., Yin, W. & Hu, B. In Vivo Study of Dynamics and Stability of Dendritic Spines on Olfactory Bulb Interneurons in Xenopus laevis Tadpoles. *PLoS One* **10**, e0140752 (2015).

30. Manzini, I., Schweer, T. S. & Schild, D. Improved fluorescent (calcium indicator) dye uptake in brain slices by blocking multidrug resistance transporters. *J. Neurosci. Methods* **167**, 140–147 (2008).

31. Dunfield, D. & Haas, K. In vivo single-cell excitability probing of neuronal ensembles in the intact and awake developing Xenopus brain. *Nat. Protoc.* **5**, 841–848 (2010).

32. Falk, J. *et al.* Electroporation of cDNA/Morpholinos to targeted areas of embryonic CNS in Xenopus. *BMC Dev. Biol.* **7**, 107 (2007).

33. Wong, H. H.-W. & Holt, C. E. Targeted electroporation in the CNS in Xenopus embryos. in *Xenopus. Methods in Molecular Biology* (ed. Vleminckx, K.) 119–130 (2018).

34. Shigeoka, T. *et al.* Dynamic Axonal Translation in Developing and Mature Visual Circuits. *Cell* **166**, 181–192 (2016).

35. Wong, H. H. W. *et al.* RNA Docking and Local Translation Regulate Site-Specific Axon Remodeling In Vivo. *Neuron* **95**, 852-868.e8 (2017).

36. Haas, K., Li, J. & Cline, H. T. AMPA receptors regulate experience-dependent dendritic

arbor growth in vivo. *Proc. Natl. Acad. Sci. U. S. A.* **103**, 12127–31 (2006).

37. Berlin, S. *et al.* A family of photoswitchable NMDA receptors. *Elife* 1–29 (2016). doi:10.7554/eLife.12040

38. Halliwell, R. F., Peters, J. A. & Lambert, J. J. The mechanism of action and pharmacological specificity of the anticonvulsant NMDA antagonist MK-801: a voltage clamp study on neuronal cells in culture. *Br. J. Pharmacol.* **96**, 480–494 (1989).

39. Beaudoin, G. M. J. *et al.* Culturing pyramidal neurons from the early postnatal mouse hippocampus and cortex. *Nat. Protoc.* **7**, 1741–1754 (2012).

40. Kaech, S. & Banker, G. Culturing hippocampal neurons. *Nat. Protoc.* **1**, 2406–2415 (2006).

41. Okamoto, K. I., Nagai, T., Miyawaki, A. & Hayashi, Y. Rapid and persistent modulation of actin dynamics regulates postsynaptic reorganization underlying bidirectional plasticity. *Nat. Neurosci.* **7**, 1104–1112 (2004).

42. Chien, C. Bin, Rosenthal, D. E., Harris, W. A. & Holt, C. E. Navigational errors made by growth cones without filopodia in the embryonic xenopus brain. *Neuron* **11**, 237–251 (1993).

43. Terni, B., Pacciolla, P., Masanas, H., Gorostiza, P. & Llobet, A. Tight temporal coupling between synaptic rewiring of olfactory glomeruli and the emergence of odor-guided behavior in Xenopus tadpoles. *J. Comp. Neurol.* **525**, 3769–3783 (2017).

44. Kikuta, S. *et al.* Sensory Deprivation Disrupts Homeostatic Regeneration of Newly Generated Olfactory Sensory Neurons after Injury in Adult Mice. *J. Neurosci.* **35**, 2657–2673 (2015).

45. Tatti, R. *et al.* A population of glomerular glutamatergic neurons controls sensory information transfer in the mouse olfactory bulb. *Nat. Commun.* **5**, (2014).

## CHAPTER 3| Alternative strategies to spatiotemporally pattern the conjugation of TCPs

### INTRODUCTION

The spatial control of conjugation with light was previously described in PTLs like MAG (Gorostiza et al. 2007) and TCP9 (Izquierdo-Serra et al. 2016), where differences in isomerization potentiate or inhibit their conjugation to the target protein, taking advantage of the "affinity labeling" mechanism of conjugation. With different light patterns at different wavelengths, it is possible to spatially control the conjugation of different PTLs. However, in the absence of light stimulation the photoswitch is still conjugated.

Now, to further increase the spatiotemporal resolution of TCPs, we modified their structural design in order to make them chemically inert in the absence of light. Instead of directly reacting with cysteines (MAGs) or lysines (TCPs), conjugation can be controlled in space and time with light. For that purpose, we chemically modified the reactive moiety of TCP9 with a photolabile group and designed a photoswitchable photoaffinity ligand named photoTCP (Figure 1). A photoaffinity ligand is a ligand containing a photoreactive group which upon irradiation generates a reactive species that covalently binds the ligand to its target macromolecule. Previously, photolabile groups such as benzophenones, aryl azides and diazirines have been used to control the release of neurotransmitters, identify receptors and their binding sites, characterize synapse function and monitor receptor trafficking in real-time (Chambers et al. 2004; Mortensen et al. 2014; Weiser, Kelz, and Eckenhoff 2013).

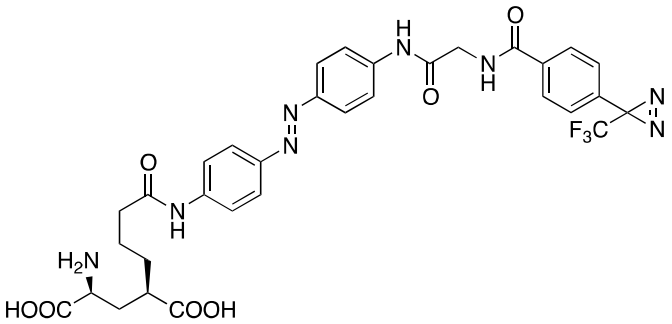


**Figure 1.** Chemical structure of photoreactive compound photoTCP.

Here, after exploring many other possibilities, we use a photoswitchable ligand containing a photoactivatable diazirine group. In comparison with other photoreactive groups, the diazirine group is preferable because of some advantages such as small size, stability at room temperature, relative stability to nucleophiles (such as thiols), absorption at longer wavelengths (350–355 nm), short lifetime upon irradiation and high subsequent reactivity(Dubinsky, Krom, and Meijler 2012). Upon irradiation, diazirines generate reactive carbenes which are bivalent carbon intermediates containing two non-bonding orbitals (Figure 2). The most significant feature of carbenes is their ability to rapidly form a covalent bond with the nearest target molecule through C–C, C–H, O–H and X–H (X = heteroatom) insertions. Photolabeling reaction results in the release of NHS that can form, as described previously, covalent bonds with any amino acid side chain of the ligand binding domain of native glutamate receptors.

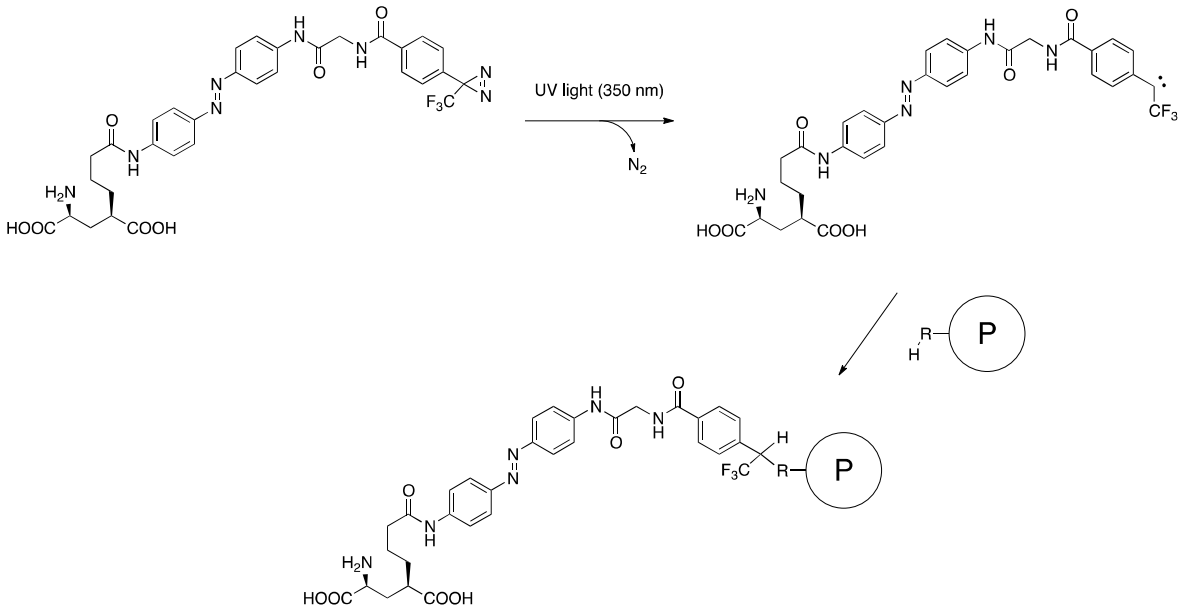


**Figure 2.** Mechanism of carbene-mediated photoaffinity labeling.

## RESULTS

### Photoaffinity labeling in primary hippocampal neuron cultures

The functionality of photoTCP was experimentally examined in primary hippocampal neural cultures with whole cell patch clamp. Neurons were incubated with photoTCP (50-150 µM; 5 min) and then illuminated with 350 nm LEDs for 30 min continuously. Light power tested was ranging from 6 to 78 µW $cm^{-2}$. After several washout cycles, neurons were current clamped at -60 mV and perfused with physiological external solution (composed of (in mM): 140 NaCl, 1 $MgCl_2$, 2.5 KCl, 10 HEPES, 2.5 $CaCl_2$ and 10–20 glucose to fix osmolarity to 310 mOsm·$kg^{-1}$, while pH 7.42 was adjusted with NaOH). Stimulation light pulses of UV light (380 nm) elicited trains of action potentials that could be reversibly silenced by pulses of green (500 nm) light (Figure 3).

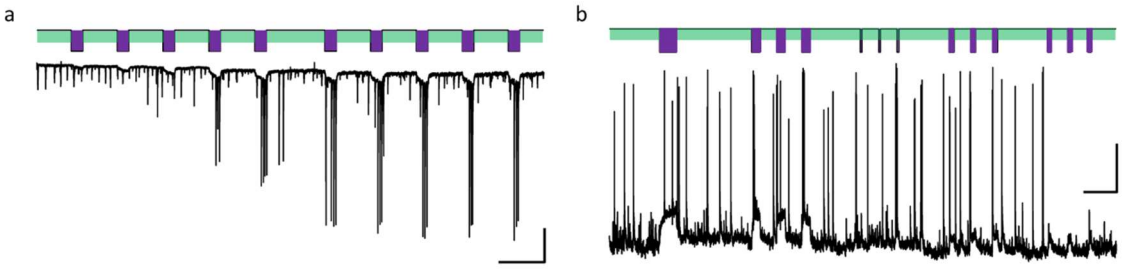


**Figure 3.** Whole-cell recordings of rat hippocampal neurons in culture (div 13) after incubation with photoTCP (150 µM) and irradiated at 350 nm for 30 min. Successful conjugation and light activation with 380 nm (purple bars) was observed in voltage clamp configuration (a, light pulse 5 s) and to some extent in current clamp configuration (b) with different duration light pulses 10 s, 5 s, 1 s, 3 s and 2 s respectively. Scale bars 500 pA, 20 s; 20 mV, 5 s.

As control experiments, neurons incubated without illumination protocol or incubated with pre-irradiated photoTCP did not present specific photoresponses to UV light (Figure 4). Photolabeling of diazirine is described to be wavelength specific between 330-370 nm (Song and

Zhang 2009; Thermo Scientific 2015). In case of using 365 nm light with our preparation, photoresponses obtained are significantly smaller than photoresponses after 350 nm light. Not even higher light power with TLC lamp at 365 nm compensate the difference in wavelength (Figure 5). However, another possible explanation is that the presence of an azobenzene might interfere in the photolabeling quenching most of the photons. Also, 365 nm light can isomerize the azobenzene and *cis* isomer may not be able to correctly conjugate to the target receptor, as observed before in other PTLs (Izquierdo-Serra et al. 2016).

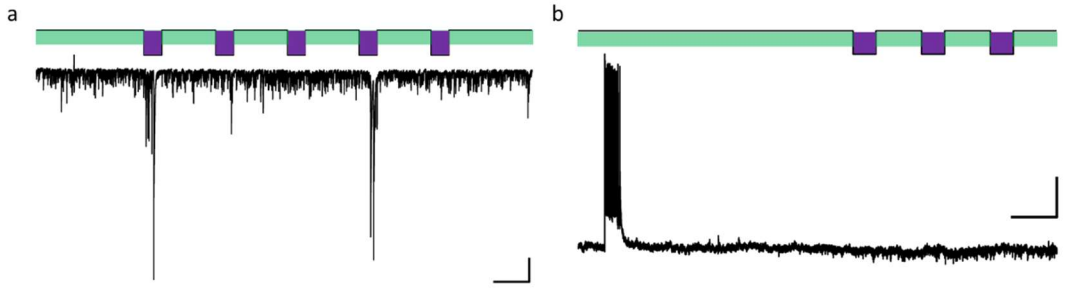


**Figure 4.** Whole-cell recordings of rat hippocampal neurons in culture (div 11-12) after incubation with photoTCP (150 µM) pre-incubated 5 min and irradiated at 350 nm for 30 min. Light activation with 380 nm (purple bars) in voltage clamp configuration (a, light pulse 5 s) and current clamp configuration (b) did not elicit photoresponses. Scale bars 200 pA, 10 s; 20 mV, 10 s.

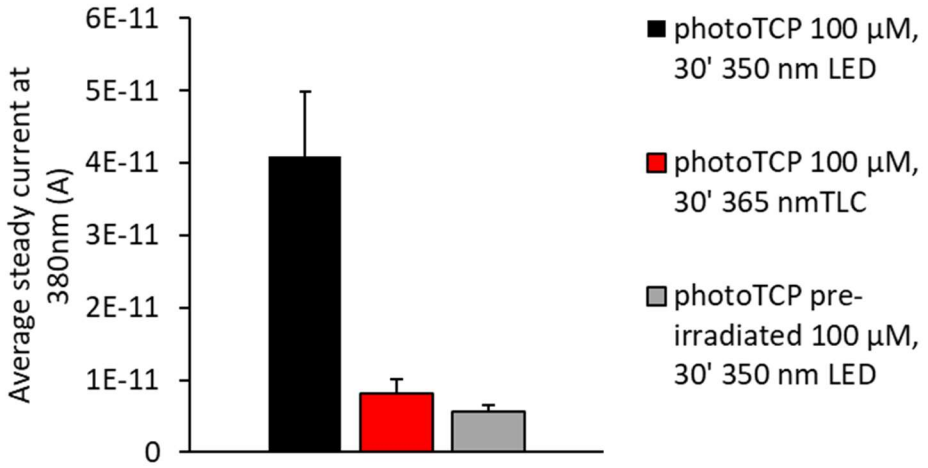


**Figure 5.** Quantification of steady state photoresponses obtained under 380 nm illumination. Whole-cell recordings of rat hippocampal neurons in culture after incubation with photoTCP (100 µM) and irradiated at 350 nm for 30 min (blue bar), photoTCP (100 µM) and irradiated at 365 nm for 30 min (orange bar), and photo-degraded photoTCP (100 µM) and irradiated at 350 nm for 30 min (grey bar). Error bars are mean ±SEM.

In conclusion, here we demonstrate for the first time the ability to specifically photolabel endogenous receptors with a photoswitchable ligand in different cell populations by targeting UV light to the region of our interest. This opens new prospective projects to in vivo spatially

and temporally control the labeling of regions, or even groups of neurons inside a circuit, and thus control their activation without affecting the whole system.

**Author contribution**

PhotoTCP and previous versions were synthesized by Carlo Matera, Antoni Bautista-Barrufet and Ana Trapero in the laboratory of Amadeu Llebaria (IQAC-CID). All electrophysiological characterizations were carried out by Aida Garrido-Charles.

**Future experiments**

PhotoTCP chemical design is based on TCP9 so all previous characterization can also be taken into account in future experiment designs. Specific labeling of single components of an excitatory circuit could elucidate their role and consequences of disrupting its balance. However, the LED illumination used in current approaches cover an area that is relatively large and not well defined. Improving the patterned illumination with filters will allow us to control better the region illuminated and possibly transfer the approach to in vivo, for example in the specific photolabeling of selected regions of the CNS like portions of the spinal cord or one single hemisphere in *Xenopus* tadpoles. Previously, *Xenopus* tadpoles have been used in developmental studies and behavior assays (Cline and Kelly 2012; Pittolo et al. 2014) because of their easy manipulation, small size, robustness and transparent skin (very convenient for our illumination protocols). Although their neural circuits are simpler compared to mammals, their basic organization maintain certain homology. In our case, this well-studied animal model could also be very useful in the study of small excitatory circuits like the ones formed by sensory and motor neurons. Controlling spatiotemporally the conjugation of photoswitches to endogenous receptors would allow us to specifically manipulate the components of the circuit and maybe understand processes behind light triggered behaviors and neural processes like command neuron concept, electrical transmission, quantal transmitter release and synaptic plasticity.

Since photoTCP is a charged, relatively big molecule to diffuse in tissue, our experimental design may require the injection of the compound at the target organ and then illuminating with 350 nm light the region of interest (for example one single hemisphere). After recovery from anesthesia from such procedure, as a proof of concept firstly, behavioral experiments upon UV light illumination (380 nm) would indicate if labeling a single hemisphere interferes in the correct function of the circuit, for example making the tadpole swim only in one direction (Sillar 2009).

In a second stage, to exploit at maximum the spatial control of photolabeling we would use a laser to precisely illuminate small regions, single cells or single spines. Although lasers of 351 nm exist, they are not common in microscopy facilities. Most common UV lasers are 405nm, but this wavelength is able to stimulate and photoisomerize azobenzene and we might encounter the same problems as using the TLC lamp (365 nm). Instead, another interesting possibility is the use of 2P stimulation, around 700nm. At this wavelength azobenzene is not stimulated and the spatial control and tissue penetration that 2P provides is much more precise than 1P laser.

**SUPPLEMENTARY INFORMATION**

Inspired by the synthesis of other PTLs like MAGs (Gorostiza et al. 2007) and TCPs (Izquierdo-Serra et al. 2016), the preparation of our photoTCP was achieved via a 5-step linear sequence where the glutamate and diazirine functions were sequentially introduced into the azobenzene-based molecular photoswitch (Scheme 1). Amide coupling of the N-Boc protected pyroglutamate derivative **1** (Ezquerra et al. 1993; Volgraf et al. 2006) with the commercially available 4,4'-azodianiline gave the intermediate **2**, which was subsequently acylated with glycine to obtain compound **3** containing an aliphatic primary amine. The pyroglutamate moiety was then opened via an alkaline hydrolysis to give compound **4**. The desired compound was finally obtained via a coupling reaction to introduce the photoreactive diazirine group (intermediate **5**) and subsequent acid removal of the *tert*-butyl carbamate protection.

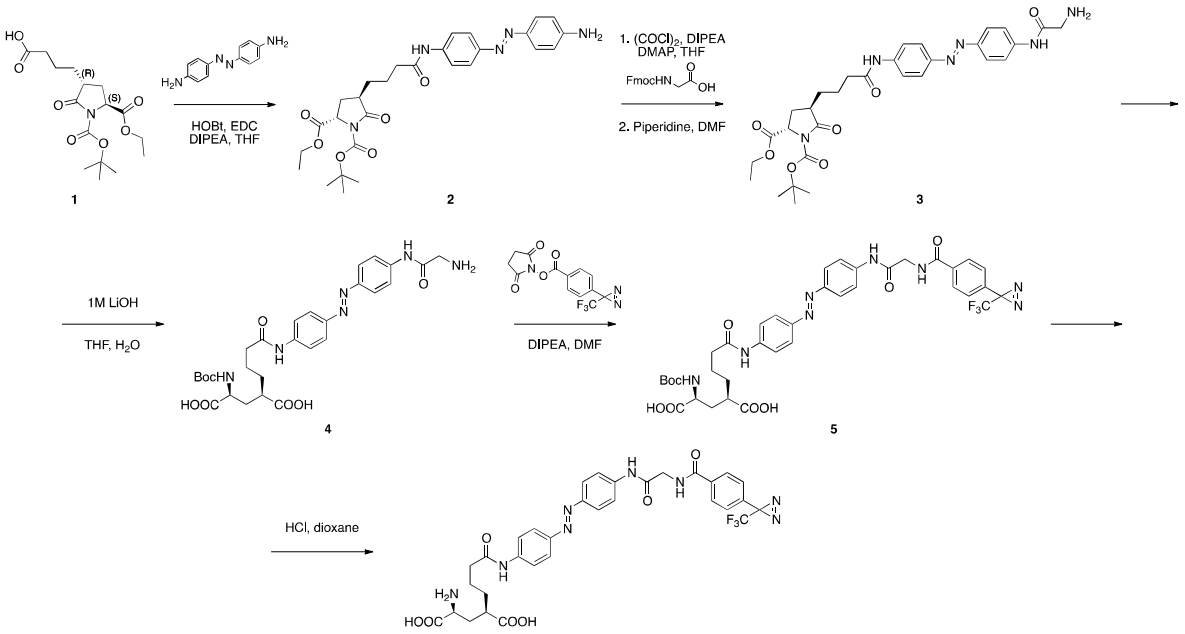


**Scheme 1.** Synthesis of photoTCP performed by Carlo Matera at the laboratory of Amadeu Llebaria (IQAC-CID).

**REFERENCES**


Chambers, James J. et al. 2004. "Photochemically Knocking out Glutamate Receptors in Vivo." *Journal of the American Chemical Society* 126(43): 13886–87.

Cline, Hollis T., and Darcy Kelly. 2012. "Xenopus as an Experimental System for Developmental Neuroscience: Introduction to a Special Issue." *Developmental Neurobiology* 72(4): 463–64.

Dubinsky, Luba, Bastiaan P. Krom, and Michael M. Meijler. 2012. "Diazirine Based Photoaffinity Labeling." *Bioorganic and Medicinal Chemistry* 20(2): 554–70. http://dx.doi.org/10.1016/j.bmc.2011.06.066.

Ezquerra, Jesús et al. 1993. "Stereoselective Reactions of Lithium Enolates Derived from N-BOC Protected Pyroglutamic Esters." *Tetrahedon* 49(38): 8665–78.

Gorostiza, Pau et al. 2007. "Mechanisms of Photoswitch Conjugation and Light Activation of an Ionotropic Glutamate Receptor." *Proceedings of the National Academy of Sciences of the United States of America* 104(26): 10865–70. http://www.pubmedcentral.nih.gov/articlerender.fcgi?artid=1904147&tool=pmcentrez&rendertype=abstract.

Izquierdo-Serra, Mercè et al. 2016. "Optical Control of Endogenous Receptors and Cellular Excitability Using Targeted Covalent Photoswitches." *Nature Communications* 7: 12221. http://www.nature.com/doifinder/10.1038/ncomms12221.

Mortensen, Martin et al. 2014. "Photo-Antagonism of the GABAA Receptor." *Nature communications* 5: 4454. http://www.ncbi.nlm.nih.gov/pubmed/25072879%5Cnhttp://www.pubmedcentral.nih.gov/articlerender.fcgi?artid=PMC4124873.

Pittolo, Silvia et al. 2014. "An Allosteric Modulator to Control Endogenous G Protein-Coupled Receptors with Light." *Nature chemical biology* 10(10): 813–15. http://www.ncbi.nlm.nih.gov/pubmed/25173999.

Sillar, Keith T. 2009. "Mauthner Cells." *Current Biology* 19(9): 353–55.

Song, Zhiquan, and Qisheng Zhang. 2009. "Fluorous Aryldiazirine Photoaffinity Labeling Reagents." *Organic Letters* 11(21): 4882–85.

Thermo Scientific. 2015. "Light Sources and Conditions for Photoactivation of Aryl Azide Crosslinking and Labeling Reagents." *Tech Tip #11* 0747(815): TR0011.2. http://tools.thermofisher.com/content/sfs/brochures/TR0011-Photoactivate-aryl-azides.pdf.

Volgraf, Matthew et al. 2006. "Allosteric Control of an Ionotropic Glutamate Receptor with an Optical Switch." *Nature chemical biology* 2(1): 47–52. http://www.pubmedcentral.nih.gov/articlerender.fcgi?artid=1447676&tool=pmcentrez&rendertype=abstract (February 2, 2014).

Weiser, Brian P., Max B. Kelz, and Roderic G. Eckenhoff. 2013. "In Vivo Activation of Azipropofol Prolongs Anesthesia and Reveals Synaptic Targets." *Journal of Biological Chemistry* 288(2): 1279–85.

## Part II. Engineering the optical properties of photoswitchable tethered ligands (PTLs)

# CHAPTER 4| High frequency photopharmacologic stimulation of endogenous AMPA receptors of cochlear neurons

Aida Garrido-Charles[1,2,*], Antoine Huet [3,4,*], Carlo Matera[1,2], Amadeu Llebaria[5], Tobias Moser[3,4,6,7,8,9], Pau Gorostiza[1,2,10]

1 Institute for Bioengineering of Catalonia (IBEC), Barcelona Institute for Science and Technology (BIST), Carrer de Baldiri Reixac 15-21, 08028 Barcelona, Spain
2 Network Biomedical Research Center in Bioengineering, Biomaterials, and Nanomedicine (CIBER-BBN), 28029 Madrid, Spain
3 Institute for Auditory Neuroscience and InnerEarLab, University Medical Center Göttingen, 37075 Göttingen, Germany.
4 Auditory Neuroscience and Optogenetics Group, German Primate Center, 37077 Göttingen, Germany.
5 Institute of Advanced Chemistry of Catalonia, Consejo Superior de Investigaciones Científicas (IQAC-CSIC), 08034 Barcelona, Spain.
6 Collaborative Research Center 889, University of Göttingen, 37075 Göttingen, Germany.
7 Göttingen Graduate School for Neurosciences and Molecular Biosciences, University of Göttingen, 37075 Göttingen, Germany.
8 Bernstein Center for Computational Neuroscience, University of Göttingen, 37077 Göttingen, Germany.
9 Center for Nanoscale Microscopy and Molecular Physiology of the Brain, University of Göttingen, 37075 Göttingen, Germany
10 Catalan Institution for Research and Advanced Studies (ICREA), 08010 Barcelona, Spain
* These authors contributed equally to this work.

## INTRODUCTION

The last 20 years, biology saw the emergence of tools allowing to control biological processes including cell excitation with light[1]. Light has the advantage that it can be spatiotemporally controlled and therefore it allows a fine remote control of cell activity[2]. Photocontrol of biology can classically be achieved by 2 approaches: i) optogenetic, which relies on native chromophores as retinal or flavins being part of light-regulated ion channels like Channelrhodopsin (ChR)[3]; ii) photopharmacology, based on synthetic light sensitive drugs[4,5]. For the second one, the reversible activation of drugs can be achieved by designing photoisomerizable derivatives of well characterized commercial drugs. A very appealing approach is called azologization and consists of inserting a small and versatile photoswitch, azobenzene, into the chemical structure of a compound while keeping most other properties unchanged. Upon light stimulation azobenzene photoisomerizes (changes configuration) which hopefully changes the activity of the drug. This approach can be used for example to control the activity of neuron as illustrated by the action of the free diffusible photochromic ligands (PCLs)[2,6]. Another interesting approach consists of adding a reactive part that fixes the photoswitch to the receptor, and so compared to PCLs accelerates the response as a result of a high local drug concentration. This type of photoswitches are called photoswitchable tethered ligands (PTLs). First described photoswitches containing azobenzene are activated with UV light and inactivated with visible light [7–9]. A second wavelength for inactivation is usually required when thermal relaxation lifetime is long and isomerized *cis* azobenzene is thermally stable. One example of this type of photoswitches is MAG (Maleimide Azobenzene Glutamate,[7,10]), which photosensitizes the ionotropic glutamate receptor GluK2 by conjugating to a genetically engineered cysteine introduced in position L439. Since its engineering, several applications of MAG have been

described: induction of depolarization and firing of action potential in hippocampal neurons [11]; control of behavioral responses in zebrafish [11]; and vision restoration [12]. However, stimulation with UV light is not optimal due to high light scattering, low tissue penetration and possible photodamage caused by overheating and DNA mutations. These disadvantages motivated the development of red-shifted PTLs that can be activated with visible light. The replacement of an amide moiety by an amine created L-$MAG_{460}$ [13], which also demonstrated its ability to photosensitize degenerated retinas, making it as a more realistic approach for vision restoration [14]. Other derivatives originated two-photon sensitive $MAG_{2P}$ and $MAGA_{2P}$ [15], or the recently described $MAG_{2P\_slow}$ and $MAG_{2P\_slowF}$ [16].

All PTLs described above require the introduction of a single mutation in GluK2 receptor to be able to conjugate. In 2016, we reported the first PTL able to anchor to endogenous native GluK1 receptors without the need of genetic modification [17]. To do so, the maleimide moiety was substituted by an NHS ester reactive group and combinatorial conjugation was made by a click reaction of two modular parts which allows to generate PTLs of different length. The best molecules obtained, called Targeted covalent photoswitch (TCP), can photosensitize and control neural activity in dorsal root ganglion neurons and degenerated blind retina [17]. Avoiding genetic modifications allows to preserve the physiological properties of native channels, as their activation kinetics. Limiting factors of TCP are its activation with UV light and its slow relaxation lifetime (~80 min) requiring a second wavelength for deactivation.

In this study we aimed to use the same design than TCPs to generate derivatives activatable with visible light while retaining their ability to conjugate with native receptors. Usually, azobenzene photoswitching wavelengths in the visible region of the spectrum are associated with fast relaxation lifetime (in the ms-s range), which in turn allows operating them with a single wavelength of activation. This is beneficial to control rapid neural firing rates, like the ones observed in certain neurons including cortical interneurons [18] or sensory retinal afferent terminals and cochlear spiral ganglion neurons (SGNs) [19].

Here, we demonstrated the ability of blue-shifted TCPs to control action potential firing in intact hippocampal neurons. As a proof of concept to model an ultrafast synaptic transmission, we used the method to photoswitch SGNs of cochlea in adult gerbils and control their activity in the range of kilohertz. The development of photopharmacological tools that work on native unaltered neural receptors expands their clinical applicability to animals or eventually to human in order to restore important disorders such as hearing loss. To materialize this concept into a real application, optical cochlear implants are also being designed in order to precisely confine neural activity with light. Process that usually is masked with classical electrical cochlear implants due to electrical crosstalk between electrodes [20].

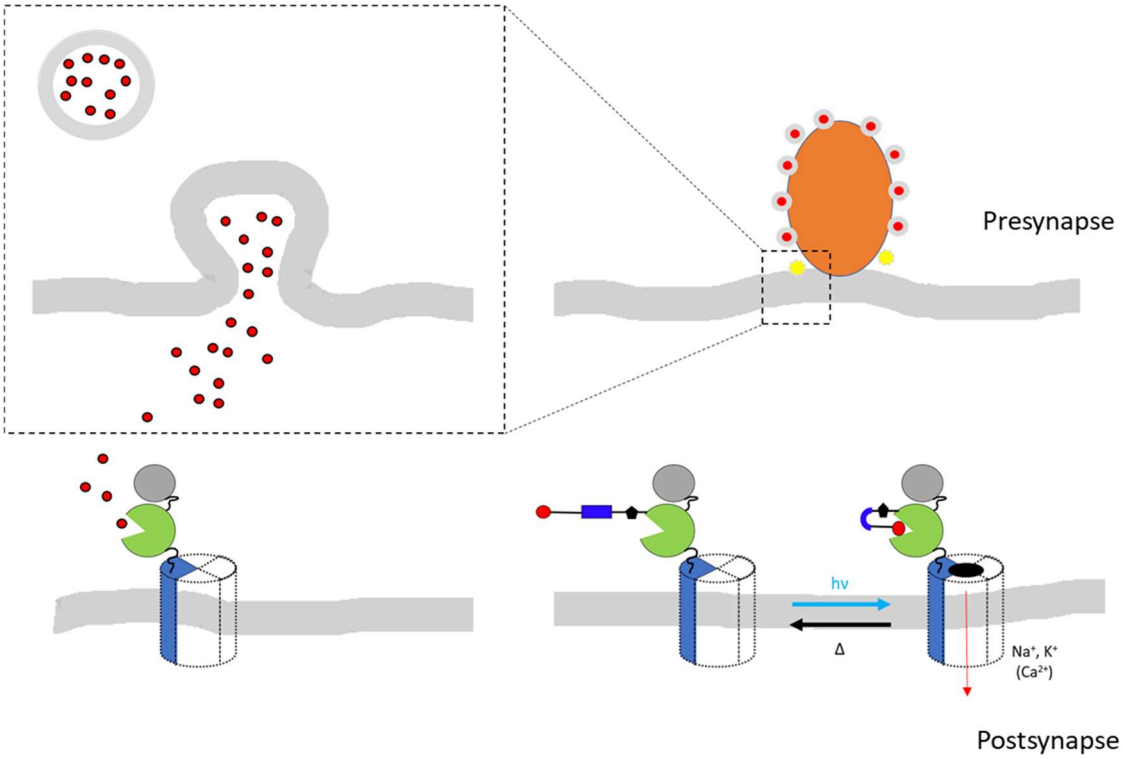


**Figure 1.** Schematic representation of neurotransmitter release from exocytosis of vesicles at the synaptic cleft (upper left panel). Post-synaptic ionotropic receptors organized as tetramers, respond to ligand binding by opening their ion pore and allowing ion influx to the post-synaptic neuron. Fast neurotransmission processes as those occurring in cochlear spiral ganglion neurons are characterized by specialized ribbon synapses. Ribbon synapses are organized organelles where multiple vesicles filled with neurotransmitter are anchored in the proximity of the membrane (upper panel right) providing a large number of filled vesicles close to the presynaptic terminal cleft. Ligand interaction with its receptor at ribbon synapses can be mimicked by a tethered ligand anchored to the LBD of an ionotropic glutamate receptor (lower panel right). With light stimulation, azobenzene core changes its conformation from *trans* to *cis* and ligand interacts with the binding pocket. In this case, fast thermal relaxation *cis-trans* of the photoswitch remove the ligand from the pocket and the receptor returns to its closed resting state.

## RESULTS

### Synthesis of the blue-TCP

Previously, we described novel photoswitchable tethered ligands able to target endogenous receptors without genetic modifications [17], also known as "Targeted covalent photoswitches" (TCPs). TCPs are composed of a ligand (in this case glutamate), a photoswitch (e.g. azobenzene), and a reactive group which attaches the TCP to any nucleophilic amino acid available on the surface of the receptor [17]. These 3 modular units are connected by 2 linkers. The mechanism leading to the opening of the glutamate receptor in presence of TCP and light is assumed to be similar to what was described for the photoswitchable light-gated Glutamate receptor (LiGluR). The main difference is that LiGluR requires a mutation of the glutamate receptor to allow conjugation of MAG (Maleimide-Azobenzene-Glutamate) on it [7,10]. Upon light stimulation, the photoswitch changes its geometric isomerism from *trans* to *cis*, allowing the ligand to reach the receptor binding pocket, thus causing the channel to open (**Figure 1**). The main disadvantages of first generation of TCPs are the need to activate neurons with ultraviolet light, which is low-penetrating and harmful to tissue; and require a second wavelength to switch off the activity

due to slow thermal relaxation in the dark. Therefore, we aimed to obtain a TCP derivative that can be activated with visible light and with a short relaxation lifetime, allowing fast operation with a single wavelength.

Absorption at longer wavelengths has been reported in MAG derivatives containing asymmetric substitutions in the azobenzene chromophore [13,15]. Thermal relaxation lifetimes of those photoswitches stand around hundreds of milliseconds. In our case, blue-TCP azide head was generated by creating a push–pull system with electron donating groups on one side of the azobenzene core and electron withdrawing groups on the other at *para* positions. This push-pull approach allows the resulting photoswitch to absorb light in the blue range of the light spectrum (λ = 470 nm) and also lowers the thermal barrier to interconversion of the isomers, leading to a thermal relaxation of the compound being now within the range of milliseconds.

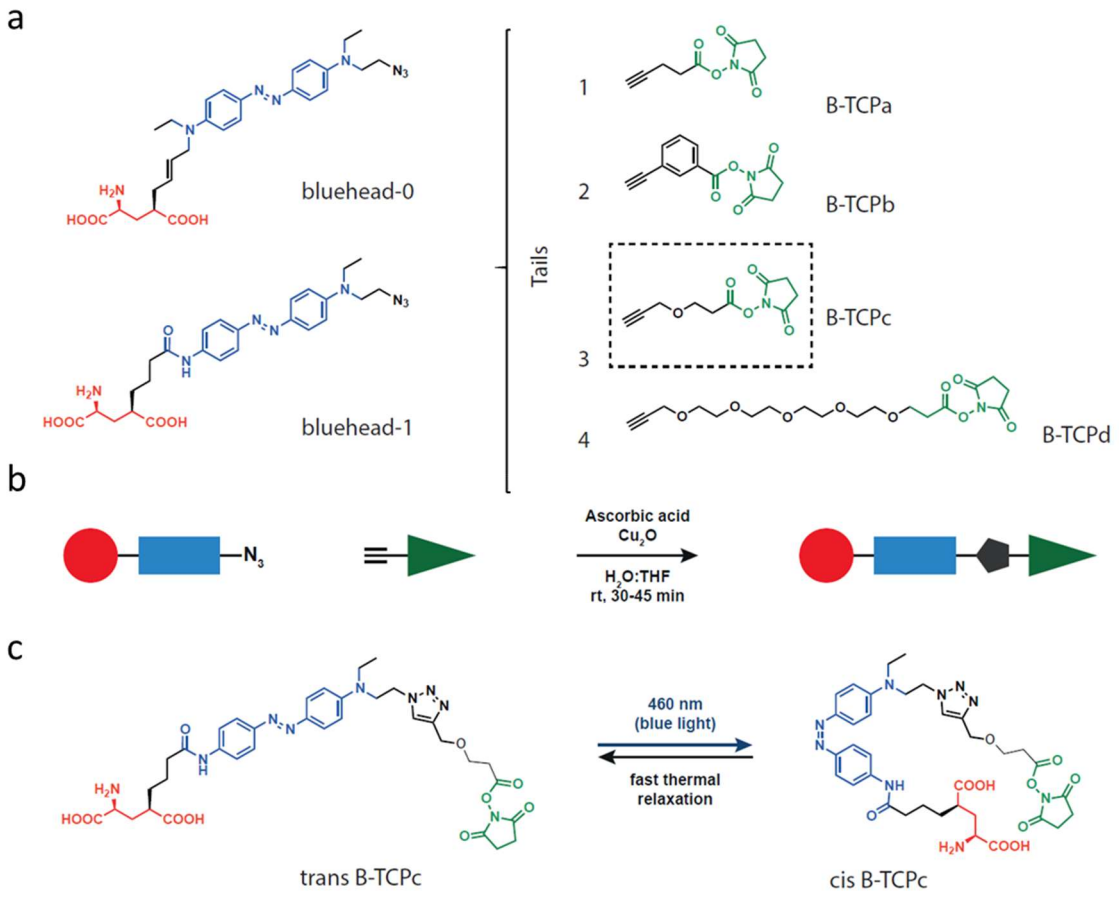


**Figure 2. Chemical structure of newly synthesized blue-TCP heads and combinatorial library of tails**. a-b) The 'head' (glutamate-azo-azide, left) and 'tail' molecules (linker-electrophile, right) are precursors of cooper catalyzed "click coupling reaction" and can be combined to yield B-TCPs of different lengths. c) Example of full B-TCPc obtained from bluehead-1 and tail 3. Photoisomerization between the *trans* (blue light, ~460 nm) and *cis* conformations (fast thermal relaxation in milliseconds).

From a library of different molecules, two Blue-shifted azide "heads" were selected and functionally tested as free ligands in vitro in transiently transfected tsA201 HEK293 cells expressing wild type GluK1 receptor, as it is the described target of TCPs first generation. Direct

application of "bluehead-0" (**Figure 2a**) induced inward currents similar to perfusion of glutamate (300 µM) (**Figure S1a**). Light stimulation slightly induces inward currents in the range of the visible spectrum (**Figure S1b**). Likewise, "bluehead-1" is able to open GluK1 receptors and evoke an inward depolarizing current similar to non-switchable glutamate perfusion. In this case, however, light stimulation produces bigger and more stable inward photocurrents (**Figure S1d**), as an indicative of better interaction and switching of the new azobenzene unit.

We exploited the versatility provided by click coupling (fast version of the azide-alkyne Huisgen cycloaddition (copper(I)-catalysed alkyne-azide cycloaddition)[21] to build a library of "tails" (compounds from 1 to 4 in **Figure 2**). Tails are ended with a reactive NHS ester group but differ in linker length and flexibility properties. In order to obtain a full tethered ligand, "bluehead-1" was systematically combined by click reaction with different "tails", all obtained from commercial suppliers, to produce complete blue-TCPs (B-TCPs) (compounds from (a) to (d) in **Figure 2**). NHS ester electrophilic groups will react with nucleophilic groups of amino acids on the surface of the receptor in order to anchor B-TCPs on the LBD.

**In vitro characterization of Blue-TCP**

Final clicked Blue-TCPs were tested in primary cultures of hippocampal neurons, where all native glutamate receptors are present. The use of systematic tests of different head-tail combinations in the "real biological scenario" displaying a wider variety of receptors offers the advantage of saving chemical products and time, and allowing to discard inactive compounds earlier. Nonetheless, subsequent confirmation of target receptor candidates overexpressed in cell lines, and proper pharmacological characterization are necessary.

The first combination with the shortest tail shows certain photocontrol of neural firing. Once conjugated, thermally stable *trans*-isomer of B-TCPa show partial neural depolarization as an indicative of persistent activation of postsynaptic neural receptors. This activation can be reversed with blue light (460 nm) illumination, which isomerizes B-TCPa to its inactive *cis*-isoform temporally removing the ligand from the binding pocket (**Figure S2a-b**). Similar hyperpolarizing effects can be observed in a range of wavelengths from 380 to 500 nm (**Figure S2c**). Without illumination, B-TCPa returns to *trans*-relaxed isoform and neurons immediately return to their basal partial depolarized state. The depolarization induced by B-TCPa is not sufficient (~20 pA) to evoke sustained action potential neural firing (**Figure S2d**). Blue light stimulation shows partial hyperpolarization of neurons in current clamp mode recordings (**Figure S2d**), but insufficient to inhibit action potential firing with light. Perfusion of subtype selective antagonists of NMDA receptors (AP5, 100 µM) and AMPA-kainate receptors (NBQX, 10 µM) cannot significantly affect photocurrents (**Figure S2e**). This finding might indicate a non-selective binding of B-TCPa to the receptors or that affinity for the binding pocket of B-TCPa is higher than the antagonists used.

The second combination of "bluehead-1" with tail 2 was intended to invert the activity of B-TCPa in a way that *cis*-isomer induced by blue light stimulation could activate the receptors while *trans*-isoform stays inert. Tail 2 is also short but a benzene substituent in meta makes it more rigid than tail 1. Thereby, we look for an extended *trans* isomer more rigid and unable to interact with the ligand binding pocket at the LBD. However, after incubation of B-TCPb no photocurrents or light-induced action potentials are evident upon light stimulation at 460 nm (5 s) (**Figure S3a-b**). As an internal control, perfusion of B-TCPb (10 µM) produces small inward photocurrents (**Figure S3c-d**). Thus, indicating that glutamate and azobenzenic core of the clicked compound is

functional and probably B-TCPb cannot correctly conjugate on the LBD or if it does, ligand is not able to reach the binding pocket upon photoisomerization.

The next strategy was to test a longer tail to allow better interaction of the ligand in the short *cis* conformation, avoiding the interaction with the extended *trans* isomer. Combination of "bluehead-1" with tail 3 resulted in B-TCPc, which also provided photocontrol of neural firing but in the opposite way of B-TCPa. Conjugation of B-TCPc and subsequent blue light illumination evokes inward photocurrents (**Figure 3a**) that can trigger trains of action potentials (**Figure 3b**). In dark, neurons repolarize and return to the basal state. This fast repolarization allows us to induce action potentials with short light pulses (as short as 50 ms) at frequencies of 1 Hz (**Figure 3c**), 5 Hz (**Figure 3d**), and 10 Hz (**Figure 3e**). Photoresponses can be inhibited by NBQX (AMPAR antagonist), but not AP5 (NMDAR antagonist) (**Figure 4a**), suggesting GluA selectivity. For this reason, Blue-TCPc was also tested in HEK cells expressing homomeric GluA1 receptors (**Figure 4b**) or GluA2 receptors (**Figure 4c**). Photoresponses registered confirm that B-TCPc conjugate and light-control channel gating, being active in its *cis*-isoform. Optimal wavelength activation is ~460 nm, but full activation spectra comprise from 360 to 510 nm (**Figure 3f-g**).

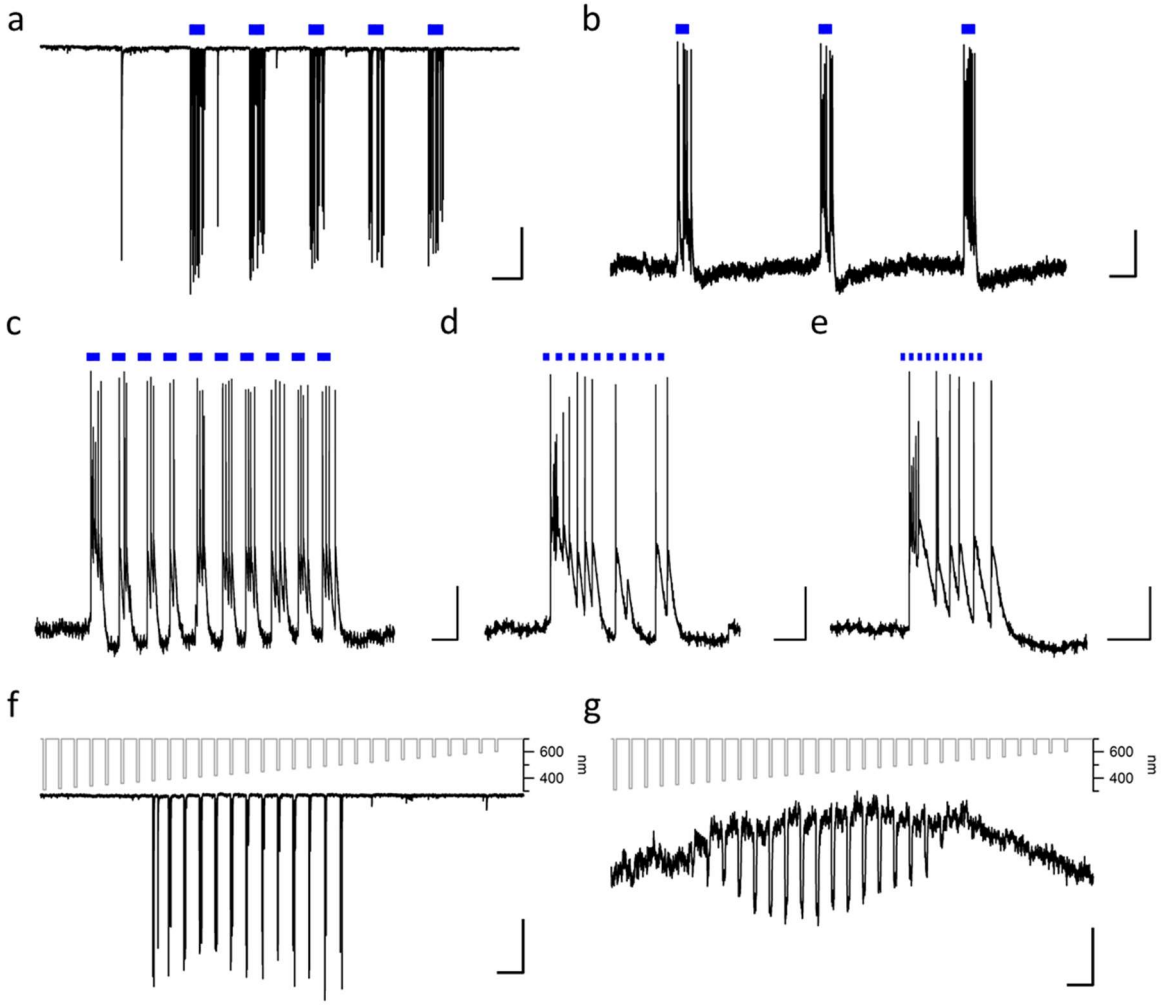


**Figure 3. Hippocampal neurons respond to light stimulation after B-TCPc conjugation.** a) Whole-cell voltage clamp recordings of rat hippocampal neurons 10 days in culture after conjugation of B-TCPc (25 µM for 2 min at pH9) and irradiation at λexc = 460 nm (5 s, blue bars). Neurons were current clamped at −60 mV. Scale bar y-axis 500 pA, time-axis 10 s. Successful action potential firing was observed with 460 nm light pulses of (b) 1 s (0.1 Hz), (c) 500ms (1Hz), (d) 0.1 s (5 Hz), and (e) 0.05s (10 Hz). Scale bar y-axis

20 mV, time-axis 1 s. f) Activation spectrum recorded in whole cell voltage clamp in rat hippocampal neurons in culture incubated with B-TCPc. Wavelength screening ranged from 300 to 600 nm, while resting wavelength was set to 690 nm. Scale bar is 500 pA and 10 s. g) Activation spectra recorded as in (f) in HEK293 cells expressing GluA1 and in presence of CTZ (25 µM) and glutamate (300 µM). Scale bar is 20 pA and 10 s.

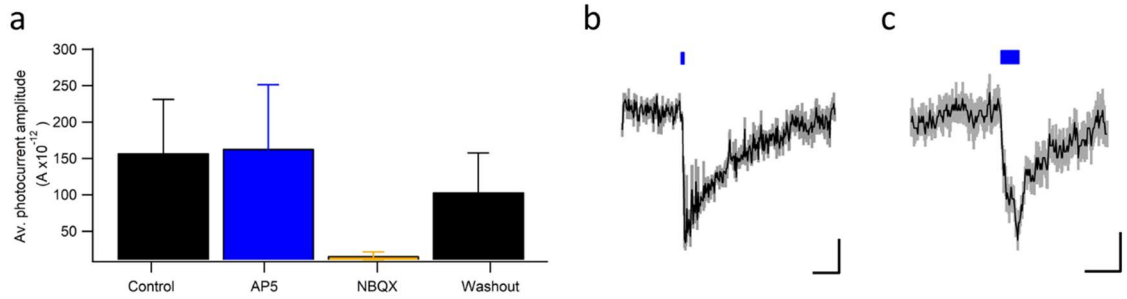


**Figure 4. Pharmacological characterization of B-TCPc induced photocurrents**. a) Quantification of photocurrent amplitude in hippocampal neurons incubated with B-TCPc under different conditions: control (B-TCPc incubated 25 µM for 2 min at pH9; n=8); AP5 (perfusion 100 µM; n=8); NBQX (perfusion 10 µM; n=8); Washout (photocurrents after perfusion of bath solution; n=8). Error bars ±SEM. b) Short light pulse (10 ms; 473 nm) induce photocurrents in HEK293 cells expressing homomeric wild type GluA1 and c) GluA2 (light pulse 50 ms) receptors, in presence of CTZ (25 µM) and glutamate (300 µM). Scale bar y-axis 10 pA, time-axis 250 ms. Error bars ±SEM are shadow in grey (GluA1 n= 10; GluA2 n=10).

In the same direction, a fourth combination with a longer tail was tested in neurons. "bluehead-1" with tail 4 lead to B-TCPd, which after being incubated in hippocampal neurons as previously done cannot evoke sizable photoresponses (**Figure S4**), not even light-induced depolarization in voltage clamp mode (**Figure S4a**). We also discard possible masked allosteric modulation of B-TCPd by light stimulation of the incubated neuron in presence of free glutamate (**Figure S4b**). Likewise, triggering action potential firing in whole-cell current clamp mode cannot be observed (**Figure S4c**). Most likely, even if B-TCPd is able to correctly conjugate to the LBD, the distance provided by tail 4 is too long to reach the binding pocket even in the *cis* configuration.

Pharmacological characterization of final clicked B-TCPs shows their ability to induce photoresponses in hippocampal neurons indicating target receptors of the family of GluA. However, selectivity of NBQX is not limited to AMPARs and also kainate receptors have to be taken into consideration. Molecular studies of LBDs comparing the main subtypes of kainate receptors GluK1 and GluK2 indicate that GluK1 ligand binding pocket is larger and so more permissive to ligand interactions[22]. Nonetheless, B-TCPa was the only clicked compound showing photoresponses in GluK1 transiently transfected tsA201 HEK293 (**Figure S5**). Once conjugated, B-TCPa has an activity *trans*-on (active constitutively) as observed in hippocampal neurons in culture. With pulses from 390 to 540 nm light we can deactivate the compound by *trans-cis* photoisomerization (**Figure S5a**). Correct physiological responses of homomeric GluK1 receptors were ensured by glutamate perfusion in the bath (**Figure S5b,d**). As described above, the maximum response obtained is around 460 nm (blue light) illumination (**Figure S5e**). Interestingly, conjugation can be light controlled as with other PTLs described in [10,17]. Illumination with 455 nm light during B-TCPa incubation induces *trans-cis* photoisomerization, which in consequence significantly reduces photoresponses (**Figure S5a,c,f**). *Cis* photoisomerization hampers the correct ligand interaction with the binding pocket and prevent

B-TCPa conjugation. These properties enable to spatially control B-TCPs conjugation by light-patterned illumination.

**Blue-TCP enables photocontrolling in vivo neural activity in gerbil's cochlea**

Encouraged by the fast control of neural firing shown in hippocampal neurons, here we tested B-TCPc in vivo in the cochlea (**Figure S6**). The mechanotransduction of the sound into a neural message is made by the inner hair cell (IHC). Following their depolarization by the traveling wave, the IHC depolarization triggers glutamate release at their ribbon synapses which is post-synaptically triggering firing of action potential in the spiral ganglion neurons facing each ribbon (SGNs). Pharmacological and electrophysiological studies pointed out AMPA as the glutamate receptor mediating this post-synaptic response[23–25]. An extraordinary feature of this synapse is its ability to faithfully encode temporal fine structure of the sound up to the low kilohertz range (~4 kHz, [26–29]) with even a higher sensitivity than encoding the envelope[30,31]. Additionally to this glutamate mediated response and high need of temporal control, the current development of an optical cochlear implant motivate us to investigate a new method to photosensitize SGNs, as a potential alternative to the currently used optogenetic approach[32–35].

B-TCPc was tested in healthy adult Mongolian gerbils (8 to 12 weeks) by directly applying the compound on the perforated round window (RW) membrane (**Figure S6b**). In order to measure cochlea potentials, a silver ball electrode was initially fixated in the RW niche. An initial concentration of 12.5 µM (<0.2 % of organic solvents) was tested and its potential toxicity was assessed by measuring cochlear potentials (8 kHz tone burst, 20 and 80 dB SPL per 20 dB step) after a baseline application of artificial perilymph (AP), B-TCPc and rinsing with AP. No significant difference (Wilcoxon signed-rank test) across the 3 conditions was observed for the cochlear microphonic (**Figure 5a**), reflecting the outer hair cell function, and for the acoustically evoked compound potential (aCAP, **Figure 5b**), reflecting the synchronized activity of recruited SGNs. These results suggest an absence of acute functional toxicity of B-TCPc in the cochlea. However, further histological studies of toxicity should be carried out to fully discard it.

After insertion of an optical fiber coupled with a blue laser (λ = 473 nm), an optically evoked compound action potential (oCAP) could be recorded (**Figure 5c**). After sacrifice of the animal, the oCAP vanished, supporting its physiological origin. The effect of the radiant flux was tested between 1 and 30 mW (100 µs light pulse duration, 10 Hz repetition rate) as illustrated by a representative example in **Figure 5d**. oCAP amplitude (**Figure 5e**) increases linearly from the threshold up to 30.87 ± 2.67 µV and oCAP latency (**Figure 5f**) decreases from 1.67 ± 0.08 to 1.51 ± 0.06 ms. The activation threshold amounted to 10.5 ± 0.88 mW and in some case oCAPs could be evoked by light pulse radian flux as low as 6 mW corresponding to 0.6 µJ. Next, the effect of the light pulse duration was tested between 20 µs and 1 ms (27 mW light radiant flux, 10 Hz) as illustrated by **Figure 5g**. oCAP amplitude (**Figure 5h**) and latency (**Figure 5i**) present a "bell" shape with a maximum at 80 µs. Interestingly 20 µs light pulse already evoked an oCAP, corresponding to 0.54 µJ. Also note that in response to long light pulse (> 200 µs), the oCAP is characterized by multiple negative peaks which can potentially reflect firing of few synchronized AP in SGNs. Finally, the effect of the repetition rate was tested between 20 and 4000 Hz (80 µs light pulse, 27 mW radiant flux pulse) as illustrated in **Figure 5j**. oCAP amplitude (**Figure 5k**) decreases and oCAP latency (Figure 5l) increases with the increase of the repetition rate. Above 1000 Hz oCAP amplitude is inferior to 2 µV, but repeated measure on scarified animal suggests a physiological contribution to the recorded potential (**Figure S7**).

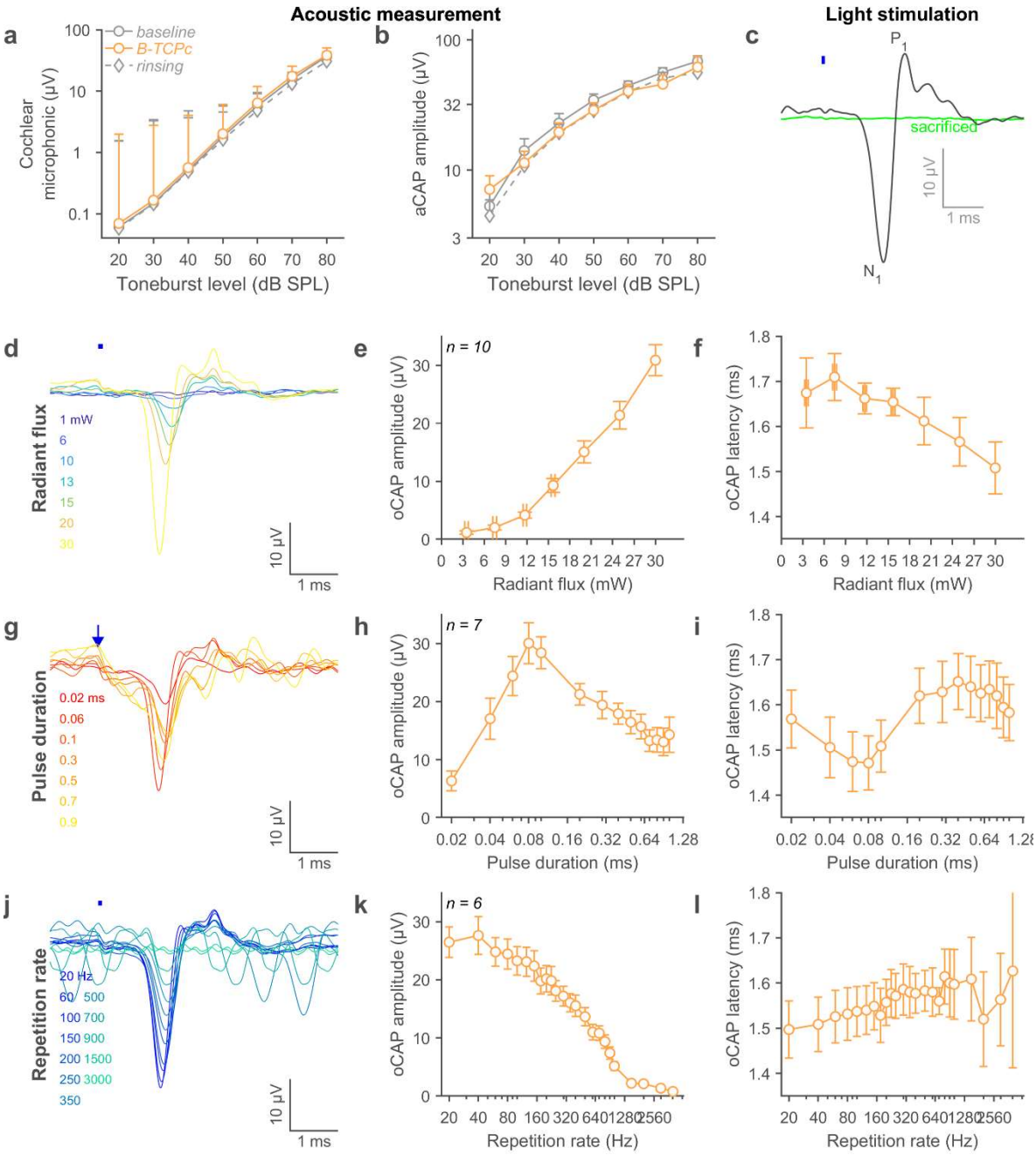


**Figure 5. Characterization of optically evoked compound action potential (oCAP) after round window application of 12.5 µM B-TCPc**. a-b)**.** The cochlear microphonic (CM, a) and the acoustically evoked CAP (b) was extracted from the round window mass potential from an electrode in response to 8 kHz tone burst (pulse duration = 8 ms, rise/fall time = 1 ms, repetition rate = 20 Hz, level : 20 to 80 dB SPL per 10 dB step). Measurements were taken 10 min after artificial perilymph application ("baseline", continuous grey line), 25 µM B-TCPc (orange) and washout (dashed gray line, *n* = 6). c) oCAP evoked by 80 µs light pulse (27 mW, 10 Hz) delivered into the cochlea by a 473 nm laser coupled to an optical fiber (50 µm) through the round window. The oCAP vanished in sacrificed animal (green trace). The blue line indicates light stimulation. d,g,j) Representative oCAP in response to various radiant flux (80 µs at 10 Hz, d), pulse duration (27 mW at 10 Hz, g) and repetition rate (80 µs at 27 mW, j). In (d) and (j), the blue line indicates the light stimulation and in (g) the blue arrow indicates the beginning of the light pulse. e,h,k) oCAP amplitude ($N_1$-$P_1$) and f,i,l) oCAP latency ($N_1$) as a function of the radiant flux (e,f), the pulse duration (h,i) and the repetition rate (k,i, respectively *n* = 10, 7, 6).

In order to enhance the recorded response, the effect of 2 higher concentrations was tested: 25 (< 0.4 % of organic solvents) and 75 µM (1.12 % of organic solvents). 75 µM concentration might slightly increase the success rate (i.e the number of cochlea having an oCAP) but the amplitude of the response is similar (Kruskal-Wallis-Test) (**Figure S8**)., therefore for the following experiments, 12.5 µM will be used.

**Photosensitization of SGNs in gerbil acute deafness model**

As B-TCPc shows its success to evoke an optical cochlear response on wild type animal, the ability to restore an optical response on acutely deafened animal was tested.

The first model tested consists of a single injection in the cochlea (via the RW) of aminoglycoside antibiotics as kanamycin (50 mg/ml[32]). Deafness was confirmed by acoustically evoked auditory brainstem response (ABR) which were absent up to 100 dB SPL stimulation (**Figure S9a**) and by histology for which no more IHCs could be observed in the injected cochleae (**Figure S9b-c**). After B-TCPc application (12.5 µM), no oCAP could be recorded. Histology revealed degeneration of the buttons following kanamycin application by the absence of post-synaptic marker (PSD95) compared to non-deafened cochlea (**Figure S9d-e**). The absence of post-synapse, implying the absence of AMPARs, most likely account for the absence of the response.

Another alternative to induce deafening is the application of a L-type $Ca^{2+}$ blocker, which blocks the calcium influx responsible of the glutamate exocytosis[36]. Isradipine is a L-type $Ca^{2+}$ blocker from the family of dihydropyridines and is used in the treatment of hypertension or as a preventive treatment for stroke and heart attack[37]. Its application in the cochlea should block the mechanotransduction and therefore induce a deafness without altering the post-synaptic integrity. The 100 µM Isradipine used in this experiment was 50 times higher than what is used in vitro to block the generation EPCS in the button facing the IHC (Lina Maria Jaime Tobon, personal communication). Prior and after Isradipine application, aCAP threshold and 8 kHz acoustic cochlear potential growth function were measured. After application, a significant threshold shift at 32 kHz (**Figure S10a**, Wilcoxon signed-rank test), and decrease of aCAP amplitude was observed for level of stimulation higher than 40 dB SPL (**Figure S10b**, Wilcoxon signed-rank test). This result suggests a partial deafening characterized by a high-frequency threshold elevation and a reduced mechanotransduction, which is lower than initially expected, probably due to a poor diffusion in the cochlea. Regardless, after B-TCPc application an oCAP of similar amplitude to the control experiment was measured (**Figure S10c**).

**DISCUSSION AND CONCLUSIONS**

The present work shows the design, development and characterization of new Targeted Covalent Photoswitches (TCPs) able to photosensitize endogenous receptors without genetic manipulation at high rate and in the visible wavelength range of the light spectrum. As designed, the new push-pull substituents in the vicinity of the azobenzenic core shifted its functional activity spectrum to the visible wavelength range. The color of optimal activation wavelength (~460 nm) gives the name to the novel blue-TCP (B-TCP). The combinatorial chemical approach used demonstrates the versatility provided by click coupling [17]. In vitro tests were aimed at

optimizing time and chemical precursors by using a full-scale experimental approach with primary cultures of hippocampal neurons.

During the systematic B-TCP functional tests in vitro, we obtained two B-TCP combinations able to conjugate to native AMPA receptors and control their activity with light. The first combination (B-TCPa) shows intrinsic neural depolarization that can only be reverted by blue light illumination ("trans-on"). Such basal receptor activation is generally not a desired feature in light-regulated drugs, so we searched for the reverse effect by combination of different precursor tails with increased rigidity or larger linker length. One out of three new tails gave rise to B-TCPc, which shows the most convenient "cis-on" activity: neuronal depolarization is induced by blue light stimulation and the frequency of action potential firing can be controlled with short light pulses (50 ms) and at low light power densities (45.9 µW $mm^{-2}$ at 460 nm).

The properties of B-TCPc obtained in vitro confirm that: 1) by chemical design we can spectrally shift TCP features without altering their reactivity to endogenous receptors; 2) new substituents provide asymmetry to the azobenzene unit, which accelerates thermal relaxation time to millisecond timescale; 3) single wavelength irradiation is sufficient for the rapid induction of neural depolarization and trigger of action potentials. Altogether leads us to consider B-TCPc a good candidate for advanced tests in vivo.

Since pharmacological characterization indicates a preference for AMPARs conjugation and kinetics of B-TCPc are in the millisecond timescale, we looked for target systems to take advantage of both features. One of the fastest neurotransmission processes is described to happen between sensory synaptic mechanotransduction between sensory hair cells and SGNs in the cochlea. Here we present, to our knowledge, the first in vivo photopharmacological approach to control cochlear spiral ganglion neurons (SGNs). Results obtained after direct perfusion of B-TCP in vivo demonstrate a higher performance than the best optogenetic tools in the field[32–34]. A first important feature is the light intensity required to evoke a neural response. The lowest light threshold were reported for the opsin CatCh in gerbil SGNs and amounted in the best case to 1-2 µJ[32]. Lower energy light pulse threshold, in the range of 0.54 µJ, were observed with B-TCPc. Another important factor is the duration of the light pulse that triggers the highest neural response, it is in the range of 1 ms for optogenetic[32–34] and of 80 µs for the B-TCPc. A last important parameter is the speed to which information can be encoded in the SGNs. Using optogenetics the maximum frequency that can be evoked is inversely proportional to the closing kinetics of the opsin. So far the fastest reported opsin, called Chronos, has a closing kinetic around 1 ms[34,38], limiting the maximum firing in SGNs at 1 kHz. Finally, for optogenetics the maximum repetition rate that can be used is directly related to the closing kinetics of the opsin[34]. Data obtained with B-TCPc suggests a neural synchronization up to 4 kHz. This last point should be confirmed by single SGN recording (see Perspective).

Besides assessing the outstanding performance of B-TCPc, we also revealed the necessity of synapse preservation for the correct photoswitching of SGNs. These findings hamper the application of this photopharmacological approach to hearing loss conditions originated by aminoglycoside antibiotics or any other cause that produce synaptic degeneration like age-related hearing loss or acoustic trauma[39,40]. Nonetheless, there is still hope for other hearing impairment cases caused by $Ca^{2+}$ channel mutations[41], due to ototoxic anticancer treatments[42] or some genetic deafnesses[43] . Confinement of local application of B-TCP will avoid current pharmacological approaches available that may have some side-effects in other tissues like heart[44].

Previously, photopharmacology demonstrated its potential in photosensitization of other sensory systems like retina[45–47]. Now, to the best of our knowledge, this is the first application of photopharmacology in the auditory system, and it sets the stage to become a new field in expansion.

## Perspective

Compound action potential (CAP) recordings reflect the synchronous firing of recruited SGNs in the cochlea, typically the first one elicited by a stimulus[48]. Single SGNs recordings would allow to inspect the firing pattern in response to light, and in theory teach us about the number of spikes triggered by the light stimulation and how fast SGNs can really follow the light stimulation. Also as the acoustic response might be preserved in this experiment, firing pattern can be correlated with the tonotopy or also to the population of SGNs[49]. However, the estimated number of recruited SGNs is ~8 % [The estimation is based on a comparison of the light response with the acoustical one (**Figure S11a**); and the read out of the number of recruited synapses from an guinea pig cochlea model (**Figure S11b-c**,[48]]. Prospective B-TCPc optimization process in terms of diffusion, conjugation and photostability will be necessary to further perform these experiments.

## Author contribution

Carlo Matera designed and performed the chemical synthesis and the photochemical study at the laboratory of Amadeu Llebaria (IQAC-CID). Amadeu Llebaria supervised the chemical synthesis. Aida Garrido-Charles performed in vitro characterization and in vivo experiments were performed by Antoine Huet and Aida Garrido-Charles at the laboratory of Tobias Moser. In vivo experiments were supervised by Tobias Moser. Pau Gorostiza conceived and supervised the project. Aida Garrido-Charles and Antoine Huet wrote the manuscript with input from all authors.

**SUPPLEMENTARY INFORMATION**

**Supplementary figures**

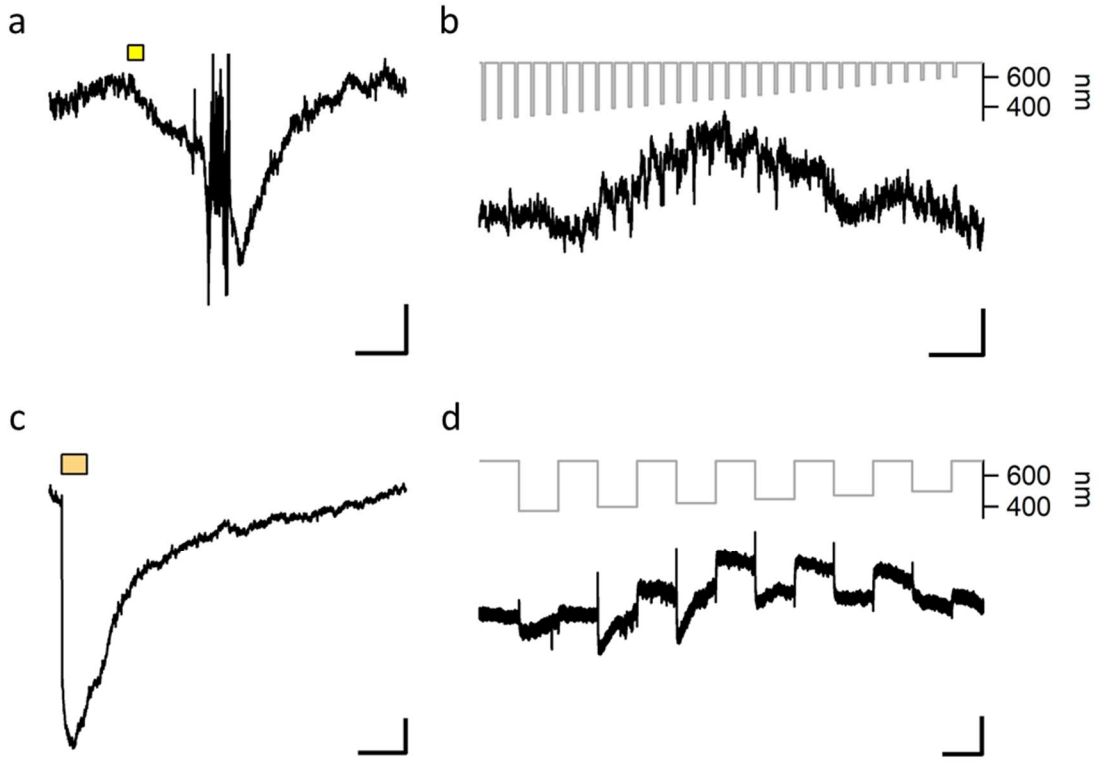


**Figure S1. In vitro photocurrents induced by free BlueTCP heads (azides) recorded using whole cell patch clamp.** a) Inward currents recorded in transiently transfected HEK293 cells with wild-type GluK1 receptor after perfusion of "bluedhead-0" (100 µM; yellow bar). b) Wavelength screening using whole-cell voltage clamp recordings in presence of bluedhead-0 (100 µM). Light pulses of 1s ranging from 300 to 600 nm. c) Inward currents induced after perfusion of "bluedhead-1" (100 µM; gold bar). d) Wavelength screening using whole-cell voltage clamp recordings in presence of "bluedhead-1" (100 µM). Light pulses of 5s ranging from 375 to 500 nm. Holding wavelength is 690 nm. Cells are incubated with ConA. Scale bar in (a-c) is 20 pA, 20 s, and in (d) 20 pA, 5 s.

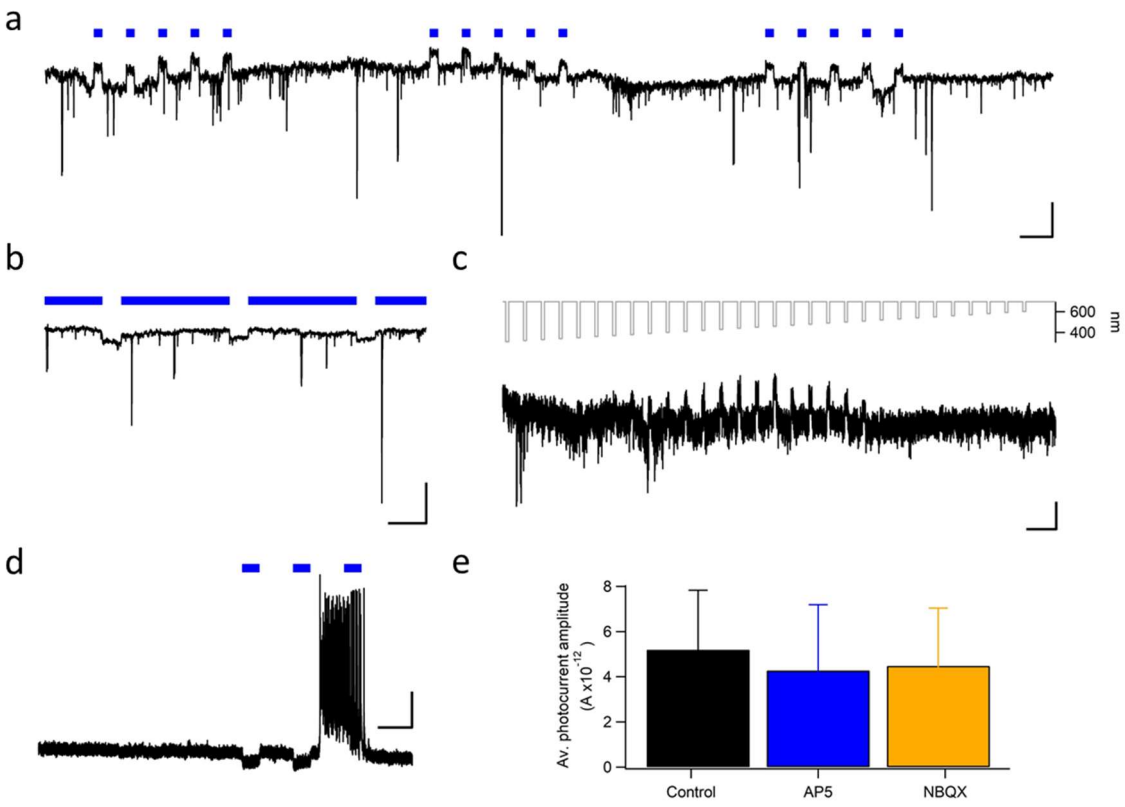


**Figure S2. In vitro photocurrents induced by B-TCPa recorded using whole cell patch clamp in rat hippocampal neurons 11 days in culture.** a) Whole-cell voltage clamp recording after conjugation of B-TCPa (25 µM; 2 min; pH9) and irradiation at $\lambda_{exc}$ = 460 nm for 5 s (blue bars). Scale bar 50 pA, 20 s. b) Whole-cell voltage clamp recordings after conjugation of B-TCPa and irradiation at $\lambda_{exc}$ = 690 nm for 5 s while setting a continue illumination at 460 nm (blue bars). Scale bar is 100 pA, 20 s. c) Activation spectra recorded in whole cell voltage clamp. Wavelength screening ranged from 300 to 600 nm, while resting wavelength was set to 690 nm to allow thermal relaxation. Neurons were current clamped at −60 mV. d) Whole-cell current clamp recording after conjugation of B-TCPa and irradiation at λexc = 460 nm for 5 s (blue bars). Scale bar 20 mV, 10 s. e) Quantification of photocurrent amplitude under different conditions: control (B-TCPa incubated 25 µM for 2 min at pH9; n = 6); AP5 (perfusion 100 µM, n = 3); NBQX (perfusion 10 µM, n = 4). Error bars are ± SEM.

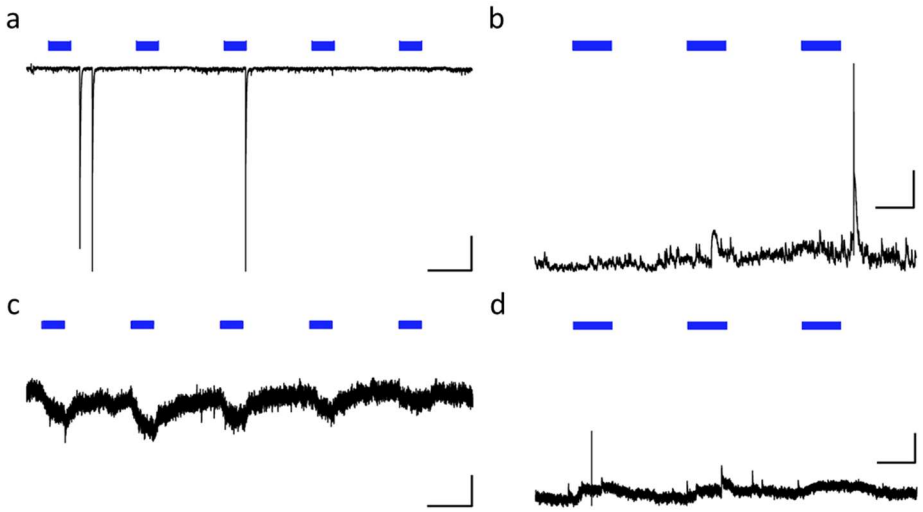


**Figure S3. In vitro photocurrents induced by B-TCPb recorded in rat hippocampal neurons (13 div) in culture using whole cell patch clamp.** a) Whole-cell voltage clamp recordings after conjugation of B-TCPb (12.5 µM; 10 min; pH7.42). Neurons were current clamped at −60 mV. Scale bar 500 pA, 10 s. b) Whole-cell current clamp recording after conjugation of B-TCPb. Scale bar 20 mV, 5 s. c) Whole-cell current clamp recordings after conjugation of B-TCPb after perfusion of 10 µM B-TCPb. Scale bar 50 pA, 10 s. d) Whole-cell current clamp recording after perfusion of 10 µM B-TCPb. Scale bar 10 mV, 5 s. Irradiation at λexc = 460 nm for 5 s is indicated with blue bars. Thermal relaxation of B-TCPb was achieved with a non-interacting resting wavelength set at 690 nm.

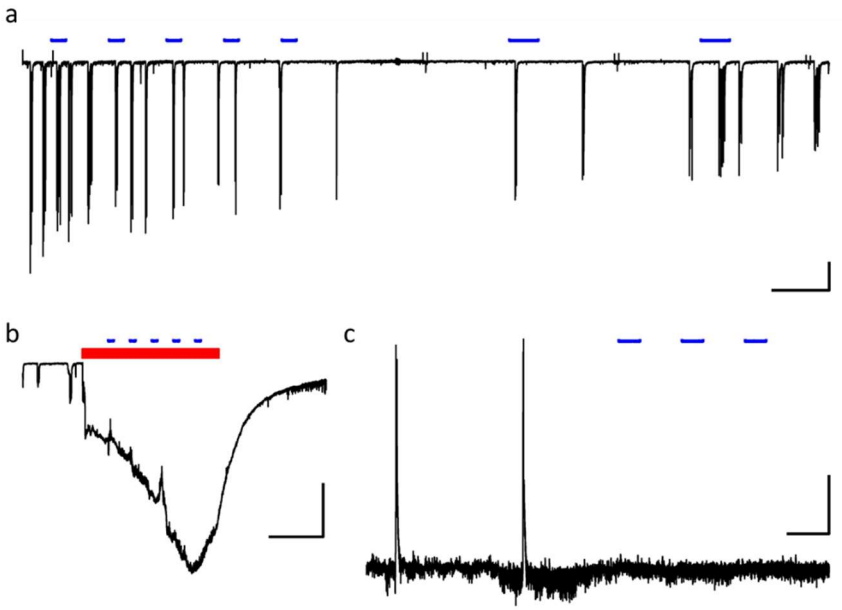


**Figure S4. In vitro photocurrents induced by B-TCPd recorded using whole cell patch clamp in rat hippocampal neurons 15 days in culture.** a) Whole-cell voltage clamp recordings after conjugation of B-TCPd (12.5 µM; 10'; pH8) and irradiation at λexc = 460 for 5 s and 10 s (blue bars) while resting wavelength was set to 690 nm. Neurons were current clamped at −60 mV. Scale bar 500 pA, 20 s. b) Whole-cell voltage clamp recordings after conjugation of B-TCPd and perfusion of glutamate (500 µM, red bar). In presence of glutamate light stimulation was done at λexc = 460 nm for 5 s (blue bars). Scale bar 200 pA, 50 s. c) Whole-cell current clamp recording after conjugation of B-TCPd and irradiation at λexc = 460 nm for 5s (blue bars). Scale bar 20 mV, 10 s.

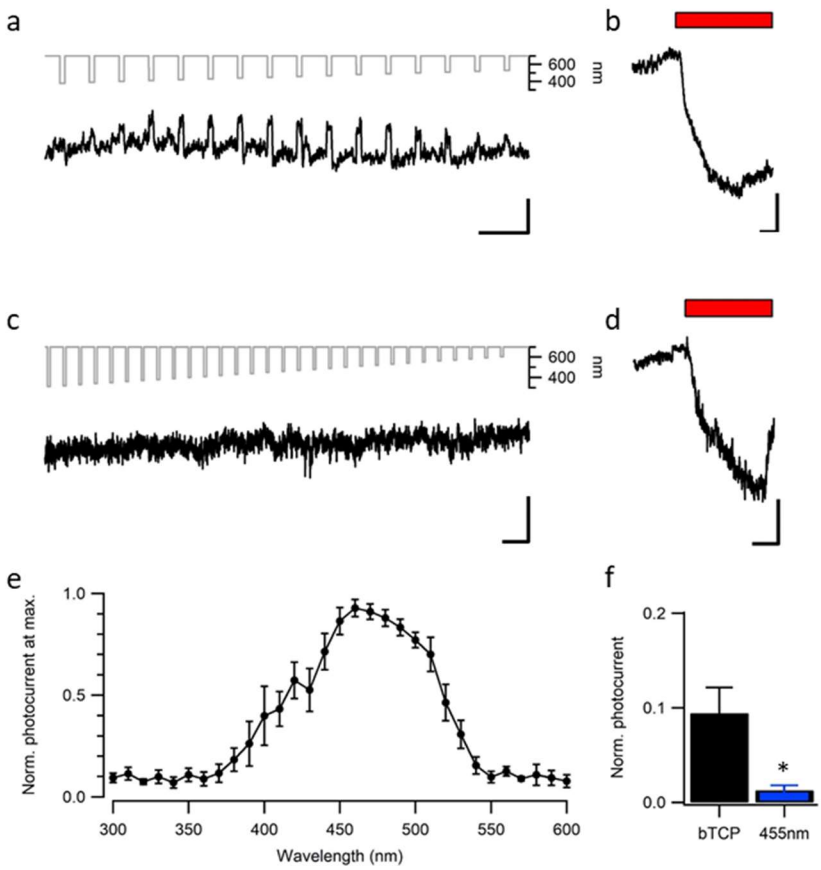


**Figure S5. In vitro photocurrents induced by B-TCPa recorded using whole cell patch clamp in transiently transfected HEK293 cells overexpressing kainate receptor GluK1.** a) Wavelength screening using whole-cell voltage clamp recordings in cells incubated with B-TCPa (25 µM for 2 min at pH9). Light pulses of 1 s ranging from 300 to 600 nm. b) Inward currents after glutamate perfusion (300 µM; red bar). c) Wavelength screening using whole-cell voltage clamp recordings after B-TCPa (25 µM for 2 min at pH9) incubation under 455 nm illumination. Light pulses of 1 s ranging from 300 to 600 nm. d) Inward currents after glutamate perfusion (300 µM; red bar) in cell of panel c. Holding wavelength is set at 690 nm. Cells are incubated with ConA to prevent receptor desensitization. Scale bar is 20 pA and 10 s (a,c) and 5 s (b,d). e) Quantification of action spectra of B-TCPa. Photocurrents are normalized to the maximum photocurrent. Data points are mean ±SEM (n = 5). f) Normalized photocurrent induced by B-TCPa compared to incubation under 455 nm illumination (0.094±0.027, n=4 and 0.013±0.005, n=4, respectively). Significance calculated by paired t-test (*P<0.05; p=0.034). Error bars are ±SEM.

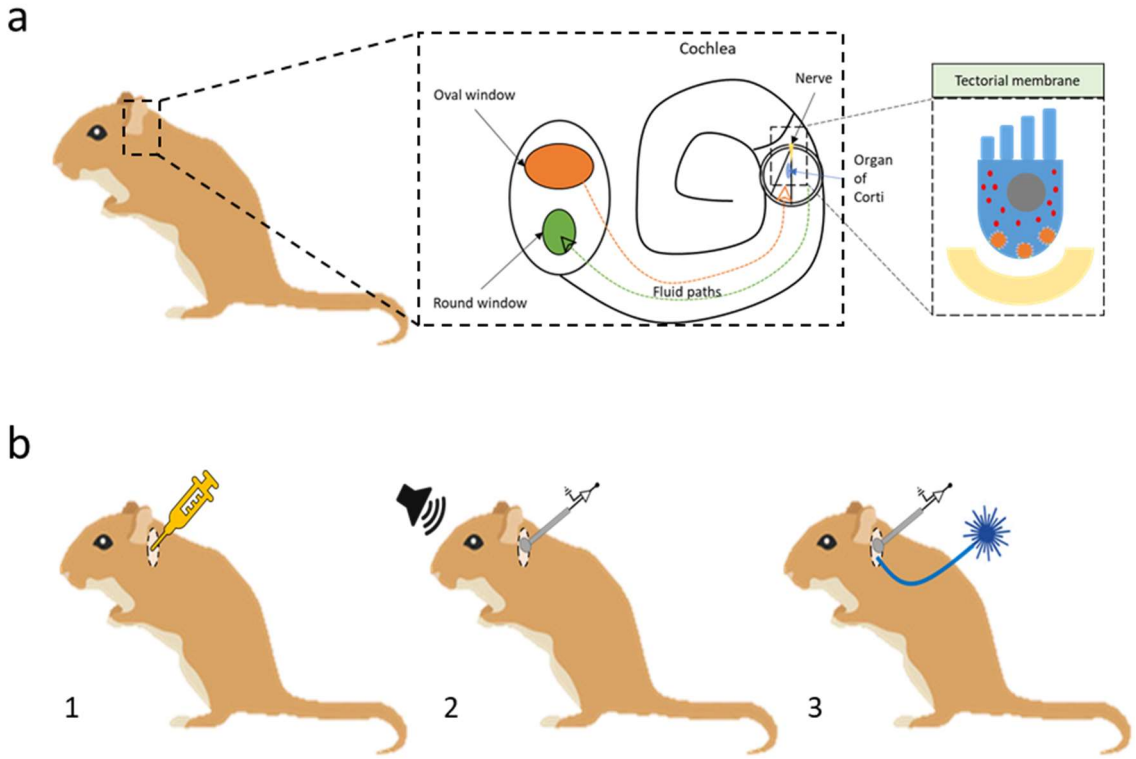


**Figure S6.** a) Schematic representation of Mongolian gerbil cochlea. b) Experimental design after surgical procedure shown in different steps: 1) injection of artificial perilymph (10 min diffusion before and after B-TCP injection) and B-TCP (20 min diffusion); 2) acoustic recording through an end-rounded silver electrode placed in the round window; 3) optical recording through the same electrode as in step 2 but replacing acoustic stimulation by light stimulation (473 nm) with an optic fiber placed in the round window.

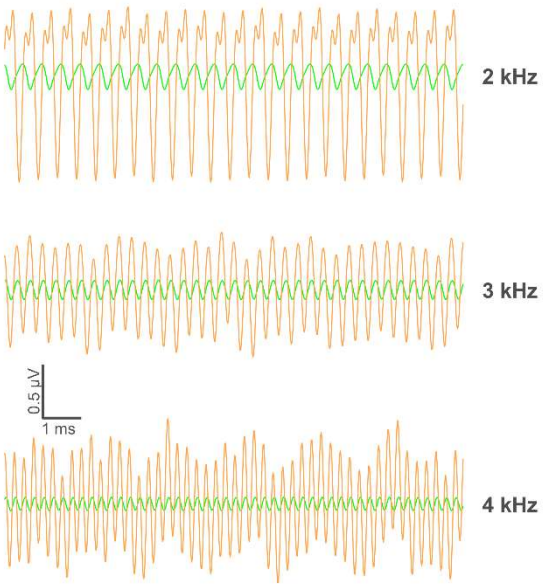


**Figure S7. Example of the high repetition rate evoked oCAP before** (orange) **and after sacrifice** (green) **of the animal.** The oscillation in the trace observed after sacrifice correspond to the onset of the laser.

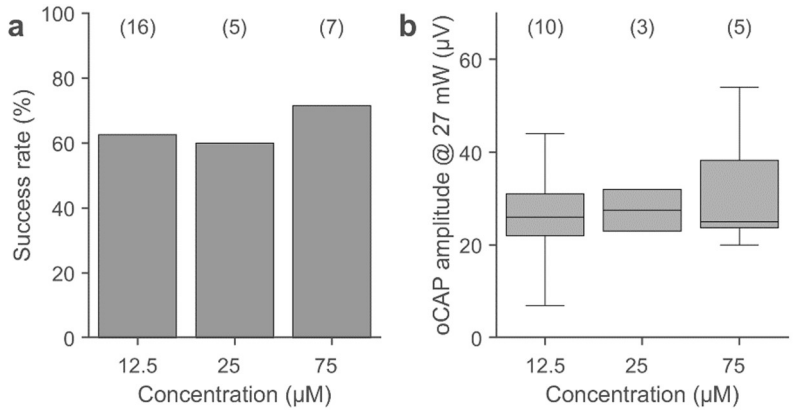


**Figure S8.** Quantification of the photosensitization success rate (a) and oCAP amplitude (27 mW, 80 µS, 10 Hz), (b) as a function of the B-TCPc concentration.

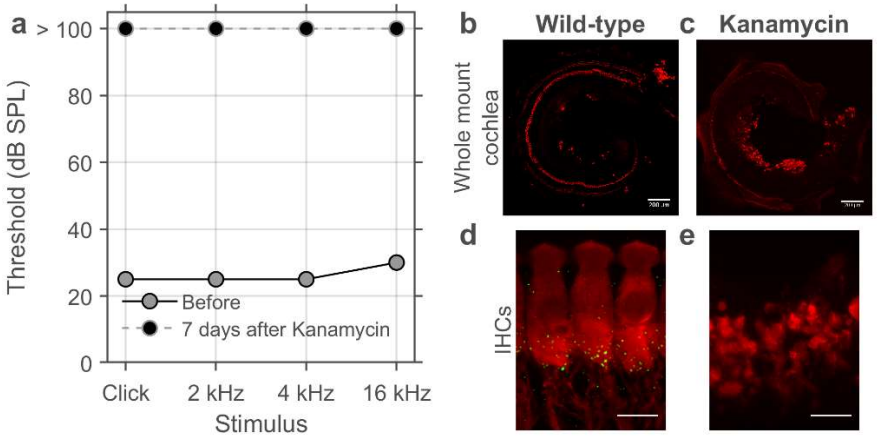


**Figure S9. Kanamycin (50 mg/ml) induced deafness.** a) Acoustically evoked auditory brainstem response threshold before and 7 days after cochlear kanamycin injection. Stimuli were acoustic click and 2-16 kHz tonebursts. b-c) Whole mount cochlea of a wild-type (b) and a kanamycin injected cochlea (c). Red labelling: Calretinin. Scale bar = 200 µm. d-e) IHCs magnified from (b) and (c). Red labelling = Calretinin, green labelling = PSD95. Scale bar = 10 µm.

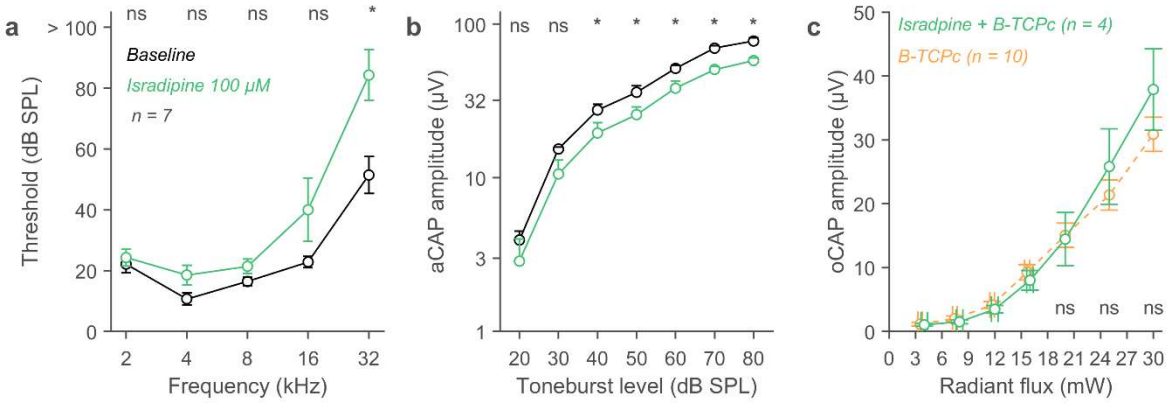


**Figure S10. SGNs light activation after pharmacological reduced mechanotransduction.** a) Audiogram based on aCAP threshold measured at 2, 4, 8, 16 kHz prior (dark) and 10 mins after

Isradipine (100 µM, green) application (*n* = 7). Significance was tested by using a Wilcoxon signed-rank test (* = *p-value* ≤ 0.05). b) aCAP amplitude ($N_1$-$P_1$, 8 kHz tone burst, 8 ms, 20 Hz) as function of the toneburst level prior and after the Isradipine application. Significance was tested by using a Wilcoxon signed-rank test (* = *p-value* ≤ 0.05). c) oCAP amplitude ($N_1$-$P_1$, light pulse, 80/100 µs, 10 Hz) as a function of the radiant flux for the control (orange, similar to figure 5.E, *n* = 10) and the Isradipine followed by B-TCPc application (green, *n* = 4). Significance was tested by Mann–Whitney U test.

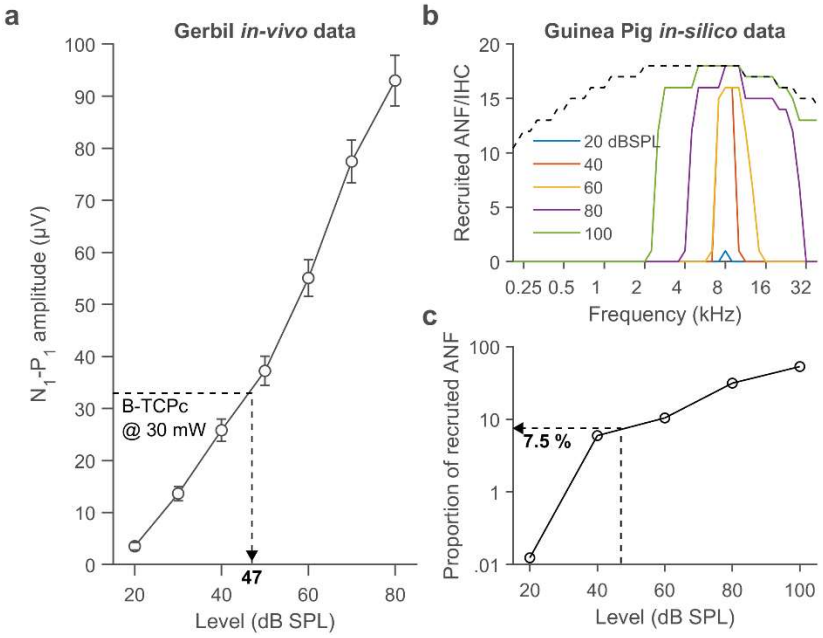


**Figure S11. Estimation of the number of synapses recruited by the light stimulation.** a) oCAP amplitude ($N_1$-$P_1$, 30 mW, light pulse 80/100 µs, 10 Hz) evoked by B-TCPc as function of the toneburst level. b) Sound-activated ANFs per IHC along the tonotopic axis. Gray dashed line shows the guinea pig synaptic cochleogram. The criterion for sound-activated ANF was 10 spikes/s above spontaneous rate (SR). Adapted from[48]. c) Estimation of the proportion of recruited ANF extracted from the correlation between toneburst level and oCAP amplitude evoked by B-TCPc.

## Supplementary results

Example traces after Blue-TCPa application in adult gerbil cochlea are illustrated in **Figure S12**. After acoustic stimulation (8 kHz tone burst), the CAP showed us a preservation of the cochlear microphonic among the 3 tested conditions: artificial perilymph ("baseline"; 10 min), 12.5 µM B-TCPa (20 min) and rinsing with artificial perilymph (10 min) (**Figure S12a**). In contrast, the aCAP, obtained by filtering the mass potential between 0.3 and 3 kHz, showed a significant decrease after rinsing the compound out of the cochlea (**Figure S12b**, p-value ≤ 0.001, Wilcoxon signed rank test). This decrease could reflect the binding of the compound to the SGN AMPA receptors, but without inducing ototoxicity because cochlear microphonic reflecting the outer hair cell function is preserved (**Figure S12a**).

To characterize the light-induced activation of the SGNs, we recorded optically evoked CAP (oCAP) using a fiber-coupled laser (Ø = 200 µm, λ = 473 nm; **Figure S12c**). Representative oCAP trace is shown in **Figure S12c** (dark trace). One millisecond blue light stimulation through the

round window evoked oCAP in B-TCPa perfused cochlea. The oCAP was inhibited by applying 1 µM tetrodotoxin (TTX; sodium channel blocker) for 30 min (**Figure S12c**, gray trace) as a prove that oCAP is evoked by the synchronous activation of SGNs. Increasing the radian flux (**Figure S12d**, pulse duration = 80 µs, repetition rate = 10 Hz) resulted in increased oCAP amplitude (**Figure S12e**) and decreased N1 latency (**Figure S12f**). Although the average threshold of oCAP amounted to 2,5 ± 0.86 mW, stimulus as low as 1 mW could elicit a synchronous response. Interestingly the oCAP amplitude obtained in response to 32 mW light pulse is rather similar to the amplitude measured in response to 80 dB SPL 8 kHz tonebursts. Measuring oCAP in response to different stimulus durations (**Figure S12g**, radiant flux = 28 mW, repetition rate = 10 Hz), we found that: i) oCAP could be elicited by stimulus as short as 20 µs (the smallest pulse duration that could be test by the set-up); ii) the oCAP amplitude as a function of the pulse duration presents a "bell" shape with the maximum amplitude obtained for pulse duration between 60 and 100 µs (**Figure S12h**). Interestingly the oCAP latency is stable across the different tested values (**Figure S12i**). Finally analyzing the dependence of oCAP on the repetition rate (**Figure S12j**, radiant flux = 28 mW, pulse duration = 80 µs) showed that increasing the repetition rate reduced oCAP amplitude (**Figure S12k**) and decreased oCAP latency (**Figure S12l**). However sizable oCAP could be measured up to 1 kHz, the highest value that could be tested by the set-up at that time.

Surprisingly, both compounds work equally well to photosensitize the cochlea and no significant differences are noticed between B-TCPa or B-TCPc in vivo. This can be explained by our experimental approach, where we are recording coordinated firing of SGNs upon light irradiation. If we consider that B-TCPa is intrinsically activating AMPAR and their fast kinetics of desensitization[50], most probably AMPAR conjugated to B-TCPa will be in their closed desensitized state. On the other hand, B-TCPc in *trans* conformation does not activate AMPARs, which in this case will be in their resting closed state. In both cases, AMPARs will departure from closed states and repetitive light stimulation cause analogous synchronized action potential firing of SGNs. Further characterization using more precise technique like single-unit recordings will clarify masked differential features of both compounds such as temporal precision, the jitter (temporal variability or deviation) and the latency.

Finally, we cannot neglect that performance of B-TCPs presented in this work makes these compounds very promising tools for optical SGN stimulation on non-genetically modified organisms.

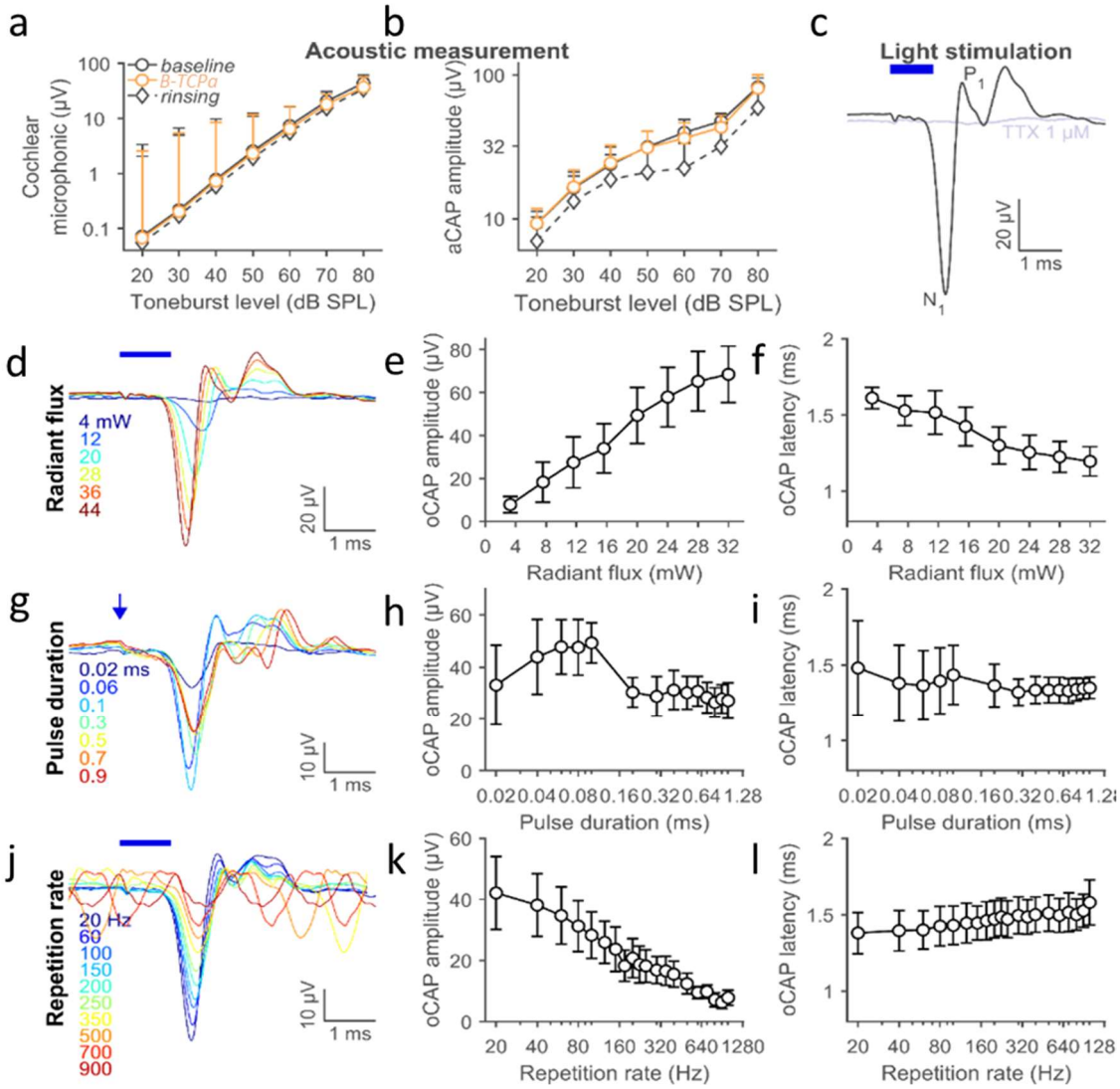


**Figure S12. Characterization of optically evoked compound action potential (CAP) after round window application of 12.5 µM B-TCPa**. a,b) In response to 8 kHz tone burst (pulse duration = 8 ms, rise/fall time = 1 ms, repetition rate = 20 Hz, level : 20 to 80 dB SPL per 10 dB step), the cochlear microphonic (a) and the CAP (b) was extracted from the round window mass potential from an electrode placed into the round window niche (n = 5) 10 min after artificial perilymph application ("baseline", continuous grey line), 12.5 µM B-TCPa (orange) and washout (dashed gray line). c) Optically evoked CAP by a 1 ms light pulse delivered into the cochlea by a 473 nm laser coupled to an optical fiber (200 µm) through the round window. The oCAP was abolished by a 1 µM TTX application (gray trace). The blue line indicated the light stimulation. d,g,j) Representative oCAP in response to various radian flux (80 µs at 10 Hz, d), pulse duration (28 mW at 10 Hz, g) and repetition rate (80 µs at 28 mW, j). A color scale + legend was used to represent the different tested value. In (d) and (j), the blue line indicates the light stimulation and in (g), the blue arrow indicates the beginning of the light pulse. e,h,k) oCAP amplitude (N1-P1) and (f,I,l) oCAP latency (N1) as a function of the radian flux (e,f), the pulse duration (h,i) and the repetition rate (k,l) (n = 4).

## Supplementary methods

**Rat hippocampal neural primary culture.** All procedures were conducted in accordance with the European guidelines for animal care and use in research and were approved by the Animal Experimentation Ethics Committee at the University of Barcelona (Spain). Low-density primary hippocampal cultures were prepared from newborn P0-P3 pups from Sprague Dawley rat and maintained in cell culture for 1-2 weeks in coverslips coated with poly-L-lysine (Sigma-Aldrich), as previously described[51–53] . Cells were cultured with complete medium (Neurobasal A, B-27 5%, GlutaMax (0.5x), glucose 15 mM, penicillin (5 U $ml^{-1}$) and streptomycin (5 µg $ml^{-1}$)). Within 48-72 h an anti-mitotic treatment with AraC 5 µM is done to avoid fibroblast and astrocyte proliferation. Half of the medium in each well was changed every 3-4 days.

**Electrophysiology recording conditions for rat hippocampal neurons.** Voltage and current-clamp recordings under whole-cell configuration were done using an EPC- 10 amplifier and data at 10 kHz was acquired with amplifier's software Patch Master (HEKA). Bath solution was composed of (in mM): 140 NaCl, 2 $MgCl_2$, 2.5 KCl, 10 HEPES, 0.2 $CaCl_2$ and 10–20 mM glucose to fix osmolarity to 310 mOsm·$kg^{-1}$, pH 7.42 adjusted with NaOH. Borosilicate glass pipettes were pulled with a typical resistance of 6–8 MΩ for neurons. Pipette solution contained (in mM): 130 KCl, 5 $MgCl_2$, 3 $Na_2ATP$, 1 $Na_2GTP$, 20 HEPES, 0.5 EGTA. Osmolarity is adjusted at 289 mOsm·$kg^{-1}$ and pH 7.2 adjusted with KOH. During recordings, neurons were maintained at room temperature (r.t., 25-27 °C) in a continuous perfusion of bath solution.

**Cell line and transfection.** HEK293 tsA201 cell line (SV40-transformed, Human Embryonic Kidney 293 cells) was maintained at 37 °C in a 5% $CO_2$ humid incubator with Dulbecco's Modified Eagle Medium/Nutrient Mixture F-12 media (DMEM) (1:1, Invitrogen) supplemented with 10% Fetal Bovine Serum (FBS) and 1% Penicillin/Streptomycin. Cells transiently expressed the receptor subunit GluK1(Q)-2b(GGAA), GluA1 or GluA2. GluK1(Q)-2b(GGAA) was kindly provided by G. Swanson (Northwestern University, Feinberg School of Medicine), with the endoplasmic reticulum retention motif of the carboxy-terminal mutated to increase surface expression[54]. The expression plasmids for GluA1 and GluA2 were kindly provided by David Soto (Universitat de Barcelona). DNA–X-tremGENE 9 Transfection Reagent (Roche) mix was used following manufacturer's instructions with a Reagent:DNA ratio of 3:1. Ionotropic glutamate receptor plasmids were co-transfected with peGFP with a Transfection Reagent:iGluR:eGPF ratio of 3:1:0.1. The mix was incubated for 20 min at room temperature, meanwhile cells were detached and freshly plated into a 12-mulltiwell plate at a density of $3 \times 10^5$ cells before the DNA-Transfection Reagent mix was added dropwise into each well. Experiments were performed after 48–72 h, and the day before the experiment cells were plated at low density on 16-mm coverslips (Fisher Scientific) treated with collagen (Sigma-Aldrich) to allow cell adhesion.

**Electrophysiology.** Whole-cell voltage-clamp recordings were done using an EPC-10 amplifier and data at 10 kHz was acquired with amplifier's software Patch Master (HEKA). Bath solution was composed of (in mM): 140 NaCl, 1 $MgCl_2$, 2.5 KCl, 10 HEPES, 2.5 $CaCl_2$ and 10–20 glucose to fix osmolarity to 310 mOsm·$kg^{-1}$, while pH 7.42 was adjusted with NaOH. Borosilicate glass pipettes were pulled with a typical resistance of 4–6 MΩ for HEK293 cells. Pipette solution contained (in mM): 120 cesium methanosulfonate, 10 TEA-Cl, 5 $MgCl_2$, 3 $Na_2ATP$, 1 $Na_2GTP$, 20 HEPES, 0.5 EGTA; osmolarity was 290 mOsm·$kg^{-1}$ and pH 7.2 was adjusted with CsOH.
Before starting the recording, cells overexpressing GluK1 were incubated 10 min with 0.3 mg $mL^{-1}$ Concanavalin A (Sigma) —to block channel desensitization— on an ES based on $NMDG^+$ (to avoid depolarization due to open GluRs, in mM): 110 $NMDG^+$, 2.5 KCl, 1 $MgCl_2$, 10 HEPES, 10–20 glucose to fix osmolarity to 300 mOsm·$kg^{-1}$, while pH 7.4 was adjusted with HCl. Before placing the coverslip to the recording chamber, cells were washed again with bath solution. Recordings

with cells overexpressing AMPA receptors were performed in presence of cyclothiazide (CTZ, 25 µM) (Sigma).
Light stimulation was done by illumination of the entire focused field using a Polychrome V monochromator (TILL Photonics) connected through the back port of an IX71 inverted microscope (Olympus) with a XLUMPLFLN 20XW x20/1 water immersion objective (Olympus). For automatically controlling wavelength, the monochromator was connected to the EPC-10 amplifier via Photochromic Manual Control (TILL Photonics) and controlled with the photometry module of Patch Master. Light power density measured with a Newport 1916-C light meter after the objective was 22.0 µW $mm^{-2}$ for 380 nm, 45.9 µW $mm^{-2}$ for 460 nm and 47.4 µW $mm^{-2}$ for 500 nm. One-photon action spectrum characterization was done during voltage-clamp recordings applying a train of 1 s light-pulses at different wavelengths (for the whole action spectrum, we ranged wavelengths from 300 to 600 nm, with 10 nm steps) with 5 s delay between pulses in which light was switched to 690 nm to allow thermal *cis-trans* back-isomerization.

**Drug preparation for in vivo cochlea infusion**. Artificial perilymph solution consisted of the following (in mM): 137 NaCl; 5 KCl; 2 $CaCl_2$; 1 $MgCl_2$; 1 $NaHCO_3$; 11 glucose; pH 7.4 adjusted with NaOH; osmolarity: 304 ± 4.3 mOsm/kg. Before each experiment, final clicked B-TCPs were diluted in artificial perilymph to a final concentration ranging from 12.5 to 75 µM[55].

**Animal surgery for recordings on the auditory pathway and round window infusion technique.** Gerbils were anesthetized with i.p. administration of a mixture of xylazine (5 mg/kg) and urethane (1.32 mg/kg) while analgesia was achieved with buprenorphine. The core temperature was maintained constant at 37 °C using a custom-designed heat plate on a vibration isolation table in a sound-proof chamber (IAC GmbH, Niederkrüchten, Germany)[33,34].
Withdrawal reflex (lack of response to toe pinch) were used to ensure a deep anesthesia and evaluate the physiological status of the animals. First, the left cochlea was exposed through a dorsal approach. Once the bulla had been open, the recording electrode was placed on the bony edge of the round window membrane, leaving enough space in the round window niche for the infusion syringe. The infusion pipette was filled with artificial perilymph alone or containing B-TCP and was introduced into the round window niche (leaving the round window intact) using a micromanipulator (Warner Instruments). After 10-20 min infusion, the solutions were wicked away from the round window niche.
The compound action potential (CAP) was recorded from the round window electrode in response to 8 kHz tone burst (pulse duration = 8 ms, rise/fall time = 1 ms, repetition rate = 20 Hz, level: 20 to 80 dB SPL per 10 dB step). CAP amplitude was measured between N1 and P1, the threshold being defined as the dB SPL needed to elicit a measurable response (> 2 µV).

**Optical stimulation in vivo.** The left bulla was reached using a retroauricular approach and opened to expose the cochlea. A 50/200-µm optical fiber coupled to a 473 nm laser (MLL-FN-473-100, 100 mW, diode pumped solid state [DPSS]; Changchun New Industry Optoelectronics) was inserted into the cochlea via the round window. Irradiance was calibrated with a laser power meter (LaserCheck; Coherent Inc.).

**Data analysis and statistics.** Amplitude of photocurrents were analyzed using IgorPro (Wavemetrics). Displayed whole-cell current traces have been filtered using the infinite impulse response digital filter from IgorPro (low-pass filter with cutoff of 50 Hz). The drift in current observed during light spectra recordings was corrected where appropriate with the IgorPro (WaveMetrics) software using a custom-made macro for drift correction. Statistics were done with Microsoft Excel (Microsoft) and Matlab (Mathworks).

**REFERENCES**


1. Paoletti, P., Ellis-Davies, G. C. R. & Mourot, A. Optical control of neuronal ion channels and receptors. *Nat. Rev. Neurosci.* (2019). doi:10.1038/s41583-019-0197-2
2. Berlin, S. & Isacoff, E. Y. Synapses in the spotlight with synthetic optogenetics. *EMBO Rep.* **18**, 677–692 (2017).
3. Nagel, G. *et al.* Channelrhodopsin-2, a directly light-gated cation-selective membrane channel. *Proc. Natl. Acad. Sci.* **100**, 13940–13945 (2003).
4. Leippe, P., Koehler Leman, J. & Trauner, D. Specificity and Speed: Tethered Photopharmacology. *Biochemistry* acs.biochem.7b00687 (2017). doi:10.1021/acs.biochem.7b00687
5. Velema, W. A., Szymanski, W. & Feringa, B. L. Photopharmacology: Beyond proof of principle. *J. Am. Chem. Soc.* **136**, 2178–2191 (2014).
6. Kienzler, M. A. & Isacoff, E. Y. Precise modulation of neuronal activity with synthetic photoswitchable ligands. *Curr. Opin. Neurobiol.* (2017). doi:10.1016/j.conb.2017.05.021
7. Volgraf, M. *et al.* Allosteric control of an ionotropic glutamate receptor with an optical switch. *Nat. Chem. Biol.* **2**, 47–52 (2006).
8. Gorostiza, P. & Isacoff, E. Optical switches and triggers for the manipulation of ion channels and pores. *Mol. Biosyst.* **3**, 686–704 (2007).
9. Gorostiza, P. & Isacoff, E. Y. Nanoengineering ion channels for optical control. *Physiology (Bethesda).* **23**, 238–47 (2008).
10. Gorostiza, P. *et al.* Mechanisms of photoswitch conjugation and light activation of an ionotropic glutamate receptor. *Proc. Natl. Acad. Sci. U. S. A.* **104**, 10865–70 (2007).
11. Szobota, S. *et al.* Remote control of neuronal activity with a light-gated glutamate receptor. *Neuron* **54**, 535–45 (2007).
12. Caporale, N. *et al.* LiGluR restores visual responses in rodent models of inherited blindness. *Mol. Ther.* **19**, 1212–1219 (2011).
13. Kienzler, M. A. *et al.* A red-shifted, fast-relaxing azobenzene photoswitch for visible light control of an ionotropic glutamate receptor. *J. Am. Chem. Soc.* **135**, 17683–17686 (2013).
14. Gaub, B. M. *et al.* Restoration of visual function by expression of a light-gated mammalian ion channel in retinal ganglion cells or ON-bipolar cells. *Proc Natl Acad Sci USA* (2014).
15. Izquierdo-Serra, M. *et al.* Two-photon neuronal and astrocytic stimulation with azobenzene-based photoswitches. *J. Am. Chem. Soc.* **136**, 8693–701 (2014).
16. Cabré, G. *et al.* Rationally designed azobenzene photoswitches for efficient two-photon neuronal excitation. *Nat. Commun.* **10**, (2019).
17. Izquierdo-Serra, M. *et al.* Optical control of endogenous receptors and cellular excitability using targeted covalent photoswitches. *Nat. Commun.* **7**, 12221 (2016).
18. Hu, H., Gan, J. & Jonas, P. Fast-spiking, parvalbumin+ GABAergic interneurons: From cellular design to microcircuit function. *Science (80-. ).* **345**, (2014).
19. Matthews, G. & Fuchs, P. The diverse roles of ribbon synapses in sensory neurotransmission. *Nat. Rev. Neurosci.* **11**, 812–822 (2010).
20. Dombrowski, T., Rankovic, V. & Moser, T. Toward the Optical Cochlear Implant. *Cold Spring Harb. Perspect. Biol.* (2019).
21. Hermanson, G. T. *Bioconjugate Techniques*. (Academic Press, 2008).

22. Traynelis, S. F. *et al.* Glutamate Receptor Ion Channels : Structure , Regulation , and Function. *Pharmacol. Rev.* **62**, 405–496 (2010).
23. Glowatzki, E. & Fuchs, P. A. Transmitter release at the hair cell ribbon synapse. *Nat. Neurosci.* **5**, 147–154 (2002).
24. Puel, J. Chemical synaptic transmission in the cochlea. Prog. Neurobiol. 47, 449–476. *Prog. Neurobiol.* 449–476 (1995).
25. Ruel, J., Chen, C., Pujol, R., Bobbin, R. P. & Puel, J. L. AMPA-preferring glutamate receptors in cochlear physiology of adult guinea-pig. *J. Physiol.* **518**, 667–680 (1999).
26. Johnson, D. H. The relationship between spike rate and synchrony in responses of auditory-nerve fibers to single tones. *J. Acoust. Soc. Am.* **68**, 1115–1122 (1980).
27. Kiang, N. Y., Watanabe, T., Thomas, E. C. & Clark, L. F. Discharge Patterns of Single Fibers in the Cat's Auditory Nerve. *Cambridge, Massachusetts MIT Press* (1965).
28. Palmer, A. R. & Russell, I. J. Phase-locking in the cochlear nerve of the guinea-pig and its relation to the receptor potential of inner hair-cells. *Hear. Res.* **24**, 1–15 (1986).
29. Rose, J. E., Brugge, J. F., Anderson, D. J. & Hind, J. E. Phase-locked response to low-frequency tones in single auditory nerve fibers of the squirrel monkey. J. Neurophysiol. 30, 769–793. *J. Neurophysiol.* **30**, 769–793 (1967).
30. Huet, A. *et al.* The interplay between spike-time and spike-rate modes in the auditory nerve encodes tone-in-noise threshold. *J. Neurosci.* **38**, 5727–5738 (2018).
31. Huet, A. *et al.* Sound Coding in the Auditory Nerve: From Single Fiber Activity to Cochlear Mass Potentials in Gerbils. *Neuroscience* **407**, 83–92 (2019).
32. Wrobel, C. *et al.* Optogenetic stimulation of cochlear neurons activates the auditory pathway and restores auditory-driven behavior in deaf adult gerbils. *Sci. Transl. Med.* **10**, (2018).
33. Mager, T. *et al.* High frequency neural spiking and auditory signaling by ultrafast red-shifted optogenetics. *Nat. Commun.* **9**, 1750 (2018).
34. Keppeler, D. *et al.* Ultrafast optogenetic stimulation of the auditory pathway by targeting-optimized Chronos. *EMBO J.* **37**, e99649 (2018).
35. Dieter, A., Duque-Afonso, C. J., Rankovic, V., Jeschke, M. & Moser, T. Near physiological spectral selectivity of cochlear optogenetics. *Nat. Commun.* **10**, 1962 (2019).
36. Robertson, D. & Paki, B. Role of L-type Ca2+ channels in transmitter release from mammalian inner hair cells. II. Single-neuron activity. *J. Neurophysiol.* **87**, 2734–2740 (2002).
37. Berjukow, S., Marksteiner, R., Gapp, F., Sinnegger, M. J. & Hering, S. Molecular Mechanism of Calcium Channel Block by Isradipine. *J. Biol. Chem.* **275**, 22114–22120 (2002).
38. Klapoetke, N. C. *et al.* Independent optical excitation of distinct neural populations. *Nat. Methods* **11**, 338–46 (2014).
39. Sergeyenko, Y., Lall, K., Charles Liberman, M. & Kujawa, S. G. Age-related cochlear synaptopathy: An early-onset contributor to auditory functional decline. *J. Neurosci.* **33**, 13686–13694 (2013).
40. Kujawa, S. G. & Liberman, M. C. Adding insult to injury: Cochlear nerve degeneration after 'temporary' noise-induced hearing loss. *J. Neurosci.* **29**, 14077–14085 (2009).
41. Pangrsic, T., Singer, J. H. & Koschak, A. Voltage-gated calcium channels: Key players in sensory coding in the retina and the inner ear. *Physiol. Rev.* **98**, 2063–2096 (2018).

42. Wake, M., Takeno, S., Ibrahim, D. & Harrison, R. Selective Inner Hair Cell Ototoxicity Induced by Carboplatin. *Laringoscope* **104**, 488–493 (1994).
43. Yasunaga, S. *et al.* A mutation in OTOF, encoding otoferlin, a FER-1-like protein, causes DFNB9, a nonsyndromic form of deafness. *Nat. Genet.* **21**, 363–369 (1999).
44. Zamponi, G. W., Striessnig, J., Koschak, A. & Dolphin, A. C. The physiology, pathology, and pharmacology of voltage-gated calcium channels and their future therapeutic potential. *Pharmacol. Rev.* **67**, 821–870 (2015).
45. Marc, R., Pfeiffer, R. & Jones, B. Retinal prosthetics, optogenetics, and chemical photoswitches. *ACS Chem. Neurosci.* **5**, 895–901 (2014).
46. Tochitsky, I., Trautman, J., Gallerani, N., Malis, J. G. & Kramer, R. H. Restoring visual function to the blind retina with a potent, safe and long-lasting photoswitch. *Sci. Rep.* **7**, 45487 (2017).
47. Yue, L., Weiland, J. D., Roska, B. & Humayun, M. S. Retinal stimulation strategies to restore vision: Fundamentals and systems. *Prog. Retin. Eye Res.* (2016). doi:10.1016/j.preteyeres.2016.05.002
48. Bourien, J. *et al.* Contribution of auditory nerve fibers to compound action potential of the auditory nerve. *J. Neurophysiol.* **112**, 1025–1039 (2014).
49. Liberman, M. C. Auditory-nerve response from cats raised in a low-noise chamber. *J. Acoust. Soc. Am.* **63**, 442–455 (1978).
50. Twomey, E. C., Yelshanskaya, M. V., Grassucci, R. A., Frank, J. & Sobolevsky, A. I. Channel opening and gating mechanism in AMPA-subtype glutamate receptors. *Nature* **549**, 60–65 (2017).
51. Beaudoin, G. M. J. *et al.* Culturing pyramidal neurons from the early postnatal mouse hippocampus and cortex. *Nat. Protoc.* **7**, 1741–1754 (2012).
52. Halliwell, R. F., Peters, J. A. & Lambert, J. J. The mechanism of action and pharmacological specificity of the anticonvulsant NMDA antagonist MK-801: a voltage clamp study on neuronal cells in culture. *Br. J. Pharmacol.* **96**, 480–494 (1989).
53. Kaech, S. & Banker, G. Culturing hippocampal neurons. *Nat. Protoc.* **1**, 2406–2415 (2006).
54. Ren, Z. *et al.* Cell surface expression of GluR5 kainate receptors is regulated by an endoplasmic reticulum retention signal. *J. Biol. Chem.* **278**, 52700–9 (2003).
55. Batrel, C. *et al.* Mass potentials recorded at the round window enable the detection of low spontaneous rate fibers in gerbil auditory nerve. *PLoS One* (2017). doi:10.1371/journal.pone.0169890

## CHAPTER 5| Rationally designed azobenzene photoswitches for efficient two-photon neuronal excitation

Gisela Cabré[1,+], Aida Garrido-Charles[2,+], Miquel Moreno[1], Miquel Bosch[2], Montserrat Porta de la Riva[3], Michael Krieg[3], Marta Gascón-Moya[1], Núria Camarero[2], Ricard Gelabert[1], José M. Lluch[1], Félix Busqué[1], Jordi Hernando[1], Pau Gorostiza[2,4,5*] and Ramon Alibés[1,*]

[1] Departament de Química, Universitat Autònoma de Barcelona (UAB), Cerdanyola del Vallès, Spain.

[2] Institut de Bioenginyeria de Catalunya (IBEC), Barcelona Institute of Science and Technology (BIST), Barcelona, Spain.

[3] Institut de Ciències Fotòniques (ICFO), The Barcelona Institute of Science and Technology (BIST), Castelldefels, Barcelona, Spain

[4] Institució Catalana de Recerca i Estudis Avançats (ICREA), Barcelona, Spain.

[5] Centro de Investigación Biomédica en Red en Bioingeniería, Biomateriales y Nanomedicina (CIBER-BBN), Zaragoza, Spain.

[+] G. Cabré and A. Garrido-Charles contributed equally to this work

**Corresponding Author:** [*] pau@icrea.cat (P. G.), ramon.alibes@uab.cat (R. A.)

## Abstract

Manipulation of neuronal activity using two-photon excitation of azobenzene photoswitches with near-infrared light has been recently demonstrated, but their practical use in neuronal tissue to photostimulate individual neurons with three-dimensional precision has been hampered by firstly, the low efficacy and reliability of NIR-induced azobenzene photoisomerization compared to one-photon excitation, and secondly, the short *cis* state lifetime of the two-photon responsive azo switches. Here we report that based on time-dependent density functional theory calculations, we rationally design and synthesize azobenzene photoswitches endowed with both high two-photon absorption cross section and slow thermal back-isomerization. These compounds provide optimized and sustained two-photon neuronal stimulation both in light-scattering brain tissue and in *Caenorhabditis elegans* nematodes, displaying photoresponse intensities that are comparable to those achieved under one-photon excitation. This finding opens the way to use both genetically targeted and pharmacologically selective azobenzene photoswitches to dissect intact neuronal circuits in three dimensions.

## Introduction

Azobenzene photoswitches[1] are at the core of most recently developed strategies to manipulate biological functions with light,[2-4] which among other systems, enable remote control of cell receptors and channels.[5-7] Towards these applications, much effort is being devoted to optimize the light-induced response of azobenzenes (e.g. long wavelength operation)[8-12] or to enhance the *cis* state thermal stability.[9,13]

A crucial aspect that must ineluctably be addressed to unleash the full potential of azobenzene photoswitches is multiphoton excitation with near-infrared radiation (NIR, ~700-1400 nm),[14,15] which enables 3D sub-micrometric resolution,[16] deeper penetration into tissue with lower photodamage,[17] and patterned illumination.[18,19] However, in contrast to the progress made with optogenetics,[20,21] efficient multiphoton operation of azobenzenes still remains a challenge, mainly due to the low two-photon (2P) absorption cross-sections ($\sigma_2$) of most of these compounds under NIR light excitation.[22,23]

This is the case of **MAG**, the first-generation azobenzene-based photoswitchable tethered ligand (PTL) used for the preparation of light-gated glutamate receptors (LiGluR, Figure 1a and Supplementary Figure 1).[24,25] Upon conjugation to a cysteine residue genetically-engineered in kainate-type ionotropic glutamate receptor GluK2, **MAG** *trans-cis* photoisomerization allows optical control of ion channel opening and closing in LiGluR,[24,25] a behavior profusely applied to the study of neurotransmission *in vitro* and *in vivo*.[26-30] While effective light-gating of LiGluR is achieved via regular one-photon (1P) absorption of UV-visible radiation,[24-30] multiphoton operation with NIR light is preferred to stimulate selected cells located deep into tissues at high spatiotemporal resolution.[31,32] Indeed, 2P switching at ~ 750-900 nm was recently demonstrated for LiGluR after functionalization with **MAG**[33] and its analogous ligand **MAG$_0$** (Supplementary Figure 1);[34] however, rather limited responses were obtained owing to the very low 2P absorption cross-section of the symmetrically-substituted azobenzene core of these compounds ($\sigma_2$ = 10 GM for *trans*-**MAG$_0$** at 820 nm,[34] Figure 1b).

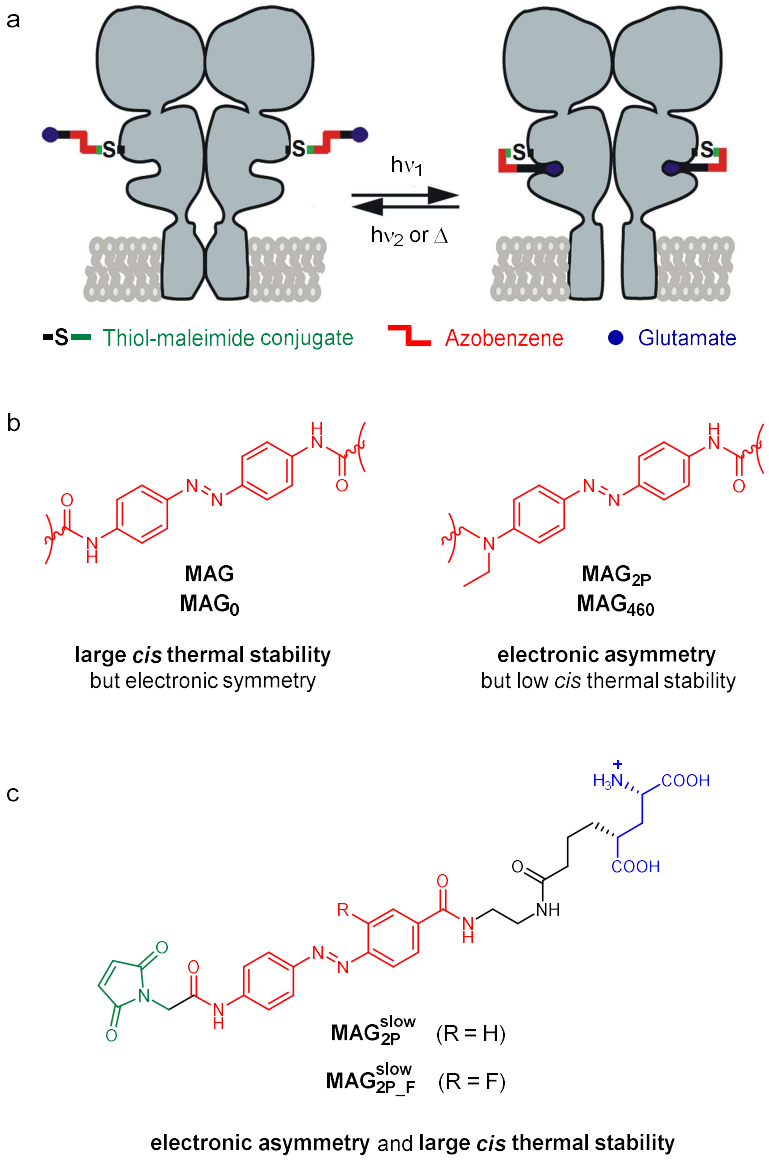


**Figure 1** Strategy towards optimized azobenzene photoswitches for the 2P excitation of LiGluR**.** (**a**) Operating mode of MAG-type PTLs on LiGluR, which are composed of three covalently-tethered units: a glutamate ligand, an azobenzene core, and a maleimide group that binds to a cysteine residue genetically-engineered in the receptor. UV-visible (1P) or NIR (2P) light excitation induces glutamate recognition and channel opening via *trans*→*cis* isomerization, which results in ion flow across the membrane. This process is reverted by illumination with visible light excitation (1P) or thermal back-isomerization of the *cis* state of the switch. (**b**) Structures of the azobenzene cores of **MAG**, **MAG$_0$**, **MAG$_{2P}$** and **MAG$_{460}$** PTLs proposed for the photoswitching of LiGluR under 1P and 2P excitation conditions. (**c**) Structures of PTLs **MAG$_{2P}^{slow}$** and **MAG$_{2P_F}^{slow}$**.

Two different strategies have been explored to enhance the 2P activity of **MAG**-type PTLs for multiphoton LiGluR operation. On one hand, sensitized photoswitching with NIR light was attempted by tethering a 2P-absorbing antenna to the ligand,[33,35] which however compromised its biological activity due to decreased solubility in water, low conjugation efficiency to cysteine-tagged GluK2 and/or reduced affinity towards the receptor binding site.[33,35] On the other hand, electronically-asymmetric azobenzenes were proposed to intrinsically increase their 2P absorption cross-sections.[22,23,36-38] For **MAG**-type PTLs and other related compounds, this concept was examined by introducing a strong electron-donating amino group in the 4 position of their azobenzene core (e.g. in **MAG$_{2p}$** and **MAG$_{460}$**, Figure 1b and Supplementary

Figure 1).[33,34,39] A notable increase in 2P absorption was observed in these cases ($\sigma_2$ = 80 GM for *trans*-**MAG$_{460}$** at 850 nm[34]), though at the expense of dramatically decreasing the thermal stability of the *cis* isomer of the photoswitch down to the sub-second time scale. As such, this prevented large photoresponses to be obtained for the 2P operation of LiGluR with **MAG$_{2p}$** and **MAG$_{460}$**, since rapid thermal relaxation of the *cis* state of the switch impeded building up a large population of the open state of the ion channel.[33,34]

Here, we report the computationally-based rational design and preparation of MAG-type photoswitches displaying both high 2P biological activity with NIR light and large *cis* isomer thermal lifetime ($\tau_{cis}$). Our approach towards this goal relies on the accurate selection of the substitution pattern of the azoaromatic core of the system, which should allow for electronic asymmetry (i.e. enhanced $\sigma_2$ in the NIR region) without compromising the thermal stability of its *cis* state. Importantly, this strategy could be expanded to other azobenzene-based photoswitches for tailoring their response under multiphoton excitation.

## Results

**Design and synthesis of high 2P photoswitchers MAG-type PTLs.** Although the most efficient manner to increase the 2P absorption cross-section of azobenzenes lies in the push-pull substitution of their aromatic core,[22,23] the introduction of strong mesomeric electron-donating (EDG) and/or electron-withdrawing (EWG) groups concomitantly accelerates their *cis*→*trans* thermal back-isomerization in the dark (e.g. with EDG=4-$NR_2$ and EWG=4-$NO_2$).[1] A compromise must therefore be met to obtain azo derivatives with both large $\sigma_2$ and $\tau_{cis}$ values. In order to rationally devise these compounds, we computed the 2P absorption cross-section and the *cis* state thermal stability for a series of model azoaromatic photochromes using the time-dependent density functional theory (TDDFT, Table 1, Supplementary Figure 2 and Supplementary Tables 1-2). The azobenzene cores of **MAG**/**MAG$_0$** (**Azo$^{MAG}$**, R= R'= 4-NHCOMe) and **MAG$_{2P}$**/**MAG$_{460}$** (**Azo$^{MAG2p}$**, R= 4-NHCOMe, R'= 4'-$NMe_2$) were taken as reference systems in these calculations, while several alternative azo compounds (**Azo1**-**Azo3**) were explored on the basis of two main design principles: (a) a push-pull substitution pattern to enhance $\sigma_2$ with respect to **MAG** and **MAG$_0$**, and (b) the use of weak mesomeric EDG (R= 4-NHCOMe) and EWG (R'= 4'-$CONH_2$) as well as a strong inductive EWG (R'= 2'-F and 2',4'-F) to increase $\tau_{cis}$ relative to **MAG$_{2P}$** and **MAG$_{460}$**. For comparison purposes, two other model cases were considered: (a) an azo group alternatively bearing a strong mesomeric electron-withdrawing substituent (**Azo4**, R'= 2'-$NO_2$); and (b) an azo core with strong inductive EWGs on both aryl rings (**Azo5**, R=R'= 2,4-F), a substitution pattern that enables long-wavelength 1P isomerization of azobenzenes[9] and was recently reported to allow for 2P operation with NIR light in biological samples.[40]

As shown in Table 1 and Supplementary Tables 1-2, null 2P absorption was predicted for both the $S_0 \rightarrow S_1$ and $S_0 \rightarrow S_2$ transitions of *trans*-**Azo$^{MAG}$**, which is in good agreement with the behavior expected for purely centrosymmetric azobenzenes[22,23] and the minimal $\sigma_{2,trans}$ value experimentally determined for **MAG$_0$**.[34] By contrast, a major $\sigma_2$ value was computed for the $S_0 \rightarrow S_2$ band of electronically-asymmetric *trans*-**Azo$^{MAG2p}$**, which is consistent with that measured for *trans*-**MAG$_{460}$**.[34] Interestingly, larger 2P absorption cross-sections were calculated for model compounds *trans*-**Azo1**-**Azo4**, which showed a clear dependence on the electronic asymmetry of their azo core: selective introduction of *o*-fluoro and *o*-nitro EWGs in one of the azobenzene aryl rings of *trans*-**Azo2**-**Azo4** led to a noteworthy increase in $\sigma_2$ with respect to *o*-unsubsituted *trans*-**Azo1**. On the contrary, electronic symmetrization of the azobenzene chromophore in *trans*-**Azo5**

bearing four *o*-fluoro substituents inhibited this effect and even resulted in a slight decrease of the 2P absorption cross-section with respect to *trans*-**Azo$^{MAG2p}$**. More importantly, the enhancement in $\sigma_{2,trans}$ observed for **Azo1**-**Azo3** was not found to detrimentally affect the stability of their *cis* isomer and rather large $\tau_{cis}$ values were predicted for these compounds in water, in contrast to the behavior observed for **Azo$^{MAG2p}$** in *cis*-**MAG$_{2p}$** /*cis*-**MAG$_{460}$** and *cis*-**Azo4** bearing a nitro group. This clearly demonstrates the advantages of designing electronically-asymmetric azoaromatic photochromes with weak mesomeric EDG and EWG as well as strong inductive EWG, which emerge as ideal candidates for the preparation of azobenzene-based switches with high 2P activity for biological applications.

**Table 1** 2P absorption cross-sections and *cis* thermal stabilities of model azo compounds in water [a]

| Azo compound [b] | | $\sigma_{2,trans}$ (GM)[c] | $\Delta E^{\ddagger}_{cis\text{-}trans}$ (kJ mol$^{-1}$) [d] |
|---|---|---|---|
| **Azo$^{MAG}$** | R=4-NHCOMe<br>R'=4'-NHCOMe | 0 [e] | 91.2 (25.5 min) [g] |
| **Azo$^{MAG2p}$** | R= 4-NHCOMe<br>R'= 4'-$NMe_2$ | 56 [f] | 67.7 (118 ms) [g] |
| **Azo1** | R= 4-NHCOMe<br>R'= 4'-$CONH_2$ | 58 | 97.2 (4.9 h) |
| **Azo2** | R= 4-NHCOMe<br>$R_1$'= 4'-$CONH_2$<br>$R_2$'= 2'-F | 69 | 98.1 (7.0 h) |
| **Azo3** | R= 4-NHCOMe<br>$R_1$'= 4'-$CONH_2$<br>$R_2$'= 2',4'-F | 82 | 101.0 (22.6 h) |
| **Azo4** | R= 4-NHCOMe<br>$R_1$'= 4'-$CONH_2$<br>$R_2$'= 2'-$NO_2$ | 112 | 46.0 (18.6 μs) |
| **Azo5** | R= 4-NHCOMe<br>$R_1$'= 4'-$CONH_2$<br>$R_2$= $R_2$'= 2',4'-F | 51 | 112.0 (80 days) |

[a] Calculations performed at the CAM-B3LYP/6-31G(d) level and accounting for solvent (water) effects with a self-consistent PCM continuum method. [b] Structures shown in Supplementary Figure 2. [c] 2P absorption cross-section for the $S_0 \rightarrow S_2$ transition of the *trans* isomer. [d] In all the cases, the lowest-energy barrier height for the thermal *cis*→*trans* isomerization was found to correspond to an inversion mechanism. In parentheses $\tau_{cis}$ values estimated at 298 K from Eyring equation are shown. [e] $\sigma_2$= 10 GM[34] for *trans*-**MAG$_0$** containing an **Azo$^{MAG}$** core. [f] $\sigma_2$= 80 GM[34] for *trans*-**MAG$_{460}$** containing an **Azo$^{MAG2p}$** core. [g] Estimated from the experimental $\tau_{cis}$ values reported for **MAG**[25] and **MAG$_{2P}$**[33] at room temperature using Eyring equation.

Because of the optimal $\sigma_{2,trans}$ and $\tau_{cis}$ values computed for **Azo1**-**Azo3**, the 2P absorption properties of the *cis* isomers of these compounds were theoretically predicted (Supplementary Tables 1-2), since they also affect the efficiency of the photoisomerization process of azobenzenes. On one hand, larger $\sigma_{2,trans}/\sigma_{2,cis}$ ratios were calculated for **Azo1**-**Azo3** with respect to **Azo$^{MAG}$** and **Azo$^{MAG2p}$** for their 2P-allowed $S_0 \rightarrow S_2$ transition. On the other hand, different excitation energies were found for both isomers of **Azo1**-**Azo3** as to favor selective 2P excitation of their *trans* states, although this behavior was observed to decrease with the number of fluorine substituents introduced. This, in combination with their high $\sigma_{2,trans}$ and $\tau_{cis}$ values and assuming similar *trans*-*cis* and *cis*-*trans* photoisomerization quantum yields,[34] should result in a large 2P activity for *trans*-**Azo1**-**Azo3** in comparison to the *trans*-azoaromatic cores of **MAG**/**MAG$_0$** and **MAG$_{2P}$**/**MAG$_{460}$**.

Encouraged by our theoretical results on *trans*-**Azo1**-**Azo3**, two MAG-type PTLs were designed (**MAG$_{2P}^{slow}$** and **MAG$_{2P_F}^{slow}$**, Figure 1c). To favor synthetic accessibility, excitation selectivity of the *trans* isomer, as well as structural resemblance with **MAG** and, as such, replication of its light-gated control of LiGluR, we: (a) took the azo chromophores of **Azo1** and **Azo2** as models for the preparation of **MAG$_{2P}^{slow}$** and **MAG$_{2P_F}^{slow}$**, and (b) employed similar linkers to those used in **MAG** to tether the maleimide and glutamate units to the azobenzene core.

The preparation of **MAG$_{2P}^{slow}$** (R= H) and **MAG$_{2P_F}^{slow}$** (R= F) was achieved via a linear sequence where glutamate and maleimide functions were sequentially introduced into the azoaromatic photochrome of choice (Figure 2). [24,25,33,35,41] In this case, however, the azobenzene cores of **MAG$_{2P}^{slow}$** and **MAG$_{2P_F}^{slow}$** were not commercially available and they had to be previously synthesized by diazotization of aminobenzoic acids **4a** (R= H) and **4b** (R= F) followed by coupling with sodium phenylaminomethanesulfonate **1**, which was readily available from aniline and the formaldehyde sodium bisulfite adduct.[42] Posterior removal of the amino protecting group delivered amino acids **5a** and **5b** in moderate yields. Then, the sequence continued by joining the monoprotected ethyldiamino tether to **5a** and **5b** using the carbodiimide coupling reagent EDCI along with HOBt and DIPEA as a base. Subsequent acid removal of the *tert*-butyl carbamate protection and introduction of previously described glutamate derivative **2**[35] using the same coupling conditions afforded intermediates **6a** and **6b** in 47% and 49%, respectively, for the three steps. The next reaction between these intermediates and the freshly prepared acid chloride of maleimide derivative **3**[43] furnished compounds **7a** and **7b**, which feature all the envisioned functional fragments of the final photoswitches. Finally, acid removal of all the protecting groups of the glutamate moiety delivered the target compounds **MAG$_{2P}^{slow}$** and **MAG$_{2P_F}^{slow}$** as their monotrifluroacetate salts in good yields.

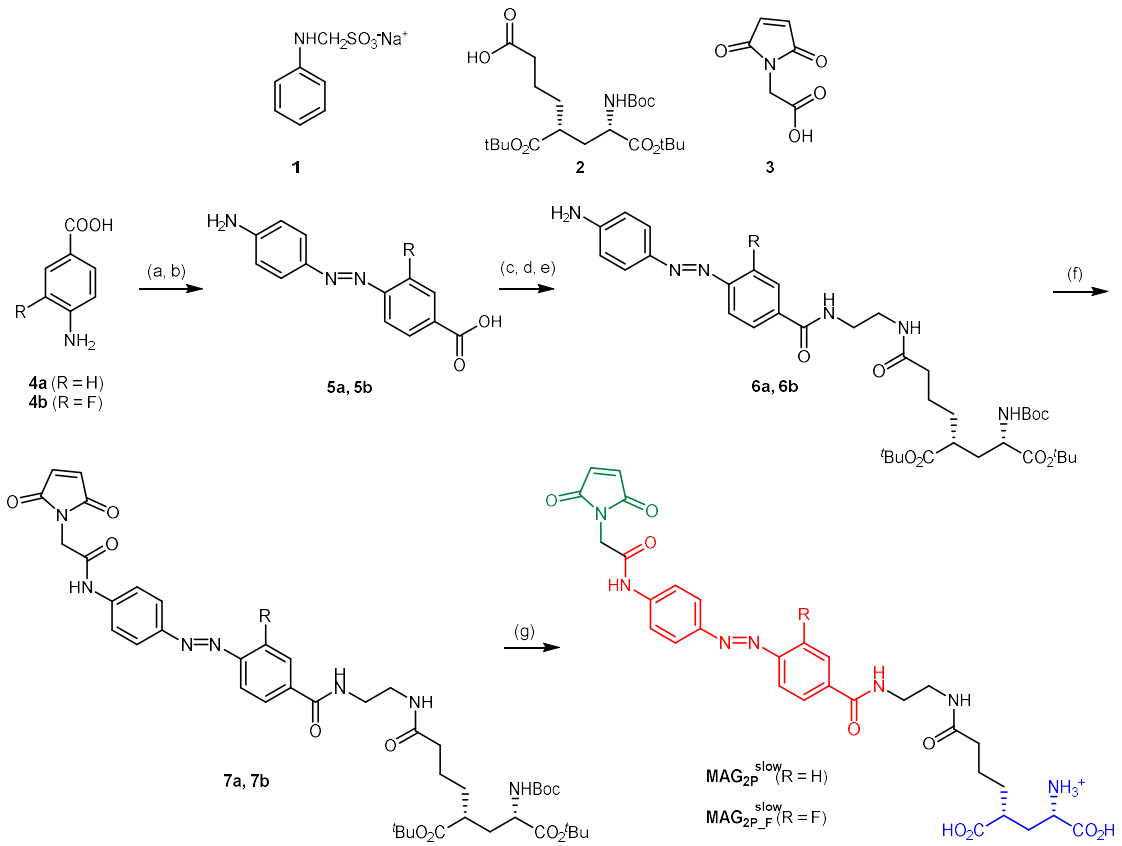

**Figure 2** Synthesis of $\mathbf{MAG_{2P}^{slow}}$ and $\mathbf{MAG_{2P\_F}^{slow}}$. Reagents and conditions: (a) 5.5 M HCl, $NaNO_2$; (b) i) **1**, 0.86 M NaOAc; ii) 1 M NaOH; iii) 5.5 M HCl (38%, over the two steps, for **5a**, 47% for **5b**); (c) *tert*-butyl (2-aminoethyl)carbamate, *N*-ethyl-*N*′-(3-dimethyldiaminopropyl)-carbodiimide HCl (EDCI), 1-hydroxybenzotriazole hydrate (HOBt), diisopropylethylamine (DIPEA), THF; (d) 37% HCl, MeOH; (e) **2**, EDCI, HOBt, DIPEA, THF (47%, over the three steps, for **6a**, 49% for **6b**); (f) i) **3**, ClCOCOCl, $CH_2Cl_2$, DMF; ii) DIPEA, THF (86% for **7a**, 84% for **7b**); (g) trifluoroacetic acid (TFA), $CH_2Cl_2$ (80% for $\mathbf{MAG_{2P}^{slow}}$, quantitative yield for $\mathbf{MAG_{2P\_F}^{slow}}$).

Figure 3a shows the 1P absorption spectra of *trans*-$\mathbf{MAG_{2P}^{slow}}$ and *trans*-$\mathbf{MAG_{2P\_F}^{slow}}$ in aqueous buffer, which are compared to those of *trans*-**MAG** and *trans*-$\mathbf{MAG_{2p}}$. As predicted by TDDFT calculations (Supplementary Table 2), very similar absorption signals were registered for the azoaromatic cores of *trans*-**MAG**, *trans*-$\mathbf{MAG_{2P}^{slow}}$ and *trans*-$\mathbf{MAG_{2P\_F}^{slow}}$, which are typical for azobenzene-type switches in the absence of strong mesomeric EDG and EWG:[1] they show an intense absorption band at $\lambda_{max}\sim$ 360 nm corresponding to the allowed 1P $S_0 \rightarrow S_2$ transition ($\pi\pi^*$ band), and a broad shoulder at $\lambda\sim$ 400-500 nm arising from the forbidden 1P $S_0 \rightarrow S_1$ transition ($n\pi^*$ band). This is in contrast with the absorption spectrum of *trans*-$\mathbf{MAG_{2p}}$ bearing an amino-substituted azo core, the $\pi\pi^*$ band of which notably red-shifts and overlaps with the $n\pi^*$ band.[33]

Upon excitation of *trans*-$\mathbf{MAG_{2P}^{slow}}$ and *trans*-$\mathbf{MAG_{2P\_F}^{slow}}$ $\pi\pi^*$ band at 365 nm in either organic (dimethylsulfoxide, (DMSO)) or aqueous (99% phosphate buffer solution (PBS):1% DMSO) media, spectral changes were observed in absorption that were consistent with 1P *trans*→*cis* photoisomerization, as confirmed by $^1$H NMR (Supplementary Figs. 3-4). High *trans*→*cis* photoisomerization quantum yields and *cis*-enriched photostationary states were determined for both $\mathbf{MAG_{2P}^{slow}}$ and $\mathbf{MAG_{2P\_F}^{slow}}$ at these irradiation conditions ($\Phi_{trans\rightarrow cis}\sim$ 0.15 and $\%cis^{PSS}\sim$ 70% in aqueous buffer), which were similar to those measured for their azoaromatic cores and **MAG** (Supplementary Table 3). UV-vis absorption spectroscopy and $^1$H NMR also revealed efficient 1P *cis*→*trans* photoisomerization of $\mathbf{MAG_{2P}^{slow}}$ and $\mathbf{MAG_{2P\_F}^{slow}}$ upon excitation of their $n\pi^*$ band at 473 nm ($\Phi_{cis\rightarrow trans}\sim$ 0.26 and $\%trans^{PSS}\sim$ 85% in aqueous buffer), in analogy to the behavior registered for their azobenzene units and **MAG** (Supplementary Figure 5 and Supplementary Table 4). In addition, thermal back-isomerization of *cis*-$\mathbf{MAG_{2P}^{slow}}$ and *cis*-$\mathbf{MAG_{2P\_F}^{slow}}$ was also observed at room temperature, which occurred in the time span of tens of minutes in aqueous media ($\tau_{cis}\sim$ 10 min in 99% PBS:1% DMSO, Supplementary Figure 6 and Supplementary Table 5). Importantly, this demonstrates that the azoaromatic cores selected for both $\mathbf{MAG_{2P}^{slow}}$ and $\mathbf{MAG_{2P\_F}^{slow}}$ possess long-lived *cis* isomers, as anticipated by our theoretical calculations. Therefore, these PTLs fairly reproduce the large $\tau_{cis}$ value of **MAG** and clearly surpass the thermal stability of *cis*-$\mathbf{MAG_{2p}}$ and *cis*-$\mathbf{MAG_{460}}$ despite the push-pull substitution pattern of their azoaromatic photochromes (Figure 3b).

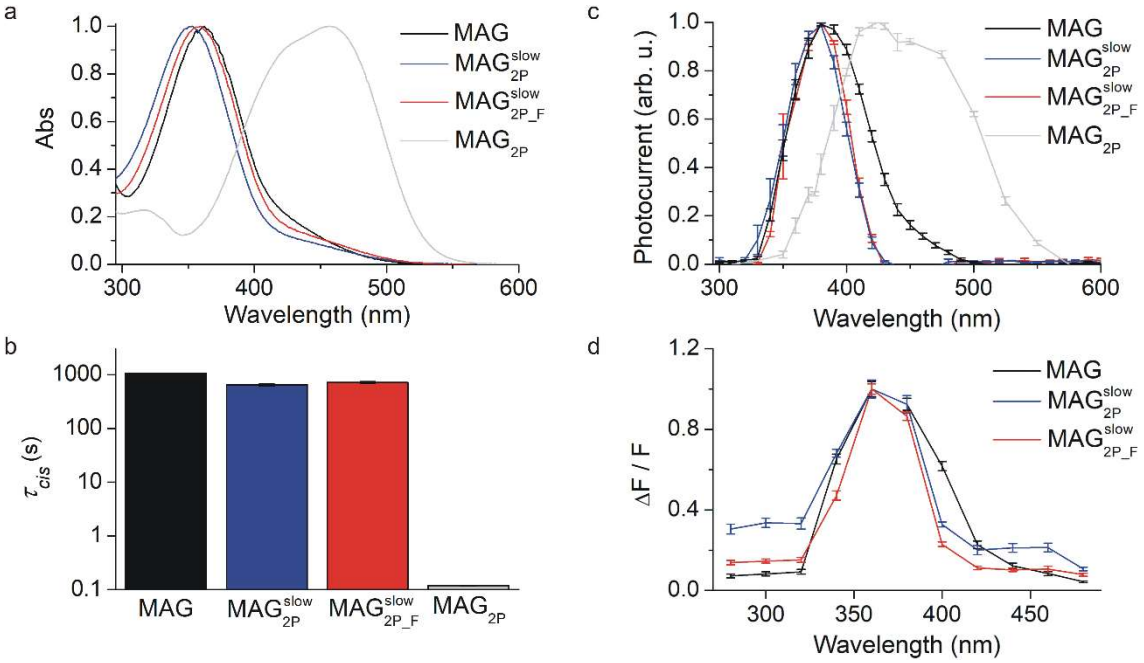


**Figure 3** Photochemical and physiological characterization of **MAG$_{2P}^{slow}$** and **MAG$_{2P_F}^{slow}$** under 1P stimulation. (**a**) Normalized absorption spectra of *trans*-**MAG**, *trans*-**MAG$_{2P}^{slow}$**, *trans*-**MAG$_{2P_F}^{slow}$** and *trans*-**MAG$_{2P}$** in 99% PBS:1% DMSO. (**b**) Thermal lifetimes of *cis*-**MAG**, *cis*-**MAG$_{2P}^{slow}$**, *cis*-**MAG$_{2P_F}^{slow}$** and *cis*-**MAG$_{2P}$** at room temperature in 99% PBS:1% DMSO. Errors from the monoexponentials fits to obtain $\tau_{cis}$ are shown. (**c**) Normalized 1P action spectra recorded using whole cell patch-clamp in human embryonic kidney cells 293 (HEK293 cells) expressing GluK2-L439C after conjugation to **MAG**, **MAG$_{2P}^{slow}$**, **MAG$_{2P_F}^{slow}$** and **MAG$_{2P}$** ($n$ = 5, 7, 3 and 8 biologically independent cells, respectively). Errors are standard error of the mean (SEM). (**d**) Normalized 1P action spectra recorded using calcium imaging in HEK293 cells co-expressing GluK2-L439C and GCaMP6s after conjugation to **MAG**, **MAG$_{2P}^{slow}$** and **MAG$_{2P_F}^{slow}$** ($n$ = 33, 20 and 25 biologically independent cells, respectively). Errors are SEM. In (**c-d**) wavelength-dependent photoresponses were normalized to the maximum signal along the spectral range measured for each cell before averaging over different cells. Source data for (**c-d**) are provided as a source Data file.

In view of the optimal photochemical behavior established for **MAG$_{2P}^{slow}$** and **MAG$_{2P_F}^{slow}$**, we next explored their capacity to photocontrol LiGluR channels in living cells under 1P stimulation. Thus, GluK2 receptors bearing a cysteine residue at position L439C (GluK2-L439C) were expressed in HEK293 cells and incubated with the azobenzene-based compound of choice for selective conjugation (**MAG$_{2P}^{slow}$**, **MAG$_{2P_F}^{slow}$**, **MAG** and **MAG$_{2P}$**).

In a first set of experiments, the photoinduced operation of the resulting LiGluRs was evaluated using whole-cell patch clamp, a technique that allows measuring the currents elicited across the cell membrane when modulating ion fluxes via channel opening and closing.[24,25] Large and repetitive electrophysiological signals were recorded in all the cases upon *trans*→*cis* photoisomerization of the PTLs (i.e. LiGluR channel opening) with UV and violet light (**MAG$_{2P}^{slow}$**, **MAG$_{2P_F}^{slow}$** and **MAG**) or broadband visible light (**MAG$_{2P}$**). Cell basal current levels could be next recovered by reverting back this process (i.e. LiGluR channel closing) upon illumination with blue and green radiation (**MAG$_{2P}^{slow}$**, **MAG$_{2P_F}^{slow}$** and **MAG**) or thermally in the dark (**MAG$_{2P}$**; Supplementary Figure 7). By scanning the excitation wavelength used to induce LiGluR channel opening, the action spectra could be measured for each of the photoswitchable compounds under analysis (Figure 3c). As expected from their photochemical properties, a very similar spectral response was registered for **MAG$_{2P}^{slow}$**, **MAG$_{2P_F}^{slow}$** and **MAG**, which generated

maximal electrophysiological signals when irradiating LiGluR-expressing cells at ~375 nm. By contrast, a broader red-shifted action spectrum was measured for **MAG$_{2P}$** peaking at ~425 nm. In addition, further electrophysiological measurements were conducted to demonstrate that the photoswitches **MAG$^{slow}_{2P}$** and **MAG$^{slow}_{2P_F}$**: (a) preserve their long thermal *cis* lifetimes after tethering to GluK2 (~ 10 min, Supplementary Figure 8) as well as the fast channel opening and closing times (< 0.5 s, Supplementary Figure 9 and Supplementary Table 6) previously reported for **MAG**;[24,25] and (b) do not inhibit the native physiological activity of the receptor, which retains their intrinsic response to free glutamate (Supplementary Figure 10) and rapid desensitization kinetics (Supplementary Figure 11) after photoswitch conjugation.

Taking advantage of the $Ca^{2+}$ permeability of LiGluR channels, their light-gated operation under 1P stimulation was further quantified by means of calcium imaging, using GCaMP6s co-expressed with GluK2-L439C in HEK293 cells. GCaMP6s is a genetically-encoded intracellular fluorescent calcium indicator that undergoes a large increase in emission upon calcium ion complexation.[44] In this case, we focused on **MAG$^{slow}_{2P}$**-, **MAG$^{slow}_{2P_F}$**- and **MAG**-tethered LiGluRs, since the low thermal stability of *cis*-**MAG$_{2P}$** is reported to lead to poor photoinduced calcium imaging signals.[33] In contrast, the large $\tau_{cis}$ values of **MAG$^{slow}_{2P}$**, **MAG$^{slow}_{2P_F}$** and **MAG** yielded intense, reversible and reproducible light-triggered fluorescent responses in GCaMP6s-expressing cells upon repetitive illumination with sequential pulses of UV-violet and green radiation (Supplementary Figure 12). Similar action spectra were again measured for these PTLs using calcium imaging (Figure 3d), and the maximal responses obtained for the three compounds at 360 nm were nearly equivalent (Supplementary Figure 13). This, together with the whole-cell patch clamp measurements conducted, proves that the 1P biological activity of **MAG** in LiGluRs is preserved for **MAG$^{slow}_{2P}$** and **MAG$^{slow}_{2P_F}$** photoswitchable ligands bearing electronically-asymmetric azoaromatic cores and slightly different structures.

**2P stimulation in cultured cells.** NIR-induced 2P operation of LiGluR with PTLs **MAG$^{slow}_{2P}$** and **MAG$^{slow}_{2P_F}$** was studied by calcium imaging, since this enabled all-optical control and monitoring of the light-gated ion channels. Experiments were conducted in a confocal fluorescence microscope equipped with both continuous-wave visible lasers and a femtosecond pulsed Ti:Sapphire laser. This allowed for sequential and independent 1P and 2P stimulation of cells by raster-scanning the focused laser beam of choice over the sample while detecting the fluorescence signal of the calcium ion indicator for the whole field of view.

To evaluate the 2P physiological activity of **MAG$^{slow}_{2P}$** and **MAG$^{slow}_{2P_F}$**, we first undertook experiments on HEK293 cells expressing both GluK2-L439C and R-GECO1,[45] a red genetically-encoded fluorescent $Ca^{2+}$ probe. Figure 4a depicts calcium imaging fluorescence responses measured for these cells after conjugation with **MAG**, **MAG$^{slow}_{2P}$** and **MAG$^{slow}_{2P_F}$** (see also Supplementary Movies 1-2). For comparison, all the cells were subjected to 2 consecutive cycles of 1P LiGluR photostimulation with violet light (405 nm) followed by 2 cycles of 2P excitation with NIR radiation (780 nm). After every stimulation, LiGluR was deactivated by 1P absorption of green light (514 nm). In averaged recordings over $n > 10$ cells in the field of view, no or very low signals were observed for **MAG**-tethered LiGluR upon irradiation with NIR light, which highlights the poor efficiency of 2P *trans*→*cis* photoisomerization for this ligand, as already reported.[33,34] In agreement with our theoretical calculations, a remarkable increase in 2P responses was observed when replacing **MAG** with **MAG$^{slow}_{2P}$** and **MAG$^{slow}_{2P_F}$** bearing push-pull azoaromatic cores. In fact, 1P- and 2P-induced calcium imaging responses of similar intensities were measured

with **MAG$^{slow}_{2P_F}$**, for which the highest $\sigma_2$ value was anticipated owing to the high electronic asymmetry of its *trans*-azobenzene photochrome. Notably, such efficient 2P stimulation of LiGluR upon conjugation to **MAG$^{slow}_{2P_F}$** was found to be reproducible, repetitive, and to occur with minimal photodegradation, since negligible variation in calcium imaging response was observed after 4 consecutive light-gating cycles for different individual cells (Figure 4b).

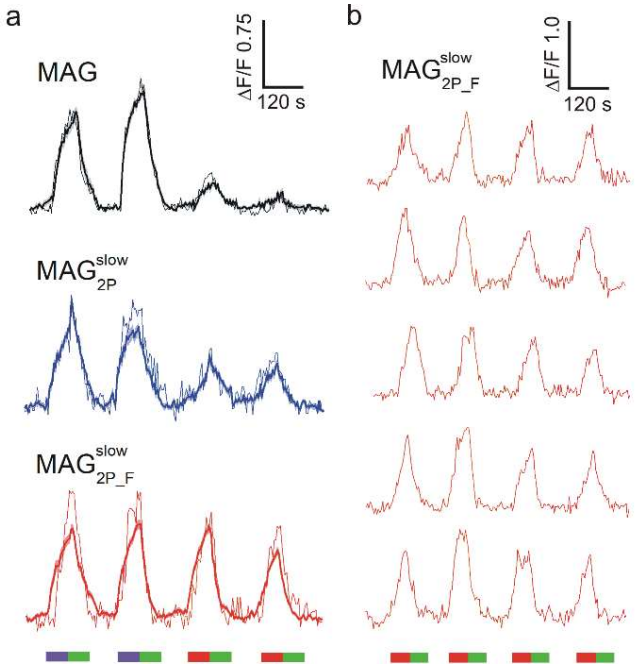


**Figure 4** 1P and 2P stimulation of **MAG**, **MAG$^{slow}_{2P}$** and **MAG$^{slow}_{2P_F}$** in cultured cells. (**a**) Individual (thin lines) and average (thick lines) calcium imaging fluorescence traces recorded for HEK293 cells co-expressing GluK2-L439C and R-GECO1 after conjugation to **MAG** ($n$ = 16 biologically independent cells), **MAG$^{slow}_{2P}$** ($n$ = 14 biologically independent cells) and **MAG$^{slow}_{2P_F}$** ($n$ = 34 biologically independent cells). The bands around average traces plot the corresponding SEM. Both 1P (violet, 405 nm, power density = 0.37 mW $\mu m^{-2}$) and 2P excitation scans (red, 780 nm, power density = 2.8 mW $\mu m^{-2}$) were applied to open LiGluR channels and trigger calcium-induced R-GECO1 fluorescence enhancement, while 1P excitation scans (green, 514 nm, power density = 0.35 mW $\mu m^{-2}$) were applied to revert back the process. (**b**) Repetitive 2P-induced calcium imaging fluorescence responses recorded in five different HEK293 cells co-expressing GluK2-L439C and R-GECO1 after conjugation to **MAG$^{slow}_{2P_F}$**. Source data for (**a**) are provided as a source Data file.

By comparing the 1P- and 2P-induced calcium imaging responses recorded on the same cells (2P/1P ratio), a detailed assessment of the high multiphoton physiological activity of **MAG$^{slow}_{2P}$** and **MAG$^{slow}_{2P_F}$** was performed. First, we determined the 2P action spectra of these compounds and **MAG** when conjugated to HEK293 cells co-expressing GluK2-L439C and R-GECO1, which showed a similar spectral distribution (Figure 5a). In all the cases, rather broad 2P action spectra were found with maxima at ~780 nm, which reasonably agrees with twice the wavelength of the 1P absorption band of the 2P allowed $S_0 \rightarrow S_2$ transition of the *trans*-azobenzene core of these compounds (~360 nm). However, much higher 2P/1P ratios were obtained for **MAG$^{slow}_{2P}$** and **MAG$^{slow}_{2P_F}$** compared to **MAG** at equivalent excitation conditions. In particular, when considering 2P stimulation of LiGluR at the spectral maximum (780 nm) and averaging over a large number of cells ($n$ > 25), 3.5- and 6-fold increases in 2P/1P intensity ratio were measured for **MAG$^{slow}_{2P}$** and **MAG$^{slow}_{2P_F}$** relative to **MAG**, respectively (Figure 5b). Even more

importantly, 2P stimulation of **MAG$^{slow}_{2P}$**- and **MAG$^{slow}_{2P_F}$**-tethered LiGluR was observed for all the cells analyzed, while no multiphoton response could be measured for ~30% of the GluK2-L439C-expressing cells conjugated with **MAG** under the same illumination conditions (Figure 5c). Overall, these results indicate that **MAG$^{slow}_{2P}$** and, especially, **MAG$^{slow}_{2P_F}$** are very advantageous photoswitches to efficiently and reliably control LiGluR in neurotransmission studies under 2P excitation with NIR radiation.

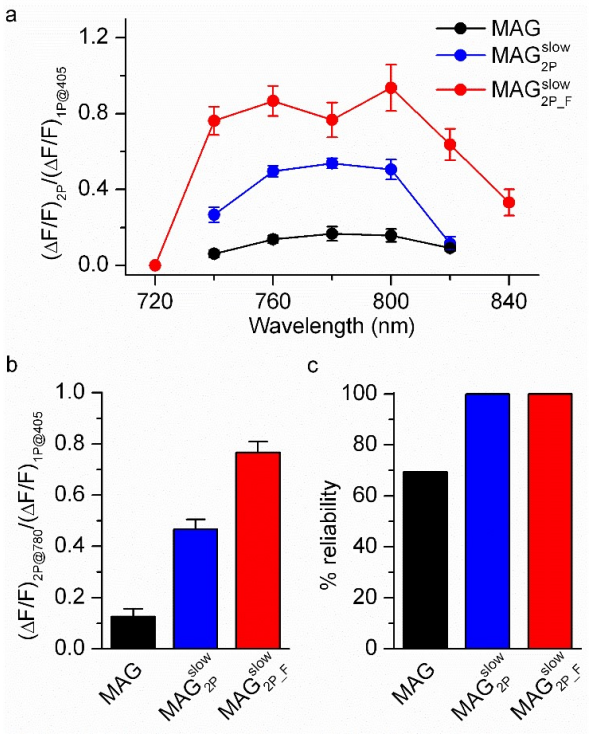


**Fig 5** Average 2P activity of **MAG**, **MAG$^{slow}_{2P}$** and **MAG$^{slow}_{2P_F}$** in cultured cells. (**a**) 2P action spectra of **MAG**, **MAG$^{slow}_{2P}$** and **MAG$^{slow}_{2P_F}$** after conjugation to GluK2-L439C-expressing HEK293 cells. Fluorescence calcium responses were measured using R-GECO1. Before averaging over different cells, the 2P responses of each cell were normalized with respect to the 1P response at 405 nm (**MAG**: 740, 760, 780, 800 and 820 nm; *n* = 28, 33, 40, 7 and 12 biologically independent cells, respectively, **MAG$^{slow}_{2P}$**: 740, 760, 780, 800 and 820 nm; *n* = 20, 9, 12, 16 and 17 biologically independent cells, respectively and **MAG$^{slow}_{2P_F}$**: 720, 740, 760, 780, 800, 820 and 840 nm; *n* = 14, 17, 18, 86, 15, 23 and 17 biologically independent cells, respectively). Errors are SEM. (**b**) Ratio between the 2P- and 1P-photon responses of **MAG**, **MAG$^{slow}_{2P}$** and **MAG$^{slow}_{2P_F}$** for the same cells excited at 780 and 405 nm, respectively. Errors are SEM. (**c**) Reliability of the 2P calcium imaging response elicited in GluK2-L439C-expressing HEK293 cells after conjugation to **MAG**, **MAG$^{slow}_{2P}$** and **MAG$^{slow}_{2P_F}$** (*n* = 72, 25 and 86 biologically independent cells, respectively). Reliability is expressed as the percentage of transfected cells showing measurable 2P stimulation signals. Source data for (**a-b**) are provided as a source Data file.

**2P stimulation in hippocampal organotypic slices.** In view of the superior 2P-stimulation performance observed for **MAG$^{slow}_{2P_F}$** in GluK2-L439C-expressing HEK cells, we explored the use of this PTL to the multiphoton control with NIR light of neuronal cells embedded in their physiological environment. In this way we could not only assess the efficiency of **MAG$^{slow}_{2P_F}$** in neurons with mature synapses naturally containing all endogenous glutamate receptors, but also test the ultimate advantages of 2P stimulation. With this aim, we prepared organotypic slice cultures from neonatal rat hippocampi and biolistically transfected them with GluK2-L439C-eGFP and RCaMP2.[46] This allowed the cells expressing LiGluR within the slices to be localized by the green fluorescence of enhanced green fluorescent protein (eGFP), while simultaneously

recording their activity after 1P or 2P stimulation by monitoring the red fluorescence of the calcium ion probe RCaMP2 (Figure 6a). Transfected hippocampal slices were finally incubated with **MAG** or $\mathbf{MAG}^{\mathbf{slow}}_{\mathbf{2P\_F}}$ and their photoresponses after consecutive 1P or 2P stimulation were measured and compared. Neither Concanavalin A nor toxins were used in these experiments to inhibit GluK2 desensitization upon prolonged binding to the glutamate unit of *trans*-**MAG** and *trans*-$\mathbf{MAG}^{\mathbf{slow}}_{\mathbf{2P\_F}}$. Thus, our measurements on brain slices truly reported on intact neuronal gating and connectivity.

As depicted in Figs. 6b and 6d, slices incubated with **MAG** showed robust photoresponses during 1P stimulation (405 nm), but no or minimal photoresponses when applying 2P stimulation (780 nm). On the contrary, slices incubated with $\mathbf{MAG}^{\mathbf{slow}}_{\mathbf{2P\_F}}$ did not only show clear photoresponses upon illumination at 405 nm, but comparable light-induced signals were also recorded for the same cells by excitation at 780 nm, thus indicating very similar 1P and 2P photoswitching efficacies (Figs. 6c and 6e). In all the cases, the photoresponses observed upon stimulation at 405 nm and/or 780 nm were completely inhibited under green light illumination (514 nm), which demonstrated the long $\tau_{cis}$ of both **MAG** and $\mathbf{MAG}^{\mathbf{slow}}_{\mathbf{2P\_F}}$ switches (see also Supplementary Movies 3-4).

To compare the efficacy of LiGluR photocontrol in slices conjugated with **MAG** or $\mathbf{MAG}^{\mathbf{slow}}_{\mathbf{2P\_F}}$, we determined both the calcium-induced fluorescence enhancement responses after 1P and 2P stimulation (Figure 6f) and the 2P/1P response ratio (Figure 6g). Clearly, **MAG** could efficiently activate LiGluR and thus induce neuronal activity under 1P excitation at 405 nm, but not upon 2P stimulation at 780 nm. In contrast, $\mathbf{MAG}^{\mathbf{slow}}_{\mathbf{2P\_F}}$ stimulation reliably activated neurons using both 1P and 2P excitation with violet and NIR light, respectively, and similar 1P and 2P signals were indeed measured at our experimental conditions. In addition, the 2P-induced control of neuronal activity with $\mathbf{MAG}^{\mathbf{slow}}_{\mathbf{2P\_F}}$ was found to be robust and reproducible in many different cells ($n$ = 9 cells) located at distinct depths of the brain tissue (0 - 100 μm) from hippocampal slices cultured for different days (8-15 days in vitro ((DIV)). Importantly, cells expressing RCaMP2 but not LiGluR-eGFP did not respond to **MAG** or $\mathbf{MAG}^{\mathbf{slow}}_{\mathbf{2P\_F}}$ photostimulation (Supplementary Figure 14).

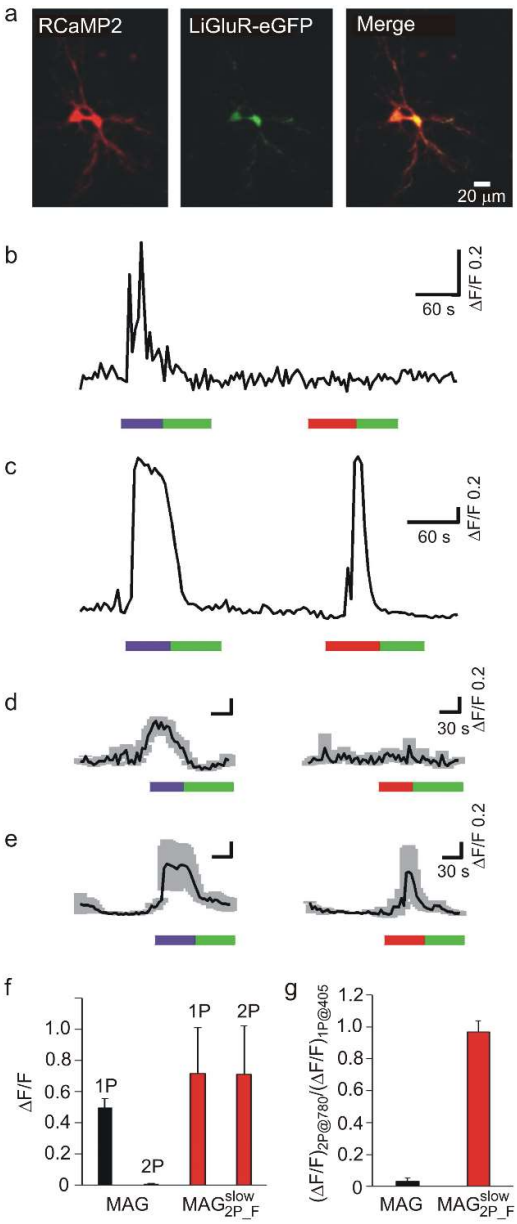


**Figure 6** 2P $Ca^{2+}$ photoresponses in rat hippocampal organotypic slices expressing GluK2-L439C-eGFP and RCaMP2. (**a**) Microphotograph of a neuron expressing both RCaMP2 (red) and GluK2L439C-eGFP (green) (scale bar = 20 µm). (**b-c**) Real time traces of a single-cell neuronal activity of slices incubated with (**b**) **MAG** or (**c**) $\mathbf{MAG^{slow}_{2P\_F}}$. (**d-e**) Average 1P and 2P responses of neurons incubated with (**d**) **MAG** ($n$ = 3 biologically independent cells) or (**e**) $\mathbf{MAG^{slow}_{2P\_F}}$ ($n$= 6 biologically independent cells). In (**b-e**) 1P stimulation was performed at 405 nm (purple bar, 0.81 mW $\mu m^{-2}$) and 514 nm (green bar, 0.35 mW $\mu m^{-2}$), and 2P-stimulation at 780 nm (red bar, 2.8 mW $\mu m^{-2}$). (**f-g**) Quantification of photoresponses in slices incubated with **MAG** (black bars, $n$= 5 biologically independent cells) and $\mathbf{MAG^{slow}_{2P\_F}}$ (red bars, $n$= 6 biologically independent cells): (**f**) fluorescence enhancement; (**g**) ratio between the 2P- and 1P-photon responses of **MAG** and $\mathbf{MAG^{slow}_{2P\_F}}$ for the same cells. Error bars are SEM. Source data for (**d-g**) are provided as a source Data file.

**2P stimulation *in vivo* in *Caenorhabditis elegans*.** We further tested the ability of $\mathbf{MAG^{slow}_{2P\_F}}$ to control neuronal activity *in vivo* using 2P excitation. For that purpose, we used *Caenorhabditis elegans* as a model of choice to analyze neuronal circuits. The morphology and function of its 302 neurons are characterized in detail, and allow scrutinizing sensory and motor circuits, among others. Figure 7 summarizes the results of all-optical experiments with GluK2-L439C-mCherry

and GCaMP6s fluorescent calcium reporter co-expressed in touch receptor neurons (TRNs). From the six TRNs, which tile the receptive field of the animal in anterior/posterior and left/right, we specifically focused on the single pair PLML/R, which is located near the tail of the nematode (Figure 7a). Like in other neurons within the nervous system, pairs of TRNs can be selectively stimulated in the anterior and posterior part of the animal using spatial light patterning, but differential unilateral activation is difficult, which poses a hurdle to photomanipulate their activity at high resolution using optogenetics.[47] This is especially relevant when neurons are overlapping along the optical axis, as shown in Figure 7b (compare confocal projection top view, and side view of the confocal sections) or are closely packed as in the head. In such cases, 2P excitation provides a unique advantage over 1P excitation to activate cells with 10 µm axial plane selectivity.[48]

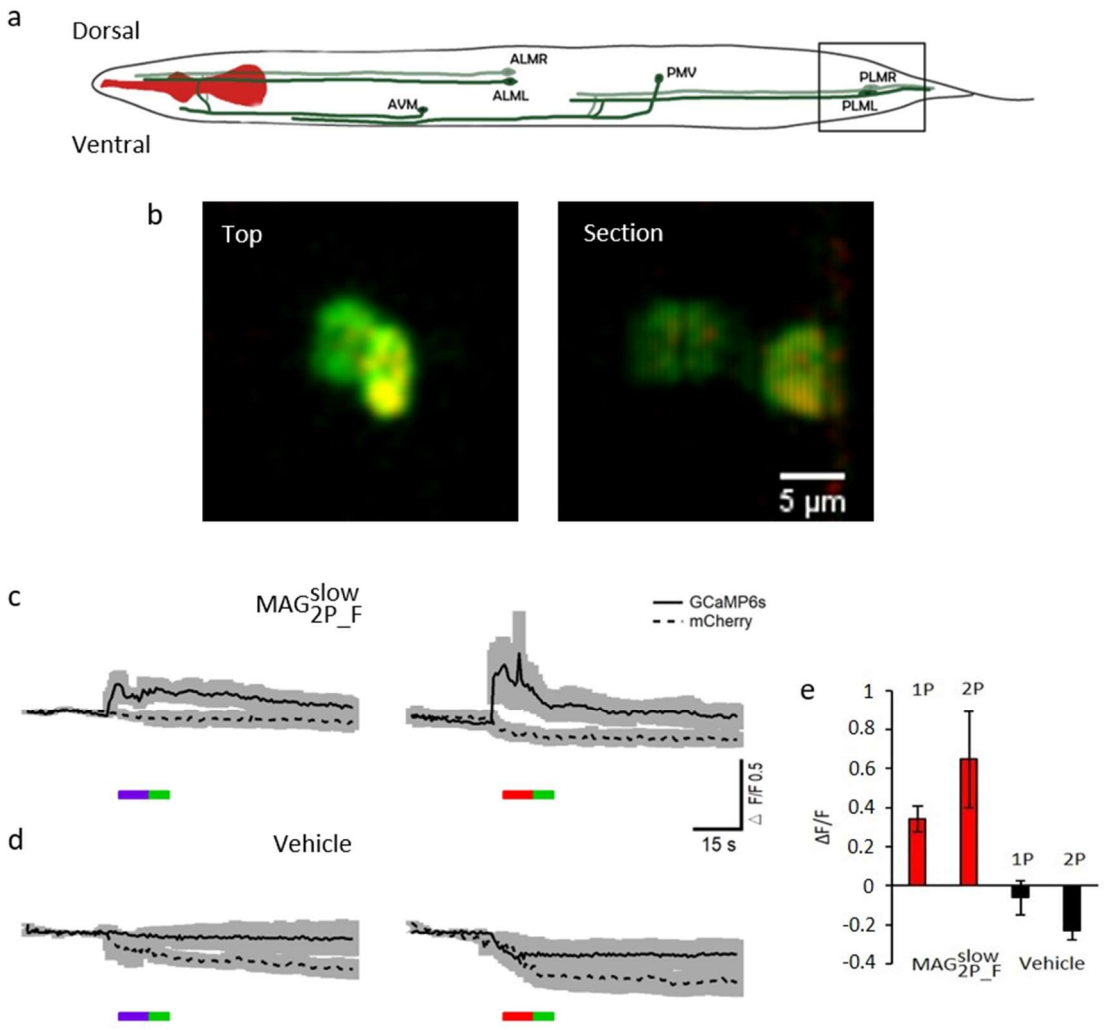


**Fig 7**. *In vivo* calcium induced photoresponses by 2P stimulation of $\mathbf{MAG}^{\mathbf{slow}}_{\mathbf{2P\_F}}$ in *C. elegans*. (**a**) Schematics of *C. elegans* in which touch receptor neurons (TRNs) are depicted. Squared region is magnified in (**b**). (**b**) Microphotograph of an animal expressing LiGluR-mCherry (red) and GCaMP6s (green) (scale bar = 5 µm). Top and lateral section view of TRN from the tail. (**c-d**) Average traces of 1P and 2P induced photoactivation of TRNs in animals treated with (**c**) $\mathbf{MAG}^{\mathbf{slow}}_{\mathbf{2P\_F}}$ ($n$ = 5 and 6 cells from 4 different animals experiments for 1P and 2P traces, respectively) or (**d**) with vehicle ($n$ = 5 and 6 cells from 4 different animals experiments for 1P and 2P traces, respectively). Continuous line trace

indicates GCaMP6s fluorescence signal and dashed trace mCherry fluorescence. In (**c-d**) 2P stimulation was performed at 780 nm (red bar, 2.8 mW $mm^{-2}$), 1P-stimulation at 405 nm (purple bar, 15 μW $mm^{-2}$) and 514 nm (green bar, 1.21 μW $mm^{-2}$). (**e**) Quantification of photoresponses (fluorescence enhancement) in animals injected with $\mathbf{MAG}^{\mathbf{slow}}_{\mathbf{2P\_F}}$ (red bars, $n$ = 5 cells from 4 different animals experiments) and Vehicle (black bars, $n$ = 5 cells from 4 different animals experiments). Error bars are SEM. Source data for (**c-e**) are provided as a source Data file.

Upon expression of GluK2-L439C-mCherry in TRNs, we observed localization of mCherry on the plasma membrane and in vesicles that are transported along the sensory neurite (Supplementary Movie 5). After delivery of $\mathbf{MAG}^{\mathbf{slow}}_{\mathbf{2P\_F}}$ to living animals (see details in the Methods section), calcium activity was monitored in the posterior TRNs (PLM) expressing GluK2-L439C-mCherry and GCaMP6s using a confocal fluorescence microscope. Clear photoresponses to 2P excitation were observed in every animal responding to 1P excitation ($n$ = 7 neurons from 4 different individuals, a 2P/1P excitation efficacy of 100%, Figure 7c, Supplementary Movies 6-7), whereas control-treated animals (Vehicle) only showed a partial fluorescence reduction due to bleaching of mCherry and GCaMP6s ($n$ = 5 neurons from 3 different individuals, Figure 7d). No signs of toxicity were observed after compound injection, during recovery and imaging. Thus, the rationally designed 2P excitation properties of $\mathbf{MAG}^{\mathbf{slow}}_{\mathbf{2P\_F}}$ can also be used *in vivo* to photomanipulate neuronal activity of single, individual neurons with high efficacy and selectivity.

## Discussion

Genetically targeted and pharmacologically-selective[49] synthetic photoswitches offer great potential to dissect neuronal circuits based respectively on specific promoters and endogenous receptors. However, the efficiency of azobenzene-based photoswitchable ligands is ultimately limited by the *cis* isomer population that can be achieved upon irradiation, which is determined by different experimental (excitation intensity and wavelength) and photochemical parameters (*trans* and *cis* absorptivities and isomerization quantum yields, *cis* state thermal lifetime). Among them, the 2P activity of long $\tau_{cis}$ azobenzene switches is mainly controlled by the $\sigma_2$ values for both isomers at the excitation conditions, since they normally show relatively similar isomerization quantum yields (e.g. $\Phi_{trans\rightarrow cis}$ = 0.18 and $\Phi_{cis\rightarrow trans}$ = 0.30 for **MAG** in 99% PBS:1% DMSO, Supplementary Table 3). In the case of **MAG** and $\mathbf{MAG_0}$ under NIR illumination, $\sigma_{2,trans}$ is low and, worse still, even smaller than $\sigma_{2,cis}$, which strongly disfavors 2P-induced *trans*→*cis* isomerization.[34] This leads to photostationary states with very low *cis* content and, as such, poor 2P LiGluR responses with NIR light even at high excitation intensities (~ 20 mW $\mu m^{-2}$).[33,34] As discussed above, compounds $\mathbf{MAG}^{\mathbf{slow}}_{\mathbf{2P}}$ and, especially, $\mathbf{MAG}^{\mathbf{slow}}_{\mathbf{2P\_F}}$ overcome this drawback by introducing rationally-designed azobenzene cores with both large $\sigma_{2,trans}$ and $\tau_{cis}$ values, which allow for robust and reliable 2P signals at milder, more cell-compatible excitation conditions (2.8 mW $\mu m^{-2}$) that are comparable to 1P responses.

As for $\mathbf{MAG_{2P}}$ and $\mathbf{MAG_{460}}$ biological photoactivity, it is mainly governed by a different factor: the millisecond *cis* state lifetime of both switches in physiological media.[33,34] Although this enables single-wavelength, fast neuronal stimulation, it dramatically limits the extent of the photostationary state reached even when using high excitation intensities. As a result, $\mathbf{MAG_{2P}}$ and $\mathbf{MAG_{460}}$ also lead to smaller 2P responses with NIR light than under 1P stimulation (~ 10-40%) despite their enhanced $\sigma_{2,trans}$ values with respect to **MAG** and $\mathbf{MAG_0}$.[33,34] This, together with their low *cis* state lifetimes, are a severe constraint for the 2P stimulation of calcium-evoked photoresponses with $\mathbf{MAG_{2P}}$ and $\mathbf{MAG_{460}}$. On the contrary, the higher stability of $\mathbf{MAG}^{\mathbf{slow}}_{\mathbf{2P}}$ and $\mathbf{MAG}^{\mathbf{slow}}_{\mathbf{2P\_F}}$ *cis* isomers enables sustained receptor activation, which combined with their optimized

2P excitability results in larger photoresponse amplitudes and allows the manipulation of calcium-regulated processes with NIR light. Thus, while very small R-GECO1 calcium responses were described for LiGluR-expressing HeLa cells under 2P stimulation of **MAG$_{460}$** ($\Delta F/F < 0.1$),[34] we obtained herein calcium-induced fluorescence enhancement values higher than 1 for the same indicator in HEK cells upon excitation of **MAG$^{slow}_{2P_F}$**-tethered LiGluR with NIR light.

Other advantages derive from the use of **MAG$^{slow}_{2P}$** and **MAG$^{slow}_{2P_F}$** over **MAG$_{2P}$** and **MAG$_{460}$** for the 2P stimulation of LiGluR. Technically, *cis*-isomer stability allows maintaining the glutamate moiety bound to the receptor in the dark, which best mimics the presence of a high neurotransmitter concentration in extracellular medium during presynaptic release. This approach is in contrast to the use of Concanavalin A to block receptor desensitization thus keeping the channel open (**MAG$_{2P}$**),[33] and to mutation K456A used in GluK2 to quicken receptor recovery from desensitization,[34] which results in higher and longer-lasting currents during illumination of a *cis*-unstable photoswitch (**MAG$_{460}$**). Such sustained calcium influx facilitates photoresponse detection in imaging experiments but could be toxic for the neurons, and is not physiological. In our case, we used Concanavalin A in order to quantify steady-state currents in recordings with cell lines (Figs. 3-5), and to obtain clear responses in the first *in vivo* studies (Figure 7), but physiological desensitization was always preserved in all the experiments with rat brain slices (Figure 6). Likely, the *cis* isomers of **MAG$^{slow}_{2P}$** and **MAG$^{slow}_{2P_F}$** cause receptor photoactivation, channel opening, and closing by desensitization, which limits the cytotoxic effects of calcium influx. The stability of *cis* isomers also allows shortening illumination pulses and reducing phototoxicity. The repetitive photoresponses that we obtained in slices and *in vivo* are in agreement with the low toxicity of our compounds. These robust calcium responses mediated by desensitizing receptors could be related to triggering of intracellular processes[50] and/or changes in synaptic receptor mobility.[51] These processes are involved in neuronal plasticity and are currently under investigation.

Photocontrol of endogenous neuronal receptors[52] and intracellular presynaptic proteins[53] has been recently shown in *C. elegans* using 1P excitation. Our 2P excitation experiments *in vivo* with **MAG$^{slow}_{2P_F}$** conjugated to GluK2-L439C take advantage of genetic manipulation for demonstration purposes (including the expression of fluorescent calcium reporters), but the robust photoresponses obtained (Figure 7, Supplementary Movies 6-7) suggest that introducing our *ortho*-fluorosubstituted azobenzene cores in freely diffusible photoswitches would also allow photocontrolling endogenous neuronal receptors and signaling proteins with high efficacy and spatial confinement. 2P excitation is currently the only method that allows photostimulation with axial plane selectivity at micrometer resolution[48] and thus has an advantage over 1P excitation to activate individual neurons in clustered 3D structures like ganglia and brain tissue. Thus, photoswitches that combine high 2P excitation efficacy and pharmacological selectivity will be an invaluable tool to investigate intact neuronal circuits and subcellular signaling pathways, and a powerful complement to optogenetic manipulation techniques.[54]

Thus, we have shown that 2P-optimized azobenzene photoswitches are an important complement to 2P-enabled caged ligands like MNI-glutamate[49] or optogenetic tools like C1V1 [48] and ChR2-H134R,[55] but they have advantages of their own. Tethered MAG derivatives allow reversible activation of glutamate receptors without the need of perfusing high concentrations of caged glutamate compounds and the disadvantages of glutamate and by-product spillover upon uncaging. Moreover, glutamate receptors have larger cation conductances than channelrhodopsins,[56] do not require illuminating large cellular regions,[57] and can be targeted by

MAG-like photoswitches at their physiological location.[58] Finally, the 2P-optimized azobenzene core reported here entails minimal structural modifications that can be grafted into other azobenzene-based photoswitches, provided that their pharmacological properties are not altered, and thus these findings have direct and general application to light-regulated ligands.[2-4]

In conclusion, we rationally designed azobenzene chromophores based on theoretical calculations to present both high 2P absorptivity of NIR light and long *cis* state lifetime, which were then exploited in the synthesis of photoswitchable tethered ligands $\mathbf{MAG_{2P}^{slow}}$ and $\mathbf{MAG_{2P\_F}^{slow}}$. Optimized 2P stimulation of light-gated ionotropic glutamate receptors was accomplished with these compounds, which far surpassed the performance of other azobenzene-based photoswitches previously assayed for the manipulation of neuronal tissues under multiphoton excitation conditions. Taking advantage of the high 2P excitability of $\mathbf{MAG_{2P}^{slow}}$ and $\mathbf{MAG_{2P\_F}^{slow}}$ with NIR radiation, reliable and sustained photocontrol over the activity of neurons could be attained in light-scattering tissue both *in vitro* and *in vivo*, such as in brain slices under nearly physiological conditions and *C. elegans* touch receptor neurons. The results presented here constitute a proof of concept that paves the way towards all-optical experiments of neuronal activity imaging and manipulation *in vivo* using azobenzene photoswitches, which ultimately require the use of multiphoton excitation with NIR light.

## Methods

**Theoretical calculations.** All calculations were carried out at the DFT (for ground electronic states) and TDDFT (for excited electronic states) levels using the long-range corrected hybrid CAM-B3LYP functional, which is known to correctly describe excited states of charge-transfer type.[59] 6-31G(d), a split-valence basis set with polarization functions in heavy atoms, was used in all the cases. 20 excited electronic states of the same multiplicity as the ground electronic state (singlet) were converged in the TDDFT calculations. Solvent (water) effects were introduced through the self-consistent polarizable continuum model (PCM) continuum method.[60] To compute 2P absorption properties, the density functional response theory was employed to calculate the two-photon transition matrix elements. 2P absorption cross-section were then estimated through the following expression:[61]

$$\boldsymbol{\sigma_2}(\omega)=\frac{\mathbf{8\pi^2 \alpha a_0^5 \omega^2}}{\boldsymbol{c\Gamma}}\boldsymbol{\delta(\omega)} \quad (1)$$

where α is the fine structure constant, $a_0$ the Bohr radius, $c$ is the speed of light in vacuum, Γ is the full width at half maximum of the Lorentzian line-shape broadening, and δ(ω) is the 2P absorption transition probability calculated through the response theory assuming linearly polarized excitation light. We set Γ=0.2 eV, which reasonably agrees with the value experimentally determined for *trans*-$\mathbf{MAG_{460}}$ (~ 0.15 eV[34]). Here we also considered the most common case of a degenerate 2P absorption process where ω is half of the transition frequency of the excited state. All TDDFT calculations and evaluation of 2P absorption properties were calculated using the Dalton suite of programs.[62] Optimizations and evaluation of energy barriers in the ground electronic state were carried out with the GAUSSIAN09 program.[63] For energy barrier calculations of thermal *cis-trans* isomerization, we investigated both the rotation and inversion mechanisms. In the case of asymmetric azobenzenes, the two feasible paths leading to inversion were analyzed.

**Synthesis.** A detailed description of the synthesis of $\mathbf{MAG_{2P}^{slow}}$ and $\mathbf{MAG_{2P\_F}^{slow}}$ is given in the Supplementary Methods.

**Photochemical characterization.** *Trans-cis* isomerization of $\mathbf{MAG_{2P}^{slow}}$, $\mathbf{MAG_{2P\_F}^{slow}}$ and their separated azobenzene photochromes in solution was investigated by: (i) $^1$H NMR for the elucidation of the photostationary state mixtures in organic solvents; (ii) steady-state UV-vis absorption spectroscopy for *trans-cis* photoisomerization in aqueous media and slow *cis-trans* thermal back-isomerization processes.

**Cell culture**. Tsa201 cells were purchased from the European Collection of Authenticated Cell Culture (ECACC). HEK293 tsA201 cells were plated on glass coverslips and transfected with GluK2-L439C-eGFP or co-transfected with GluK2-L439C and GCaMP6s or R-GECO1. Prior to each experiment, coverslips were incubated with the PTL of choice to allow chemical conjugation to the receptor channel. A second incubation with Concavalin A was done to inhibit

desensitization of the glutamate receptor. Cells were mounted on the recording chamber filled with a bath solution composed of (in mM): 140 NaCl, 1 $MgCl_2$, 2.5 KCl, 10 4-(2-hydroxyethyl)-1-piperazineethanesulfonic acid (HEPES), 2.5 $CaCl_2$ and 10–20 glucose to fix osmolarity to 310 mOsm $kg^{-1}$. NaOH was added to adjust the pH to 7.42. To activate GluK2-L439C, 300 μM glutamate in bath solution was perfused.

**Electrophysiology**. Voltage-clamp recordings under whole-cell configuration were acquired at 1 kHz. Borosilicate glass pipettes were pulled with a typical resistance of 4–6 MOhm and filled with a solution containing (in mM): 120 cesium methanesulfonate, 10 tetraethylamonium chloride (TEACl), 5 $MgCl_2$, 3 $Na_2ATP$, 1 $Na_3GTP$, 20 HEPES, 0.5 EGTA; osmolarity was 290 mOsm $kg^{-1}$ and pH 7.2 was adjusted with CsOH. Cell membrane voltage was held at -70 mV. Photostimulation during electrophysiological recordings was induced by illuminating the entire focused field with monochromatic light in an inverted microscope (power density: 22.0 μW $mm^{-2}$ at 380 nm, 45.9 μW $mm^{-2}$ at 460 nm, and 47.4 μW $mm^{-2}$ at 500 nm).

**Calcium imaging and 1P stimulation**. Cells were imaged on an inverted fully motorized digital microscope at room temperature with a frame rate of 2 s and exciting GCaMP6s at 490 nm during 10 ms. Photoisomerization was achieved by illuminating the focused sample with flashes of violet (380 nm, 0.5 s duration) and green (500 nm, 0.5 s duration) light for activation and deactivation, respectively. Calcium imaging activation spectra under 1P stimulation ranged from 280 to 480 nm at 20 nm steps. Light flashes were nested in between GCaMP6s fluorescence measurements. Photostimulation intervals lasted a total of 3.2 min for activation and 2.4 min for deactivation. At the end of this protocol, 300 μM free glutamate solution was added and the calcium imaging response was measured.

**Calcium imaging and 2P stimulation in HEK cells**. Two-photon experiments were performed in the Advanced Digital Microscopy Core Facility of IRB Barcelona with a confocal multiphoton microscope equipped with a 80 MHz Ti:Sapphire for 2P stimulation with NIR light (710-990 nm), and cw diode (405 nm) and Ar (514 nm) lasers for 1P stimulation and calcium imaging with visible light. In these experiments, R-GECO1 was used as a $Ca^{2+}$ fluorescent indicator instead of GCaMP6s because it does not absorb at 405 nm, the excitation wavelength used to test the 1P activity of LiGluR. Imaging of R-GECO1 was done at 514 nm with a frame rate of 4 s. Photostimulation was achieved by raster-scanning the tightly focused laser of choice over a selected area of the field of view: 405 nm (0.37 mW $\mu m^{-2}$) for 1P activation, 514 nm (0.35 mW $\mu m^{-2}$) for 1P deactivation, and 720-840 nm (2.8 mW $\mu m^{-2}$) for 2P activation of LiGluR. Photostimulation scans were fit to keep imaging interval, and illumination periods at a given wavelength lasted in total 1 min. Interstimulus imaging periods also lasted 1 min.

**Calcium imaging and 2P stimulation in hippocampal slices.** All procedures were conducted in accordance with the European guidelines for animal care and use in research and were approved by the Animal Experimentation Ethics Committee at the University of Barcelona (Spain). Hippocampal organotypic slices of 400 μm in thickness were obtained from postnatal day 6-8 rats and cultured for 5-7 days until biolistically transfected with RCaMP2a and GluK2-L439C-eGFP, as described in 46. Although transfection with R-GECO1 was also assayed, RCaMP2a was finally used as a fluorescent indicator in hippocampal slice cultures because of the higher level of expression achieved. Before each experiment, slices were incubated with the PTL of choice for 10 min in artificial cerebrospinal fluid (ACSF) containing 119 mM NaCl, 2.5 mM KCl, 3 mM $CaCl_2$, 0.2 mM $MgCl_2$, 26.2 mM $NaHCO_3$, 1 mM $NaH_2PO_4$ and 11 mM glucose, equilibrated with 5% $CO_2$/95% $O_2$. After washes with fresh ACSF, slices were placed on the recording chamber and were continuously perfused with ACSF. RCaMP2a was excited at 561nm with an imaging interval of 4 s. eGFP was excited at 488 nm. Photostimulation was achieved by raster-scanning the tightly focused laser of choice over the whole field of view at 400 Hz: 405 nm (0.81 mW $\mu m^{-2}$) for 1P activation, 514 nm 0.35 mW $\mu m^{-2}$) for 1P deactivation, and 780 nm (2.8 mW $\mu m^{-2}$) for 2P activation of LiGluR. Photostimulation scans were fit to keep imaging interval, and illumination periods at a given wavelength lasted in total 1 min. Interstimulus imaging periods lasted 1.5 min.

**Calcium imaging and 2P stimulation in vivo in *C. elegans*.** Animal experiments carried out have been approved by the ethics committee of the ERC and the animal welfare has been respected. *C. elegans* are nematodes and therefore not covered by EU Directive 2010/63/EU, which only covers vertebrates and cephalopods. Likewise, worms are not covered by the Spanish "Código de protección y bienestar animal". For these reasons, there is no need for authorizations, personal licenses, standards for procedures or detailed description of number of animals to be used, nature of experiments or anticipated impact and minimization thereof. We generated strain MSB104 [mirEx22(mec-17p::iGluR6::mCherry;myo-2p::mCherry);ljSi123(mec-7p:GCaMP6s::SL2::tagRFP);lite-1(ce314)X]. Transgenesis was performed according to standard methods for microinjection[64] by microinjecting a DNA mix containing 50 ng/μl pNMSB18 (mec-17p::iGluR6::mCherry, Supplementary Table 7), 1.5 ng/μl myo-2p:mCherry as a coinjection marker and 50 ng/μl 1Kb Plus DNA ladder (Invitrogen) as a carrier into the gonad of GN692 young adults worms.[65] $\mathbf{MAG}^{\mathbf{slow}}_{\mathbf{2P\_F}}$ (10 mM in M9 buffer and 0.3 mg/ml ConA) was administered to the animals by microinjection into the body cavity. Control group was performed microinjecting with vehicle (10% DMSO, 0.3mg/ml ConA in M9 buffer), and allowed to recover. Only roaming worms surviving the treatment were considered for the following imaging experiments. After

four hours of compound administration, TRN neurons co-expressing GluK2-L439C-mCherry and GCaMP6s were imaged in a single focused plane. Calcium imaging was performed on a Leica confocal microscope (SP5) through a 63x/1.4-NA Oil objective (HCX PL APO, Leica). Calcium sensitive GCaMP6s and calcium insensitive RFP fluorescent proteins were simultaneously excited at 488 nm and 561 nm for 343 ms, using bidirectional laser scanning at 400 Hz. Images were recorded with a resolution of 512x512 and a digital zoom of 4, with an imaging interval of 660 ms. GCaMP6s and RFP fluorescence were recorded with two different HyD detectors with a detection range from 500 to 550 nm and from 569 to 648 nm, respectively. Pinhole aperture was set at ~500 μm. Whole field photostimulation flashes were fit to keep imaging interval. Photostimulation was done at 256x256 resolution with bidirectional laser scan, with a digital zoom of 4. One-photon photostimulation was done at 405 nm (15 μW $\mu m^{-2}$), and two-photon stimulation at 780 nm (2.8 mW $\mu m^{-2}$). Back-photoisomerization was achieved at 514 nm (1.21 μW $\mu m^{-2}$). Intensity and duration of the photostimulation intervals were adjusted to obtain the optimal photoresponse and reproducibility.

**Data availability**

The authors declare that the main data supporting the findings of this study are available within the article and its Supplementary Information. Extra data are available from the corresponding author upon request.

## References


1. Bandara, H. M. D. & Burdette, S. C. Photoisomerization in different classes of azobenzene. Chem. Soc. Rev. 41, 1809–1825 (2012).
2. Ankenbruck, N., Courtney, T., Naro, Y. & Deiters, A. Optochemical control of biological processes in cells and animals. Angew. Chem. Int. Ed. 57, 2768–2798 (2018).
3. Broichhagen, J., Frank, J. A. & Trauner, D. A roadmap to success in photopharmacology. Acc. Chem. Res. 48, 1947–1960 (2015).
4. Lerch, M. M., Hansen, M. J., van Dam, G. M., Szymanski, W. & Feringa, B. L. Emerging targets in photopharmacology. Angew. Chem. Int. Ed. 55, 10978–10999 (2016).
5. Gorostiza, P. & Isacoff, E. Y. Optical switches for remote and noninvasive control of cell signaling. Science 322, 395–399 (2008).
6. Fehrentz, T., Schönberger, M. & Trauner, D. Optochemical genetics. Angew. Chem. Int. Ed. 50, 12156–12182 (2011).
7. Kramer, R. H., Mourot, A. & Adesnik, H. Optogenetic pharmacology for control of native neuronal signaling proteins. Nat. Neurosci. 16, 816–823 (2013).
8. Hansen, M. J., Lerch, M. M., Szymanski, W. & Feringa, B. L. Direct and versatile synthesis of red-shifted azobenzenes. Angew. Chem. Int. Ed. 55, 13514–13518 (2016).
9. Bléger, D., Schwarz, J., Brouwer, A. M. & Hecht, S. o-Fluoroazobenzenes as readily synthesized photoswitches offering nearly quantitative two-way isomerization with visible light. J. Am. Chem. Soc. 134, 20597–20600 (2012).
10. Hammerich, M. et al. Heterodiazocines: synthesis and photochromic properties, trans to cis switching within the bio-optical window. J. Am. Chem. Soc. 138, 13111–13114 (2016).
11. Dong, M. et al. Near-Infrared photoswitching of azobenzenes under physiological conditions. J. Am. Chem. Soc. 139, 13483–13486 (2017).
12. Wegener, M., Hansen, M. J., Driessen, A. J. M., Szymanski, W. & Feringa, B. L. Photocontrol of antibacterial activity: shifting from UV to red light activation. J. Am. Chem. Soc. 139, 17979–17986 (2017).
13. Siewertsen, R. et al. Highly efficient reversible Z-E photoisomerization of a bridged azobenzene with visible light through resolved S(1)(n pi*) absorption bands. J. Am. Chem. Soc. 131, 15594–15595 (2009).
14. Pawlicki, M., Collins, H. A., Denning, R. G. & Anderson, H. L. Two-photon absorption and the design of two-photon

dyes. Angew. Chem. Int. Ed. 48, 3244–3266 (2009).
15. Bort, G., Gallavardin, T., Ogden, D. & Dalko, P. I. From one-photon to two- photon probes: “caged” compounds, actuators, and photoswitches. Angew. Chem. Int. Ed. 52, 4526–4537 (2013).
16. Denk, W., Strickler, J. H. & Webb, W. W. Two-photon laser scanning fluorescence microscopy. Science 248,73–76 (1990).
17. Papagiakoumou, E. et al. Functional patterned multiphoton excitation deep inside scattering tissue. Nat. Photon. 7, 274–278 (2013).
18. Oron, D., Papagiakoumou, E., Anselmi, F. & Emiliani, V. Two-photon optogenetics. Prog. Brain Res. 196, 119–143 (2012).
19. Watson, B. O., Nikolenko, V. & Yuste, R. Two-photon imaging with diffractive optical elements. Front. Neural Circuits 3, 6 (2009).
20. Packer, A. M. et al. Two-photon optogenetics of dendritic spines and neural circuits. Nat. Methods 9, 1202–1205 (2012).
21. Rowlands, C. J. et al. Wide-field three-photon excitation in biological samples. Light Sci. Appl. 6, e16255 (2017).
22. de Boni, L., Misoguti, L., Zilio, S. C. & Mendonça, C. R. Degenerate two- photon absorption spectra in azoaromatic compounds. Chemphyschem 6, 1121–1125 (2005).
23. Silva, D. L., Krawczyk, P., Bartkowiak, W. & Mendonça, C. R. Theoretical study of one- and two-photon absorption spectra of azoaromatic compounds. J. Chem. Phys. 131, 244516 (2009).
24. Volgraf, M. et al. Allosteric control of an ionotropic glutamate receptor with an optical switch. Nat. Chem. Biol. 2,47–52 (2006).
25. Gorostiza, P. et al. Mechanisms of photoswitch conjugation and light activation of an ionotropic glutamate receptor. Proc. . Natl Acad. Sci. USA 104, 10865–10870 (2007).
26. Szobota, S. et al. Remote control of neuronal activity with a light-gated glutamate receptor. Neuron 54, 535–545 (2007).
27. Wyart, C. et al. Optogenetic dissection of a behavioural module in the vertebrate spinal cord. Nature 461, 407–410 (2009).
28. Li, D., Hérault, K., Isacoff, E. Y., Oheim, M. & Ropert, N. Optogenetic activation of LiGluR-expressing astrocytes evokes anion channel-mediated glutamate release. J. Physiol. 590, 855–873 (2012).
29. Izquierdo-Serra, M., Trauner, D., Llobet, A. & Gorostiza, P. Optical modulation of neurotransmission using calcium photocurrents through the ion channel LiGluR. Front. Mol. Neurosci. 6, 3 (2013).
30. Kauwe, G. & Isacoff, E. Y. Rapid feedback regulation of synaptic efficacy during high-frequency activity at the Drosophila larval neuromuscular junction. Proc. Natl Acad. Sci. USA 110, 9142–9147 (2013).
31. Kienzler, M. A. & Isacoff, E. Y. Precise modulation of neuronal activity with synthetic photoswitchable ligands. Curr. Opin. Neurobiol. 45, 202–209 (2017).
32. Berlin, S. & Isacoff, E. Y. Synapses in the spotlight with synthetic optogenetics. EMBO Rep. 5, 677–692 (2017).
33. Izquierdo-Serra, M. et al. Two-photon neuronal and astrocytic stimulation with azobenzene-based photoswitches. J. Am. Chem. Soc. 136, 8693–8701 (2014).
34. Carroll, E. C. et al. Two-photon brightness of azobenzene photoswitches designed for glutamate receptor optogenetics. Proc. Natl Acad. Sci. USA 112, E776–E785 (2015).
35. Gascón-Moya, M. et al. An optimized glutamate receptor photoswitch with sensitized azobenzene isomerization. J. Org. Chem. 80, 9915–9925 (2015).
36. Antonov, L., Kamada, K., Ohta, K. & Kamounah, F. S. A systematic femtosecond study on the two-photon absorbing D-π-A molecules–π-bridge nitrogen insertion and strength of the donor and acceptor groups. Phys. Chem. Chem. Phys. 5, 1193–1197 (2003).

37. Magennis, S. W., Mackay, F. S., Jones, A. C., Tait, K. M. & Sadler, P. J. Two-photon-induced photoisomerization of an azo dye. Chem. Mater. 17, 2059–2062 (2005).
38. Pokladek, Z. et al. Linear and third-order nonlinear optical properties of triazobenzene-1,3,5-triazinane-2,4,6-trione (isocyanurate) derivatives. ChemPlusChem 82, 1372–1383 (2017).
39. Laprell, L. et al. Optical control of NMDA receptors with a diffusible photoswitch. Nat. Commun. 6, 8076 (2015).
40. Passlick, S., Richers, M. T. & Ellis-Davies, G. C. R. Thermodynamically stable, photoreversible pharmacology in neurons with one- and two-photon excitation. Angew. Chem. Int. Ed. 57, 12554–12557 (2018).
41. Kienzler, M. A. et al. A Red-shifted, fast-relaxing azobenzene photoswitch for visible light control of an ionotropic glutamate receptor. J. Am. Chem. Soc. 135, 17683–17686 (2013).
42. Supuran, C., Vullo, D., Scozzafava, A., Maresca, A. & Carta, F. Carbonic anhydrase inhibitors. Diazenylbenzenesulfonamides are potent and selective inhibitors of the tumor-associated isozymes IX and XII over the cytosolic isoforms I and II. Bioorg. Med. Chem. 17, 7093–7099 (2009).
43. Pearson, R. J., Kassianidis, E., Slawin, A. M. Z. & Philp, D. Self-replication vs. reactive binary complexes—manipulating recognition-mediated cycloadditions by simple structural modifications. Org. Biomol. Chem. 2, 3434–3441 (2004).
44. Nakai, J., Ohkura, M. & Imoto, K. A high signal-to-noise Ca(2+) probe composed of a single green fluorescent protein. Nat. Biotechnol. 19, 137–141 (2001).
45. Zhao, Y. et al. An expanded palette of genetically encoded $Ca^{2+}$ indicators. Science 333, 1888–1891 (2011).
46. Bosch, M. et al. Structural and molecular remodeling of dendritic spine substructures during long-term potentiation. Neuron 16, 444–459 (2014).
47. Stirman, J. N. et al. Real-time multimodal optical control of neurons and muscles in freely behaving Caenorhabditis elegans. Nat. Methods 8, 153–158 (2011).
48. Prakash, R. et al. Two-photon optogenetic toolbox for fast inhibition, excitation and bistable modulation. Nat. Methods 9, 1171–1179 (2012).
49. Shoham, S., O'Connor, D. H., Sarkisov, D. V. & Wang, S. S. Rapid neurotransmitter uncaging in spatially defined patterns. Nat. Methods 2, 837–843 (2005).
50. Lauri, S. E. et al. A role for Ca2+stores in kainate receptor-dependent synaptic facilitation and LTP at mossy fiber synapses in the hippocampus. Neuron 39, 327–341 (2003).
51. de Luca, E. et al. Inter-synaptic lateral diffusion of GABAA receptors shapes inhibitory synaptic currents. Neuron 95,63–69.e5 (2017).
52. Damijonaitis, A. et al. AzoCholine enables optical control of alpha 7 nicotinic acetylcholine receptors in neural networks. ACS Chem. Neurosci. 6, 701–707 (2015).
53. Frank, J. A. et al. Photoswitchable diacylglycerols enable optical control of protein kinase C. Nat. Chem. Biol. 72, 510–516 (2016).
54. Rost, B. R., Schneider-Warme, F., Schmitz, D. & Hegemann, P. Optogenetic tools for subcellular applications in neuroscience. Neuron 96, 572–603 (2017).
55. dal Maschio, M., Donovan, J. C., Helmbrecht, T. O. & Baier, H. Linking neurons to network function and behavior by two-photon holographic optogenetics and volumetric imaging. Neuron 94, 774–789 (2017).
56. Izquierdo-Serra, M., Trauner, D., Llobet, A. & Gorostiza, P. Optical control of calcium-regulated exocytosis. Biochim. Biophys. Acta 1830, 2853–2860 (2013).
57. Rickgauer, J. P. & Tank, D. W. Two-photon excitation of channelrhodopsin-2 at saturation. Proc. Natl Acad. Sci. USA 106, 15025–15030 (2009).

58. Izquierdo-Serra, M. et al. Optical control of endogenous receptors and cellular excitability using targeted covalent photoswitches. Nat. Commun. 7, 12221 (2016).
59. Pittolo, S. et al. Reversible silencing of endogenous receptors in intact brain tissue using two-photon pharmacology bioRxiv 515288; doi: https://doi.org/ 10.1101/515288.
60. Yanay, T., Dew, D. P. & Handy, N. C. A new hybrid exchange- correlation functional using the Coulomb-attenuating method (CAM-B3LYP). Chem. Phys. Lett. 393, 51-57 (2004).
61. Improta, R., Barone, V., Scalmani, G. & Frisch, M. J. A state-specific polarizable continuum model time dependent density functional theory method for excited state calculations in solution. J. Chem. Phys. 125, 054103 (2006).
62. Murugan, N. A. et al. Hybrid density functional theory/molecular mechanics calculations of two-photon absorption of dimethylamino nitro stilbene in solution. Phys. Chem. Chem. Phys. 13, 12506–12516 (2011).
63. Aidas, K. et al. The Dalton quantum chemistry program system. Comput. Mol. Sci. 4, 269–284 (2014).
64. Frisch, M. J. et al. Gaussian 09, Revision C.01 (Gaussian, Inc., Wallingford, CT, 2009).
65. Evans, T. Transformation and microinjection. WormBook 1–15, https://doi. org/10.1895/wormbook.1.108.1 (2006).
66. Nekimken, A. L. et al. Pneumatic stimulation of C. elegans mechanoreceptor neurons in a microfluidic trap. Lab Chip 17, 1116–1127 (2017).

## Acknowledgments

G. C. acknowledges the "Generalitat de Catalunya" for her pre-doctoral FI grant. A. G.-C. was supported by fellowship BES-2014-068169. M. B. was supported by a Marie Curie Reintegration Grant (H2020-MSCA-IF). We are grateful to Ehud Isacoff (UC Berkeley) for sharing the LiGluR clone, to Dirk Trauner (NYU) for providing MAG compound and to Anna Lledó i Lidia Bardia (IRBB imaging facility) for support in imaging experiments. We would like to acknowlegde César Alonso, Angel Sandoval and Merche Rivas from the Biolab at ICFO for technical support in *C. elegans* experiments. We also acknowledge financial support from AGAUR/Generalitat de Catalunya (CERCA Programme and projects 2017-SGR-00465, 2017-SGR-1442 and 2017-SGR-1012), Severo Ochoa (SEV-2015-0522), Fundacion Privada Cellex, FEDER funds, ERANET SynBio MODULIGHTOR and Human Brain Project WAVESCALES projects, MINECO/FEDER (projects CTQ2015-65439-R, CTQ2016-80066-R, CTQ2016- 75363-R, CTQ2017-84745-P, and RYC-2015-17935) and Fundaluce and Ramón Areces foundations. MK acknowledges support through HFSP CDA and ERC MechanoSystems (715243).

## Author contributions

P.G., J.H., F.B. and R.A. conceived and supervised the project. J.M.L., M.M. and R.G. performed the theoretical calculations. R.A., F.B. and J.H. designed and supervised the chemical synthesis. J.H. designed and supervised the photochemical study. G.C. performed the synthesis and the photochemical study. M.G.-M. collaborated in the synthesis. A.G.-C. and N.C. prepared cultured HEK cells. A.G.-C. and G.C. performed the study on cultured HEK cells. A.G.-C. and M.B. performed the experiments with neurons. M. K. and M.P.R designed and supervised the

experiments in vivo with *C. elegans* nematodes. A.G.-C. and M.P.R performed the experiments in vivo with *C. elegans* worms. All the authors contributed to the preparation of the article.

## Competing interest.

The authors declare no competing interest.

## Additional information

**Supplementary Information**. General materials and methods, detailed description of the synthesis of $\mathbf{MAG_{2P}^{slow}}$ and $\mathbf{MAG_{2P\_F}^{slow}}$ and additional data on theoretical calculations, and photochemical and biological measurements.

# Supplementary Figures

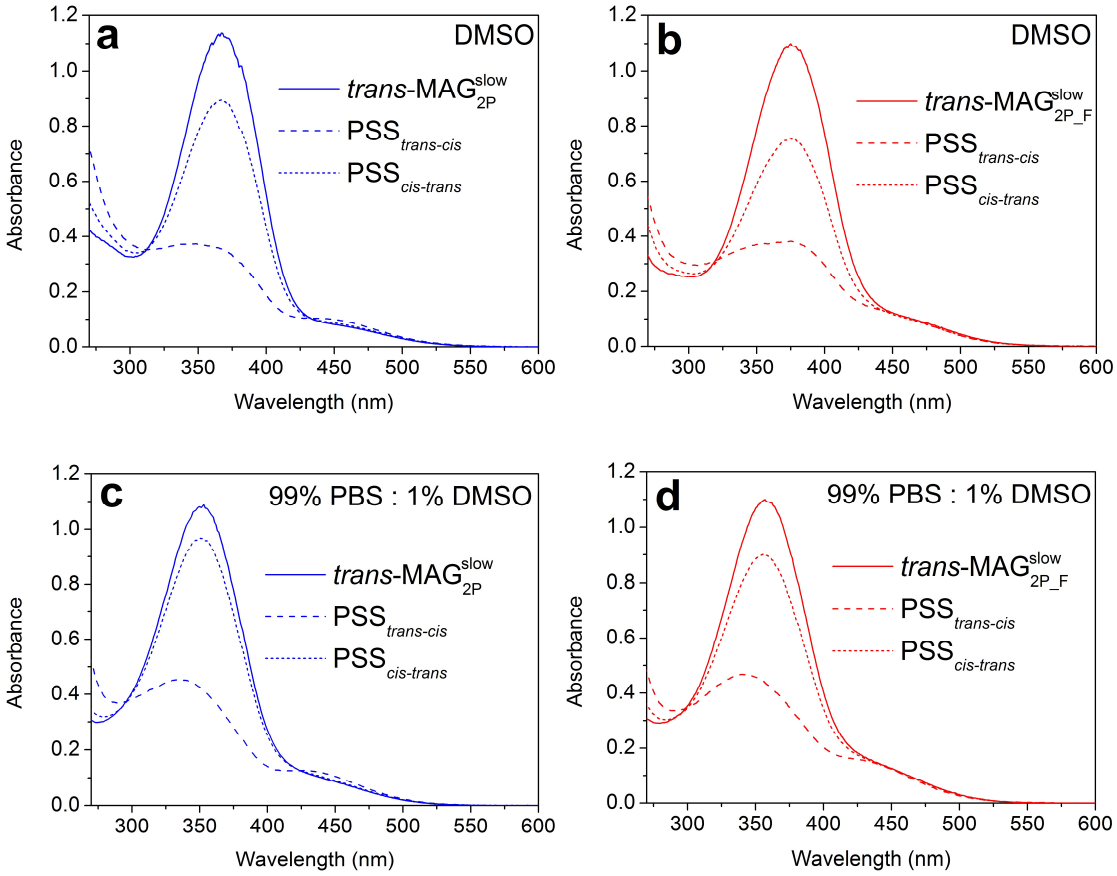


**Supplementary Figure 5** *Cis→trans* photoisomerization of **MAG$^{slow}_{2P}$** and **MAG$^{slow}_{2P_F}$**. (**a, c**) Absorption spectra of *trans*-**MAG$^{slow}_{2P}$**, the photostationary state mixture obtained upon irradiation at $\lambda_{exc}$ = 366 nm to induce *trans→cis* photoisomerization ($PSS_{trans-cis}$), and the photostationary state mixture obtained upon irradiation at $\lambda_{exc}$ = 473 nm to induce *cis→trans* photoisomerization ($PSS_{cis-trans}$) in (**a**) DMSO and (c) 99% PBS:1% DMSO. (**b, d**) Absorption spectra of *trans*-**MAG$^{slow}_{2P_F}$**, the $PSS_{trans-cis}$ mixture obtained upon irradiation at $\lambda_{exc}$ = 366 nm, and the $PSS_{cis-trans}$ mixture obtained upon irradiation at $\lambda_{exc}$ = 473 nm in (b) DMSO and (**d**) 99% PBS:1% DMSO.

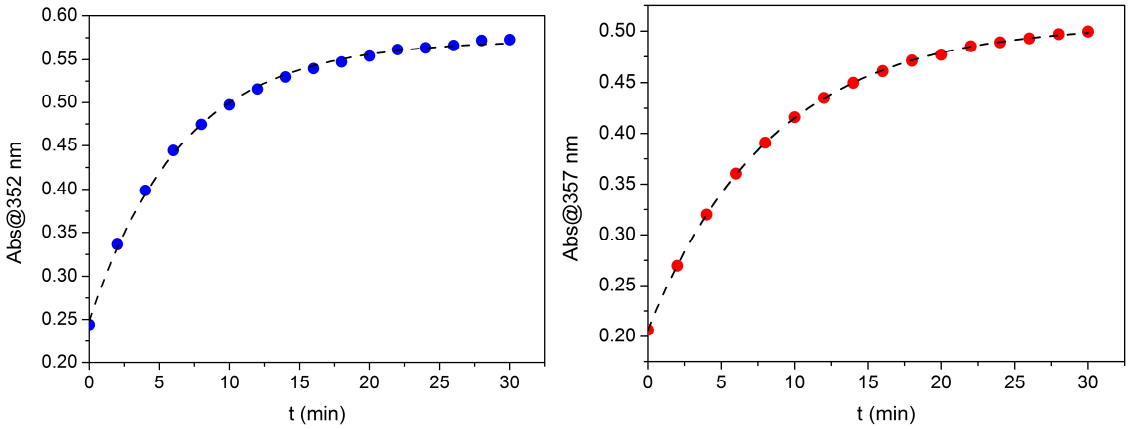


**Supplementary Figure 6** *Cis-trans* thermal back-isomerization of **MAG$_{2P}^{slow}$** and **MAG$_{2P_F}^{slow}$**. Variation of the absorption of the *trans-cis* photostationary state mixture of **MAG$_{2P}^{slow}$** (blue) and **MAG$_{2P_F}^{slow}$** (red) in the dark at 25 ºC in 99% PBS:1% DMSO. At these conditions, thermal *cis-trans* back-isomerization takes place, thus restoring the inital concentration of the *trans* state of the ligands, which presents a larger extinction coefficient at $\lambda_{abs}$ = 352 nm and $\lambda_{abs}$ = 357 nm. Points correspond to the experimental data, while lines were obtained from monoexponential fits.

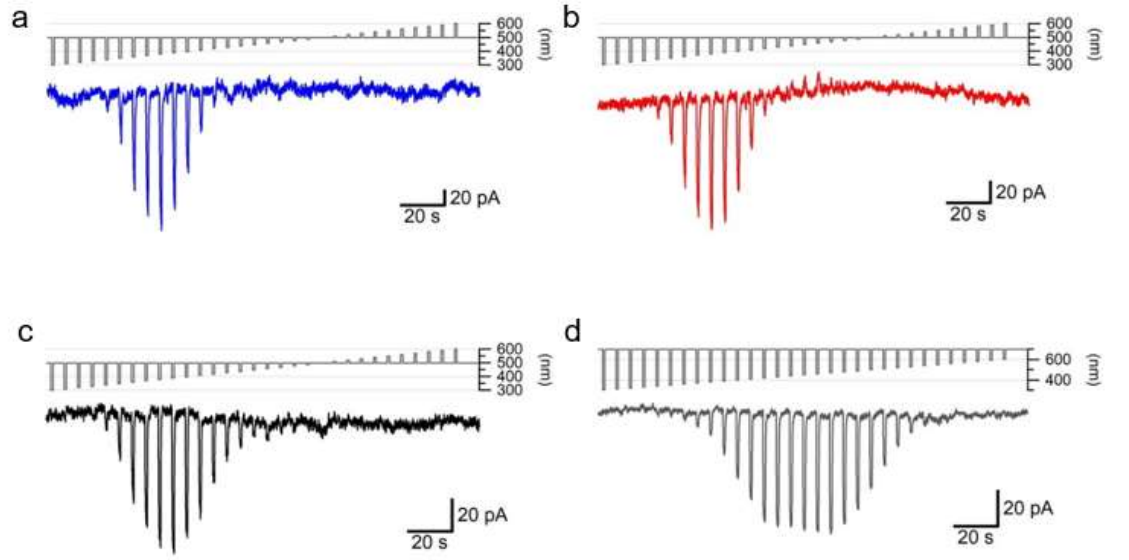


**Supplementary Figure 7** 1P patch-clamp traces of LiGluR-expressing HEK293 cells**.** Wavelength-dependent whole-cell voltage-clamp currents recorded in HEK293 cells expressing GluK2-L439C after conjugation to (**a**) **MAG$_{2P}^{slow}$**, (**b**) **MAG$_{2P_F}^{slow}$**, (**c**) **MAG**, and (**d**) **MAG$_{2P}$**. Excitation light pulses to induce channel opening ranged from 300 to 600 nm, while channel closure was accomplished by excitation at 500 nm in (**a-c**) and thermally in (**d**).

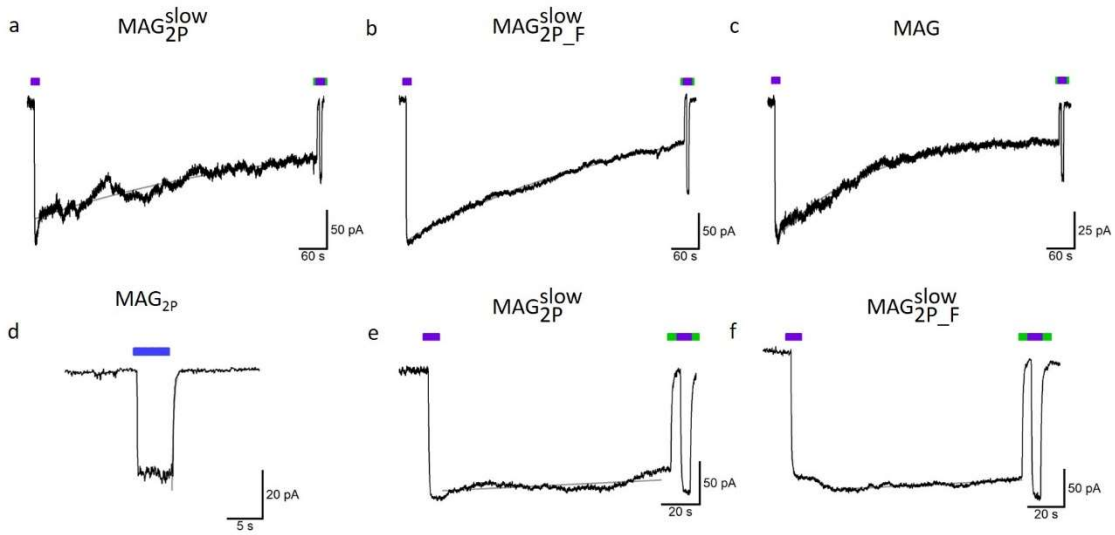


**Supplementary Figure 8** 1P thermal relaxation of in LiGluR-expressing HEK293 cells**.** Electrophysiological recordings and quantification of thermal relaxation lifetimes at room temperature of **MAG$_{2P}^{slow}$**, **MAG$_{2P_F}^{slow}$**, **MAG,** and **MAG$_{2P}$** photoswitches after conjugation to GluK2-L439C. Time course of photocurrent relaxation in the dark after initial 380 nm light pulse (whole cell patch clamp in HEK293 cells). Exponential fits are indicated by grey curves. The slow thermal relaxation of *cis* isomers of (**a**) **MAG$_{2P}^{slow}$**, (**b**) **MAG$_{2P_F}^{slow}$**, and (**c**) **MAG**, confirms slow deactivation in the dark ($\tau$ = 570 ± 14 s, 534 ± 3 s, and 900 ± 54 s respectively), in agreement with measurements in cuvette (Supplementary Figure 6). A second light pulse at the end of the traces shows that partial current run-down occurs in these long-lasting current recordings. This is usually due to cell dialysis in whole cell patch clamp configuration, but in our case it does not cause overestimation of lifetimes. In contrast to these long lifetimes, **MAG$_{2P}$** photoswitch (**d**) relaxes much faster in the dark and yields an average lifetime of 0.25 ± 0.013 s. Current rundown and stability of **MAG$_{2P}^{slow}$** and **MAG$_{2P_F}^{slow}$** can be improved in shorter relaxation experiments (2 min in the dark, (**e**) and (**f**) respectively) but do not allow determining reliable lifetime values. However, they show that in contrast to fast relaxing photoswitches, **MAG$_{2P}^{slow}$** and **MAG$_{2P_F}^{slow}$** induce stable channel activation with short light pulses, as intended to achieve higher 2P excitation efficacy.

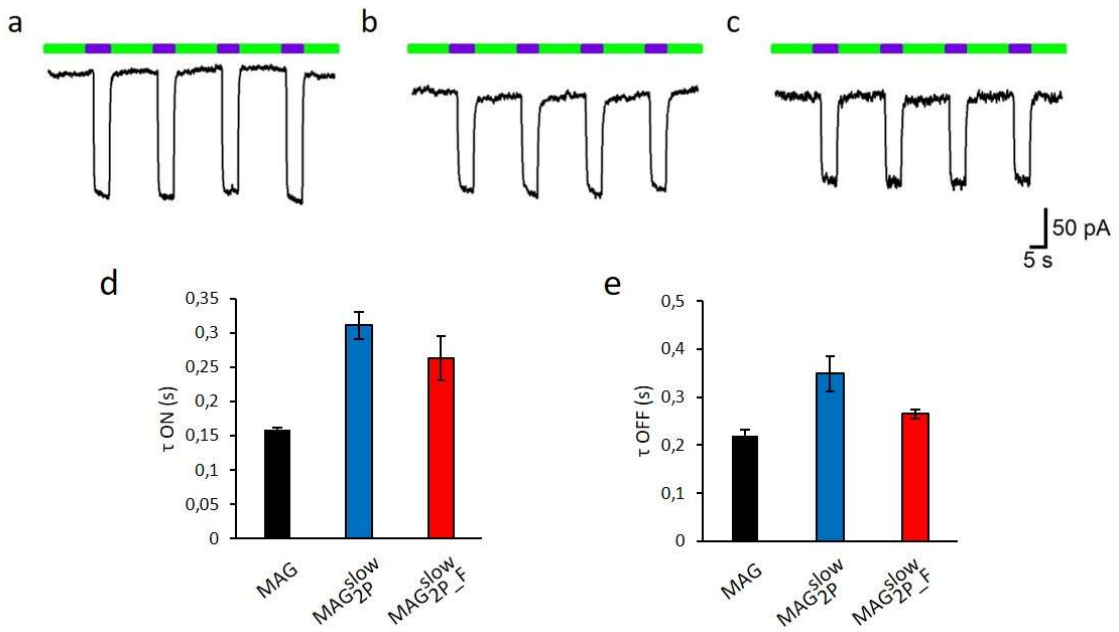


**Supplementary Figure 9** Activation and deactivation kinetics in LiGluR-expressing HEK293 cells. Whole cell patch-clamp current traces from HEK293 cells expressing GluK2-L439C after conjugation to (**a**) **MAG**, (**b**) **MAG$_{2P}^{slow}$** and, (**c**) **MAG$_{2P_F}^{slow}$**. Cells were treated with 0.3 mg/mL Concanavalin A to block receptor desensitization and obtain steady currents. The photocurrent onset and offset were fitted to an exponential function to calculate $\tau_{ON}$ and $\tau_{OFF}$, respectively. Light stimulation wavelengths were 405 nm (purple bars, 38 µW mm$^{-2}$) and 500 nm (green bars, 48 µW mm$^{-2}$). (**d, e**) Quantification of $\tau_{ON}$ and $\tau_{OFF}$ for **MAG** (black bars, $n$ = 4 biologically independent cells), **MAG$_{2P}^{slow}$** (blue bars, $n$ = 5 biologically independent cells), and **MAG$_{2P_F}^{slow}$** (red bars, $n$ = 3 biologically independent cells). Error bars are SEM. Source data for (**d, e**) are provided as a soured Data file.

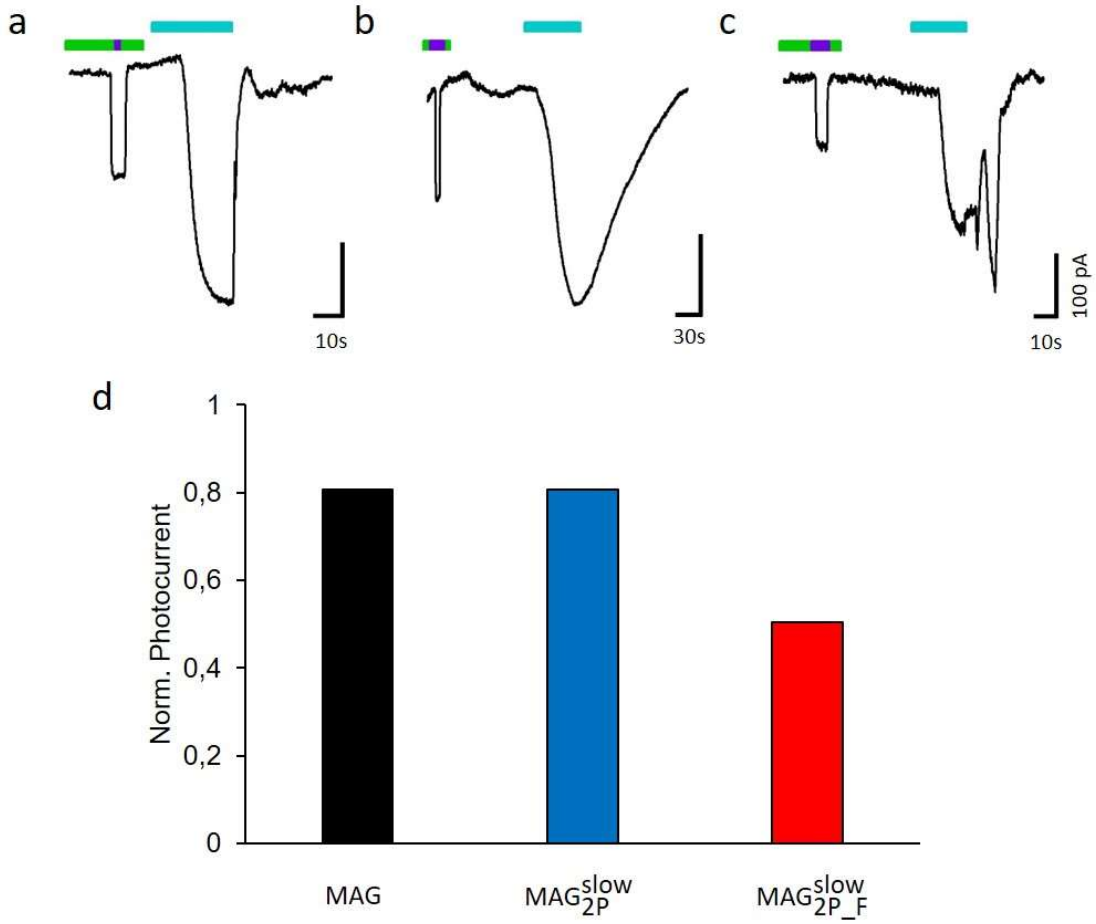


**Supplementary Figure 10** 1P patch clamp traces of LiGluR-expressing HEK293 cells**.** Whole cell patch-clamp current traces from HEK293 cells expressing GluK2-L439C after conjugation to (**a**) **MAG**, (**b**) **MAG$_{2P}^{slow}$**, (**c**) **MAG$_{2P_F}^{slow}$** (incubation with 50 μM solutions of each photoswitch). Cells were treated with 0.3 mg/mL Concanavalin A to block receptor desensitization and obtain steady currents. Light stimulation wavelengths were 405 nm (purple bars, 37.7 μW mm$^{-2}$) and 500 nm (green bars, 47.4 μW mm$^{-2}$). After photoinduced opening-closing, LiGluR activation was achieved by addition of 300 μM free glutamate. (**d**) Quantification of photocurrents normalized by the response to free glutamate (300 μM). Thus, photoswitch conjugation allows the receptor to respond to illumination, while preserving its physiological responses to free glutamate, as reported for other **MAG** analogs.[1,2]

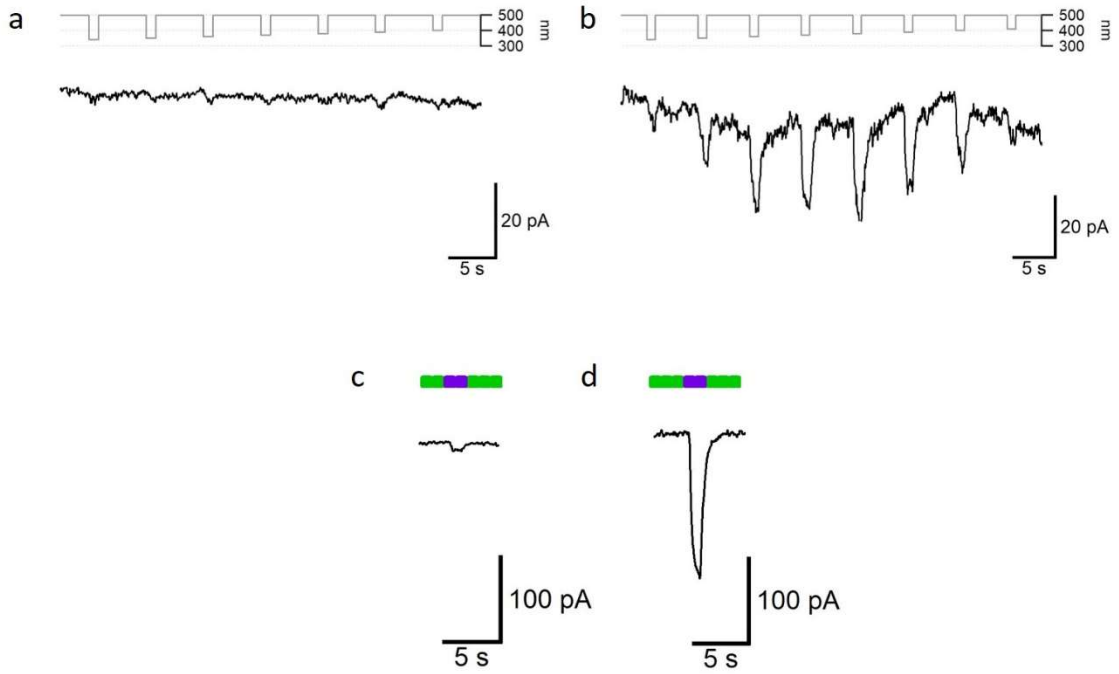


**Supplementary Figure 11** Desensitization of LiGluR after conjugation to **MAG$^{slow}_{2P}$**. Example of wavelength-dependent photoresponses of **MAG$^{slow}_{2P}$** conjugated to GluK2-L439C in HEK293 cells and measured using whole cell patch-clamp. Action spectra with averaged photoresponses are shown in Figure 3. Prior to incubation in Concanavalin A, rapid receptor desensitization precludes detection of the fast transient responses (**a, c**), which are readily measurable as steady photocurrents upon blocking desensitization with Concanavalin A (**b**, **d**). In (**c**) and (**d**) light stimulation wavelengths were 405 nm (purple bars, 38 µW mm$^{-2}$) and 500 nm (green bars, 48 µW mm$^{-2}$). Conjugation of **MAG$^{slow}_{2P}$** to GluK2-L439C does not slow down desensitization, in agreement to a previous report using MAG.[3]

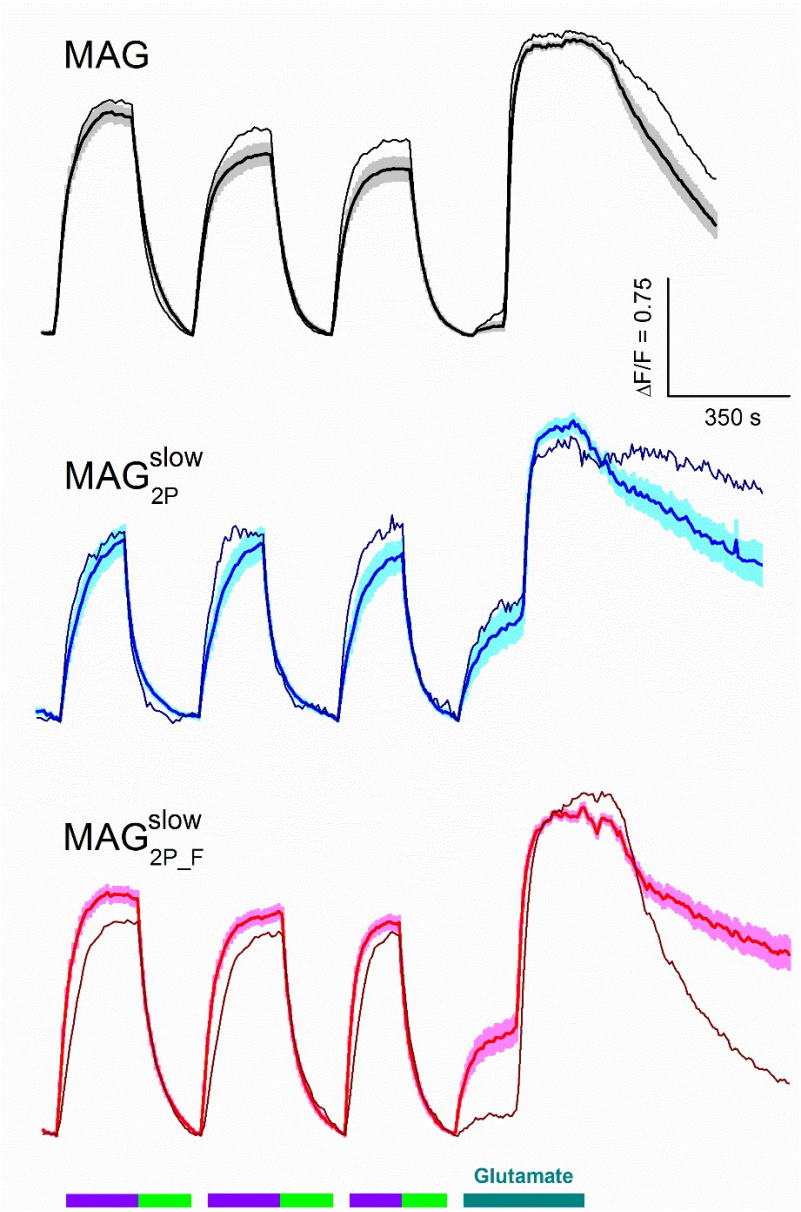


**Supplementary Figure 12** 1P calcium imaging traces of LiGluR-expressing HEK293 cells. Individual (thin lines) and average (thick lines) calcium imaging fluorescence traces registered for HEK293 cells co-expressing GluK2-L439C and GCaMP6s after conjugation to **MAG** (*n* = 31 biologically independent cells), **MAG$^{slow}_{2P}$** (*n* = 20 biologically independent cells) and **MAG$^{slow}_{2P_F}$** (*n* = 45 biologically independent cells) (50 μM each photoswitch). The bands around average traces plot the corresponding SEM. 1P excitation at 360 nm (violet) was applied to open LiGluR channels and trigger calcium-induced GCaMP6s fluorescence enhancement, while 1P excitation at 500 nm (green) was applied to revert back the process. After three photoinduced opening-closing cycles, LiGluR activation was achieved by addition of 300 μM free glutamate. Source data are provided as a soured Data file.

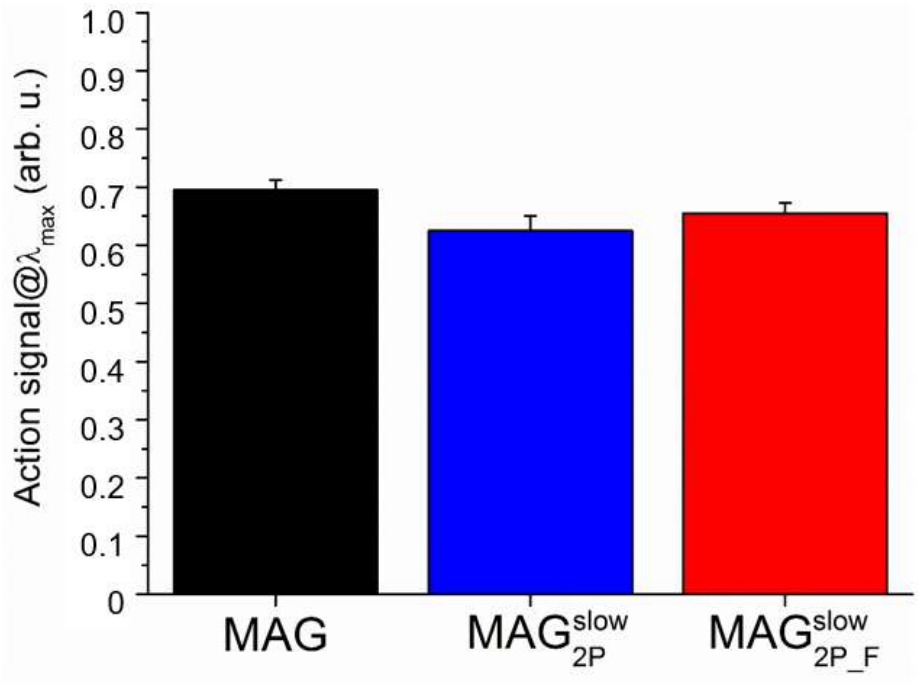


**Supplementary Figure 13** 1P calcium imaging responses.1P responses of **MAG**, **$MAG^{slow}_{2P}$** and **$MAG^{slow}_{2P\_F}$** after conjugation to GluK2-L439C-expressing HEK293 cells (50 µM each photoswitch). Photoresponses were measured by means of calcium imaging measurements using GCaMP6s as fluorescence indicator. Before averaging over different cells, the 1P responses of each cell were normalized with respect to the free glutamate response (300µM) (*n* = 81, 63 and 76 biologically independent cells, respectively). Errors are SEM. Source data are provided as a soured Data file.

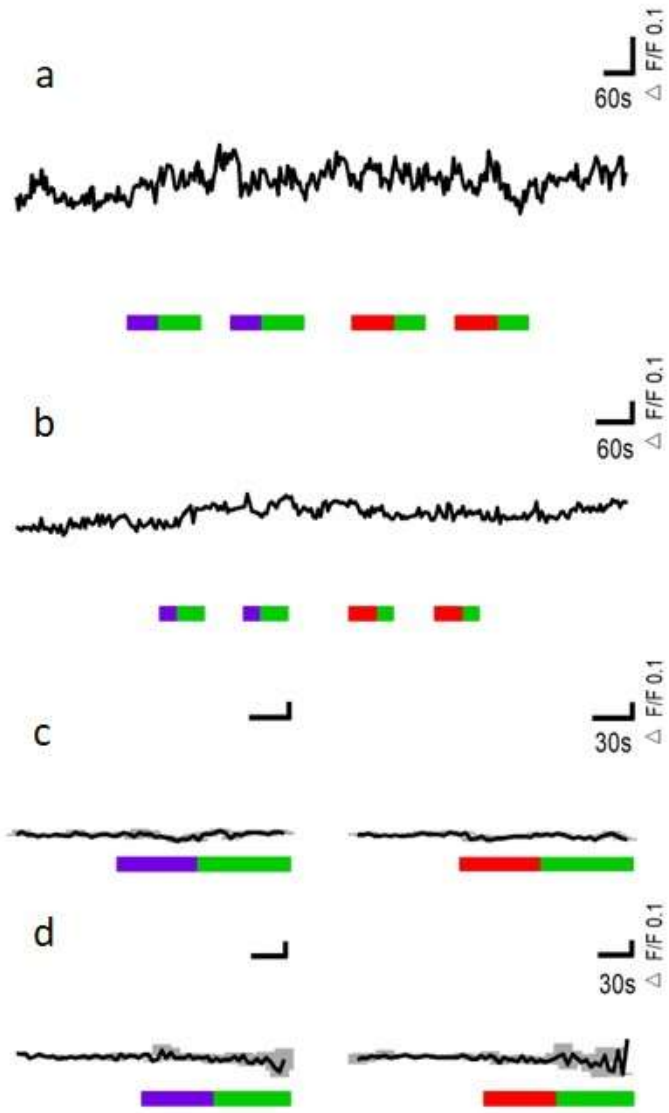


**Supplementary Figure 14** Calcium imaging traces for control samples of hippocampal slices. Cells in rat hippocampal organotypic slices expressing RCaMP2 but not LiGluR-eGFP did not respond to **MAG** or $\mathbf{MAG}^{\mathbf{slow}}_{\mathbf{2P\_F}}$ photostimulation. (**a-b**) Real time traces of a single-cell neuronal activity of slices incubated with (**a**) **MAG** or (b) $\mathbf{MAG}^{\mathbf{slow}}_{\mathbf{2P\_F}}$. (**c-d**) Average 1P and 2P responses of neurons incubated with (**c**) **MAG** (*n* = 3 cells from different animals experiments) or (d) $\mathbf{MAG}^{\mathbf{slow}}_{\mathbf{2P\_F}}$ (*n* = 4 cells from different animals experiments). Error bars are SEM. 1P stimulation was performed at 405 nm (purple bar) and 514 nm (green bar), and 2P stimulation at 780 nm (red bar). Source data fare provided as a soured Data file.

# Supplementary Tables

**Supplementary Table 1.** Theoretical results in gas phase at the CAM-B3LYP/6-31G(d) level.

| | DFT [a] | | TDDFT [b] | | | | | |
|---|---|---|---|---|---|---|---|---|
| | $\Delta E_{trans\text{-}cis}$ | $\Delta E^{\ddagger}_{cis\text{-}trans}$ [c] | $S_0 \rightarrow S_1$ transition | | | $S_0 \rightarrow S_2$ transition | | |
| | (kJ mol$^{-1}$) | | $E_{exc}$ (eV) | f | $\sigma_2$ | $E_{exc}$ (eV) | f | $\sigma_2$ |
| ***trans*-Azo$^{MAG}$** | 67.3 | 113.1 | 2.77 | 0.0 | 0.0 | 3.79 | 1.2 | 0 |
| ***cis*-Azo$^{MAG}$** | | | 2.69 | 0.0 | 0.1 | 4.43 | 0.3 | 10 |
| ***trans*-Azo$^{MAG2p}$** | 69.9 | 108.2 | 2.83 | 0.0 | 0.0 | 3.62 | 1.2 | 19 |
| ***cis*-Azo$^{MAG2p}$** | | | 2.66 | 0.01 | 0.1 | 4.17 | 0.4 | 40 |
| ***trans*-Azo1** | 64.9 | 95.4 | 2.71 | 0.0 | 0.0 | 3.87 | 1.2 | 19 |
| ***cis*-Azo1** | | | 2.72 | 0.0 | 0.1 | 4.43 | 0.4 | 38 |
| ***trans*-Azo2** | 53.1 | 94.7 | 2.71 | 0.0 | 0.0 | 3.98 | 1.0 | 21 |
| ***cis*-Azo2** | | | 2.75 | 0.0 | 0.1 | 4.42 | 0.2 | 42 |
| ***trans*-Azo3** | 49.2 | 97.3 | 2.73 | 0.0 | 0.0 | 4.00 | 1.1 | 27 |
| ***cis*-Azo3** | | | 2.82 | 0.0 | 0.1 | 4.38 | 0.4 | 39 |
| ***trans*-Azo4** | 64.7 | 46.8 | 2.78 | 0.0 | 0.0 | 3.89 | 0.9 | 32 |
| ***cis*-Azo4** | | | 2.84 | 0.0 | 0.6 | 3.85 | 0.1 | 14 |
| ***trans*-Azo5** | 33.9 | 111.5 | 2.64 | 0.1 | 0.0 | 4.22 | 1.2 | 18 |
| ***cis*-Azo5** | | | 2.87 | 0.0 | 0.1 | 4.41 | 0.2 | 34 |

[a] The difference in energy between the *cis* and *trans* isomers ($\Delta E_{trans\text{-}cis}$) and the minimum barrier height for the thermal *cis*→*trans* isomerization are given ($\Delta E^{\ddagger}_{cis\text{-}trans}$). [b] The excitation energy ($E_{exc}$), the oscillator strength of the 1P absorption process (f), and the absorption cross-section of the 2P absorption process ($\sigma_2$, in GM units) are given for the both isomers of each compound. [c] In all the cases, the lowest-energy barrier height for the thermal *cis*→*trans* isomerization was found to correspond to an inversion mechanism.

**Supplementary Table 2.** Theoretical results in water at the CAM-B3LYP/6-31G(d) level.

| | DFT [a] | | TDDFT [b] | | | | | |
|---|---|---|---|---|---|---|---|---|
| | $\Delta E_{trans\text{-}cis}$ | $\Delta E^{\ddagger}_{cis\text{-}trans}$ [c] | $S_0 \rightarrow S_1$ transition | | | $S_0 \rightarrow S_2$ transition | | |
| | (kJ mol$^{-1}$) | | $E_{exc}$ (eV) | f | $\sigma_2$ | $E_{exc}$ (eV) | f | $\sigma_2$ |
| ***trans*-Azo$^{MAG}$** | 58.3 | 117.4 | 2.77 | 0.0 | 0.0 | 3.44 | 1.4 | 0 |
| ***cis*-Azo$^{MAG}$** | | | 2.71 | 0.0 | 0.3 | 4.20 | 0.4 | 23 |
| ***trans*-Azo$^{MAG2p}$** | 61.4 | nd [d] | 2.85 | 0.0 | 0.0 | 3.15 | 1.4 | 56 |
| ***cis*-Azo$^{MAG2p}$** | | | 2.67 | 0.1 | - [e] | 3.82 | 0.5 | - [f] |
| ***trans*-Azo1** | 56.0 | 97.2 | 2.71 | 0.0 | 0.0 | 3.54 | 1.4 | 58 |
| ***cis*-Azo1** | | | 2.75 | 0.0 | 0.4 | 4.22 | 0.5 | 81 |
| ***trans*-Azo2** | 46.1 | 98.1 | 2.73 | 0.0 | 0.0 | 3.68 | 1.2 | 69 |
| ***cis*-Azo2** | | | 2.77 | 0.0 | 0.5 | 4.19 | 0.3 | 91 |
| ***trans*-Azo3** | 44.1 | 101.0 | 2.74 | 0.1 | 0.1 | 3.67 | 1.4 | 82 |
| ***cis*-Azo3** | | | 2.78 | 0.0 | 0.5 | 4.11 | 0.6 | 97 |
| ***trans*-Azo4** | 57.7 | 46.0 | 2.81 | 0.1 | 0.5 | 3.58 | 1.3 | 110 |
| ***cis*-Azo4** | | | 2.85 | 0.1 | 1.8 | 3.78 | 0.1 | 32 |
| ***trans*-Azo5** | 34.4 | 112.0 | 2.65 | 0.1 | 0.0 | 3.74 | 1.5 | 51 |
| ***cis*-Azo5** | | | 2.85 | 0.0 | 0.8 | 4.16 | 0.3 | 85 |

[a] The difference in energy between the *cis* and *trans* isomers ($\Delta E_{trans\text{-}cis}$) and the barrier height for the thermal *cis*→*trans* isomerization are given ($\Delta E^{\ddagger}_{cis\text{-}trans}$). [b] The excitation energy ($E_{exc}$), the oscillator strength of the 1P absorption process (f), and the absorption cross-section of the 2P absorption process ($\sigma_2$, in GM units) are given for both isomers of each compound. [c] In all the cases, the lowest-energy barrier height for the thermal *cis*→*trans* isomerization was found to correspond to an inversion mechanism. [d] Accurate description of the thermal isomerization barrier height would require inclusion of explicit water molecules in the calculation. [e] Calculation did not converge. [f] Calculation did not converge. From the $\sigma_2$ value computed in the gas phase and the equations given in reference 4 for the solvent dependence of $\sigma_2$, an estimate of the 2P absorption cross-section in water was made ($\sigma_2$ = 100 GM).

**Supplementary Table 3.** *Trans-cis* photoisomerization of **$MAG^{slow}_{2P}$** and **$MAG^{slow}_{2P\_F}$**.

| | DMSO | | | 99% PBS : 1% DMSO | | |
|---|---|---|---|---|---|---|
| | $\lambda^{abs}_{max,trans}$ (nm) | %*cis* PSS | $\Phi_{trans\text{-}cis}$ | $\lambda^{abs}_{max,trans}$ (nm) | %*cis* PSS | $\Phi_{trans\text{-}cis}$ |
| **$MAG^{slow}_{2P}$** | 367 | 72 | 0.20 | 351 | 71 | 0.13 |
| **$MAG^{slow}_{2P\_F}$** | 376 | 68 | 0.27 | 358 | 69 | 0.16 |
| **Azo1'** [a] | 369 | 75 | 0.25 | nd | nd | nd |
| **Azo2'** [a] | 378 | 66 | 0.29 | nd | nd | nd |
| **MAG** | nd | nd | nd | 361 | 70 | 0.18 |

[a] The photochemical properties of *trans*-**Azo1'** and *trans*-**Azo2'** were not determined in 99% PBS:1% DMSO because of the low solubility of these compounds in aqueous media.

**Supplementary Table 4.** *Cis-trans* photoisomerization of **$MAG^{slow}_{2P}$** and **$MAG^{slow}_{2P\_F}$.**

| | DMSO | | 99% PBS : 1% DMSO | |
|---|---|---|---|---|
| | %*trans* PSS | $\Phi_{cis\text{-}trans}$ | %*trans* PSS | $\Phi_{cis\text{-}trans}$ |
| **$MAG^{slow}_{2P}$** | 78 | 0.77 | 88 | 0.26 |
| **$MAG^{slow}_{2P\_F}$** | 69 | 0.81 | 80 | 0.26 |
| **Azo1'** | 75 | 0.79 | nd | nd |
| **Azo2'** | 63 | 0.62 | nd | nd |
| **MAG** | nd | nd | 91 | 0.30 |

[a] The photochemical properties of *cis*-**Azo1'** and *cis*-**Azo2'** were not determined in 99% PBS:1% DMSO because of the low solubility of these compounds in aqueous media.

**Supplementary Table 5.** Thermal stability of *cis*-**MAG$_{2P}^{slow}$** and *cis*-**MAG$_{2P_F}^{slow}$** at rt.

| | $\tau_{cis}$ (h) in DMSO | $\tau_{cis}$ (min) in 99% PBS:1% DMSO |
|---|---|---|
| **MAG$_{2P}^{slow}$** | 10 | 10.5 |
| **MAG$_{2P_F}^{slow}$** | 23 | 11.9 |
| **Azo1'** | 22.3 | nd |
| **Azo2'** | 29.3 | nd |
| **MAG** | nd | 25.5 [b] |

[a] The $\tau_{cis}$ values of **Azo1'** and **Azo2'** were not determined in 99% PBS:1% DMSO because of the low solubility of these compounds in aqueous media. [b] From reference 1.

**Supplementary Table 6.** Activation and deactivation lifetimes ($\tau_{ON}$, $\tau_{OFF}$).[a]

| | $\tau_{ON}$ (s) | $\tau_{OFF}$ (s) | *N* (cells) |
|---|---|---|---|
| **MAG** | 0.16 ± 0.01 | 0.22 ± 0.01 | 4 |
| **MAG$_{2P}^{slow}$** | 0.31 ± 0.02 | 0.35 ± 0.038 | 5 |
| **MAG$_{2P_F}^{slow}$** | 0.26 ± 0.03 | 0.27 ± 0.01 | 3 |

[a] Activation and deactivation lifetimes ($\tau_{ON}$, $\tau_{OFF}$) of GluK2-L439C conjugated to **MAG**, **MAG$_{2P}^{slow}$**, and **MAG$_{2P_F}^{slow}$**. The number of recordings from different cells used for averaging is indicated. In each recording, the calculated lifetimes were averaged from four photoswitching cycles (see Supplementary Figure 10).

**Supplementary Table 7.** Primers used for Gibson assembly in the construction of pNMSB18.

| | Primer sequence | Anneals |
|---|---|---|
| FW | GATAACATGGCAATTATTAAAGAGTTTATG | mCherry |
| RV | GATCGAATCGTCTCACAACTGATCC | mec-17p |
| FW | AGTTGTGAGACGATTCGATCATGAAGATTATTTCCCCAGTTTTAAG | LiGluR6Q |
| RV | TTAATAATTGCCATGTTATCGGTTTCTTTACCTGGCAAC | LiGluR6Q |

## Supplementary Methods

**Photochemical characterization of $MAG_{2P}^{slow}$ and $MAG_{2P\_F}^{slow}$:** All spectroscopic and photochemical experiments were carried out in HPLC- or spectroscopy-quality solvents and in Ar-degassed samples. Steady-state UV-vis absorption measurements were recorded on a HP 8453 spectrophotometer with temperature control. Isomerization quantum yields were determined relative to azobenzene in acetonitrile ($\Phi^{\pi\rightarrow\pi^*}_{trans\rightarrow cis,\ azobenzene}$ = 0.15[8] and $\Phi^{n\rightarrow\pi^*}_{cis\rightarrow trans,\ azobenzene}$= 0.46[8]). Different excitation sources were used in the photochemical experiments depending on the spectral requirements: a Xe lamp coupled to a spectrograph, the third harmonic of a ns-pulsed Nd:YAG laser ($\lambda_{exc}$ = 355 nm, Brilliant, Quantel), and cw DPSS lasers ($\lambda_{exc}$ = 405 nm, SciTec; $\lambda_{exc}$ = 473 nm, SciTec).

**Cell line and transfection:** HEK293 tsA201 cell line (SV40-transformed, Human Embryonic Kidney 293 cells) was maintained at 37 ºC in a 5% $CO_2$ humid incubator with Dulbecco's Modified Eagle Medium/Nutrient Mixture F-12 media (DMEM) (1:1, Invitrogen) supplemented with 10% Fetal Bovine Serum (FBS) and 1% Penicillin/Streptomycin. The expression plasmids for GluK2-L439C and GluK2-L439C-eGFP were kindly provided by Ehud Y. Isacoff (University of California) and subcloned as previously described.[9] Cells were transfected with pcDNA3-GluK2-L439C-eGFP for electrophysiology, co-transfected with pcDNA3-GluK2-L439C:GCaMP6s (1:1) for 1P calcium imaging, and with pcDNA3-GluK2-L439C-eGFP::RGECO1 (2:1) for 2P calcium imaging.
DNA–X-tremGENE 9 Transfection Reagent (Roche) mix was used following manufacturer's instructions with a Reagent:DNA ratio of 3:1. The mix was incubated for 20 min at room temperature, meanwhile cells were placed into a 6-multiwell plate at a density of $7.5\cdot10^5$ cells per well. After incubation, the mix was added dropwise into each well. The day after, cells were harvested with accutase (Sigma-Aldrich) and seeded onto 16-mm glass coverslips (Fisher Scientific) pretreated with poly-L-lysine (Sigma-Aldrich) to allow cell adhesion. Electrophysiologcal experiments were performed 24–48 h after transfection, with cells plated at low density. One-photon calcium imaging experiments were performed 48–72 h after transfection with cells plated on PLL-coverslips at high density. Two-photon calcium imaging experiments were performed 48 h after transfection with cells plated at high density on 25 mm diameter glass coverslips (Fisher Scientific) pretreated with PLL into a 6-multiwell plate.

**Conjugation of LiGluR with photoswitched tethered ligands:** All MAG-type compounds were stored at 10 mM in DMSO at –20 ºC. Before each experiment cells were incubated with one of the compounds for 10 min in the absence of light in an extracellular solution (ES) composed of (in mM): 140 NaCl, 1 $MgCl_2$, 2.5 KCl, 10 HEPES, 0.5 $CaCl_2$ and 10–20 glucose to fix osmolarity to 300 $mOsm\cdot kg^{-1}$, while pH 7.4 was adjusted with NaOH. For HEK cell line, **MAG**, $\mathbf{MAG_{2P}^{slow}}$, $\mathbf{MAG_{2P\_F}^{slow}}$ or $\mathbf{MAG_{2p}}$ were added at a concentration of 50 µM. After incubation, cells were washed three times with ES and incubated 10 min with 0.3 mg $mL^{-1}$ Concanavalin A (Sigma) -to block GluK2 desensitization- on an ES based on $NMDG^+$ (to avoid depolarization due to open LiGluRs, in mM): 110 NMDG+, 2.5 KCl, 1 $MgCl_2$, 10 HEPES, 10–20 glucose to fix osmolarity to 300 $mOsm\cdot kg^{-1}$, while pH 7.4 was adjusted with HCl. Before placing the coverslip to the recording chamber, cells were washed again three times with ES.

**Electrophysiology:** For one-photon stimulation, voltage-clamp recordings under whole-cell configuration were done using an EPC-10 amplifier and data at 10 kHz was acquired with amplifier's software Patch Master (HEKA). Bath solution was composed of (in mM): 140 NaCl, 1 $MgCl_2$, 2.5 KCl, 10 HEPES, 2.5 $CaCl_2$ and 10–20 glucose to fix osmolarity to 310 mOsm·kg$^{-1}$, while pH 7.42 was adjusted with NaOH. Borosilicate glass pipettes were pulled with a typical resistance of 4–6 MΩ for HEK293 cells. Pipette solution contained (in mM): 120 cesium methanosulfonate, 10 TEA-Cl, 5 $MgCl_2$, 3 $Na_2ATP$, 1 $Na_2GTP$, 20 HEPES, 0.5 EGTA; osmolarity was 290 mOsm·kg$^{-1}$ and pH 7.2 was adjusted with CsOH.
One-photon action spectrum characterization was done by illumination of the entire focused field using a Polychrome V monochromator (TILL Photonics) connected through the back port of an IX71 inverted microscope (Olympus) with a XLUMPLFLN 20XW x20/1 water immersion objective (Olympus). For automatically controlling wavelength, the monochromator was connected to the EPC-10 amplifier via Photochromic Manual Control (TILL Photonics) and controlled with the photometry module of Patch Master. During voltage-clamp recordings we applied a train of 1 s light-pulses at different wavelengths (for the whole action spectrum, we ranged wavelengths from 300 to 600 nm, with 10 nm steps) with 5 s delay between pulses in which light was switched to 500 nm for **MAG**, **MAG$_{2P}^{slow}$** and **MAG$_{2P_F}^{slow}$** (to close LiGluR) or 690 nm for **MAG$_{2p}$**. Light power density measured with a Newport 1916-C light meter after the objective was 22.0 μW mm$^{-2}$ for 380 nm, 45.9 μW mm$^{-2}$ for 460 nm and 47.4 μW mm$^{-2}$ for 500 nm.

**Calcium imaging with 1P stimulation:** Cells were imaged on an inverted fully motorized digital microscope (iMic 2000, Till Photonics) controlled with the Live Acquisition 2.1 software (Till Photonics). Images were acquired at room temperature with a UV Apochromat 40× oil objective lens (Olympus) with an imaging interval of 2 s. GCaMP6s was excited during 10 ms at 490 nm by using a Polychrome V light source (Till Photonics) equipped with a Xenon Short Arc lamp (Ushio) and a 505-nm dichroic beam splitter (Chroma Technology). Emission was filtered by a D535/40nm emission filter (Chroma Technology) and finally collected by a cooled CCD camera (Interline Transfer IMAGO QE, Till Photonics).
Addition of agonists was carried out by carefully pipetting 100 μl of a 3 mM glutamate stock solution directly into the accessory pool of the recording chamber (final concentration 300 μM). Cells with no response to free glutamate were excluded from the analysis.
Photoisomerization was achieved by illuminating the focused sample with flashes of violet (380 nm, 0.5 s duration) light for activation, and flashes of green (500 nm, 0.5 s duration) light for deactivation, using the same light source as for the dye excitation. Calcium imaging activation spectra at one-photon ranged from 280 to 480 increasing 20 nm at a time. Light flashes were nested in between GCaMP6s fluorescence measures keeping the frame rate. Photostimulation intervals lasted a total of 3.2 min for activation and 2.4 min for deactivation.

**Calcium imaging with 2P stimulation:** All two-photon experiments were performed in the Advanced Digital Microscopy Core Facility of IRB Barcelona with a SP5 spectral confocal multiphoton microscope (Leica) equipped with: a 405 nm cw diode laser, an Ar laser (514nm), and a pulsed broadband Ti:Sapphire laser (Mai Tai, Spectra-Physics,

Santa-Clara, CA-USA) which can be tuned from 710-990 nm (80 MHz repetition rate, 80 fs pulse). We used a 40x/1.25-0.75-NA Oil objective (HCX PL APO, Leica).
In HEK cell experiments, R-GECO1 was used as a $Ca^{2+}$ fluorescent indicator instead of gcamp6 because it does not absorb at 405 nm, the excitation wavelength used to test the 1P activity in the confocal multiphoton microscope employed. Imaging of R-GECO1 was done at was done at 561 nm (6.37 uW $\mu m^{-2}$) with a frame rate of 4 s, a minimal exposition time of 343 ms, and using bidirectional laser scanning at 400 Hz. Images were recorded with a HyD detector with a detection range from 569 to 648 nm, at 512x512 pixel resolution. Pinhole aperture was set at maximum (600 µm).
Photostimulation flashes were fit to keep imaging interval, and periods lasted in total 1 min. One-photon photostimulation was done at 405 nm (0.37 mW $\mu m^{-2}$), and two-photon stimulation was done at 780 nm (2.8 mW $\mu m^{-2}$). Back-photoisomerization was achieved at 514 nm (0.35 mW $\mu m^{-2}$). Inter-stimulus imaging periods lasted 1 min. Photostimulation was done at 256x256 resolution with bidirectional laser scan (400 Hz) by zooming in (x3) in the center of the image.
To characterize the wavelength dependence of two-photon LiGluR activation, we measured photoresponses at different wavelengths: from 720 nm to 840 nm for **$MAG^{slow}_{2P\_F}$**, and from 740 nm to 820 nm for **MAG** and **$MAG^{slow}_{2P}$**.
Imaging conditions were adjusted to obtain the best signal to noise ratio and minimal photobleaching of the sample during long temporal recordings. Wavelength, intensity and duration of the photostimulation intervals were adjusted to obtain optimal photoresponses with high reproducibility while keeping cell integrity

**Hippocampal slice culture and gene transfection:** All procedures were conducted in accordance with the European guidelines for animal care and use in research, and were approved by the Animal Experimentation Ethics Committee at the University of Barcelona (Spain). Hippocampal organotypic slice cultures were prepared from postnatal day 6-7 rats as described.[10] Slices were cultured at 35 ºC on interface membranes (Millipore) and fed with MEM media containing 20% horse serum, 27 mM D-glucose, 6 mM $NaHCO_3$, 2 mM $CaCl_2$, 2 mM $MgSO_4$, 30 mM HEPES, 0.01 % ascorbic acid and 1 µg/ml insulin. pH was adjusted to 7.3 and osmolality to 300-320 mOsm $kg^{-1}$. Slices were biolistically transfected (BioRad) after 5-7 DIV with GluK2-L439C-eGFP and RCaMP2a (Addgene) under CAG promoter as described.[11-12]

**PTL conjugation in hippocampal slice culture:** For hippocampal organotypic slice cultures, MAG or $MAG^{slow}_{2P\_F}$ were incubated at 250 µM in a 12-multiwell plate in artificial cerebrospinal fluid (ACSF) containing: 119 mM NaCl, 2.5 mM KCl, 3 mM $CaCl_2$, 0.2 mM $MgCl_2$, 26.2 mM $NaHCO_3$, 1 mM $NaH_2PO_4$ and 11 mM glucose, equilibrated with 5% $CO_2$/95% $O_2$. Three different steps of washout with fresh ACSF were done in different wells of the same plate, lasting 1 min, 5 min and 5 min. Afterwards, slices were placed on the recording chamber. Slices were maintained at room temperature (r.t., 25-27 °C) in a continuous perfusion of ACSF.

**Calcium imaging with 2P stimulation:** Time-lapse fluorescence imaging was carried out in the Advanced Digital Microscopy Core Facility of IRB Barcelona with a SP5 spectral confocal multiphoton microscope (Leica) equipped with a 405 nm cw diode laser, an Argon laser (488 and 514 nm), and a pulsed broadband Ti:Sapphire laser (Mai Tai, Spectra-Physics, Santa-Clara, CA-USA) which can be tuned from 710-990 nm (80

MHz repetition rate, 80 fs pulse). We used a 40x/1.25-0.75-NA Oil objective (HCX PL APO, Leica).
Imaging was performed at 8-15 DIV in pyramidal neurons co-expressing GluK2-L439C-eGFP and RCaMP2 in a single focused plane. Selected neurons presented healthy morphology and no signs of fluorescent aggregates.
Green and red fluorescent proteins were simultaneously excited at 488 nm for 343 ms, using bidirectional laser scanning at 400 Hz. Images were recorded with a resolution of 512x512, and with an imaging interval of 4 s. Green and red fluorescence were recorded with two different HyD detectors with a detection range from 500 to 550 nm and from 569 to 648 nm, respectively. Pinhole aperture was set at maximum (600 µm).
Whole field photostimulation flashes were fit to keep imaging interval, and periods lasted in total for 1 min. Photostimulation was done at 256x256 resolution with bidirectional laser scan. One-photon photostimulation was done at 405 nm (0.81 mW $\mu m^{-2}$), and two-photon stimulation at 780 nm (2.8 mW $\mu m^{-2}$). Back-photoisomerization was achieved at 514 nm (0.35 mW $\mu m^{-2}$). Inter-stimulus imaging periods lasted 1.5 min. Intensity and duration of the photostimulation intervals were adjusted to obtain the optimal photoresponse and reproducibility. At the end of each experiment we reconfirmed that the neuron kept its healthy morphology.

***C.elegans* nematodes and calcium imaging with 2P stimulation in vivo:** KG1180 [lite-1(ce314)X] worms were obtained from CGC and GN692 [ljSi123;lite-1(ce314)X] was a kind gift of Dr Miriam Goodman.[13] We generated strains MSB104 [mirEx22(mec-17p::iGluR6::mCherry;myo-2p::mCherry);ljSi123(mec-7p:GCaMP6s: :SL2::tagRFP);lite-1(ce314)X]. Standard nematode growth medium and conditions were used for *C. elegans* growth and maintenance.[14]

Molecular constructs pNMSB18 (mec-17p::LiGluR::mCherry::unc-54 3'UTR) were generated by Gibson assembly with the primers indicated in the table below. Transgenesis was performed according to standard methods for microinjection.[11] To generate MSB104 strain a DNA mix containing 50 ng/ul pNMSB18, 1.5 ng/ul myo-2p:mCherry and 50 ng/ul Plus DNA ladder as carrier was injected into the gonad of GN692 young adult worms. The Primers used for Gibson assembly in the construction of pNMSB18 are shown in Supplementary Table 7
$\mathbf{MAG}^{\mathbf{slow}}_{\mathbf{2P\_F}}$ was administered to the worms by microinjection into the body cavity. A 10 mM solution in 10% DMSO and M9 (22 mM KH2PO4, 42 mM $Na_2HPO_4$, 86 mM NaCl, 1 mM $MgSO_4$) was freshly prepared. Control group was performed microinjecting with vehicle (10% DMSO in M9). In the case of MSB104, Concanavalin A was also added to the injection mix at a final concentration of 0.3 mg/ml. After compound administration worms were allowed to recover for a minimum of one hour.

**Calcium imaging with 2P stimulation:** As mentioned above, time-lapse fluorescence imaging was carried out in the Advanced Digital Microscopy Core Facility of IRB Barcelona. We used a 63x/1.4-NA Oil objective (HCX PL APO, Leica).
Imaging was performed 4 h after compound injection in TRN neurons co-expressing GluK2-L439C-mCherry and GCaMP6s in a single focused plane. Neurons with healthy morphology and no signs of fluorescent aggregates were selected for photostimulation.
Green and red fluorescent proteins were simultaneously excited at 488 nm and 561 nm for 343 ms, using bidirectional laser scanning at 400 Hz. Images were recorded with a

resolution of 512x512 and a digital zoom of 4, with an imaging interval of 660 ms. Green and red fluorescence were recorded with two different HyD detectors with a detection range from 500 to 550 nm and from 569 to 648 nm, respectively. Pinhole aperture was set at ~500 µm.
Whole field photostimulation flashes were fit to keep imaging interval. Photostimulation was done at 256x256 resolution with bidirectional laser scan, with a digital zoom of 4. One-photon photostimulation was done at 405 nm (15 µW $\mu m^{-2}$), and two-photon stimulation at 780 nm (2.8 mW $\mu m^{-2}$). Back-photoisomerization was achieved at 514 nm (1.2 µW $\mu m^{-2}$). Intensity and duration of the photostimulation intervals were adjusted to obtain the optimal photoresponse and reproducibility. At the end of each experiment we reconfirmed that the neuron kept its healthy morphology.

**Data analysis and statistics:** Amplitude of LiGluR photocurrents were analyzed using IgorPro (Wavemetrics). Displayed whole-cell current traces have been filtered using the infinite impulse response digital filter from IgorPro (low-pass filter with cutoff of 50 Hz). The drift in current observed during light spectra recordings was corrected where appropriate with the IgorPro (WaveMetrics) software using a custom-made macro for drift correction.
1P and 2P calcium images were acquired with the Live Acquisition 2.1 software (Till Photonics) and stored by the Arivis Browser 2.5.5 (Arivis AG). These images were analyzed with ImageJ and the mean fluorescence value for each cell profile was calculated using the same software. The fluorescence signals were treated to obtain Δ*F*/*F* values according to:

$$\frac{\Delta F}{F} = \frac{F - F_0}{F_0} \quad (1)$$

where $F_0$ is each cell's average signal for the experiment's baseline and $F$ is the fluorescence signal upon stimulation. The resulting fluorescence ratios were analyzed in OriginLab. To obtain cell-averaged 1P action spectra, Δ*F*/*F* values were first normalized with respect to the maximum photoresponse obtained for each cell after perfusion of free glutamate at the end of the experiment. To obtain cell-averaged 2P action spectra, 2P Δ*F*/*F* responses were first normalized with respect to the 1P Δ*F*/*F* response at 405 nm for the same cell.

## Supplementary References


[1] Gorostiza, P., Volgraf, M., Numano, R., Szobota, S., Trauner, D. & Isacoff, E. Y. Mechanisms of photoswitch conjugation and light activation of an ionotropic glutamate receptor. *Proc. Natl. Acad. Sci. USA*, **104**, 10865-10870 (2007).

[2] Numano, R. et al. Nanosculpting reversed wavelength sensitivity into a photoswitchable iGluR. *Proc. Natl. Acad. Sci. U. S. A.* **106**, 6814–9 (2009).

[3] Reiner, A. & Isacoff, E. Y. Tethered ligands reveal glutamate receptor desensitization depends on subunit occupancy. *Nat. Chem. Biol.* **10**, 273-280 (2014).

[4] Murugan, N.A., Kongsted, J., Rinkevicius, Z., Aidas, K., Mikkelsen, K. V. & Agren, H. Hybrid density functional theory/molecular mechanics calculations of two-photon absorption of dimethylamino nitro stilbene in solution. *Phys. Chem. Chem. Phys.* **13**, 12506-12516 (2011).

[5] Gascón-Moya, M. et al. An optimized glutamate receptor photoswitch with sensitized azobenzene isomerization. *J. Org. Chem.* **80**, 9915-9925 (2015).

[6] Pearson, R. J., Kassianidis, E., Slawin, A. M. Z. & Philp, D. Self-replication vs. reactive binary complexes—manipulating recognition-mediated cycloadditions by simple structural modifications. *Org. Biomol. Chem.* **2**, 3434–3441 (2004).

[7] Carta, F., Maresca, A., Scozzafava, A. Vullo, D. & Supuran, C. Carbonic anhydrase inhibitors. Diazenylbenzenesulfonamides are potent and selective inhibitors of the tumor-associated isozymes IX and XII over the cytosolic isoforms I and II. *Bioorg. Med. Chem.* **17**, 7093-7099 (2009).

[8] Bortolus, P. & Monti, S. Cis-trans photoisomerization of azobenzene. Solvent and triplet donors effects. *J. Phys. Chem.* **83**, 648–652 (1979).

[9] Izquierdo-Serra M. et al. Two-photon neuronal and astrocytic stimulation with azobenzene-based photoswitches. *J. Am. Chem. Soc.* **136**, 8693-8701 (2014).

[10] Okamoto, K., Nagai, T., Miyawaki, A. & Hayashi, Y. Rapid and persistent modulation of actin dynamics regulates postsynaptic reorganization underlying bidirectional plasticity. *Nat. Neurosci.* **7**, 1104-1112 (2004).

[11] Bosch, M., Castro, J., Sur, M. & Hayashi, Y. Photomarking Relocalization Technique for Correlated Two-Photon and Electron Microcopy Imaging of Single Stimulated Synapses. *Methods Mol. Biol.* **1538**, 185-214 (2017).

[12] Bosch, M., Castro, J., Saneyoshi, T., Matsuno, H., Sur. M. & Hayashi, Y. Structural and molecular remodeling of dendritic spine substructures during long-term potentiation. *Neuron* **16**, 444-459 (2014).

[13] Nekimken, A. L., Mazzochette, E. A., Goodman, M. B. & Pruitt, B. L. Forces applied during classical touch assays for Caenorhabditis elegans. *PLoS One* **12**, 1–11 (2017).

[14] Stiernagle, T. Maintenance of C. elegans. *WormBook* 1–11 (2006). doi:10.1895/wormbook.1.101.1 .

[15] Evans, T. Transformation and microinjection. *WormBook* 1–15 (2006). doi:10.1895/wormbook.1.108.1 .

## CHAPTER 6| Nanoengineered light-harvested proteins for optogenetics and photopharmacology

Aida Garrido-Charles[1], Gisela Cabré[2], Marta Gascón-Moya[2], Jordi Hernando[2,*] & Pau Gorostiza[1,3,4,*]

[1] Institut de Bioenginyeria de Catalunya (IBEC), the Barcelona Institute of Science and Technology, Barcelona 08028, Spain.
[2] Departament de Química, Universitat Autònoma de Barcelona (UAB), Cerdanyola del Vallès 08193, Spain.
[3] Institució Catalana de Recerca i Estudis Avançats (ICREA), Barcelona 08010, Spain.
[4] Centro de Investigación Biomédica en Red en Bioingeniería, Biomateriales y Nanomedicina (CIBER-BBN), Zaragoza 50018, Spain.
[*] Corresponding authors. E-mails: jordi.hernando@uab.cat (J. H.), pau@icrea.cat (P. G.)

**ABSTRACT**

Chemical modification with nanometer precision can be used to probe and to improve the function of complex molecular entities, from organic materials to proteins and their assemblies. Using the pigment arrangement in photosynthetic light-harvesting as inspiration, we show that molecular photosensitizers can be located at well-defined distances from a photoisomerizable unit in order to enhance and spectrally shift its photoresponses. The approach is demonstrated in Channelrhodopsin-2 (ChR2) and in the light-gated ionotropic glutamate receptor (LiGluR), two archetypical actuators in optogenetics and photopharmacology that have been used both for fundamental and therapeutic purposes. These proof-of-concept experiments together with theoretical simulations predict that the photosensitivity can be increased several orders of magnitude using these means, thus providing a unique methodology to boost the performance of current optogenetic and photopharmacological toolboxes.

## INTRODUCTION

The function of most proteins and materials depends on the precise three-dimensional arrangement of their molecular components, including the chemical groups that conform catalytic sites(Ribeiro et al. 2018)) and drug binding pockets (Kufareva, Ilatovskiy, and Abagyan 2012), or that are involved in protein-protein interactions (Aloy and Russell 2006). Redox sites and photosynthetic pigments are disposed at well-defined orientations and nanometric separations (Figure 1a)(Noy, Moser, and Dutton 2006) which allow electron and energy transfer at optimized conditions. Chemical modification of proteins has been achieved by genetic engineering and synthetic biology (Gibney et al. 1998) mainly for the purpose of understanding their structure-function relationships, and has been largely based on natural amino acids and protein cofactors, and applied to relatively small proteins and complexes. However, direct chemical approaches provide higher versatility and can be applied to protein assemblies of any kind, potentially allowing to improve specific functional aspects.

In order to demonstrate this possibility, we focused on the amplification and spectral modification of the response of photoswitchable proteins. They lie at the core of optogenetics (Deisseroth 2011, 2015) and photopharmacology (Fehrentz, Schönberger, and Trauner 2011; Velema, Szymanski, and Feringa 2014), two rapidly evolving techniques that enable light-induced manipulation of cellular activity. Optogenetics takes advantage of the particular properties of Channelrhodopsins (ChRs) and other opsins, naturally photosensitive proteins found in microorganisms and vertebrates that are constituted by a seven transmembrane domain scaffold bearing a photoisomerizable retinal chromophore in its interior (Ernst et al. 2014) (Fig 1b, left). Microbial ChRs control diverse biological functions under visible light illumination and, upon expression in mammalian cells (e.g. neurons), allow their activity to be remotely triggered by irradiation (Deisseroth 2011, 2015). By contrast, photopharmacology makes use of synthetic photoswitches (typically, azobenzenes), which are chemically appended to biologically-active moieties (e.g. agonists, antagonists or blockers) (Fehrentz et al. 2011; Velema et al. 2014). In photoswitchable tethered ligands (PTLs), the resulting molecular structures are covalently anchored to natural (Bartels, Wassermann, and Erlanger 1971; Izquierdo-Serra et al. 2016) or engineered (Fehrentz et al. 2011) residues in proteins, thus endowing them with light-controlled activity reminiscent of optogenetic actuators. Several examples of PTLs have been reported to date (Hüll, Morstein, and Trauner 2018), which target a plethora of channels and receptors: Shaker voltage-gated potassium channel (SPARK), (Banghart M, Borges K, Isacoff E, Trauner D 2004), ionotropic glutamate receptor GluK2 (LiGluR) (Volgraf et al. 2006), acetylcholine receptor (LinAChR) (Tochitsky et al. 2012), $GABA_A$ receptors (LiGABARs) (Lin et al. 2014), metabotropic glutamate receptors (LimGluRs) (Levitz et al. 2013), and NMDA receptors (LiGluNs) (Berlin et al. 2016), among others.

Because of their ability to remotely photocontrol biological activity in spatiotemporal patterns, optogenetics and photopharmacology are applied in many different fields; for example, to investigate neural circuits (Förster et al. 2017) and behavioral patterns in animals (Caporale et al. 2011; Levitz et al. 2013; Szobota et al. 2007), to restore vision (Yue et al. 2016; Polosukhina et al. 2012) and hearing (Keppeler et al. 2018; Mager et al. 2018), to promote circuit formation in the olfactory bulb (Braubach et al. 2018), or pain inhibition (Iyer et al. 2016). However, many of these (and other) applications are ultimately hampered by the actual photochemical performance of optogenetic and photopharmacological actuators, which in turn depends on the properties of their photoswitchable molecular core (e.g. light wavelength and

intensity sensitivity, photoisomerization kinetics and efficiency, and thermal stability of the photoinduced state). Among them, much attention has been paid to tune the spectral response of these systems, aiming to achieve photostimulation with less phototoxic, more penetrating red and near-infrared radiation (NIR) and, even better, under multiphoton absorption to enhance excitation resolution(Cabré et al. 2019; Pittolo et al. 2019). In addition, broadening their action spectra will increase their sensitivity under white light illumination, a requirement for several therapeutic applications (e.g. vision restoration) because of the rather moderate absorptivities of their photochromes (typically, < 50000 $M^{-1}$ $cm^{-1}$ at $\lambda_{abs,max}$) (Carroll et al. 2015; Ernst et al. 2008). Unfortunately, such spectral manipulation is contingent on the discovery of new ChR variants or mutants (Klapoetke et al. 2014; Lin 2010) and the synthetic development of novel PTLs (Cabré et al. 2019; Carroll et al. 2015; Izquierdo-Serra et al. 2014; Kienzler et al. 2013), which is not orthogonal with ligand activity. Indeed, it may also cause undesired detrimental effects like lower temporal precision (Nagel et al. 2005) and slower kinetics (Bamann et al. 2010; Berndt et al. 2009) than ChR2; and reduced PTL-protein interaction (Izquierdo-Serra et al. 2014).

Alternative, simpler strategies are therefore demanded to tailor the photochemical behavior of optogenetic and photopharmacology tools without requiring direct modification of their photoswitchable core. Recently, this was achieved by injecting NIR-absorbing, blue-emitting upconverting nanoparticles into tissue, whose luminescence was employed to excite nearby ChRs (Ai et al. 2017; Bansal et al. 2016; Chen et al. 2018; Hososhima et al. 2015; Wu et al. 2016). However, the low upconversion efficiencies of these nanoparticles required high NIR irradiation power (~ W $cm^{-2}$) in order to stimulate optogenetic proteins.

To overcome this drawback while preserving the photochromic core of optogenetic and photopharmacology actuators, a fundamentally different approach is proposed herein, which is inspired from the exquisite behavior of light-harvesting complexes in photosynthetic chains. In these systems a network of spectrally-different, close-by chromophores (mainly, chlorophylls) are responsible for efficient sunlight absorption and energy transfer towards the reaction center, thus decisively contributing to the high efficacy of light-to-chemical energy conversion in photosynthesis (Fig. 1a) (Mirkovic et al. 2017). Actually, if sunlight excitation only occurred for the reaction-center chromophores, the rate of photon absorption under ambient irradiation conditions would be insufficient to trigger the multistep redox processes resulting in oxygen and carbohydrate production (Mirkovic et al. 2017). In this work we aim to bring the concept of photosynthetic light-harvesting into optogenetics and photopharmacology by decorating the vicinity of the photochromes in optogenetic and PTL-tagged proteins with photosensitizing chromophores (Fig. 1b). This should result in stronger and spectrally broader absorption of photons, thereby ensuring a larger supply of excitation to the photoswitchable units via energy transfer processes and, as such, enhanced light sensitivity. In particular, incoherent Förster-type resonant energy transfer (RET), one of the principal mechanisms involved in natural light-harvesting (Mirkovic et al. 2017), is to be exploited in this approach to funnel electronic excitation from the photosensitizing antennas (energy donors) to the protein photochromes (energy acceptors).

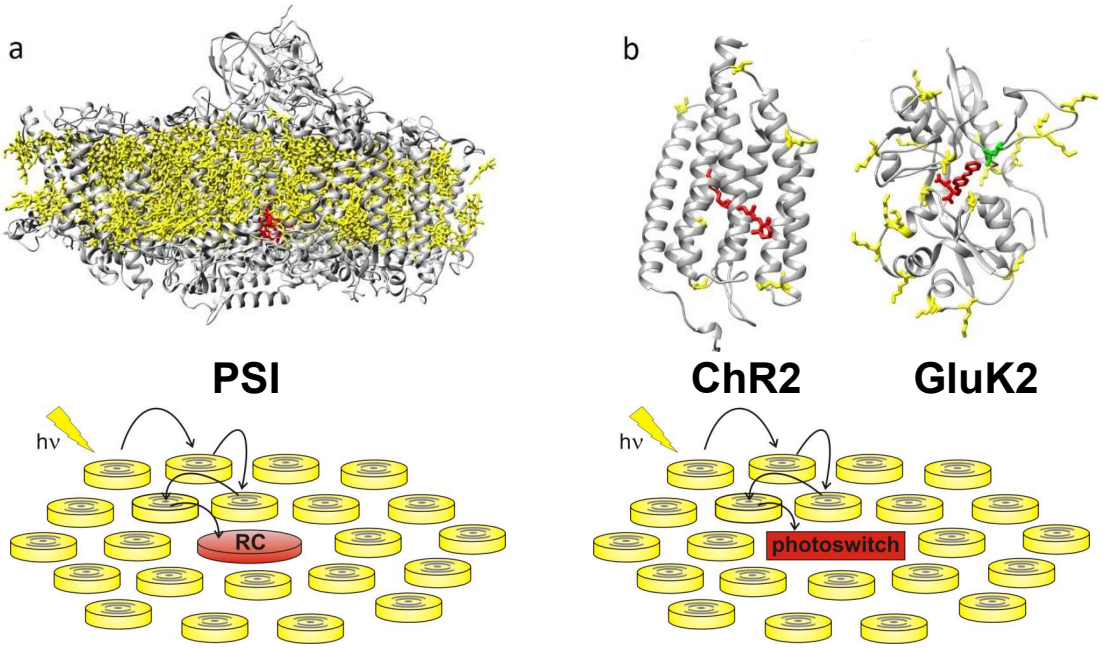


**Figure 1. Photosensitizing toolkit.** a) (top) 3D structure of photosystem I complex (PSI) in *Pisum sativum* and *Arabidopsis thaliana* (PDB 5L8R)(Mazor et al. 2017), one of the most well-studied photosynthetic systems. The reaction center (RC) composed of redox cofactors P700 and located inside the protein backbone is shown in red, while surrounding chlorophyll antennae are depicted in yellow. Maximum dimensions are 10 nm top to bottom and 16 nm across. (bottom) Upon photoexcitation of these moieties, electronic excited state energy is funneled towards RC via energy transfer processes, as shown in the cartoon. b) (top) 3D structures of ChR2 (PDB 6EID)(Volkov et al. 2017) and the ligand binding domain of GluK2 in complex with photochromic ligand GluAzo (PDB 4H8I)(Reiter et al. 2013), two paradigmatic examples of optogenetic and photopharmacological actuators. In LiGluR, a cysteine residue is genetically introduced at L439 of GluK2 (colored in green). The photoswitchable units of ChR2 and LiGluR are shown in red while natural lysine residues are highlighted in yellow. (bottom) Chemical functionalization of these nucleophilic residues with proper antennae (photosensitizers) should allow light-harvesting the photoisomerization reaction of their molecular photoswitches. Maximum dimensions of ChR2 are 7 nm top to bottom and 4 nm across, and LiGluR 6 nm top to bottom and 5 nm across.

## RESULTS

### Design of antenna-decorated optogenetic and photopharmacology actuators

To validate our strategy to manipulate light excitability in optogenetics and photopharmacology tools, we chose as benchmark systems two of the pioneering photoresponsive actuators used in these fields: Channelrhodopsin-2 (ChR2) (Nagel et al. 2003) and light-sensitive ionotropic glutamate receptor LiGluR (Volgraf et al. 2006), which rely respectively on *trans-cis* isomerizable all-*trans* retinal and azobenzene photoswitches (Fig. 1b and 2a). In both cases, expression of these proteins in cells enable reversible light-induced aperture of ion channels through the membrane, which result in ion flux between the extra- and intracellular media (Fig. S1). For LiGluR, different types of photoswitchable tethered ligands based on maleimide-azobenzene-glutamate triads (MAG, Fig 2a) have been reported, which are anchored to a cysteine residue engineered in position L439C of GluK2 (GluK2-L439C shown in green in Fig 1b top) (Hüll et al. 2018). Among them, compound $MAG_{2P}$ previously developed by

us was chosen in this study because of: (i) its absorption spectrum in the visible region, which resembles that of the ChR2 retinal chromophore (Fig. 2b) and accounts for the similar action spectra registered for ChR2 and LiGluR-$MAG_{2P}$ under one-photon excitation (Fig. S2); (ii) the short thermal lifetime of photoinduced *cis*-$MAG_{2P}$, which results in fast, sub-second deactivation of LiGluR-$MAG_{2P}$ upon cessation of light ($\tau_{off}$ = 150 ms) (Izquierdo-Serra et al. 2014), in a similar fashion to ChR2 ($\tau_{off}$ = 10-400 ms)(Nagel et al. 2003).

Efficient, RET-induced photosensitization of ChR2 and LiGluR-$MAG_{2P}$ requires proper selection of the light-absorbing antennae, which must be strongly fluorescent and show large emission overlap with acceptor absorption (Lakowicz 2006). This is the case of Alexa Fluor™ 350 (Alexa350), which was chosen as a proof-of-concept photosensitizing unit in this work (Fig. 2a-b). Our selection was further motivated by the dye's clear blue-shifted absorption relative to the photochromes in ChR2 and LiGluR-$MAG_{2P}$ (Fig. 2b), which should lead to an additional band in the action spectrum of these actuators under photosensitized operation. Another requisite must however be met for this behavior to be observed: nanometric donor-acceptor distances to favor energy transfer processes over the intrinsic radiative decay of the fluorescent antennae (Lakowicz 2006). In particular, they should be preferably lower than the Förster radius ($R_0$) for each donor-acceptor pair, which we estimated to be 5.2 and 4.5 nm for Alexa350-ChR2 and Alexa350-*trans*-$MAG_{2P}$, respectively (Table S1).

To introduce Alexa350 photosensitizing units in the close vicinity of the photochrome in ChR2 and LiGluR-$MAG_{2P}$, we relied on amino-functionalization of their natural lysine residues. Accordingly, we examined the location of such residues by analysis of the crystal structures of ChR2 (PDB 6EID) (Volkov et al. 2017) and of LiGluR in complex with photoisomerizable ligand GluAzo (PDB 4H8I) (Reiter et al. 2013). For ChR2, only 2 lysines were identified in the extracellular region of the protein that could be accessible to amino-reactive dye molecules for conjugation and are placed at short enough distances with respect to the retinal photoswitch for RET to take place (1.7 and 2.2 nm, Fig. 1b and 2c). In the case of LiGluR, a larger number of potential aminoacid residues for dye conjugation were found because its binding site domain is extracellular and contains up to 20 lysines (Fig. 1b). All of them sit at distances below $R_0$ for the Alexa350-$MAG_{2P}$ pair, thus favoring energy transfer processes between the antennae and the azobenzene-based PTL (Fig. 2c).

Functionalization of ChR2 and LiGluR-$MAG_{2P}$ was then attempted with the commercially available NHS ester of Alexa350. For ChR2, successful antenna conjugation was observed upon incubation of ChR2-YFP-expressing HEK cells with the dye of choice, which did not interfere with the regular light-induced behavior of the protein (see below). However, this was not the case for GluK2-L439C-dsRed2 expressed in HEK cells, where loss of LiGluR-$MAG_{2P}$ photoactivity was observed regardless of the functionalization conditions applied (Fig. S3). When attempting Alexa350 conjugation before $MAG_{2P}$ introduction, this was ascribed to undesired reaction between the NHS ester group of the dye and the thiol moiety of Cys439, which took place at our experimental conditions despite the lower reactivity described for cysteines over lysines with activated esters (Ward, Kleinman, and Nomura 2017). As a consequence, this prevented subsequent introduction of the PTL. On the other hand, when $MAG_{2P}$ was first conjugated, functionalization of its free amino group with Alexa350 destroyed the agonist character of the ligand and prevented binding. This effect could not be avoided when minimizing exposure of the

ligand to the solution by favoring the bound, *cis* state of LiGluR-$MAG_{2P}$ under UV illumination.

To overcome this difficulty, we devised a functionalization protocol that warranted orthogonal Alexa350-Lys and $MAG_{2P}$-Cys439 conjugation, and takes advantage of cysteine protection and deprotection strategies (Fig. 2d) (Albericio, Isidro-llobet, and Mercedes 2009; Islam, Berggren, and Larsson 1993; Rabanal, DeGrado, and Dutton 1996). In particular, we first incubated GluK2-L439C-dsRed2 expressing HEK cells with 2,2'-dithiobis(5-nitropyridine) (DTNP), which resulted in thiol oxidation and disulfide bond formation. Next, the dye molecules were tethered to lysines by reaction with Alexa350 NHS ester and cysteines were subsequently deprotected by reductive treatment with dithiothreitol (DTT). This exposed the free thiol of Cys439 that was finally conjugated by incubation with $MAG_{2P}$. To our knowledge, this constitutes one of the first examples of chemoselective functionalization of Lys and Cys in proteins (Luo et al. 2019), which enabled LiGluR-$MAG_{2P}$ labeling with photosensitizing antennae (Fig. S4) without detrimentally affecting its photoactivity (see below).

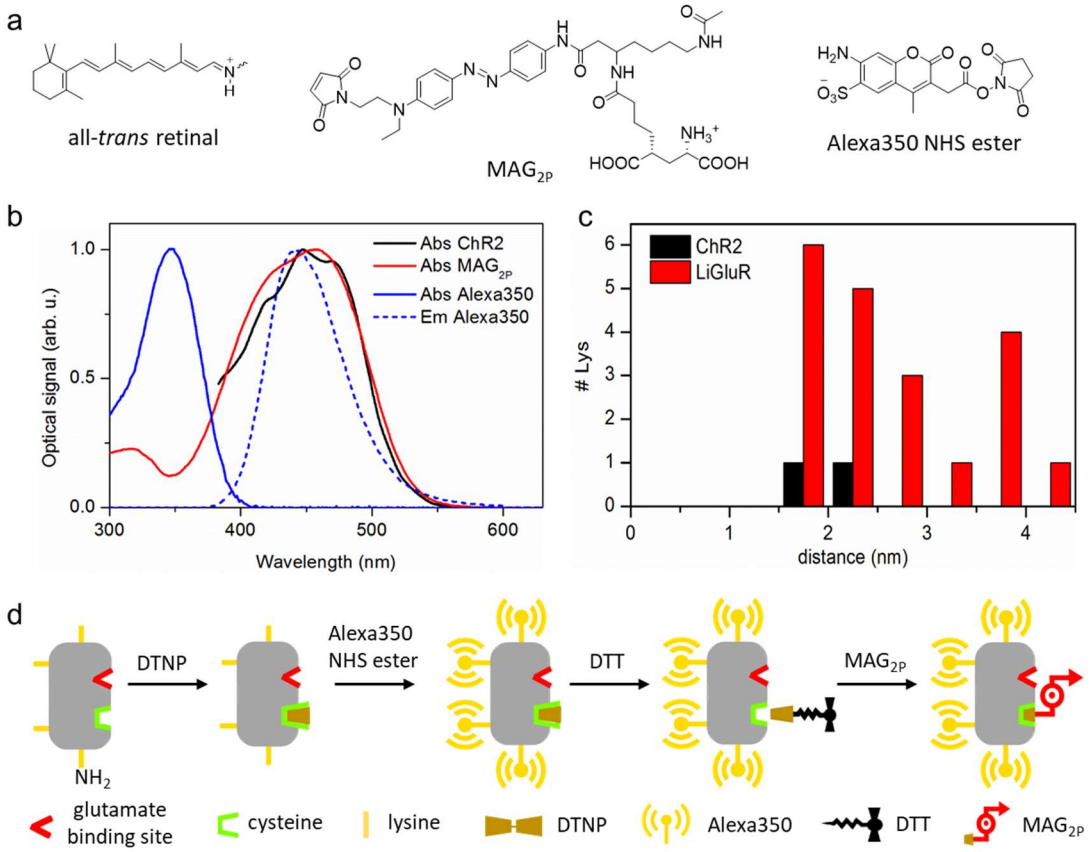


**Figure 2. Protein nanoengineering toolkit for photosensitized optogenetics and photopharmacology.** a) Chemical structures of the all-*trans* retinal photoswitch of ChR2, the azobenzene-based $MAG_{2P}$ photoswitchable tethered ligand of LiGluR, and fluorophore Alexa350. b) Absorption spectra of ChR2 (Verhoefen et al. 2010), $MAG_{2P}$ and Alexa350 as well as emission spectrum of Alexa350 ($\lambda_{exc}$ = 355 nm). All measurements taken in aqueous buffer. c) Histogram of separation distance between nanomodification sites (extracellular lysine residues) and photoswitch sites to be sensitized (black: all-*trans* retinal photoswitch of ChR2, crystal structure PDB 6EID(Volkov et al. 2017); red: Cys439 of LiGluR, crystal structure PDB 4H8I of GluK2 in complex with photoisomerizable ligand GluAzo (Reiter et al. 2013). d) Protocol followed for the orthogonal Alexa350-Lys and $MAG_{2P}$-Cys439 functionalization of the ligand binding domain of LiGluR: (i) protection of Cys439 thiol by disulfide formation with DTNP; (ii) conjugation

of Alexa350 NHS ester to Lys on the surface of the LBD; (iii) deprotection of Cys439 thiol with reducing agent DTT; (iv) functionalization of Cys439 with $MAG_{2P}$ by reaction with its maleimide group.

**Channelrhodopsin photosensitization**

To investigate photosensitization effects on optogenetic proteins, whole cell voltage clamp recordings of HEK cells transiently transfected with ChR2-YFP were conducted before and after incubation with Alexa350 NHS ester (1 mM). In both cases, strong inward photocurrents were elicited by light pulses (0.5 s) ranging from 300 to 600 nm, which were characterized by a fast signal transient followed by a plateau that remained constant till illumination was switched off (Fig. 3a). These are typical features of the regular electrophysiological behavior of ChR2 (Nagel et al. 2003), which do not only prove correct opsin expression in our cultured cells but also negligible impact of protein modification by Alexa350 conjugation. In spite of this, a small variation of ChR2 action spectrum was observed after incubation: significantly larger signals were registered in the 340-360 nm region, which corresponds to the absorption maximum of Alexa350 (see Fig. 2b) and, as such, can be attributed to photosensitization of all-*trans* retinal isomerization. Unfortunately, xenon lamp emission provides lower excitation intensities in this spectral range (top gray trace in Fig 3a), which therefore led to attenuated amplification effects in our raw electrophysiological data. Nonetheless, normalization of this data to equivalent light intensity over the 300-600 nm window unambiguously demonstrated the modification of the action spectrum of ChR2 due to light-harvesting by nearby fluorophores (Fig. 3b). This light-harvested channelrhodopsin (LH-ChR2) evidences the viability of our strategy to adjust the photosensitivity of optogenetic actuators without the need to mutating ChR2 or identifying new variants (Klapoetke et al. 2014).

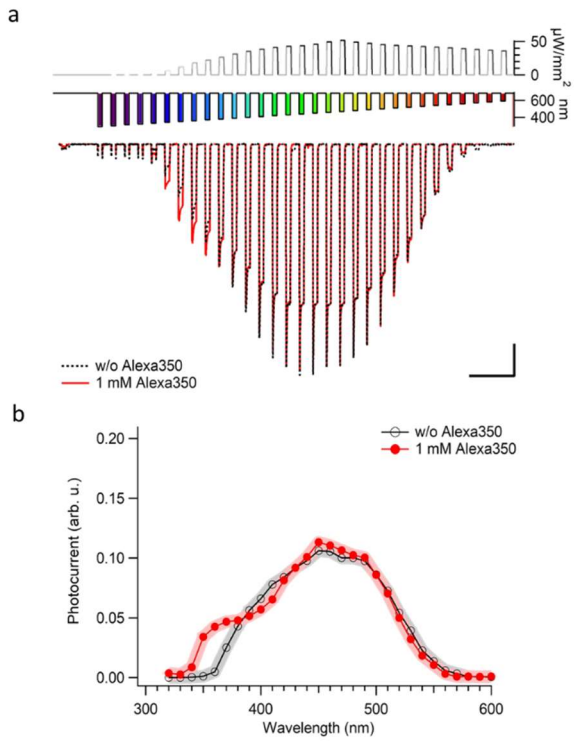


**Figure 3. Light-harvested ChR2 (LH-ChR2).** a) Wavelength-dependent whole-cell voltage-clamp currents

recorded in HEK293 cells expressing ChR2-YFP before and after incubation with 1 mM Alexa350 to photosensitize retinal. Excitation light pulses to induce channel opening ranged from 300 to 600 nm (0.5 s), while channel closure was accomplished thermally (1 s). Scale bar is 5 s and 34 pA (without Alexa350) and 48 pA (1 mM Alexa350). b) Action spectra (320-600 nm) determined for HEK293 cells expressing ChR2-YFP before (n=5) and after (n=5) incubation with Alexa350 (1 mM). Photocurrents were power-corrected to a nominal irradiation power density of 0.5 mW $cm^{-2}$. For the sake of comparison, both spectra were normalized to unit area for the 430-600 nm spectral range, where no photosensitization effects should be observed according to Alexa350 absorbance.

**LiGluR photosensitization**

In the case of ChR2 only moderate broadening of spectral sensitivity was accomplished by photosensitization with Alexa350, which we attribute to the low number of extracellular lysine anchoring points available in this protein. Accordingly, better results should be expected for LiGluR-$MAG_{2P}$, which offers multiple functionalization sites for the light-harvesting antennae in the nearby region around the azobenzene photoswitch. Whole cell voltage clamp recordings were therefore conducted for $MAG_{2P}$-tagged GluK2-L439C-dsRed2-expressing HEK cells with and without conjugation to Alexa350 (100 µM). In the presence of Concanavalin A (ConA) to inhibit receptor desensitization, similar inward photocurrents were measured in both cases, which decayed as soon as illumination ceased due to the short lifetime of *cis*-$MAG_{2P}$ (Fig. 4a). Consequently, this corroborates that modification of Lys around the binding site of the PTL-protein tether does not inhibit its photocontrolled activity. More interestingly, a significant expansion of the action spectrum of the antenna-functionalized system was observed between 340-390 nm, which became clearly bimodal after correcting for the wavelength-dependence of the photoexcitation intensity in our electrophysiological experiments (Fig. 4b). The high energy component of this spectrum nicely matches Alexa350 absorption (see Fig. 2b), which supports the assignment of these results to light-harvested $MAG_{2P}$ isomerization and LiGluR-$MAG_{2P}$ operation. Thus, we termed the resulting photoswitchable proteins as light-harvested LiGluRs (LH-LiGluRs). As anticipated, larger photosensitization effects were observed in this case relative to ChR2 and, indeed, photosensitized currents could be measured for LiGluR-$MAG_{2P}$ that are considerably higher than those elicited under direct irradiation of the photoswitchable tethered ligand. Thus, the photocurrent ratio registered for $\lambda_{exc}$ = 350 nm (i.e. at the absorption maximum of the photosensitizer) and $\lambda_{exc}$ = 450 nm (i.e. at the maximum of the intrinsic action spectrum of LiGluR-$MAG_{2P}$) noticeably augmented from $I_{350}/I_{450}$ = 0.12 in the absence of Alexa350 to $I_{350}/I_{450}$ = 1.32 after incubation with this dye.

Additional experiments were performed to further substantiate the stimulation of LH-LiGluR with $MAG_{2P}$. First, we tested incubation with different concentrations of Alexa350 (10 µM and 1 mM). Although no significant changes were observed by increasing Alexa350 concentration to 1 mM, a major loss of the photosensitization effect was encountered at $c_{Alexa350}$ = 10 µM (Fig. 4b). Therefore, this demonstrates that the intensity of the additional band observed in the action spectrum within the 340-390 nm range depends on the extent of the functionalization process of LH-LiGluR with Alexa350. Second, we replaced Alexa350 with a red-shifted dye that cannot transfer its electronic excitation energy to $MAG_{2P}$ due to the lack of spectral overlap (Texas Red NHS ester, Fig. S5a-b). After incubation with Texas Red, no appreciable photosensitization effects could be registered, which confirms that they rely on energy transfer processes (Fig. S5c-d). Finally, Alexa350-based photosensitization experiments were conducted on a new version of

$MAG_{2P}$ synthesized in our group: $MAG_{2P\_long}$, which presents a 4-aminoazobenzene core related to that of $MAG_{2P}$ and, as a consequence, similar photochemical properties in aqueous media and action spectrum after conjugation to LiGluR (Fig. S6a-c). However, $MAG_{2P\_long}$ lacks the *N*-butylacetamide side chain that $MAG_{2P}$ bears close to its glutamate unit, a structural variation introduced to favor the interaction with the binding site of LiGluR upon illumination. Actually, this should account for the larger electrophysiological signals measured using this compound for LH-LiGluR (~ 25% higher for $MAG_{2P\_long}$ than for $MAG_{2P}$ when compared to 300 µM free glutamate) with slower thermal deactivation kinetics ($\tau_{off}$ = 530 ms, Fig. S6d). These differences, however, did not prevent efficient sensitization of the photoactivity of LiGluR-$MAG_{2P\_long}$ with Alexa350 (Fig. 4c-d). As expected from the large Förster radius estimated for the Alexa350-*trans*-$MAG_{2P\_long}$ pair ($R_0$ = 4.7, Table S1), enhanced photocurrents were again registered for the 340-390 nm spectral range where the photosensitizer shows maximal absorption, whose intensity clearly correlated with the concentration of Alexa350 used for LH-LiGluR functionalization. In particular, the $I_{350}/I_{430}$ ratio increased from 0.11 to 0.95 after conjugation with $c_{Alexa350}$ = 1 mM, in a similar fashion to what was observed for LH-LiGluR with $MAG_{2P}$. Importantly, this provides unambiguous evidence that the photosensitized operation of LH-LiGluR is not restricted $MAG_{2P}$, but it can also be accomplished with other ligands as long as appropriate selection of the light-harvesting antennae is made on the basis of the photochemical properties of the PTL.

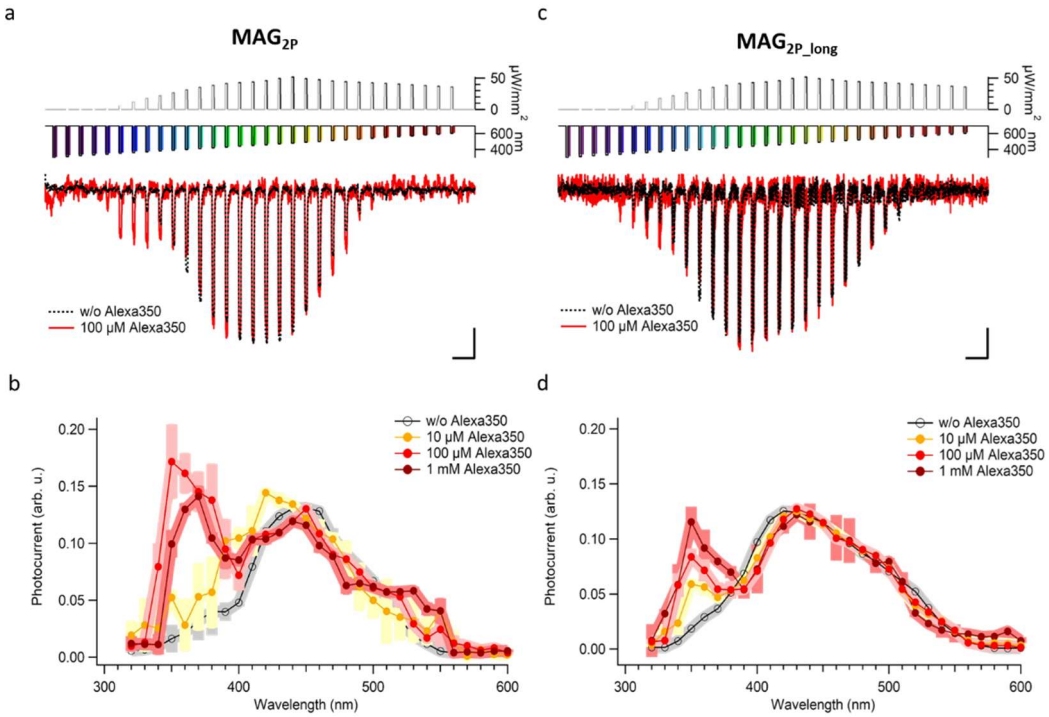


**Figure 4. Light-harvested LiGluR (LH-LiGluR).** a) Wavelength-dependent whole-cell voltage-clamp currents recorded in HEK293 cells expressing GluK2-L439C-dsRed2 and incubated with $MAG_{2P}$ (50 µM) before and after conjugation to Alexa350 (100 µM). Excitation light pulses to induce channel opening ranged from 300 to 600 nm (1 s), while channel closure was accomplished thermally (5 s). Scale bar is 10 s and 20 pA (without Alexa350) and 13 pA (100 µM Alexa350). b) Action spectra (320-600 nm) determined for HEK293 cells expressing GluK2-L439C-dsRed2 and conjugated to $MAG_{2P}$ (50 µM) after incubation with different Alexa350 concentrations (0, 10 µM, 100 µM and 1 mM) (n=3-7; 2; 3; 4, respectively). c) Wavelength-dependent whole-cell voltage-clamp currents recorded in HEK293 cells expressing GluK2-

L439C-dsRed2 and incubated with $MAG_{2P\_long}$ (50 μM) before and after conjugation to Alexa350 (100 μM). Scale bar is 10 s and 10 pA (without Alexa350) and 18 pA (100 μM Alexa350). d) Action spectra (320-600 nm) determined for HEK293 cells expressing GluK2-L439C-dsRed2 and conjugated to $MAG_{2P\_long}$ (50 μM) after incubation with different Alexa350 concentrations (0, 10 μM, 100 μM and 1 mM) (n=5; 4; 3; 3, respectively). For b) and d), photocurrents were power-corrected to a nominal irradiation power density of 0.5 mW $cm^{-2}$. For the sake of comparison, all spectra were normalized to unit area for the 430-600 nm spectral range, where no photosensitization effects should be observed according to Alexa350 absorbance. Errors in b) and d) are SEM.

**Simulations of photosensitization in LH-LiGluR**

Because of the larger photosensitized currents measured for LH-LiGluR, we took this system as a model to analyze the operation of light-harvested proteins based on theoretical simulations. In particular, we estimated the action spectra of LiGluR-$MAG_{2P}$ at different degrees of Lys functionalization with Alexa350, assuming that: (i) upon *trans* → *cis* photoisomerization, $MAG_{2P}$ binds to each of the subunits of the LiGluR homotetramer independently (Reiner and Isacoff 2014); (ii) the photocurrents elicited upon ligand interaction depend both on receptor occupancy (0, ~50, ~75 and 100% for 1, 2, 3 and 4 subunits of LiGluR simultaneously binding to $MAG_{2P}$) (Reiner and Isacoff 2014) and, since we blocked desensitization with ConA, on the lifetime of the LBD-*cis*-$MAG_{2P}$ complex; (iii) LiGluR shows ergodic behavior (Byrne 2014). Together, these conditions allow the probability of LiGluR-$MAG_{2P}$ interaction for a single protein subunit to be calculated by means of Monte Carlo simulations of its time evolution upon continuous illumination. In those simulations, we evaluated the efficiencies for all the possible processes that could induce $MAG_{2P}$ isomerization and, as a result, LBD-$MAG_{2P}$ complex formation and dissociation under our experimental conditions: direct photoisomerization by excitation of the *trans* or *cis* states, sensitized photoisomerization by excitation of Alexa350 chromophores followed by energy transfer to *trans*-$MAG_{2P}$ or *cis*-$MAG_{2P}$, and thermal *cis* → *trans* isomerization (see Methods for further details).

When these calculations were conducted for a $MAG_{2P}$-tagged LH-LiGluR receptor where all the 20 lysines of its LBD were functionalized with Alexa350, a dramatic light-harvesting effect was observed ($I_{350}/I_{450}$ = 132, Fig. S7). The intensity of the photosensitization component of the action spectrum of LiGluR-$MAG_{2P}$ steadily decreases with the number of conjugated chromophores and, according to these simulations, our experimental results registered at $c_{Alexa350}$ = 100 μM were consistent with a much lower number of light-harvesting antennae introduced (on average, ~ 1-2 Alexa350 molecules per LiGluR-$MAG_{2P}$ tether, Fig. S7). Although this should be taken as an approximate value given the assumptions made in our calculations, two main conclusions can be drawn from this result. First, it suggests incomplete and, probably heterogeneous, functionalization of the lysine residues of LH-LiGluR LBD, a quite common observation when labeling proteins with NHS esters in excess because of the different factors that affect the conjugation reaction (e.g. local pH)(Chen et al. 2012). Actually, we have observed a very low efficacy of the direct reaction of NHS esters with lysines near the binding site of glutamate receptors compared to the affinity assisted reaction (Izquierdo-Serra et al. 2016). In our case, it cannot be overlooked either that extensive LBD functionalization with photosensitizers may impose severe steric constraints to the posterior step of $MAG_{2P}$-Cys439 conjugation, thus disfavoring the formation of photoresponsive LiGluR-$MAG_{2P}$ tethers with high degree of Alexa350 labeling. In spite of all this, the fact that significant light-harvesting effects could be observed even under such moderate functionalization efficiencies further proves the

potential of photosensitization to amplify and extend the spectral response of photopharmacological and optogenetic actuators.

## DISCUSSION

We have described a procedure for light harvesting in photosensitive proteins by means of conjugating synthetic antenna molecules to nanometrically precise locations on the protein surface. Such direct and selective chemical modification enables nanoengineering the protein's structure and function. The procedure is relatively simple and can be scaled up, it is compatible with large proteins and complexes, and allows incorporating higher numbers of cofactors than protein maquettes (Gibney et al. 1998). Light-harvested stimulation of optogenetic and photopharmacology actuators aims at spectrally tuning the photoresponse of these systems without the need for mutagenesis or for replacing their photoswitchable chromophores with new compounds. Light sensitivity could also be substantially increased in this way, a requirement both for fundamental purposes (as intense illumination has been shown to damage neural tissue(Picot et al. 2018)) and for potential therapeutic applications (like enhancing photosensitivity in vision restoration procedures(Izquierdo-Serra et al. 2016)).

However, photosensitization efficacy is very dependent on a number of experimental parameters, as already suggested by the electrophysiological measurements and simulation data shown above. For this reason, a series of factors must be taken into consideration to accomplish optimal light-harvesting in optogenetics and photopharmacology.

First, the photochemical and thermal properties of the photoswitchable core of the optogenetic and photopharmacological actuators must be analyzed in detail. Ideally, it should present well-separated absorption spectra for its two states, thus allowing for selective photosensitization of the isomerization reaction that leads to receptor activation by modulating the spectral overlap with the molecular antennae. Unfortunately, most photochromes used in optogenetics and photopharmacology such as all-*trans* retinal and common azobenzenes do not fulfill this condition, and their *trans* and *cis* isomers typically absorb in the same spectral region. Consequently, both *trans* $\rightarrow$ *cis* and *cis* $\rightarrow$ *trans* reactions (i.e. receptor activation and deactivation) would be inevitably photosensitized, as it is the case for $MAG_{2P}$ ($R_0$ = 4.5 and 3.4 nm for the Alexa350-*trans*-$MAG_{2P}$ and Alexa350-*cis*-$MAG_{2P}$ pairs, Table S1). Although this did not prevent us from obtaining large photosensitized currents for LiGluR-$MAG_{2P}$ with Alexa350 dyes, the intensity of these signals could dramatically decrease if deactivation kinetics were highly accelerated by energy transfer from the antennae. Based on our simulations for the LiGluR-$MAG_{2P}$ system, we identified two main situations where this phenomenon could occur. On one hand, light-harvesting effects attenuated when increasing the excitation power density and, eventually, the photosensitized currents were predicted to be even lower than those evoked under direct irradiation of $MAG_{2P}$ (Fig. S8a). Under such high illumination intensities, the deactivation kinetics of LiGluR is no longer regulated by the short thermal stability of $MAG_{2P}$ as it occurs at low power densities ($\tau_{off} \sim 150$ ms at 0.5 mW $cm^{-2}$); instead, most *cis* $\rightarrow$ *trans* $MAG_{2P}$ isomerization proceeds through photosensitization within the 320-390 spectral range, which results in a dramatic decrease in $\tau_{off}$ and ultimately sets an upper limit to the photocurrents obtained under these irradiation conditions (e.g. $\tau_{off}$ = 0.47 ms at $\lambda_{exc}$ = 350 for 20 Alexa350 photosensitizers). A similar behavior was observed when $MAG_{2P}$-type ligands with equivalent

photochemical properties but increasing *cis* state lifetimes ($\tau_{cis}$) were considered in our simulations (Fig. S8b). Extending $\tau_{cis}$ favors photoinduced over thermal *cis* $\rightarrow$ *trans* back isomerization of the ligands even at low excitation power, which again leads to faster receptor deactivation and attenuation of the photocurrents evoked (e.g. $\tau_{off}$ =4.8 ms at 0.5 mW $cm^{-2}$ for a ligand with $\tau_{cis}$ = 1500 s surrounded by 20 Alexa350 molecules). Actually, this could account for the slightly lower photosensitization effects measured for LiGluR-$MAG_{2P\_long}$ with longer-lived receptor-ligand bound complexes (see Fig. 4), though other experimental conditions may also contribute to this result (e.g. variation in the photochemical properties of the azo core). In any case, our simulations indicate that to improve light-harvested stimulation of optogenetic and photopharmacological actuators bearing photoswitchable cores with nonresolvable absorption spectra for their two states, the following conditions are preferable: (i) low illumination intensities (ii) thermally fast relaxing photochromes, such as all-*trans* retinal in ChR2 or $MAG_{2P}$.

The choice of the molecular antennae is another key aspect to reach effective photosensitization. To favor resonance energy transfer towards their photoswitchable core, highly absorbing and emitting fluorophores are to be selected as photosensitizers, and more importantly, their emission should spectrally overlap with photochrome absorption. In practice, only fluorescent dyes absorbing in the same region as the photoswitch or showing blue-shifted absorption will meet the latter condition, which might be considered as a limitation of photosensitization for spectrally tuning the photoactivity of optogenetic and photopharmacological systems. However, two-photon sensitization of the isomerization of visible-light absorbing azobenzenes with near-infrared radiation has already been demonstrated(Izquierdo-Serra et al. 2014; Moreno et al. 2016), which opens the door to exploit the light-harvesting strategy introduced herein to boost the otherwise low-to-moderate multiphoton activity of common optogenetic and photopharmacological tools (Cabré et al. 2019; Carroll et al. 2015; Izquierdo-Serra et al. 2014; Prakash et al. 2012).

Finally, efficient photosensitization requires surrounding optogenetic and photopharmacology actuators with a large number of antennae at nanometric distances. Although this can be achieved by exploiting exposed lysine residues and efficient functionalization procedures, alternative methodologies might overcome some of the limitations uncovered by our work. On one hand, antennae-like residues could be genetically engineered at the desired locations in the receptor of interest, thus avoding posterior conjugation steps. This is the case of tryptophan, whose emission within the 300-450 nm spectral range could be used to photosensitize all-*trans* retinal or azobenzene isomerization under one-(Vivian and Callis 2001) or two-photon excitation(Lippitz et al. 2002). On the other hand, site-directed mutagenesis could alternatively be exploited to introduce additional accessible reactive residues around the photoswitchable core of the protein for subsequent labeling (e.g. lysines), which may be insufficient in the wildtype protein (e.g. in ChR2). This, together with the use of more efficient and selective tagging protocols(Chen et al. 2012; Luo et al. 2019), should allow the flexibility of chemical functionalization to be preserved while warranting profuse decoration of the photoactive domain of the receptor with photosensitizers. Under such circumstances, light-harvesting effects could enhance biological photoactivity up to several orders of magnitude, as predicted by our simulations.

**Acknowledgements**

We acknowledge financial support from MINECO/FEDER (projects CTQ2015-65439-R, CTQ2016-80066-R), AGAUR/Generalitat de Catalunya (CERCA Programme and projects 2017-SGR-00465 and 2017-SGR-1442), Human Brain Project WAVESCALES projects and Fundaluce foundation. A. G.-C. was supported by fellowship BES-2014-068169. G. C. acknowledges the Generalitat de Catalunya for her pre-doctoral FI grant. We are grateful to Prof. Ernest Giralt for helpful discussions on the in vitro cysteine protection procedure.

**Author contribution**

Jordi Hernando and Pau Gorostiza conceived and supervised the project. Aida Garrido-Charles performed in vitro experiments. Jordi Hernando performed theoretical simulations. Gisela Cabré and Marta Gascón performed chemical synthesis and photochemical characterization.

## METHODS

**Cell line and transfection**: HEK293 tsA201 cell line (SV40-transformed, Human Embryonic Kidney 293 cells) was maintained at 37 °C in a 5% $CO_2$ humid incubator with Dulbecco's Modified Eagle Medium/Nutrient Mixture F-12 media (DMEM) (1:1, Invitrogen) supplemented with 10% Fetal Bovine Serum (FBS, Biological Industries) and 1% Penicillin/Streptomycin (Sigma-Aldrich). The expression plasmids for ChR2 were kindly provided by Georg Nagel (University of Würzburg); in the case of GluK2-L439C and GluK2-L439C-eGFP, they were kindly provided by Ehud Y. Isacoff (University of California) and subcloned as previously described (Izquierdo-Serra et al. 2014). To avoid fluorophore crosstalk with eGFP, GluK2-L439C was also co-transfected with dsRed2 (Clontech) (2:1). Cells were transfected using DNA–XtremGENE 9 Transfection Reagent (Roche) mix as manufacturer's instructions recommend with a Reagent:DNA ratio of 3:1. The mix was incubated for 20 min at room temperature, while cells were placed into a 12-multiwell plate at a density of $4.5 \cdot 10^5$ cells per well. After incubation, the mix was added dropwise into each well. The day after, cells were harvested with accutase (Sigma-Aldrich) and seeded onto 16-mm glass coverslips (Fisher Scientific) pretreated with collagen (Sigma-Aldrich) to allow cell adhesion. Electrophysiological experiments were performed 24–48 h after transfection, with cells plated at low density.

**Conjugation of ChR2 with sensitizing fluorophores:** Cells were incubation with 100 μM Alexa Fluor™ 350 NHS Ester (Succinimidyl Ester) (A10168; ThermoFisher Scientific) for 10 min. Afterwards, coverslips were carefully rinsed with fresh bath solution composed of (in mM): 140 NaCl, 1 MgCl2, 2.5 KCl, 10 HEPES, 2.5 CaCl2 and 10–20 glucose to fix osmolarity to 310 mOsm $kg^{-1}$, and pH 7.42 adjusted with NaOH.

**Conjugation of LiGluR with photoswitched tethered ligands and sensitizing fluorophores**: $MAG_{2P}$ was previously synthesized by us (Izquierdo-Serra et al. 2014), while $MAG_{2P\_long}$ was prepared as described in the Supporting Information. All MAG-type compounds were stored at 10 mM in DMSO at –20 °C. Prior to each experiment, cells were incubated with $MAG_{2P}$ or $MAG_{2P\_long}$ (50 μM) to allow chemical conjugation with the receptor channel. In those cases where functionalization with sensitizing fluorophores was also required, a more elaborate

protocol was followed to achieve orthogonal fluorophore-Lys and $MAG_{2P}$-Cys439 conjugation: (i) incubation with DTNP (50 µM, Sigma) for 5 min; (ii) incubation with the NHS ester of the fluorophore of choice for 10 min at the desired concentration (10 µM, 100 µM, or 1 mM); (iii) incubation with DTT (50 µM, Sigma) for 5 min; (iv) incubation with $MAG_{2P}$ or $MAG_{2P\_long}$ (50 µM) for 10 min. Fluorophores tested were: Alexa Fluor™ 350 NHS Ester (Succinimidyl Ester) (A10168; ThermoFisher Scientific), Texas Red™-X, Succinimidyl Ester, mixed isomers (T6134, ThermoFisher Scientific). Afterwards, cells were incubated for 10 min with 0.3 mg $mL^{-1}$ Concanavalin A (Sigma) (to block GluK2 desensitization) on an bath solution based on NMDG+ (to avoid depolarization due to open LiGluRs, in mM): 110 NMDG+, 2.5 KCl, 1 $MgCl_2$, 10 HEPES, 10–20 glucose to fix osmolarity to 300 $mOsm \cdot kg^{-1}$, while pH 7.4 was adjusted with HCl. In between each step, coverslips were carefully rinsed with bath solution**.**

**Electrophysiology measurements:** Cells were mounted on the recording chamber continuously perfused with bath solution. Voltage-clamp recordings under whole-cell configuration were done using an EPC-10 amplifier and data at 10 kHz was acquired with amplifier's software Patch Master (HEKA). Cell membrane was held at -70 mV. Borosilicate glass pipettes were pulled with a typical resistance of 4–6 MΩ for HEK293 cells. Pipette solution contained (in mM): 120 cesium methanosulfonate, 10 TEA-Cl, 5 $MgCl_2$, 3 $Na_2ATP$, 1 $Na_2GTP$, 20 HEPES, 0.5 EGTA; osmolarity was 290 $mOsm \cdot kg^{-1}$ and pH 7.2 was adjusted with CsOH. Fast switching of solutions was done with a VC-6 six-channel valve controller (Warner Instruments Corp.). A solution of 300 µM of free glutamate was perfused to activate GluK2-L439C.

One-photon action spectrum characterization was done by illumination of the entire focused field using a Polychrome V monochromator (TILL Photonics) connected through the back port of an IX71 inverted microscope (Olympus) with a XLUMPLFLN 20XW x20/1 water immersion objective (Olympus). For automatically controlling the irradiation wavelength, the monochromator was connected to the EPC-10 amplifier via Photochromic Manual Control (TILL Photonics) and controlled with the photometry module of Patch Master. During voltage-clamp recordings we applied a train of light-pulses at different wavelengths (300-600 nm with 10 nm steps) of 0.5 s with 1 s delay between pulses for ChR2 or 1 s with 5 s delay for LiGluR. Between light pulses stimulation light was switched to 690 nm for not interfering with thermal back isomerization. Light power density measured with a Newport 1916-C light meter after the objective was 2.2 $mW \cdot cm^{-2}$ for 380 nm, 4.6 $mW \cdot cm^{-2}$ for 460 nm, and 4.7 $mW \cdot cm^{-2}$ for 500 nm.

To correct the action spectra obtained for the variation in light power density at each excitation wavelength, the following methodology was applied in each case. First, measurements were taken at different light attenuation values (0%, 40%, 70%, 90%, 97%, 99%) and the power-dependent photocurrents obtained were plotted separately for each excitation wavelength. A linear interpolation method was applied to this data to determine photocurrents for all the excitation wavelengths at a single power density value, thus obtaining a power-corrected action spectrum. As a power density value of reference we took 0.5 $mW \cdot cm^{-2}$, since this was the maximum power density achieved in our experimental setup in the UV tail of the spectral range. Actually, the data for $\lambda_{exc}$ = 300 and 310 nm was discarded because we could not even reach this minimum value of irradiation power density in our electrophysiology measurements. Finally, when plotting the corrected action spectra for distinct experimental conditions (e.g. with and without photosensitizers), different normalization criteria were used that are indicated in each

case (e.g. to the maximum spectral value, to the area for all the spectral range, to the area for the spectral range that is not affected by photosensitization).

**Estimation of Förster radii for energy donor-acceptor pairs:** To evaluate the efficiency of resonance energy transfer from excited photosensitizers (donor) to ground-state photoswitches (acceptor), we calculated the Förster radius ($R_0$) of each donor-acceptor pair of interest using equation S1 (Lakowicz 2006).

$$R_0 = \left(8.88\text{x}10^{-25} k^2 n^{-4} \Phi_D J\right)^{\frac{1}{6}} \quad (in\ cm) \qquad \text{(S1)}$$

The following parameters were used in these calculations: i) *J*, which is the spectral overlap integral between the absorption spectrum of the acceptor and the emission spectrum of the donor, was determined from the spectral data reported for ChR2 in aqueous buffer (HEPES) (Verhoefen et al. 2010) and measured by us for all the photosensitizers in aqueous buffer (PBS), for *trans*-$MAG_{2P}$ and *trans*-$MAG_{2P\_long}$ in aqueous buffer (PBS:DMSO 4:1), and for *cis*-$MAG_{2P}$ and *cis*-$MAG_{2P\_long}$ in DMSO; ii) $\Phi_D$, which is the fluorescence quantum yield of the photosensitizer donor, was taken to be 0.87 for Alexa350, as determined in PBS using 9,10-diphenylanthracene in cyclohexane as a reference (Brouwer 2011); iii) $k^2$= 2/3, since we assumed random orientation between donors and acceptors as an approximation; iv) $n$= 1.333, which is the refractive index of water. In this way, we obtained the $R_0$ values shown in Table S1. By introducing these parameters into equation S2 (Lakowicz 2006), we could estimate the efficiency of the RET process for each donor-acceptor pair separated by a certain distance *r*.

$$\text{E}= \frac{1}{1+\left(\frac{r}{R_0}\right)^6} \qquad \text{(S2)}$$

**Simulation of action spectra:** To calculate the action spectra of LiGluR-$MAG_{2P}$ with a variable number of surrounding photosensitizing units, the following principles were assumed: (i) photoisomerization into *cis*-$MAG_{2P}$ always leads to interaction with the LBD binging site; (ii) each of the subunits of the LiGluR homotetramer bind to $MAG_{2P}$ independently (Reiner and Isacoff 2014); (iii) the photocurrents elicited upon channel opening due to ligand interaction depend on receptor occupancy (0, ~50, ~75 and 100% for 1, 2, 3 and 4 subunits of LiGluR simultaneously binding to $MAG_{2P}$) (Reiner and Isacoff 2014); (iv) channel opening and photocurrent generation last until LBD-$MAG_{2P}$ complex dissociation by *cis* → *trans* isomerization, since ConA was used in our electrophysiological measurements to inhibit endogenous receptor desensitization; (v) as already described for nonfunctionalized ionotropic channels (Byrne 2014), the photoinduced operation of LiGluR-$MAG_{2P}$ is an ergodic process (i.e. the statistical properties of a single unit over time are the same as the statistical properties of an ensemble of channels at an instant of time); (vi) energy transfer processes only occur between the photosensitizers and photoswitches tethered to the same LBD of the LiGluR homotetramer, since the distance between adjacent LBD units (> 5 nm) is larger than the $R_0$ values computed. If these assumptions hold, single LBD-$MAG_{2P}$ complex formation and dissociation under illumination can be considered as stochastic processes controlled by the probabilities of $MAG_{2P}$ being in the active *cis* ($p_{cis}$) or inactive *trans* ($p_{trans}$, $p_{trans}$ = 1 - $p_{cis}$) states, and an estimate of the photocurrents

produced by the corresponding homotetramer can be obtained from these probabilities, the different conductance levels of the receptor depending on ligand occupancy(Reiner and Isacoff 2014), and the relative proportions of the five possible occupancy states (0, 1, 2, 3 or 4 subunits of LiGluR binding to $MAG_{2P}$) obtained from a binomial expansion:

$$\text{Photocurrent} \propto 6\, p_{cis}^2(1-p_{cis})^{\,2}\, 0.50 \;+\; 4\, p_{cis}^3(1-p_{cis})\, 0.75 \;+\; p_{cis}^4 \qquad \text{(S3)}$$

We then exploited the ergodic hypothesis to compute $p_{cis}$, for which we conducted Monte Carlo simulations of the time evolution of one single LBD-$MAG_{2P}$ construct when subjected to continuous irradiation at the excitation wavelength and power density of choice. In these simulations, we evaluated the probability densities of all the events that contribute to the isomerization of $MAG_{2P}$: (i) light absorption by *trans*-$MAG_{2P}$, *cis*-$MAG_{2P}$ or the photosensitizers, which depends on the absorptivity coefficients of each molecule at the excitation wavelength and the excitation power density selected; (ii) energy transfer for photosensitizer-*trans*-$MAG_{2P}$, photosensitizer-*cis*-$MAG_{2P}$, and photosensitizer-photosensitizer pairs, whose efficiency was computed from equation S2, the $R_0$ values previously estimated for all the possible donor-acceptor pairs (see Table S1), and assuming that the interchromophoric distances correspond to the separation distances between the lysine and cysteine residues to which the photosensitizers and $MAG_{2P}$ are tethered; (iii) isomerization of directly photoexcited or photosensitized *trans*-$MAG_{2P}$ and *cis*-$MAG_{2P}$, whose probability is defined by the photoisomerization quantum yields of these compounds ($\Phi_{trans\text{-}cis}$ = 0.39 and $\Phi_{cis\text{-}trans}$ = 0.52 as determined in DMSO using azobenzene as a reference (Cabré et al. 2019); (iv) thermal back isomerization of *cis*-$MAG_{2P}$ when tethered to LiGluR at the temperature of choice (298 K), to which we assigned the rate constant measured for the thermal deactivation of LiGluR-$MAG_{2P}$ channels (k = 6.67 $s^{-1}$) (Izquierdo-Serra et al. 2014). It must be noted that exciton annihilation processes arising from energy transfer between simultaneously excited photosensitizers and/or $MAG_{2P}$ were not taken into account because of the low power densities considered. With this data at hand and Monte Carlo random sampling, we evaluated the occurrence of light-induced and thermal $MAG_{2P}$ isomerization at each time step of our simulation, which allowed us finally obtaining a time trace of the variation between the two states of the system. Then, we calculated the total time spent by the system in the *trans*- and *cis*-$MAG_{2P}$ state to obtain $p_{cis}$. In our calculations, we used a time step of $10^{-5}$ - $10^{-4}$ s, which is much shorter than the thermal lifetime of *cis*-$MAG_{2P}$ ($\tau$ = 0.150 s) and the average time that takes between the absorption of consecutive photons by the $MAG_{2P}$-photosensitizer system. As for the total time of the simulation, it was set long enough (1 $10^4$ - 1 $10^6$ s) as to warrant statistically meaningful sampling over the *trans-cis* isomerization process for a single LBD-$MAG_{2P}$ tether (typically, more than $10^3$ isomerization events).

**SUPPLEMENTARY FIGURES & INFORMATION**

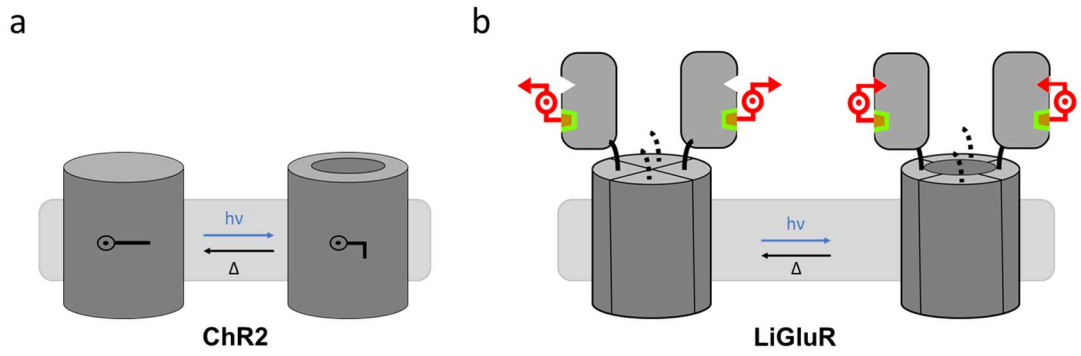


**Figure S1. Schematic operation of optogenetic and photopharmacological tools used for the control of neural function.** a) ChR2 is a microbial ion channel whose *trans*-retinal photoswitch modifies its configuration upon visible light illumination. This change opens the ion channel enabling the pass of ions through the membrane. Subsequent thermal *cis-trans* back-isomerization of the retinal switch allows the pore to close within 10-400 ms depending on the pH (Nagel et al. 2003). b) Ionotropic glutamate receptor GluK2 with a modification in position L439C (green) allows MAG-derivatives to be anchored to its ligand binding domain. The resulting light-sensitive receptor is called LiGluR. *Trans-cis* photoisomerization of the azobenzene core of MAGs (red) induces the interaction of the ligand (red triangle) with the binding site, which triggers an allosteric conformational change in the protein that opens its ion pore. In the case of $MAG_{2P}$ this process is induced by visible light (blue) and is spontaneously reversed on a sub-second scale.

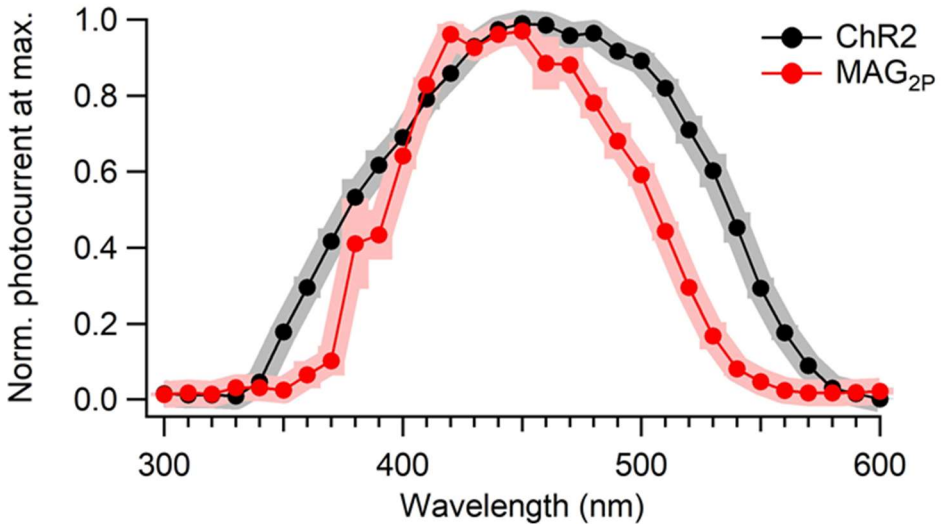


**Figure S2. Action spectra of ChR2 and $MAG_{2P}$-functionalized LiGluR.** Quantification of photocurrents recorded in HEK293 cells overexpressing ChR2-YFP (black, n=5) and GluK2-L439C-(eGFP or dsRed2) after conjugation to $MAG_{2P}$ (red, n=3-7). Light pulse stimulation is of 0.5 s for ChR2 or 1 s for $MAG_{2P}$-functionalized LiGluR and ranged from 300 to 600 nm in steps of 10 nm. Error bars are SEM.

**Table S1. Förster radii ($R_0$) for different acceptor-donor pairs.**

| Acceptor | Donor |
|---|---|
| | Alexa350 |
| ChR2 | 5.2 nm |
| *trans*-$MAG_{2P}$ | 4.5 nm |
| *cis*-$MAG_{2P}$ | 3.4 nm |
| *trans*-$MAG_{2P\_long}$ | 4.7 nm |
| photosensitizer (Alexa350) | 1.4 nm |

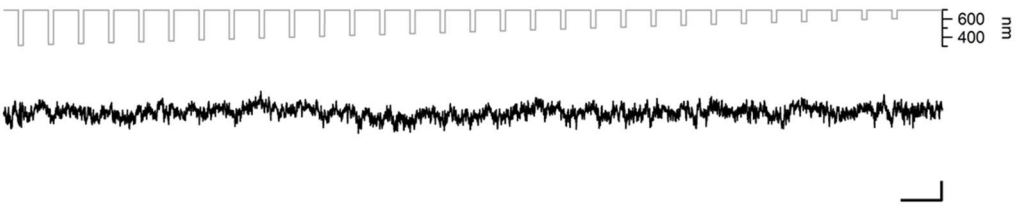


**Figure S3. Photosensitization of LiGluR–$MAG_{2P}$ without protecting conjugation strategy.** Wavelength-dependent whole-cell voltage-clamp currents recorded in HEK293 cells expressing GluK2-L439C-dsRed2 after conjugation to $MAG_{2P}$ (50 µM) followed by incubation with Alexa 350 (1 mM) under 430 nm illumination. Excitation light pulses to induce channel opening ranged from 300 to 600 nm (1 s), while channel closure was expected to occur thermally. Scale bar= 20 pA, 10 s.

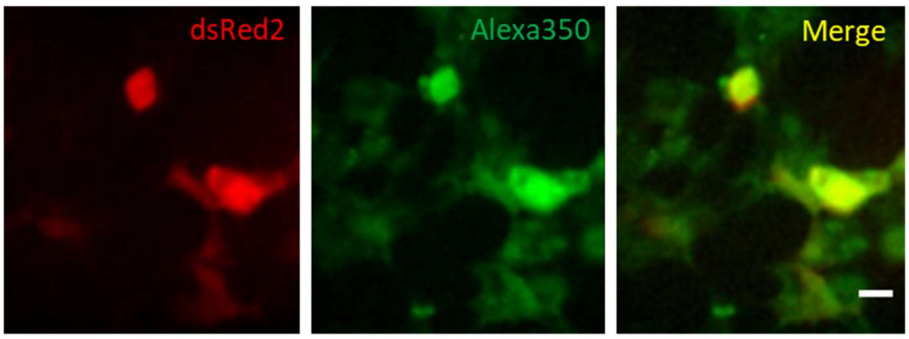


**Figure S4. Microphotograph of HEK293 cells expressing GluK2-L439C-dsRed2 (red) after conjugation to Alexa350 (green).** Scale bar = 20 µm.

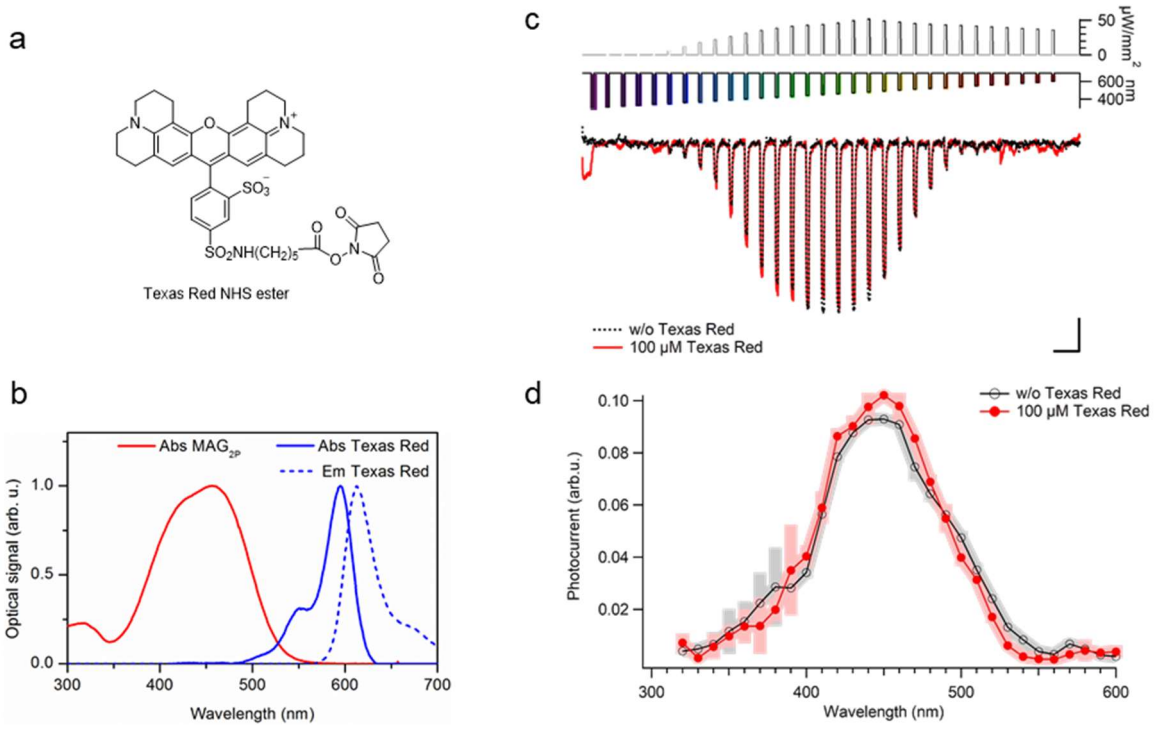


**Figure S5. LiGluR-MAG$_{2P}$ expressing cells incubated with a red-shifted dye.** a) Structure of the NHS ester of Texas Red (Texas Red) used for the functionalization of LiGluR. b) Absorption and emission spectra of MAG$_{2P}$ and Texas Red in aqueous buffer. c) Wavelength-dependent whole-cell voltage-clamp currents recorded in HEK293 cells expressing GluK2-L439C-eGFP and incubated with MAG$_{2P}$ (50µM) before and after conjugation to Texas Red (100 µM). Excitation light pulses to induce channel opening ranged from 300 to 600 nm (1 s), while channel closure was accomplished thermally (5 s). Scale bar is 10 s and 20 pA (w/o Texas Red) and 26 pA (100 µM Texas Red). d) Action spectra (320-600 nm) determined for HEK293 cells expressing GluK2-L439C-dsRed2 and incubated with MAG$_{2P}$ (50 µM) before and after conjugation to Texas Red (100 µM) (n=3). Photocurrents were power-corrected to a nominal irradiation power density of 0.5 mW cm$^{-2}$. For sake of comparison, both spectra were normalized to unit area for the whole spectral range. Error bars are ±SEM.

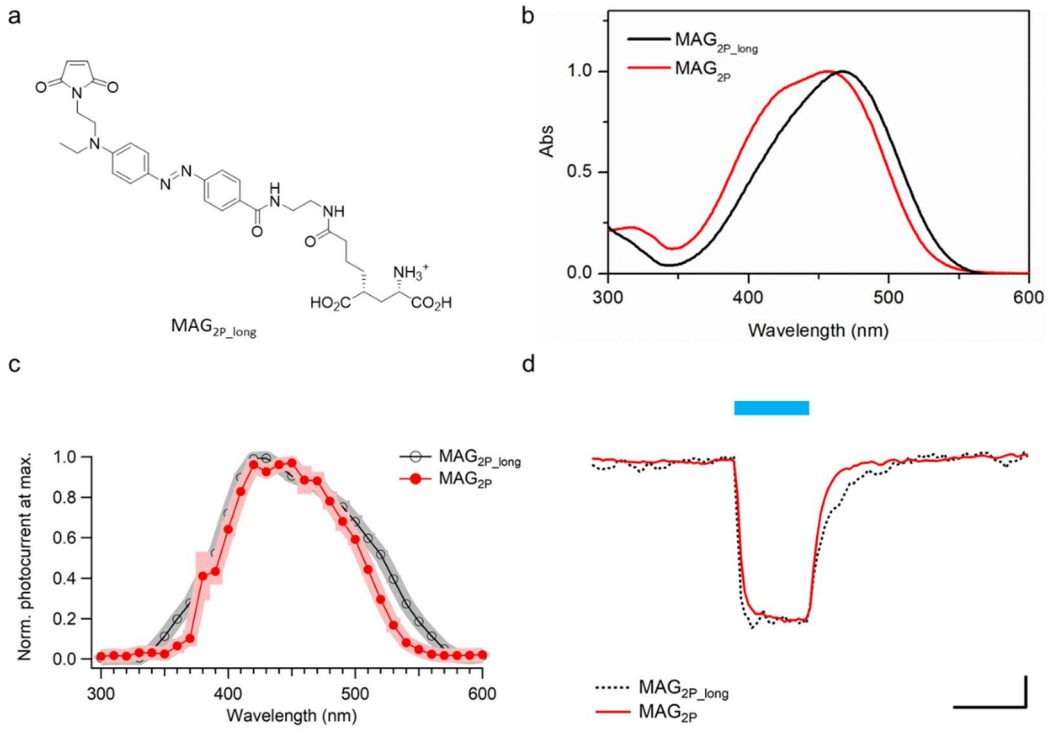


**Figure S6. $MAG_{2P\_long}$, a new version of $MAG_{2P}$.** a) Structure of $MAG_{2P\_long}$. The main structural differences relative to $MAG_{2P}$ are: (i) tethering of the amido substituent to the azobenzene core through its carbonyl group; (ii) lack of the *N*-butylacetamide side chain. b) Absorption spectra of $MAG_{2P\_long}$ (PBS:DMSO 99:1) and $MAG_{2P}$ (PBS:DMSO 4:1) in aqueous buffer. Because of its 4-aminoazobenzene photochrome, $MAG_{2P\_long}$ preserves the red-shifted absorption of $MAG_{2P}$ and its low *cis* thermal stability ($\tau_{cis}$ = 5.5 and 118 ms for $MAG_{2P\_long}$ and $MAG_{2P}$ in aqueous buffer at room temperature) with respect to regular azobenzenes. In addition, it shows similar photoisomerization quantum yields, as determined in DMSO using azobenzene as a reference ($\Phi_{trans\text{-}cis}$ = 0.10 and $\Phi_{cis\text{-}trans}$ = 0.47)(Cabré et al. 2019) c) Action spectra registered for HEK293 cells overexpressing GluK2-L439C-(eGFP or dsRed2) after conjugation to $MAG_{2P\_long}$ (n=5) and $MAG_{2P}$ (n=3-7). Light pulse stimulation is of 1 s and ranged from 300 to 600 nm in steps of 10 nm. Error bars are SEM. d) Comparison of the thermal deactivation kinetics of the photocurrents elicited in HEK293 cells overexpressing GluK2-L439C-(eGFP or dsRed2) after conjugation to $MAG_{2P\_long}$ and $MAG_{2P}$ by a pulse of light at 460 nm (1 s). Scale bar is 1 s and 9 pA ($MAG_{2P\_long}$) and 19 pA ($MAG_{2P}$). Although $MAG_{2P\_long}$ presents a less stable *cis* state in aqueous media, it leads to slower deactivation rates of LiGluR ($\tau_{off}$ = 530 and 150 ms for $MAG_{2P\_long}$ and $MAG_{2P}$, respectively). This is ascribed to a stronger binding to the LBD of GluK2, probably due to absence of the steric effects imparted by *N*-butylacetamide side chain of $MAG_{2P}$.

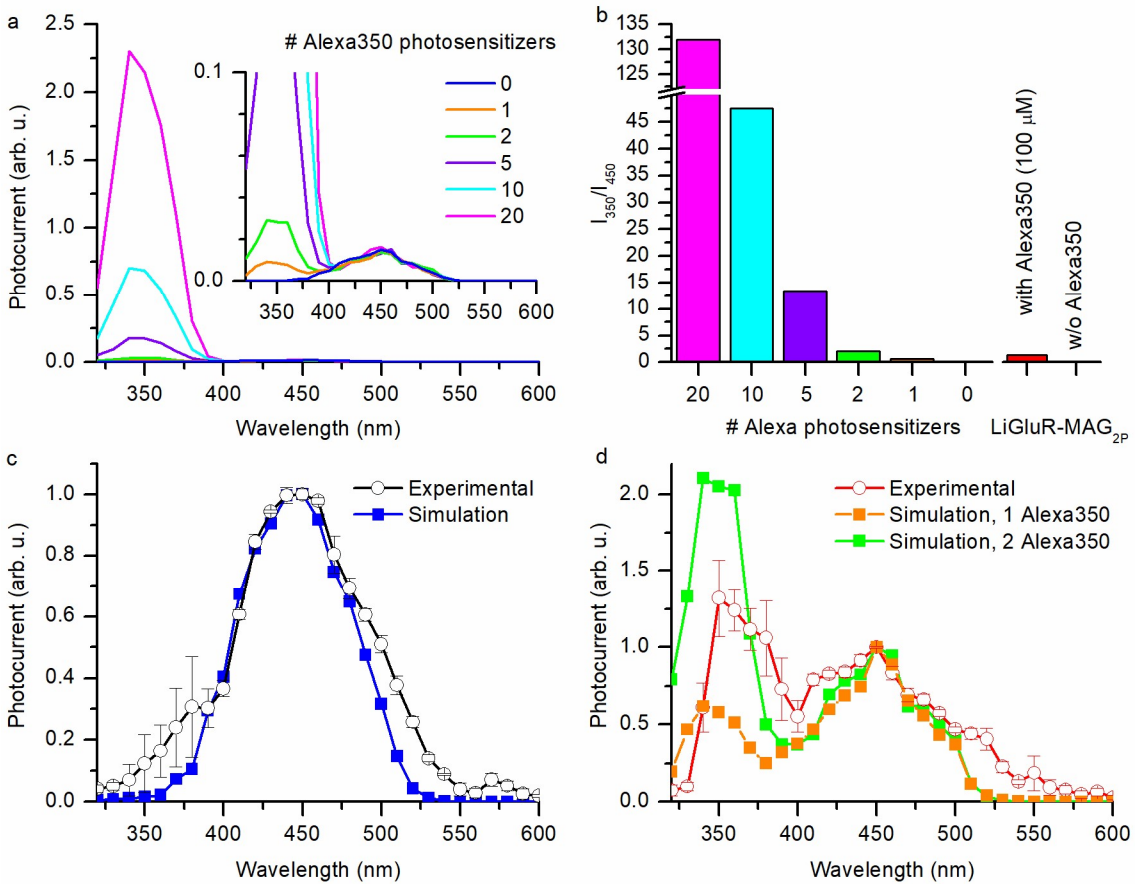


**Figure S7. Simulations of LiGluR-MAG$_{2P}$ photosensitization with Alexa350.** a) Photocurrents calculated for LiGluR-MAG$_{2P}$ functionalized with an increasing number of Alexa350 photosensitizers when subjected to constant illumination at 0.5 mW cm$^{-2}$. The inset shows a zoom-in of the signals estimated for the spectral range where photosensitizing does not take place (410-600 nm), which remain essentially constant with the number of Alexa350 molecules. b) $I_{350}/I_{450}$ photocurrent ratios estimated from the data at $\lambda_{exc}$ = 350 and 450 nm shown in a), which are compared to those experimentally determined for HEK293 cells expressing GluK2-L439C-dsRed2 and incubated with MAG$_{2P}$ (50 µM) before and after conjugation to Alexa350 (100 µM). c) Experimental and simulated action spectra for these cells at 0.5 mW cm$^{-2}$ before conjugation to Alexa350. For sake of comparison, both spectra were normalized to their spectral maxima. Error bars are SEM. d) Experimental and simulated (1 or 2 Alexa350 photosensitizers) action spectra for these cells at 0.5 mW cm$^{-2}$ after conjugation to Alexa350. For the sake of comparison, both spectra were normalized to the photocurrent at $\lambda_{exc}$ = 450 where photosensitization effects do not take place. Error bars are SEM.

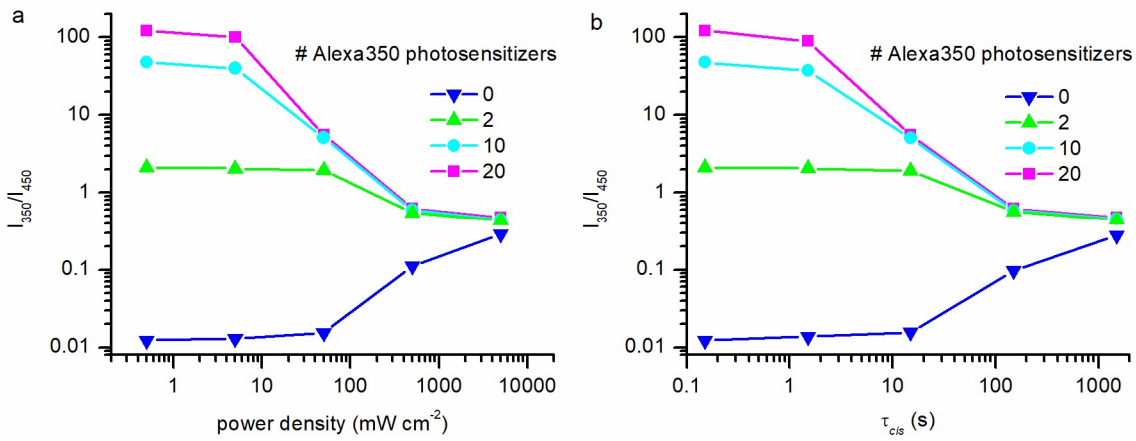


**Figure S8. Effect of power density and *cis* state thermal lifetime on LiGluR photosensitization.** a) $I_{350}/I_{450}$ photocurrent ratios estimated for LiGluR-$MAG_{2P}$ from simulations conducted at different excitation power densities (0.5, 5, 50, 500 and 5000 mW cm$^{-2}$) for a variable number of Alexa350 photosensitizers (0, 2, 10 and 20). b) $I_{350}/I_{450}$ photocurrent ratios estimated for LiGluR from simulations conducted for $MAG_{2P}$-type ligands with tunable *cis* state thermal lifetimes (0.150, 1.50, 15.0, 150, 1500 s), at 0.5 mW cm$^{-2}$ and for a variable number of Alexa350 photosensitizers (0, 2, 10 and 20).

## Experimental procedure for the synthesis of $MAG_{2P\ long}$

***Materials and methods:*** Commercially available reagents were used as received. Solvents were dried by distillation over the appropriate drying agents. All reactions were monitored by analytical thin-layer chromatography (TLC) using silica gel 60 precoated aluminum plates (0.20 mm thickness). Flash column chromatography was performed using silica gel (230-400 mesh). $^{1}H$ NMR and $^{13}C$ NMR spectra were recorded at 250 or 400 MHz and 100.6 MHz, respectively. Proton chemical shifts are reported in ppm (δ) ($CDCl_3$, δ 7.26 or DMSO-$d_6$, δ 2.50). Carbon chemical shifts are reported in ppm (δ) ($CDCl_3$, δ 77.16 or DMSO-$d_6$, δ 39.5). NMR signals were assigned with the help of COSY, HSQC, HMBC and DEPT135. Infrared peaks are reported in $cm^{-1}$. Melting points were determined on hot stage and are uncorrected. HRMS were recorded using electron ionization (EI) or electrospray ionization (ESI). Optical rotations were measured at 20 ± 3 °C.

***Synthesis of* $MAG_{2P\_long}$*:*** The synthesis of $MAG_{2P\_long}$ proceeded as follows.

**10-oxa-4-azatricyclo[5.2.1.$0^{2,6}$]dec-8-ene-3,5-dione, 3**

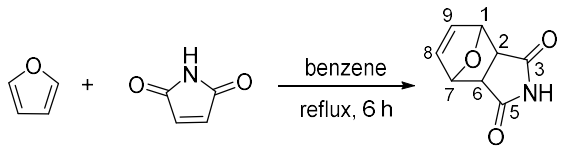


1 2 3

Furan (**1**, 374 µL, 5.14 mmol) and maleimide (**2**, 500 mg, 5.15 mmol) were dissolved in benzene (4.8 mL) in a sealed tube, and then heated at 90-100 °C for 6 h. The furan-masked maleimide precipitated after cooling the mixture down to rt. Then, the product was filtered and washed with cool $Et_2O$ (3 x 5 mL) to remove unreacted maleimide, affording **3** (511 mg, 3.09 mmol, 60% yield) as a white powder. The NMR spectra indicate that the product is exclusively the *exo* isomer. $^{1}H$ NMR (250 MHz, $CDCl_3$): δ 7.87 (br s, 1H, NH), 6.52 (t, $J_{9,1} = J_{8,7} = 0.9$ Hz, 2H, H-9, H-8), 5.32 (t, $J_{1,9} = J_{7,8} = 0.9$ Hz, 2H, H-1, H-7), 2.89 (s, 2H, H-2, H-6).

**4-{2-[ethyl(phenyl)amino]ethyl}-10-oxa-4-azatricyclo[5.2.1.$0^{2,6}$]dec-8-ene-3,5-dione, 4**

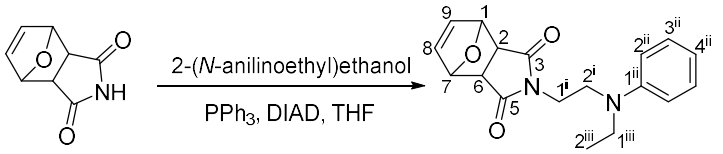


3 4

To an ice-cooled solution of compound **3** (110 mg, 0.67 mmol), 2-(*N*-anilinoethyl)ethanol (83.8 mg, 0.51 mmol), $PPh_3$ (165 mg, 0.63 mmol) in anhydrous THF (10.7 mL), and DIAD (0.13 mL, 0.66 mmol) were added dropwise during a period of 10 minutes. The reaction mixture was stirred overnight at rt. The resulting solution was concentrated under vacuum and the residue obtained was purified by column chromatography (hexane/EtOAc, 1:1) to furnish **4** (143 mg, 0.46 mmol, 91% yield) as a beige solid. Mp = 75-77 °C (from hexane/EtOAc); $^{1}H$ NMR (400 MHz, $CDCl_3$): δ

7.23 (dd, $J_{3^{ii},2^{ii}}$ = 8.8 Hz, $J_{3^{ii},4^{ii}}$ = 7.2 Hz, 2H, H-3$^{ii}$), 6.78 (d, $J_{2^{ii},3^{ii}}$ = 8.8 Hz, 2H, H-2$^{ii}$), 6.66 (t, $J_{4^{ii},3^{ii}}$ = 7.2 Hz, 1H, H-4$^{ii}$), 6.49 (t, $J_{8,7} = J_{9,1}$ = 1.2 Hz, 2H, H-8, H-9), 5.25 (t, $J_{7,8} = J_{1,9}$ = 1.2 Hz, 2H, H-1, H-7), 3.66 (m, 1H, H-1$^{i}$), 3.45 (m, 1H, H-2$^{i}$), 3.38 (q, $J_{1^{iii},2^{iii}}$ = 7.0 Hz, 2H, H-1$^{iii}$), 2.72 (s, 2H, H-2, H-6), 1.16 (t, $J_{2^{iii},1^{iii}}$ = 7.0 Hz, 3H, H-2$^{iii}$); $^{13}$C NMR (100.6 MHz, $CDCl_3$): δ 176.3 (C-3, C-5), 147.6 (C-1$^{ii}$), 136.6 (C-8, C-9), 129.5 (C-3$^{ii}$), 116.4 (C-4$^{ii}$), 112.3 (C-2$^{ii}$), 80.9 (C-1, C-7), 47.6 (C-2, C-6), 46.9 (C-2$^{i}$), 44.7 (C-1$^{iii}$), 36.3 (C-1$^{i}$), 12.5 (C-2$^{ii}$); IR (ATR): 3245, 3015, 2976, 1768, 1695, 1506, 1395, 1177 cm$^{-1}$; HRMS (HR-EI) calcd. for [$C_{18}H_{20}N_2O_3$]: 312.1474; found: 312.1466. COSY, DEPT 135 and $^{1}$H/$^{13}$C correlation were recorded.

**4-((*E*)-{4-[[2-(3,5-dioxo-10-oxa-4-azatricyclo[5.2.1.0$^{2,6}$]dec-8-en-4-yl)ethyl](ethyl)amino]phenyl}diazenyl)benzoic acid, 7**

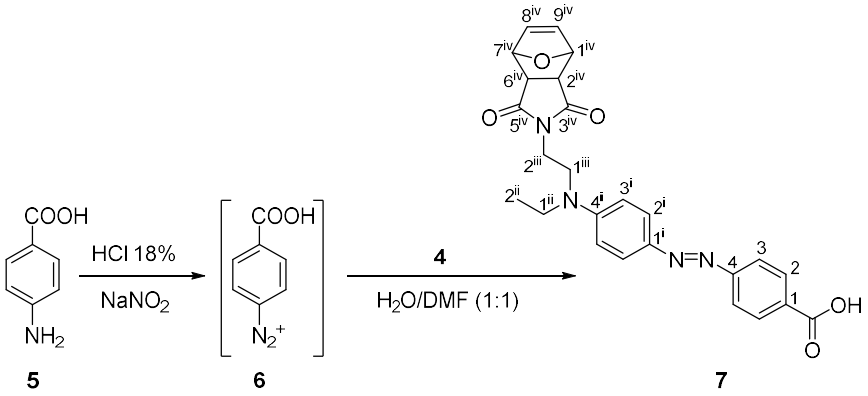


**5** **6** **7**

To an ice-cooled suspension of 4-aminobenzoic acid (**5**, 87.9 mg, 0.64 mmol) in HCl 18% (0.64 mL), an aqueous solution of $NaNO_2$ (0.27 mL, 78.2 µmol) was slowly poured. The resulting mixture was let stir for 30 minutes. Afterwards, it was added dropwise to an ice-cooled solution of **4** (202 mg, 645 µmol) in $H_2O$/DMF (1:1, 1.3 mL). The reaction mixture was stirred overnight at 4 °C. The dark red precipitate formed was filtered and washed with $Et_2O$/hexane (1:1) to afford **7** (140 mg, 304 µmol, 47% yield) as a dark red solid. Mp = 215-220 °C (from $Et_2O$/hexane); $^{1}$H NMR (250 MHz, DMSO-$d_6$): δ 8.08 (d, $J_{2,3}$ = 8.8 Hz, 2H, H-2), 7.84 (d, $J_{3,2}$ = 8.7 Hz, 2H, H-3), 7.83 (d, $J_{2^{i},3^{i}}$ = 9.3 Hz, 2H, H-2$^{i}$), 6.89 (d, $J_{3^{i},2^{i}}$ = 9.3 Hz, 2H, H-3$^{i}$), 6.49 (t, $J_{8^{iv},7^{iv}} = J_{9^{iv},1^{iv}}$ = 0.9 Hz, 2H, H-8$^{iv}$, H-9$^{iv}$), 5.16 (t, $J_{7^{iv},8^{iv}} = J_{1^{iv},9^{iv}}$ = 0.9 Hz, 2H, H-1$^{iv}$, H-7$^{iv}$), 3.59 (m, 2H, H-2$^{iii}$), 3.48 (m, 4H, H-1$^{ii}$, H-1$^{iii}$), 2.93 (s, 2H, H-2$^{iv}$, H-6$^{iv}$), 1.13 (t, $J_{2^{ii},1^{ii}}$ = 6.9 Hz, 3H, H-2$^{ii}$); $^{13}$C NMR (100.6 MHz, DMSO-$d_6$):): δ 176.8 (C-3$^{iv}$, C-5$^{iv}$), 167.9 (-COOH), 155.0 (C-4), 150.6 (C-4$^{i}$), 142.8 (C-1$^{i}$), 136.5 (C-8$^{iv}$, C-9$^{iv}$), 132.6 (C-1), 130.4 (C-2), 125.4 (C-2$^{i}$), 121.6 (C-3), 111.4 (C-3$^{i}$), 80.3 (C-1$^{iv}$, C-7$^{iv}$), 47.3 (C-2$^{iv}$, C-6$^{iv}$), 46.7 (C-1$^{iii}$), 44.8 (C-1$^{ii}$), 35.5 (C-2$^{iii}$), 12.2 (C-2$^{ii}$); IR (ATR): 2975, 2667, 2532, 1773, 1701, 1682, 1597, 1516, 1394, 1140 cm$^{-1}$; HRMS (HR-ESI) calcd. for [$C_{25}H_{24}N_4O_5$+H]$^{+}$: 461.1819; found: 461.1817. COSY, DEPT 135 and $^{1}$H/$^{13}$C correlation were recorded.

***tert*-butyl (2-{[4-((*E*)-{4-[[2-(3,5-dioxo-10-oxa-4-azatricyclo[5.2.1.0$^{2,6}$]dec-8-en-4-yl)ethyl](ethyl)amino]phenyl}diazenyl)benzoyl]amino}ethyl)carbamate, 8**

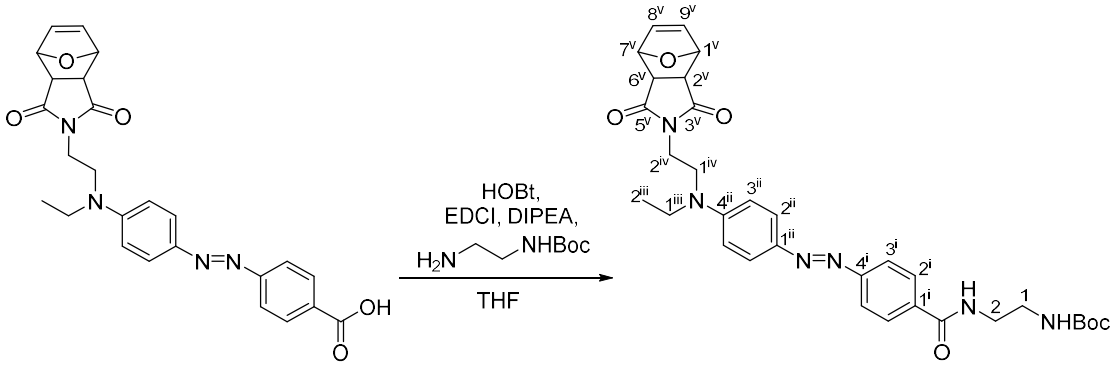


**7** **8**

To a solution of acid **7** (580 mg, 1.26 mmol) in anhydrous THF (60 mL), a solution of HOBt (271 mg, 1.95 mmol), EDCI (0.32 mL, 1.78 mmol), DIPEA (0.95 mL, 5.42 mmol) and *tert*-butyl (2-aminoethyl)carbamate (0.26 mL, 1.61 mmol) in anhydrous THF (30 mL) was added. The reaction mixture was stirred overnight at rt. The solution was washed with $H_2O$ (2 x 50 mL) and the resulting aqueous extracts were extracted with $CH_2Cl_2$ (2 x 30 mL). The combined organic extracts were dried over anhydrous $Na_2SO_4$ and concentrated under vacuum. The resulting residue was purified by column chromatography ($CH_2Cl_2$/THF, 4:1) to obtain a red solid identified as **8** (740 mg, 1.23 mmol, 98% yield). Mp = 58-61 ºC (from $CH_2Cl_2$/THF); $^1$H NMR (400 MHz, $CDCl_3$): δ 7.93 (d, $J_{2^i,3^i}$ = 8.6 Hz, 2H, H-2$^i$), 7.88 (d, $J_{2^{ii},3^{ii}}$ = 9.2 Hz, 2H, H-2$^{ii}$), 7.85 (d, $J_{3^i,2^i}$ = 8.6 Hz, 2H, H-3$^i$), 7.31 (m, 1H, CONH), 6.83 (d, $J_{3^{ii},2^{ii}}$ = 9.2 Hz, 2H, H-3$^{ii}$), 6.49 (t, $J_{8^v,7^v}$ = $J_{9^v,1^v}$ = 0.9 Hz, 2H, H-8$^v$, H-9$^v$), 5.26 (t, $J_{7^v,8^v}$ = $J_{1^v,9^v}$ = 0.9 Hz, 2H, H-1$^v$, H-7$^v$), 5.06 (t, $J_{NH,1}$ = 6.1 Hz, 1H, NHBoc), 3.73 (t, $J_{2^{iv},1^{iv}}$ = 8.0 Hz, 2H, H-2$^{iv}$), 3.56 (m, 4H, H-2, H-1$^{iv}$), 3.48 (q, $J_{1^{iii},2^{iii}}$ = 7.1 Hz, 2H, H-1$^{iii}$), 3.44 (m, 2H, H-1), 2.77 (s, 2H, H-2$^v$, H-6$^v$), 1.43 (s, 9H, C(CH$_3$)$_3$)), 1.22 (t, $J_{2^{iii},1^{iii}}$ = 7.1 Hz, 3H, H-2$^{iii}$); $^{13}$C NMR (100.6 MHz, $CDCl_3$): δ 176.3 (C-3$^v$, C-5$^v$), 167.5 (C-3), 157.8 (C, carbamate), 155.1 (C-4$^i$), 150.6 (C-4$^{ii}$), 143.9 (C-1$^{ii}$), 136.7 (C-8$^v$, C-9$^v$), 134.4 (C-1$^i$), 128.1 (C-2$^i$), 125.8 (C-2$^{ii}$), 122.4 (C-3$^i$), 111.6 (C-3$^{ii}$), 81.1 (C-1$^v$, C-7$^v$), 80.2 (*C*(CH$_3$)$_3$), 47.7 (C-2$^v$, C-6$^v$), 47.0 (C-1$^{iv}$), 45.2 (C-1$^{iii}$), 41.6 (C-1), 41.2 (C-2), 36.1 (C-2$^{iv}$), 12.5 (C-2$^{iii}$); IR (ATR): 3338, 2974, 2932, 1772, 1696, 1596, 1512, 1390, 1133 cm$^{-1}$; HRMS (HR-ESI) calcd. for [$C_{32}H_{38}N_6O_6$+H]$^+$: 603.2926; found: 603.2927. COSY, DEPT 135 and $^1$H/$^{13}$C correlation were recorded.

**_N_-(2-aminoethyl)-4-((_E_)-{4-[[2-(3,5-dioxo-10-oxa-4-azatricyclo[5.2.1.0$^{2,6}$]dec-8-en-4-yl)ethyl](ethyl)amino]phenyl}diazenyl)benzamide, 9**

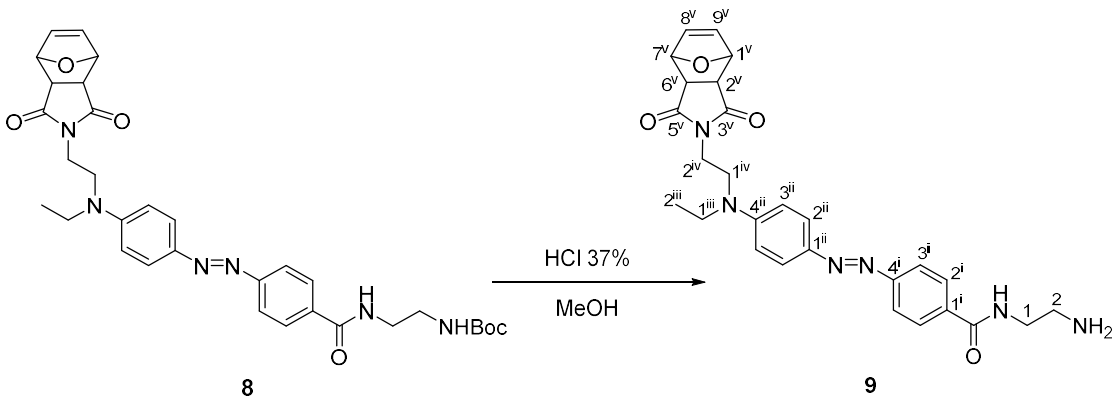


**8** **9**

To a solution of carbamate **8** (700 mg, 1.16 mmol) in MeOH (70 mL), HCl 37% (13.2 mL, 159 mmol) was added dropwise. The mixture was stirred at rt for around 5 h. Afterwards, the mixture was neutralised with a saturated aqueous solution of $NaHCO_3$, extracted with $CH_2Cl_2$ and the combined organic extracts were dried over anhydrous $Na_2SO_4$. The solvent was evaporated under vacuum and the resulting residue was purified by column chromatography ($CH_2Cl_2$/MeOH, 15:1) to furnish **9** (360 mg, 0.72 mmol, 62% yield) as an orange solid. Mp = 94-96 ºC (from $CH_2Cl_2$/MeOH); $^1$H NMR (400 MHz, $CDCl_3$): δ 7.91 (d, $J_{2^i,3^i}$ = 8.3 Hz, 2H, H-$2^i$), 7.84 (d, $J_{2^{ii},3^{ii}}$ = 9.1 Hz, 2H, H-$2^{ii}$), 7.81 (d, $J_{3^i,2^i}$ = 8.3 Hz, 2H, H-$3^i$), 7.15 (br s, 1H, CONH), 6.80 (d, $J_{3^{ii},2^{ii}}$ = 9.1 Hz, 2H, H-$3^{ii}$), 6.49 (s, 2H, H-$8^v$, H-$9^v$), 5.25 (s, 2H, H-$1^v$, H-$7^v$), 3.70 (t, $J_{2^{iv},3^{iv}}$ = 7.2, 2H, H-$2^{iv}$), 3.53 (m, 4H, H-1, H-$1^{iv}$), 3.47 (q, $J_{1^{iii},2^{iii}}$ = 7.1, 2H, H-$1^{iii}$), 3.03 (t, $J_{2,1}$ = 5.7, 2H, H-2), 2.76 (s, 2H, H-$2^v$, H-$6^v$), 1.20 (t, $J_{2^{iii},1^{iii}}$ = 7.1 Hz, 3H, H-$2^{iii}$); $^{13}$C NMR (100.6 MHz, $CDCl_3$): δ 176.3 (C-$3^v$, C-$5^v$), 167.6 (C-3), 155.1 (C-$4^i$), 150.6 (C-$4^{ii}$), 143.9 (C-$1^{ii}$), 136.7 (C-$8^v$, C-$9^v$), 134.6 (C-$1^i$), 128.2 (C-$2^i$), 125.8 (C-$2^{ii}$), 122.4 (C-$3^i$), 111.6 (C-$3^{ii}$), 81.0 (C-$1^v$, C-$7^v$), 47.6 (C-$2^v$, C-$6^v$), 46.9 (C-$1^{iv}$), 45.2 (C-$1^{iii}$), 41.6 (C-1), 41.1 (C-2), 36.1 (C-$2^{iv}$), 12.5 (C-$2^{iii}$); IR (ATR): 3286, 2926, 1770, 1696, 1596, 1512, 1390, 1132 $cm^{-1}$; HRMS (HR-ESI) calcd. for $[C_{27}H_{30}N_6O_4+H]^+$: 503.2401; found: 503.2403. $^1$H/$^{13}$C correlation was recorded.

**di-*tert*-butyl (2*S*,4*R*)-2-[(*tert*-butoxycarbonyl)amino]-4-{4-[(2-{[4-((*E*)-{4-[[2-(3,5-dioxo-10-oxa-4-azatricyclo[5.2.1.0$^{2,6}$]dec-8-en-4-yl)ethyl](ethyl)amino]phenyl}diazenyl) benzoyl]amino}ethyl)amino]-4-oxobutyl}pentanedioate, 11**

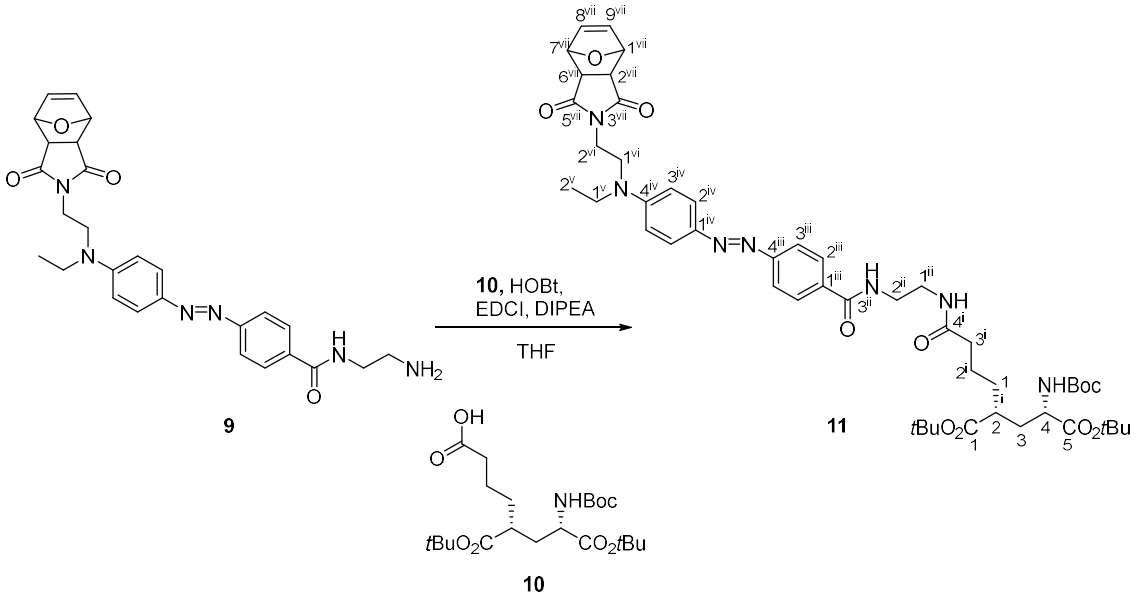


To a solution of amine **9** (250 mg, 0.50 mmol) in anhydrous THF (26 mL), a solution of acid **10** (Gascón-Moya et al. 2015)(248 mg, 0.56 mmol), HOBt (107 mg, 0.77 mmol), EDCI (0.12 mL, 0.67 mmol) and DIPEA (0.36 mL, 2.06 mmol) in anhydrous THF (18.5 mL) was added. The reaction mixture was stirred overnight at rt. The orange solution was washed with $H_2O$ (2 x 50 mL) and the resulting aqueous extracts were extracted with $CH_2Cl_2$ (2 x 30 mL). The combined organic extracts were dried over anhydrous $Na_2SO_4$ and concentrated under vacuum. The resulting residue was purified by column chromatography ($CH_2Cl_2$/MeOH, 9:0.5) to give **11** (350 mg, 0.38 mmol, 76% yield), as a red solid. Mp = 85-88 ºC (from $CH_2Cl_2$/MeOH); $[\alpha]_D^{20}$ = 8.3 (*c* 0.33, $CHCl_3$); $^1$H NMR (400 MHz, $CDCl_3$): δ 7.92 (d, $J_{2^{iii},3^{iii}}$ = 8.7 Hz, 2H, H-$2^{iii}$), 7.87 (d, $J_{2^{iv},3^{iv}}$ = 9.5 Hz, 2H, H-$2^{iv}$),

7.85 (d, $J_{3^{iii},2^{iii}}$ = 8.7 Hz, 2H, H-3$^{iii}$), 7.47 (t, $J_{NH,2^{ii}}$ = 4.8 Hz, 1H, CONH-3$^{ii}$), 6.83 (d, $J_{3^{iv},2^{iv}}$ = 9.5 Hz, 2H, H-3$^{iv}$), 6.54 (t, $J_{NH,1^{ii}}$ = 5.0 Hz, 1H, CONH-4$^{i}$), 6.49 (t, $J_{8^{vii},7^{vii}} = J_{9^{vii},1^{vii}}$ = 1.0 Hz, 2H, H-8$^{vii}$, H-9$^{vii}$), 5.26 (t, $J_{7^{vii},8^{vii}} = J_{1^{vii},9^{vii}}$ = 1.0 Hz, 2H, H-1$^{vii}$, H-7$^{vii}$), 5.09 (d, $J_{NHBoc,4}$ = 8.3 Hz, 1H, NHBoc), 4.16 (m, 1H, H-4), 3.72 (t, $J_{2^{vi},1^{vi}}$ = 7.2 Hz, 2H, H-2$^{vi}$), 3.53 (m, 8H, H-1$^{ii}$, H-2$^{ii}$, H-1$^{v}$, H-1$^{vi}$), 2.77 (s, 2H, H-2$^{vii}$, H-6$^{vii}$), 2.35 (m, 1H, H-2), 2.22 (m, 2H, H-3$^{i}$), 2.07 (m, 1H, H-3), 1.62 (m, 5H, H-3, 2xH-1$^{i}$, 2xH-2$^{i}$), 1.44 (s, 9H, C(CH$_3$)$_3$), 1.43 (s, 9H, C(CH$_3$)$_3$), 1.41 (s, 9H, C(CH$_3$)$_3$), 1.22 (t, $J_{2^{v},1^{v}}$ = 7.1 Hz, 3H, H-2$^{v}$); $^{13}$C NMR (100.6 MHz, CDCl$_3$): δ 176.2 (C-3$^{vii}$, C-5$^{vii}$), 174.6/174.5 (C-4$^{i}$/C-1), 171.7 (C-5), 167.8 (C-3$^{ii}$), 155.4 (C, carbamate), 155.1 (C-4$^{iii}$), 150.6 (C-4$^{iv}$), 143.9 (C-1$^{iv}$), 136.6 (C-8$^{vii}$, C-9$^{vii}$), 134.2 (C-1$^{iii}$), 128.1 (C-2$^{iii}$), 125.8 (C-2$^{iv}$), 122.4 (C-3$^{iii}$), 111.5 (C-3$^{iv}$), 82.1 (*C*(CH$_3$)$_3$), 81.1 (*C*(CH$_3$)$_3$), 81.0 (C-1$^{vii}$, C-7$^{vii}$), 79.8 (*C*(CH$_3$)$_3$), 52.8 (C-4), 47.6 (C-2$^{vii}$, C-6$^{vii}$), 47.0 (C-1$^{vi}$), 45.2 (C-1$^{v}$), 42.3 (C-2), 41.8 (C-2$^{ii}$), 39.9 (C-1$^{ii}$), 36.3 (C-3$^{i}$), 36.1 (C-2$^{vi}$), 34.8 (C-3), 31.9 (C-1$^{i}$), 28.5 (C(*C*H$_3$)$_3$), 28.2 (C(*C*H$_3$)$_3$), 28.1 (C(*C*H$_3$)$_3$), 23.2 (C-2$^{i}$), 12.5 (C-2$^{v}$); IR (ATR): 3302, 2974, 2933, 1773, 1699, 1597, 1513, 1136 cm$^{-1}$; HRMS (HR-ESI) calcd. for [C$_{49}$H$_{67}$N$_7$O$_{11}$+H]$^+$: 930.4971; found: 930.4965. COSY, DEPT 135 and $^1$H/$^{13}$C correlation were recorded.

**di-*tert*-butyl (2*S*,4*R*)-2-[(*tert*-butoxycarbonyl)amino]-4-{4-[(2-{[4-((*E*)-{4-[[2-(2,5-dioxo-2,5-dihydro-1*H*-pyrrol-1-yl)ethyl](ethyl)amino]phenyl}diazenyl)benzoyl]amino} ethyl)amino]-4-oxobutyl}pentanedioate, 12**

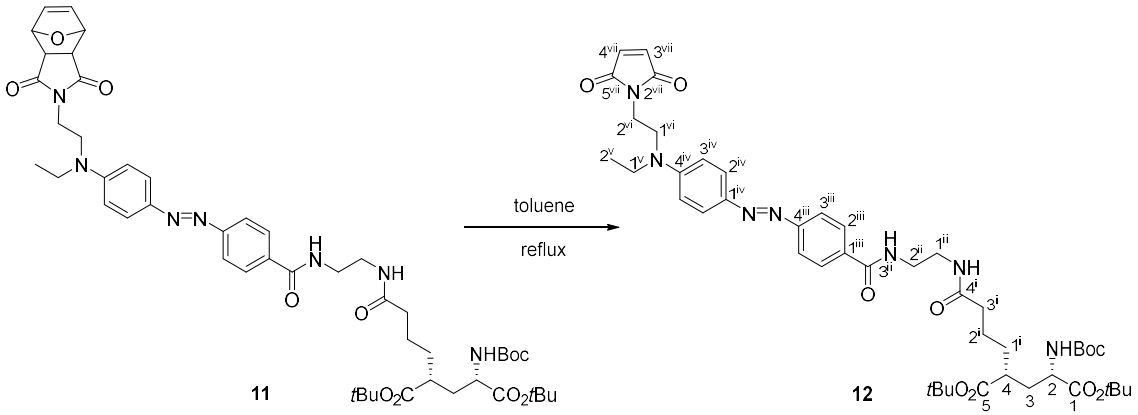


11 12

A solution of compound **11** (270 mg, 0.29 mmol) in toluene (28 mL) was heated at reflux temperature for 5 h. When TLC analysis (EtOAc) showed no presence of starting material the solvent was removed under vacuum and the resulting residue was purified by column chromatography (EtOAc) to furnish a red solid identified as **12** (200 mg, 0.23 mmol, 80% yield). Mp = 67-70 $^o$C (from EtOAc); $[\alpha]_D^{20}$ = 0.9 (*c* 0.34, CHCl$_3$); $^1$H NMR (400 MHz, CDCl$_3$): δ 7.92 (d, $J_{2^{iii},3^{iii}}$ = 8.6 Hz, 2H, H-2$^{iii}$), 7.87 (d, $J_{2^{iv},3^{iv}}$ = 9.0 Hz, 2H, H-2$^{iv}$), 7.86 (d, $J_{3^{iii},2^{iii}}$ = 8.6 Hz, 2H, H-3$^{iii}$), 7.47 (br s, 1H, CONH-3$^{ii}$), 6.80 (d, $J_{3^{iv},2^{iv}}$ = 9.0 Hz, 2H, H-3$^{iv}$), 6.68 (s, 2H, H-4$^{vii}$, H-3$^{vii}$), 6.46 (br s, 1H, CONH-4$^{i}$), 5.08 (d, $J_{NHBoc,2}$ = 8.6 Hz, 1H, NHBoc), 4.17 (m, 1H, H-2), 3.77 (t, $J_{2^{vi},1^{vi}}$ = 7.0 Hz, 2H, H-2$^{vi}$), 3.58 (m, 6H, H-1$^{ii}$, H-2$^{ii}$, H-1$^{vi}$), 3.49 (q, $J_{1^{v},2^{v}}$ = 7.1 Hz, 2H, H-1$^{v}$), 2.35 (m, 1H, H-4), 2.22 (m, 2H, H-3$^{i}$), 2.07 (m, 1H, H-3), 1.67 (m, 5H, H-3, 2xH-1$^{i}$, 2xH-2$^{i}$), 1.45 (s, 9H, C(CH$_3$)$_3$), 1.44 (s, 9H, C(CH$_3$)$_3$), 1.42 (s, 9H, C(CH$_3$)$_3$), 1.24 (m, 3H, H-2$^{v}$); $^{13}$C NMR (100.6 MHz, CDCl$_3$): δ 174.6/174.5 (C-4$^{i}$/C-5), 171.7 (C-1), 170.7 (C-2$^{vii}$, C-5$^{vii}$), 167.8 (C-3$^{ii}$), 155.4 (C, carbamate), 155.2 (C-4$^{iii}$), 150.5 (C-4$^{iv}$), 144.0 (C-1$^{iv}$), 134.4 (C-3$^{vii}$, C-4$^{vii}$), 134.2 (C-1$^{iii}$), 128.1 (C-2$^{iii}$), 125.8 (C-2$^{iv}$), 122.4 (C-3$^{iii}$), 111.5 (C-3$^{iv}$), 82.1 (*C*(CH$_3$)$_3$), 81.1 (*C*(CH$_3$)$_3$), 79.8 (*C*(CH$_3$)$_3$), 52.8 (C-2), 47.8 (C-1$^{vi}$), 45.1 (C-1$^{v}$), 42.3 (C-4), 41.8 (C-2$^{ii}$), 39.9 (C-1$^{ii}$), 36.3 (C-3$^{i}$), 35.1 (C-2$^{vi}$), 34.9 (C-3), 31.9 (C-1$^{i}$), 28.5 (C(*C*H$_3$)$_3$), 28.2

(C($CH_3$)$_3$), 28.1 (C($CH_3$)$_3$), 22.8 (C-2$^{i}$), 12.5 (C-2$^{v}$); IR (ATR): 3297, 3070, 2976, 2932, 1706, 1600, 1515, 1136 cm$^{-1}$; HRMS (HR-ESI) calcd. for $[C_{45}H_{63}N_7O_{10}+H]^+$: 862.4709; found: 862.4707. COSY, DEPT 135 and $^1H/^{13}C$ correlation were recorded.

**(1*S*,3*R*)-1,3-dicarboxy-7-[(2-{[4-((*E*)-{4-[[2-(2,5-dioxo-2,5-dihydro-1*H*-pyrrol-1-yl)ethyl](ethyl)amino]phenyl}diazenyl)benzoyl]amino}ethyl)amino]-7-oxoheptan-1-aminium trifluoroacetate, $MAG_{2P\_long}$**

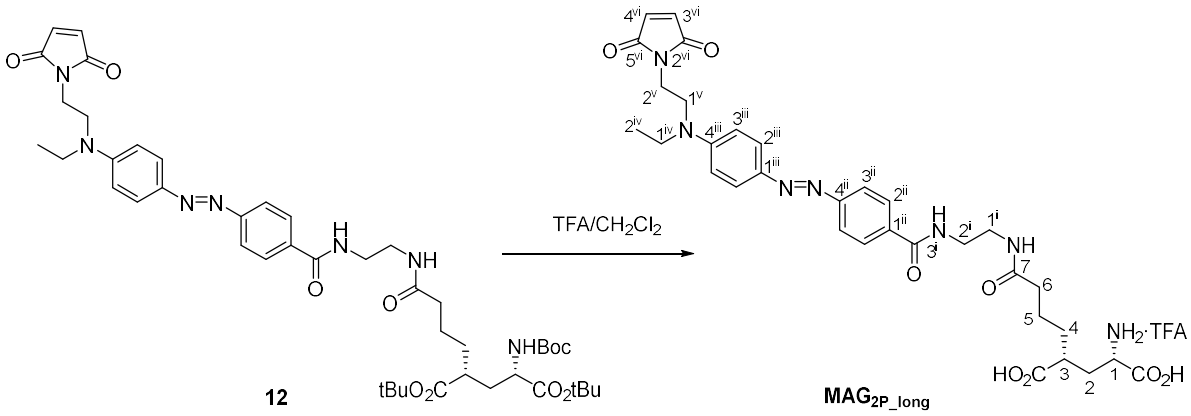


To a stirred solution of compound **12** (170 mg, 0.20 mmol) in $CH_2Cl_2$ (40 mL), trifluoroacetic acid (15 mL, 196 mmol) was added. The mixture was stirred at rt until the starting material was consumed. Then, the solution was concentrated under vacuum and the resulting dark purple solid was washed with $Et_2O$ to furnish **$MAG_{2P\_long}$** (150 mg, 0.20 mmol, quantitative yield). Mp = 94-98 $^{o}$C (from $Et_2O$); $[\alpha]_D^{20}$ = 6.7 (*c* 0.33, DMSO); $^1$H NMR (400 MHz, DMSO-$d_6$, 310 K): δ 8.55 (br t, $J_{NH,2^i}$ = 5.0 Hz, 1H, CONH-3$^{i}$), 8.24 (br s, 3H, $NH_3^+$), 7.98 (d, $J_{2^{ii},3^{ii}}$ = 8.3 Hz, 2H, H-2$^{ii}$), 7.91 (br t, $J_{NH,1^i}$ = 5.0 Hz, 1H, CONH-7), 7.80 (m, 4H, H-2$^{iii}$, H-3$^{ii}$), 7.00 (s, 2H, H-3$^{vi}$, H-4$^{vi}$), 6.84 (d, $J_{3^{iii},2^{iii}}$ = 9.0 Hz, 2H, H-3$^{iii}$), 3.82 (m, 1H, H-1), 3.65 (m, 2H, H-2$^{v}$), 3.60 (m, 2H, H-1$^{v}$), 3.44 (m, 2H, H-1$^{iv}$), 3.33 (m, 2H, H-2$^{i}$), 3.25 (m, 2H, H-1$^{i}$), 2.57 (m, 1H, H-3), 2.15 (m, 3H, H-2, 2xH-6), 1.76 (m, 1H, H-2), 1.51 (m, 4H, 2xH-4, 2xH-5), 1.14 (t, $J_{2^{iv},1^{iv}}$ = 7.0 Hz, 3H, H-2$^{iv}$); $^{13}$C NMR (100.6 MHz, DMSO-$d_6$, 310 K): δ 175.4/170.7 (2xCOOH), 172.0 (C-7), 170.8 (C-2$^{vi}$, C-5$^{vi}$), 165.8 (C-3$^{i}$), 153.9 (C-4$^{ii}$), 150.6 (C-4$^{iii}$), 142.6 (C-1$^{iii}$), 134.8 (C-1$^{ii}$), 134.6 (C-3$^{vi}$, C-4$^{vi}$), 128.2 (C-2$^{ii}$), 125.2 (C-2$^{iii}$), 121.4 (C-3$^{ii}$), 111.2 (C-3$^{iii}$), 50.9 (C-1), 47.1 (C-1$^{v}$), 44.5 (C-1$^{iv}$), 40.4 (C-3), 39.3 (C-1$^{i}$), 38.2 (C-2$^{i}$), 35.1 (C-6), 34.7 (C-2$^{v}$), 31.7 (C-2), 31.2 (C-4), 22.4 (C-5), 12.0 (C-2$^{iv}$); IR (ATR): 2927, 1708, 1596, 1539, 1260, 1160, 1132 cm$^{-1}$; HRMS (HR-ESI) calcd. for $[C_{32}H_{40}N_7O_8]^+$: 650.2933; found: 650.2926. COSY, DEPT 135 and $^1H/^{13}C$ correlation were recorded.

## REFERENCES


Ai, Xiangzhao, Linna Lyu, Yang Zhang, Yanxia Tang, Jing Mu, Fang Liu, Yixi Zhou, Zhenghong Zuo, Gang Liu, and Bengang Xing. 2017. "Remote Regulation of Membrane Channel Activity by Site-Specific Localization of Lanthanide-Doped Upconversion Nanocrystals." *Angewandte Chemie - International Edition* 56(11):3031–35.

Albericio, Fernando, Albert Isidro-llobet, and A. Mercedes. 2009. "Amino Acid-Protecting Groups." 2455–2504.

Aloy, Patrick and Robert B. Russell. 2006. "Structural Systems Biology: Modelling Protein Interactions." *Nature Reviews Molecular Cell Biology* 7(3):188–97.

Bamann, Christian, Ronnie Gueta, Sonja Kleinlogel, Georg Nagel, and Ernst Bamberg. 2010. "Structural Guidance of the Photocycle of Channelrhodopsin-2 by an Interhelical Hydrogen Bond." *Biochemistry* 49(2):267–78.

Banghart M, Borges K, Isacoff E, Trauner D, Kramer RH. 2004. "Light-Activated Ion Channels for Remote Control of Neuronal Firing." *Nature Neuroscience* 7:1381–86.

Bansal, Akshaya, Haichun Liu, Muthu Kumara Gnanasammandhan Jayakumar, Stefan Andersson-Engels, and Yong Zhang. 2016. "Quasi-Continuous Wave Near-Infrared Excitation of Upconversion Nanoparticles for Optogenetic Manipulation of C. Elegans." *Small* 12(13):1732–43.

Bartels, E., N. H. Wassermann, and B. F. Erlanger. 1971. "Photochromic Activators of the Acetylcholine Receptor." *Proceedings of the National Academy of Sciences of the United States of America* 68(8):1820–23.

Berlin, Shai, Stephanie Szobota, Andreas Reiner, Elizabeth C. Carroll, Michael A. Kienzler, Alice Guyon, Tong Xiao, Dirk Trauner, and Ehud Y. Isacoff. 2016. "A Family of Photoswitchable NMDA Receptors." *ELife* 1–29.

Berndt, André, Ofer Yizhar, Lisa A. Gunaydin, Peter Hegemann, and Karl Deisseroth. 2009. "Bi-Stable Neural State Switches." *Nature Neuroscience* 12(2):229–34.

Braubach, Oliver, Tuce Tombaz, Tristan Geiller, Ryota Homma, Thomas Bozza, Lawrence B. Cohen, and Yunsook Choi. 2018. "Sparsened Neuronal Activity in an Optogenetically Activated Olfactory Glomerulus." *Scientific Reports* 8(1):1–17.

Brouwer, Albert M. 2011. "Standards for Photoluminescence Quantum Yield Measurements in Solution (IUPAC Technical Report)." *Pure and Applied Chemistry* 83(12):2213–28.

Byrne, John H. 2014. "Section II: Physiology of Ion Channels, Excitable Membranes and Synaptic Transmission." Pp. 489–507 in *From Molecules to Networks (Third Edition) An Introduction to Cellular and Molecular Neuroscience*, edited by J. H. Byrne, R. Heidelberger, and M. N. Waxham.

Cabré, G., A. Garrido-Charles, M. Moreno, M. Bosch, M. Porta-de-la-Riva, M. Krieg, M. Gascón-Moya, N. Camarero, R. Gelabert, J. M. Lluch, F. Busqué, J. Hernando, P. Gorostiza, and R. Alibés. 2019. "Rationally Designed Azobenzene Photoswitches for Efficient Two-Photon Neuronal Excitation." *Nature Communications* 10(1).

Caporale, Natalia, Kathleen D. Kolstad, Trevor Lee, Ivan Tochitsky, Deniz Dalkara, Dirk Trauner, Richard Kramer, Yang Dan, Ehud Y. Isacoff, and John G. Flannery. 2011. "LiGluR Restores Visual Responses in Rodent Models of Inherited Blindness." *Molecular Therapy* 19(7):1212–19.

Carroll, Elizabeth C., Shai Berlin, Joshua Levitz, Michael a Kienzler, Zhe Yuan, Dorte Madsen, Delmar S. Larsen, and Ehud Y. Isacoff. 2015. "Two-Photon Brightness of Azobenzene Photoswitches Designed for Glutamate Receptor Optogenetics." *Proceedings of the National Academy of Sciences of the United States of America* 112(7):E776-85.

Chen, Shuo, Adam Z. Weitemier, Xiao Zeng, Linmeng He, Xiyu Wang, Yanqiu Tao, Arthur J. Y. Huang, Yuki Hashimotodani, Masanobu Kano, Hirohide Iwasaki, Laxmi Kumar Parajuli, Shigeo Okabe, Daniel B.

Loong Teh, Angelo H. All, Iku Tsutsui-Kimura, Kenji F. Tanaka, Xiaogang Liu, and Thomas J. Mchugh. 2018. “Near-Infrared Deep Brain Stimulation via Upconversion Nanoparticle–Mediated Optogenetics.” *Science* 359(February):679–84.

Chen, Xi, Kasturi Muthoosamy, Anne Pfisterer, Boris Neumann, and Tanja Weil. 2012. “Site-Selective Lysine Modification of Native Proteins and Peptides via Kinetically Controlled Labeling.” *Bioconjugate Chemistry* 23(3):500–508.

Deisseroth, Karl. 2011. “Optogenetics.” *Nature Methods* 8(1):26–29.

Deisseroth, Karl. 2015. “Optogenetics: 10 Years of Microbial Opsins in Neuroscience.” *Nature Neuroscience* 18(9):1213–25.

Ernst, Oliver P., David T. Lodowski, Marcus Elstner, Peter Hegemann, Leonid S. Brown, and Hideki Kandori. 2014. “Microbial and Animal Rhodopsins: Structures, Functions, and Molecular Mechanisms.” *Chemical Reviews* 114(1):126–63.

Ernst, Oliver P., Pedro A. Sánchez Murcia, Peter Daldrop, Satoshi P. Tsunoda, Suneel Kateriya, and Peter Hegemann. 2008. “Photoactivation of Channelrhodopsin.” *Journal of Biological Chemistry* 283(3):1637–43.

Fehrentz, Timm, Matthias Schönberger, and Dirk Trauner. 2011. “Optochemical Genetics.” *Angewandte Chemie - International Edition* 50(51):12156–82.

Förster, Dominique, Marco Dal Maschio, Eva Laurell, and Herwig Baier. 2017. “An Optogenetic Toolbox for Unbiased Discovery of Functionally Connected Cells in Neural Circuits.” *Nature Communications* 8(1):116.

Gascón-Moya, Marta, Arnau Pejoan, Mercè Izquierdo-Serra, Silvia Pittolo, Gisela Cabré, Jordi Hernando, Ramon Alibés, Pau Gorostiza, and Félix Busqué. 2015. “An Optimized Glutamate Receptor Photoswitch with Sensitized Azobenzene Isomerization.” *Journal of Organic Chemistry* 80(20):9915–25.

Gibney, Brian R., Francesc Rabanal, Konda S. Reddy, and P. Leslie Dutton. 1998. “Effect of Four Helix Bundle Topology on Heme Binding and Redox Properties.” *Biochemistry* 37(13):4635–43.

Hososhima, Shoko, Hideya Yuasa, Toru Ishizuka, Mohammad Razuanul Hoque, Takayuki Yamashita, Akihiro Yamanaka, Eriko Sugano, Hiroshi Tomita, and Hiromu Yawo. 2015. “Near-Infrared (NIR) up-Conversion Optogenetics.” *Scientific Reports* 5:1–10.

Hüll, Katharina, Johannes Morstein, and Dirk Trauner. 2018. “In Vivo Photopharmacology.” *Chemical Reviews* 118(21):10710–47.

Islam, Md Shahidul, Per Olof Berggren, and Olof Larsson. 1993. “Sulfhydryl Oxidation Induces Rapid and Reversible Closure of the ATP-Regulated K+ Channel in the Pancreatic β-Cell.” *FEBS Letters* 319(1–2):128–32.

Iyer, Shrivats M., Sam Vesuna, Charu Ramakrishnan, Karen Huynh, Stephanie Young, Andre Berndt, Soo Yeun Lee, Christopher J. Gorini, Karl Deisseroth, and Scott L. Delp. 2016. “Optogenetic and Chemogenetic Strategies for Sustained Inhibition of Pain.” *Scientific Reports* 6(July):1–10.

Izquierdo-Serra, Mercè, Antoni Bautista-Barrufet, Ana Trapero, Aida Garrido-Charles, Ariadna Díaz-Tahoces, Nuria Camarero, Silvia Pittolo, Sergio Valbuena, Ariadna Pérez-Jiménez, Marina Gay, Alejandro García-Moll, Carles Rodríguez-Escrich, Juan Lerma, Pedro de la Villa, Eduardo Fernández, Miquel À. Pericàs, Amadeu Llebaria, and Pau Gorostiza. 2016. “Optical Control of Endogenous Receptors and Cellular Excitability Using Targeted Covalent Photoswitches.” *Nature Communications* 7:12221.

Izquierdo-Serra, Mercè, Marta Gascón-Moya, Jan J. Hirtz, Silvia Pittolo, Kira E. Poskanzer, Eric Ferrer, Ramon Alibés, Félix Busqué, Rafael Yuste, Jordi Hernando, and Pau Gorostiza. 2014. “Two-Photon Neuronal and Astrocytic Stimulation with Azobenzene-Based Photoswitches.” *Journal of the American Chemical Society* 136(24):8693–8701.

Keppeler, Daniel, Ricardo Martins Merino, David Lopez de la Morena, Burak Bali, Antoine Tarquin Huet, Anna Gehrt, Christian Wrobel, Swati Subramanian, Tobias Dombrowski, Vladan Rankovic, Andreas Neef, and Tobias Moser. 2018. "Ultrafast Optogenetic Stimulation of the Auditory Pathway by Targeting-optimized Chronos." *The EMBO Journal* 37(24):e99649.

Kienzler, Michael A., Andreas Reiner, Eric Trautman, Stan Yoo, Dirk Trauner, and Ehud Y. Isacoff. 2013. "A Red-Shifted, Fast-Relaxing Azobenzene Photoswitch for Visible Light Control of an Ionotropic Glutamate Receptor." *Journal of the American Chemical Society* 135(47):17683–86.

Klapoetke, Nathan C., Yasunobu Murata, Sung Soo Kim, Stefan R. Pulver, Amanda Birdsey-Benson, Yong Ku Cho, Tania K. Morimoto, Amy S. Chuong, Eric J. Carpenter, Zhijian Tian, Jun Wang, Yinlong Xie, Zhixiang Yan, Yong Zhang, Brian Y. Chow, Barbara Surek, Michael Melkonian, Vivek Jayaraman, Martha Constantine-Paton, Gane Ka-Shu Wong, and Edward S. Boyden. 2014. "Independent Optical Excitation of Distinct Neural Populations." *Nature Methods* 11(3):338–46.

Kufareva, Irina, Andrey V. Ilatovskiy, and Ruben Abagyan. 2012. "Pocketome: An Encyclopedia of Small-Molecule Binding Sites in 4D." *Nucleic Acids Research* 40(D1):535–40.

Lakowicz, Joseph R. 2006. *Principles of Fluorescence Spectroscopy*. 3rd ed. Springer US.

Levitz, Joshua, Carlos Pantoja, Benjamin Gaub, Harald Janovjak, Andreas Reiner, Adam Hoagland, David Schoppik, Brian Kane, Philipp Stawski, Alexander F. Schier, Dirk Trauner, and Ehud Y. Isacoff. 2013. "Optical Control of Metabotropic Glutamate Receptors." *Nature Neuroscience* 16(4):507–16.

Lin, John Y. 2010. "A User's Guide to Channelrhodopsin Variants: Features, Limitations and Future Developments." *Experimental Physiology* 96(1):19–25.

Lin, Wan Chen, Christopher M. Davenport, Alexandre Mourot, Devaiah Vytla, Caleb M. Smith, Kathryne A. Medeiros, James J. Chambers, and Richard H. Kramer. 2014. "Engineering a Light-Regulated GABA A Receptor for Optical Control of Neural Inhibition." *ACS Chemical Biology* 9(7):1414–19.

Lippitz, M., W. Erker, H. Decker, K. E. Van Holde, and T. Basche. 2002. "Two-Photon Excitation Microscopy of Tryptophan-Containing Proteins." *Pnas* 99(5):2772–77.

Luo, Qunfeng, Youqi Tao, Wangjian Sheng, Jingxia Lu, and Huan Wang. 2019. "Dinitroimidazoles as Bifunctional Bioconjugation Reagents for Protein Functionalization and Peptide Macrocyclization." *Nature Communications* 10(1):1–9.

Mager, Thomas, David Lopez de la Morena, Verena Senn, Johannes Schlotte, Anna D´Errico, Katrin Feldbauer, Christian Wrobel, Sangyong Jung, Kai Bodensiek, Vladan Rankovic, Lorcan Browne, Antoine Huet, Josephine Jüttner, Phillip G. Wood, Johannes J. Letzkus, Tobias Moser, and Ernst Bamberg. 2018. "High Frequency Neural Spiking and Auditory Signaling by Ultrafast Red-Shifted Optogenetics." *Nature Communications* 9(1):1750.

Mazor, Yuval, Anna Borovikova, Ido Caspy, and Nathan Nelson. 2017. "Structure of the Plant Photosystem i Supercomplex at 2.6 Å Resolution." *Nature Plants* 3(March):1–9.

Mirkovic, Tihana, Evgeny E. Ostroumov, Jessica M. Anna, Rienk Van Grondelle, Govindjee, and Gregory D. Scholes. 2017. "Light Absorption and Energy Transfer in the Antenna Complexes of Photosynthetic Organisms." *Chemical Reviews* 117(2):249–93.

Moreno, Javier, Mario Gerecke, Lutz Grubert, Sergey A. Kovalenko, and Stefan Hecht. 2016. "Sensitized Two-NIR-Photon Z→E Isomerization of a Visible-Light-Addressable Bistable Azobenzene Derivative." *Angewandte Chemie - International Edition* 55(4):1544–47.

Nagel, Georg, Martin Brauner, Jana F. Liewald, Nona Adeishvili, Ernst Bamberg, and Alexander Gottschalk. 2005. "Light Activation of Channelrhodopsin-2 in Excitable Cells of Caenorhabditis Elegans Triggers Rapid Behavioral Responses." *Current Biology* 15(24):2279–84.

Nagel, Georg, Tanjef Szellas, Wolfram Huhn, Suneel Kateriya, Nona Adeishvili, Peter Berthold, Doris Ollig, Peter Hegemann, and Ernst Bamberg. 2003. "Channelrhodopsin-2, a Directly Light-Gated Cation-Selective Membrane Channel." *Proceedings of the National Academy of Sciences*

100(24):13940–45.

Noy, Dror, Christopher C. Moser, and P. Leslie Dutton. 2006. “Design and Engineering of Photosynthetic Light-Harvesting and Electron Transfer Using Length, Time, and Energy Scales.” *Biochimica et Biophysica Acta - Bioenergetics* 1757(2):90–105.

Picot, Alexis, Soledad Dominguez, Chang Liu, I. Wen Chen, Dimitrii Tanese, Emiliano Ronzitti, Pascal Berto, Eirini Papagiakoumou, Dan Oron, Gilles Tessier, Benoît C. Forget, and Valentina Emiliani. 2018. “Temperature Rise under Two-Photon Optogenetic Brain Stimulation.” *Cell Reports* 24(5):1243-1253.e5.

Pittolo, Silvia, Hyojung Lee, Anna Lladó, Sébastien Tosi, Miquel Bosch, Lídia Bardia, Xavier Gómez-Santacana, Amadeu Llebaria, Eduardo Soriano, Julien Colombelli, Kira E. Poskanzer, Gertrudis Perea, and Pau Gorostiza. 2019. “Reversible Silencing of Endogenous Receptors in Intact Brain Tissue Using 2-Photon Pharmacology.” *Proceedings of the National Academy of Sciences of the United States of America* 116(27):13680–89.

Prakash, Rohit, Ofer Yizhar, Benjamin Grewe, Charu Ramakrishnan, Nancy Wang, Inbal Goshen, Adam M. Packer, Darcy S. Peterka, Rafael Yuste, Mark J. Schnitzer, and Karl Deisseroth. 2012. “Two-Photon Optogenetic Toolbox for Fast Inhibition, Excitation and Bistable Modulation.” *Nature Methods* 9(12):1171–79.

Rabanal, Francesc, William F. DeGrado, and P. Leslie Dutton. 1996. “Use of 2,2′-Dithiobis(5-Nitropyridine) for the Heterodimerization of Cysteine Containing Peptides. Introduction of the 5-Nitro-2-Pyridinesulfenyl Group.” *Tetrahedron Letters* 37(9):1347–50.

Reiner, Andreas and Ehud Y. Isacoff. 2014. “Tethered Ligands Reveal Glutamate Receptor Desensitization Depends on Subunit Occupancy.” *Nature Chemical Biology* (february):1–10.

Reiter, Alwin, Arne Skerra, Dirk Trauner, and André Schiefner. 2013. “A Photoswitchable Neurotransmitter Analogue Bound to Its Receptor A Photoswitchable Neurotransmitter Analogue Bound to Its.” *Biochemistry* 52:8972–74.

Ribeiro, António J. M., Gemma L. Holliday, Nicholas Furnham, Jonathan D. Tyzack, Katherine Ferris, and Janet M. Thornton. 2018. “Mechanism and Catalytic Site Atlas (M-CSA): A Database of Enzyme Reaction Mechanisms and Active Sites.” *Nucleic Acids Research* 46(D1):D618–23.

Szobota, Stephanie, Pau Gorostiza, Filippo Del Bene, Claire Wyart, Doris L. Fortin, Kathleen D. Kolstad, Orapim Tulyathan, Matthew Volgraf, Rika Numano, Holly L. Aaron, Ethan K. Scott, Richard H. Kramer, John Flannery, Herwig Baier, Dirk Trauner, and Ehud Y. Isacoff. 2007. “Remote Control of Neuronal Activity with a Light-Gated Glutamate Receptor.” *Neuron* 54(4):535–45.

Tochitsky, Ivan, Matthew R. Banghart, Alexandre Mourot, Jennifer Z. Yao, Benjamin Gaub, Richard H. Kramer, and Dirk Trauner. 2012. “Optochemical Control of Genetically Engineered Neuronal Nicotinic Acetylcholine Receptors.” *Nature Chemistry* 4(2):105–11.

Velema, Willem A., Wiktor Szymanski, and Ben L. Feringa. 2014. “Photopharmacology: Beyond Proof of Principle.” *Journal of the American Chemical Society* 136(6):2178–91.

Verhoefen, Mirka Kristin, Christian Bamann, Rene Blöcher, Ute Förster, Ernst Bamberg, and Josef Wachtveitl. 2010. “The Photocycle of Channelrhodopsin-2: Ultrafast Reaction Dynamics and Subsequent Reaction Steps.” *ChemPhysChem* 11(14):3113–22.

Vivian, James T. and Patrik R. Callis. 2001. “Mechanisms of Tryptophan Fluorescence Shifts in Proteins.” *Biophysical Journal* 80(5):2093–2109.

Volgraf, Matthew, Pau Gorostiza, Rika Numano, Richard H. Kramer, Ehud Y. Isacoff, and Dirk Trauner. 2006. “Allosteric Control of an Ionotropic Glutamate Receptor with an Optical Switch.” *Nature Chemical Biology* 2(1):47–52.

Volkov, Oleksandr, Kirill Kovalev, Vitaly Polovinkin, Valentin Borshchevskiy, Christian Bamann, Roman Astashkin, Egor Marin, Alexander Popov, Taras Balandin, Dieter Willbold, Georg Büldt, Ernst

Bamberg, and Valentin Gordeliy. 2017. “Structural Insights into Ion Conduction by Channelrhodopsin 2.” *Science* 358(6366).

Ward, Carl C., Jordan I. Kleinman, and Daniel K. Nomura. 2017. “NHS-Esters As Versatile Reactivity-Based Probes for Mapping Proteome-Wide Ligandable Hotspots.” *ACS Chemical Biology* 12(6):1478–83.

Wu, Xiang, Yuanwei Zhang, Kendra Takle, Osman Bilsel, Zhanjun Li, Hyungseok Lee, Zijiao Zhang, Dongsheng Li, Wei Fan, Chunying Duan, Emory M. Chan, Carlos Lois, Yang Xiang, and Gang Han. 2016. “Dye-Sensitized Core/Active Shell Upconversion Nanoparticles for Optogenetics and Bioimaging Applications.” *ACS Nano* 10(1):1060–66.

Yue, Lan, James D. Weiland, Botond Roska, and Mark S. Humayun. 2016. “Retinal Stimulation Strategies to Restore Vision: Fundamentals and Systems.” *Progress in Retinal and Eye Research*.

## Part III. Engineering the optical properties of diffusible photochromic ligands (PCLs)

# CHAPTER 7| Light-controlled activation of iGluRs by non-destructive caged ligands based on stilbene chromophore

### INTRODUCTION

Classical photopharmacology started with the modification of small molecules to make them light-activatable and to overcome poor drug specificity and undesired side effects. As previously described in the introduction, one strategy to achieve this goal is to protect the active drug with a photolabile group (caged compounds). Upon illumination the active drug is released together with other by-products. This widely used strategy started in 1978 by Hoffman and co-workers with the synthesis of the first "caged ATP". Since then, many other biological applications have benefit from the use of light controlled uncaging [1]: small molecules like neurotransmitters or ions ($Ca^{2+}$), nucleotides, nucleosides and inositols (ATP and cAMP); macromolecules like peptides and proteins to regulate enzymatic activity; or mRNA and DNA in the first application in vivo of uncaging compounds [2]. The success over years of caged compounds resides in their unique features: they are biologically inert before photolysis; the active drug is released with spatiotemporal control, in intracellular compartments or extracellularly with subcellular resolution with focused light beam; speed of the release is crucial, for example in the study of fast processes like neurotransmission; timing of the release is only controlled by the experimenter, orthogonal to physiological activity of the cell or animal before uncaging; amplitude and frequency of the activity can also be modulated by finely control light stimulation; and release can be quantified by coupling a fluorescent indicator to the uncaging event. In the field of neuroscience there are many attempts in the development of useful tools for the study of neural circuits, but complex biological environment required some special features for a caged compound to be useful. It must be water soluble but stable enough, and with a high rate of uncaging. First caged glutamate that combined all these characteristics was developed by Hess and co-workers with the name CNB-Glu [3]. Although the release is fast, CNB-Glu is not sensitive to two-photon uncaging, which limits its tissue penetration and possibly could induce phototoxicity. Next caged glutamate compounds were designed to be more two-photon sensitive, among them the most widely used is MNI-Glu[4], but others emerged later on: MDNI-Glu [5], CDNI-Glu [6], RuBi-Glu [7] and DEAC450-Glu [8].

However, the main inconvenience of previous described caged-glutame is the need to apply high concentration (mM) in the tissue to be effective. This overdose of compound has some side effect in other receptors like competition of glycine binding site in NMDA receptor subunit NR1[9], or antagonizing GABA-A receptors[8]. This crosstalk interferes in the study of circuit connectivity by inhibition of GABAergic responses and altering the correct excitatory-inhibitory balance. Also, important to take into account possible toxicity side-effects from by-products from incomplete or incorrect photolysis.

Another possible solution emerged from the introduction of a photochrome that can reversibly change its conformation, thereby modifying the activity of the drug reversibly controlled by light. These light-sensitive modified drugs are called photochromic ligands (PCLs). Ideally, the chemical design would combine drug activation upon illumination of the thermally stable inactive isoform while photo-preserving the entity of the PCL. But usually PCL design uses "*azologization*" strategy, which means that the most similar structure to parent drug is the active, and most of the times is the trans isomer. As an example, GluAzo synthesis was based on the introduction of an azobenzene in the glutamate analogue LY339434 (Figure 1), which was

sufficient to provide the compound with light sensitivity, with reversible activation of GluK1 and GluK2 glutamate receptors[10]. As with caged compounds, a lot of interest is put in the development of 2P sensitive PCLs to gain in spatial and subcellular resolution. Very encouraging results recently published demonstrate the potential of PCLs to be 2P-activated in complex tissue environment at significant lower concentrations compared to 2P uncaging [11]. However, compared with caged compounds, in both cases PCLs are constitutively active.

Here we aimed to design a cis-inactive drug, thermally stable, that only upon light stimulation is activated but without spillover of by-products of photo-uncaging. Chemical design and synthesis, together with photochemical characterization, were performed by Gisela Cabré in the laboratories of the Department of organic chemistry at the *Universitat Autonoma de Barcelona* (UAB). Her group named this new generation of PCLs as "non-destructive photocaged ligands".

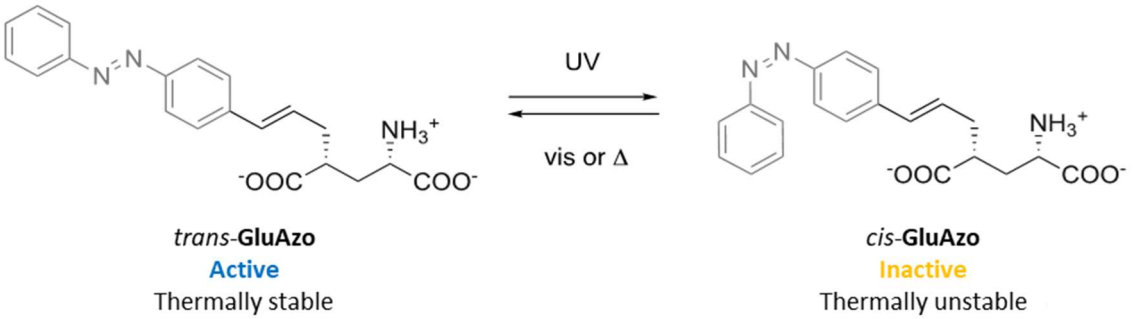


**Figure 1. Structure of GluAzo.** Thermally stable trans isomer can be reversible isomerized with pulses of UV light to the inactive cis-isomer. Thermally unstable cis-Gluazo (relaxation time 18h) can be back isomerized by visible light (500 nm)[10].

As for the design of caged compounds, important modifications in drug properties like water solubility, sensitivity to hydrolysis and rate of photoisomerization must be considered. The introduction of a hydrophobic chromophore to a moderately soluble natural drug makes it barely soluble at physiological pH. Also, the other main limitation of PCLs is the small change of activity with light (typically differences in activity of both isomers is less than 10-fold). The first strategy used was based on the substitution of the azobenzenic core of GluAzo (Volgraf et al., 2007), which constitutively activates glutamate receptors GluK1 and GluK2 because trans-isomer is thermally stable and active. By replacing the azobenzene with a stilbene photochrome (GluS) we aim to avoid integral receptor activation with an inactive cis-isomer thermally stable. Trans-cis photoisomerization of stilbenes is prevented so light-induced activation occurs irreversibly like caged compounds, but with 100% efficiency and without generating any by-product from photolysis. Previously described PCLs containing a stilbene as chromophore were used to photoregulate gene expression[12], inhibition of kinases[13], allosteric control of GPCRs[14] or as caging compounds of anticancer drugs[15].

## RESULTS

Now, as a proof of concept we want to explore its potential in the field of neuroscience taking as reference GluAzo. Photochemical characterization of **GluS1** (Figure S1) demonstrate a typical absorption spectrum for stilbenes in the UV-range (Figure S2) in polar media (MeOH solution). No changes over time in these spectral properties confirm the thermal stability of both isomers.

*Cis-trans* photoisomerization is achieved by 355 nm illumination and photostationary state reached perfectly matches with *trans*-**GluS1** spectra (Figure S3).

To test the different biological activity of both isomers of **GluS1**, whole-cell voltage clamp recordings were conducted on HEK293 cells expressing wild type GluK1(-eGFP). The activation by free glutamate in the media induce physiological channel opening and ion flux across the membrane (Traynelis et al., 2010). After perfusion of *trans*-**GluS1**, similar current as glutamate perfusion is evoked in these cells (Figure 2a). Perfusion of *cis*-GluS1 showed no change on membrane potential, as an indicative of no activation of the receptor. After, irradiation at 365nm isomerizes stilbene from cis to trans and we should see an increase in inward currents, thus indicating light-induced manipulation of GluK1. However, no light induced activity can be observed (Figure 2b) possibly due to photodimerization of stilbenes in aqueous buffer and formation of aggregates [16,17] that prevent trans isomer interaction with the receptor. These results were confirmed by photochemical characterization in aqueous media, where **GluS1** absorption spectra decreased and intensity of absorption band broadened over time irradiation. To counteract photocycloaddition reaction, spectral measurements where conducted in presence of surfactants to prevent aggregation in aqueous media. However, biological tests were not possible with high proportions of surfactants in the cell media so new chemical synthesis was carried out to improve water solubility.

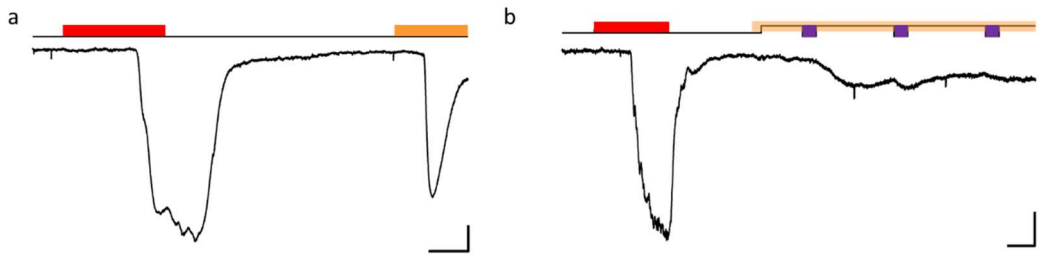


**Figure 2. Whole-cell voltage clamp recordings in tsA 201 HEK293 overexpressing GluK1 – eGFP**. Cells were incubated with ConA 10 min before recordings to prevent channel desensitization. Perfusion of 300 µM glutamate is indicated by a red bar, perfusion of *trans*-**GluS1** (30 µM) with an orange bar, and *cis*-**GluS1** (30 µM) with light orange bar. Light pulses at 380 nm (10 s) are shown in purple bars. Scale bar corresponds to 200 pA, 20 s.

A second generation of GluAzo-stilbene (**GluS2**) was designed and synthesized to improve all these drawbacks. In order to increase water solubility a carboxylic group was added to the phthalimide aromatic ring of **GluS1** (most non-polar part of the compound) (Figure S4). Photochemical properties of **GluS2** are comparable to features observed in **GluS1**: absorption band in the UV-range and thermal stability of both isomers (Figure S5). Spectral interrogation of **GluS2** in aqueous buffer showed better performance, being able to achieve cis-trans photostationary state comparable to *trans*-**GluS2** isomer spectra (Figure S6).

Both isomers of **GluS2** were tested under whole-cell voltage clamp conditions on HEK293 cells expressing wild type GluK2(-eGFP). The activation by free glutamate in the media prove physiological channel opening and ion flux across the membrane (Traynelis et al., 2010). Perfusion of *trans*-**GluS2** induced similar inward current as glutamate perfusion (Figure 3a).

Subsequent perfusion of *cis*-**GluS2** showed no change on membrane potential, as an indicative of no activation of the receptor. But upon irradiation at 350nm, *cis* to *trans* isomerization takes place and we can see an increase in inward currents, thus indicating light-induced manipulation of GluK2 (Figure 3b).

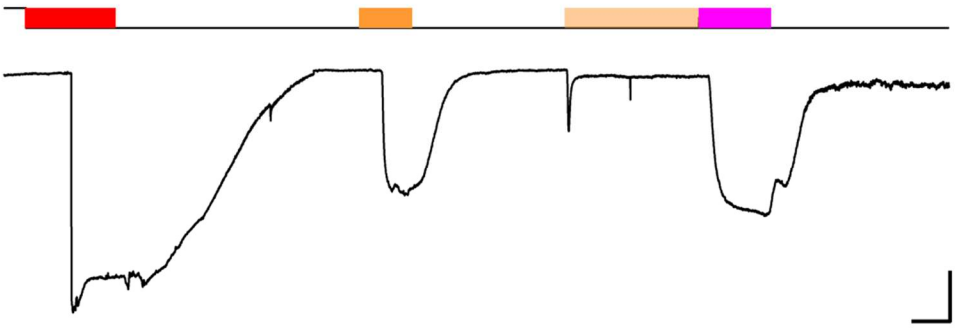

**Figure 3. Whole-cell voltage clamp recordings in tsA 201 HEK293 overexpressing GluK2 – eGFP.** Cells were incubated with ConA 10 min before recordings to prevent channel desensitization. Perfusion of 300 µM glutamate is indicated by a red bar, perfusion of *trans*-**GluS2** (3 µM) with an orange bar, and *cis*-**GluS2** (3 µM) with light orange bar. In presence of *cis*-**GluS2** (3 µM) stimulation with 350 nm light (purple bar) induces inward currents comparable to *trans*-**GluS2** (3 µM). Scale bar 500 pA, 20 s.

## DISCUSSION AND CONCLUSIONS

As a proof of concept here we demonstrate for the first time the capacity of stilbene-based compounds to specifically light-induce excitatory responses in native glutamate receptors.

As designed, stilbene-based compounds absorb in the UV-range of the spectra. Photoisomerization achieved in polar media demonstrate the capacity of one-way *cis-trans* isomerization with high efficiency and thermal stability of both isomers. However, solubility issues in non-polar media (bio-friendly) seemed compromised and new chemical synthesis was required. Chemical improvements accomplish by **GluS2** demonstrate in vitro isomer selective activation of endogenous glutamate receptors. Photoactivation of inactive *cis*-**GluS2** can evoke significant photoresponses comparable to direct *trans*-**GluS2** perfusion and in the same direction than native free glutamate response. Presumably, affinity of **GluS2** for GluK2 receptor seem high, eliciting around 50% of free glutamate response with 10-fold less concentration than **GluS1**, and compared with negligible photoresponses obtained with GluAzo at similar concentrations[10].

It is noteworthy that **GluS2** can be photoisomerized very efficiently with low light power (6.3 $\mu W \cdot mm^{-2}$, at 350 nm), as an indicative of high efficiency of photoconversion, and at low concentration (µM), facts that in future will prevent possible phototoxicity problems and side-effect issues with other neural receptors.

In vitro biological data obtained in this study agree with chemical design and further photochemical characterization of the compounds tested. I want to emphasize the importance to note that biological conditions do not always match with “cuvette” optimal conditions, and here we demonstrate that final chemical design can adapt to solve biological problems in its real environment, as good as a compenetrated gear machinery.

**Future experiments**

Further experiments to complete the pharmacological characterization are important to determine a dose response curve of **GluS2** in GluK1 and GluK2 receptors, as previously done for similar PCLs [10]. Stablish affinity compared to free glutamate will indicate us a more precise working concentration to be used in brain slice preparations. Additionally, determine if other glutamate receptors may be susceptible of **GluS2** activation and if they show any preference or interference will fully complete their characterization.

Promising results with stilbene **GluS2** encourage us in future applications in 3D tissues, where spatial resolution is crucial. As described before for caged-compounds for glutamate [18], 2P uncaging is the final approach in the spatial control of light activation. Specific activation with 2P will avoid spillover of glutamate or activated stilbene from planes unfocused and provide subcellular spatial resolution in complex circuits. Further modifications in the substituents of the stilbene core may enhance a push-pull effect that theoretically will shift its absorption spectra to the visible range or even make it susceptible to NIR light or 2P stimulation.

**Author contribution**

Ramon Alibés, Félix Busqué and Jordi Hernando conceived and supervised the project. Gisela Cabré designed and performed the chemical synthesis and the photochemical study. Aida Garrido-Charles performed in vitro electrophysiological characterization and organotypic slices were prepared by Miquel Bosch. Pau Gorostiza supervised in vitro experiments.

## SUPPLEMENTARY INFORMATION

### Supplementary figures

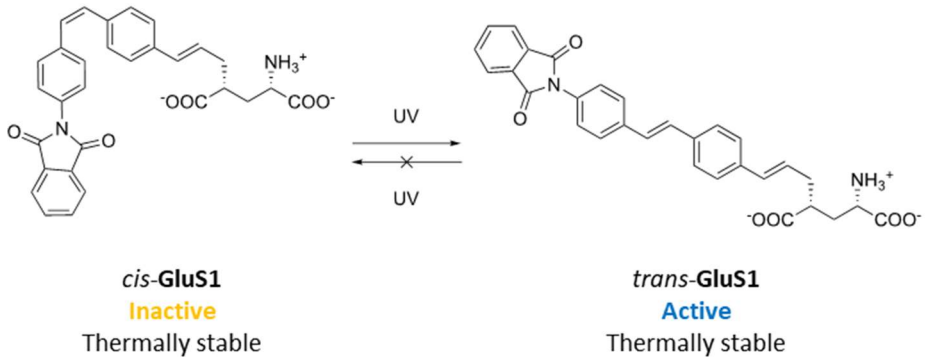


**Supplementary figure 1.** Photoinduced *cis*→*trans* isomerisation of novel NDCL *cis*-**GluS1** upon stilbene excitation with UV light. According to our design principles, the *trans*→*cis* photoisomerisation of this compound should be inhibited in polar media.

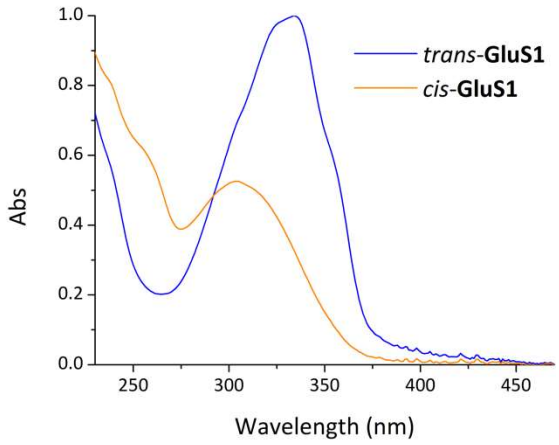


**Supplementary figure 2.** Absorption spectra of *cis*-**GluS1** and *trans*-**GluS1** in MeOH.

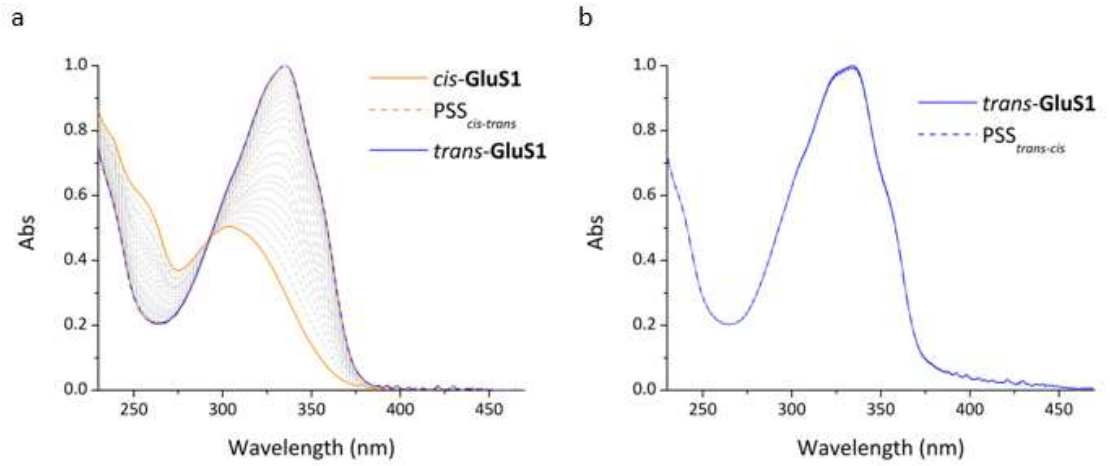


**Supplementary figure 3.** (a) Changes registered in the absorption spectra of *cis*-**GluS1** in MeOH upon irradiation at $\lambda_{exc}$ = 355 nm until a photostationaty state ($PSS_{cis\text{-}trans}$) was achieved. For sake of comparison, the absorption spectrum of *trans* -**GluS1** is also shown. (b) Absorption spectra of *trans*-**GluS1** upon irradiation at $\lambda_{exc}$ = 355 nm, which suffered no changes in time.

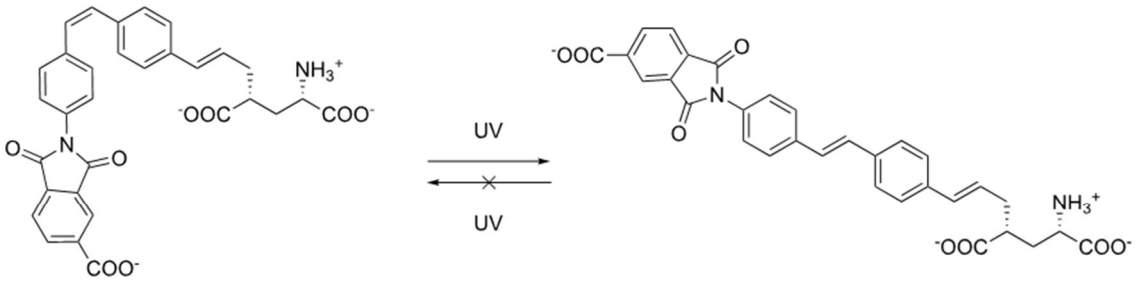


*cis*-**GluS2**
**Inactive**
Thermally stable

*trans*-**GluS2**
**Active**
Thermally stable

**Supplementary figure 4.** Photoinduced *cis*→*trans* isomerisation of novel NDCL *cis*-**GluS2** upon stilbene excitation with UV light. According to our design principles, the *trans*→*cis* photoisomerisation of this compound should be inhibited in polar media.

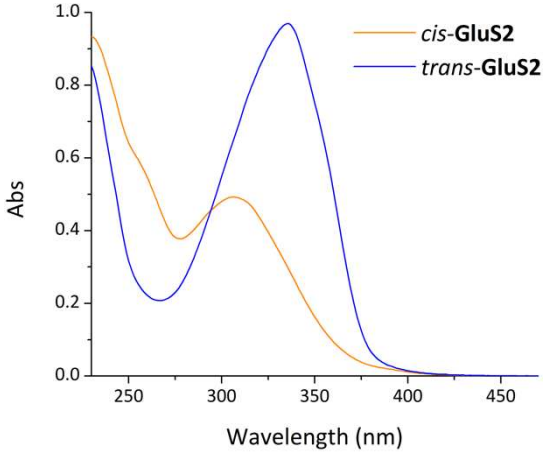

**Supplementary figure 5.** Normalised absorption spectra of *cis*-**GluS2** and *trans*-**GluS2** in PBS:MeOH, 2:1.

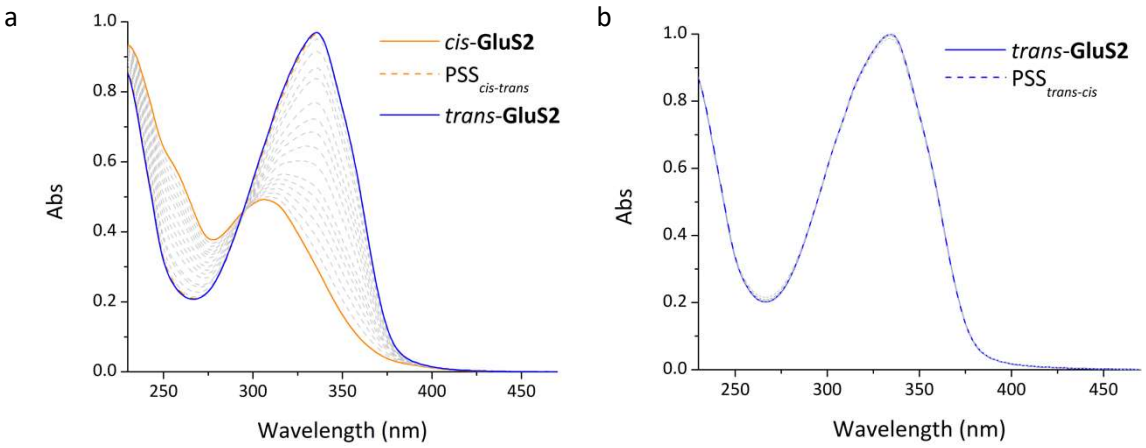


**Supplementary figure 6.** (a) Changes in the absorption spectra of *cis*-**GluS2** upon irradiation at $\lambda_{exc}$ = 355 nm in PBS:MeOH 2:1. Clear *cis*→ *trans* photoisomerisation occured, leading quantitatively to the *trans* isomer. (b) Absorption spectra of *trans*-**GluS2** upon irradiation of the *trans* isomer at $\lambda_{exc}$ = 355 nm in PBS:MeOH 2:1. Neither *trans*→ *cis* photoisomerisation nor photodegradation can be observed.

**Supplementary results**

Caged compounds in neuroscience are mostly used in the study of connectivity of circuits in complex tissues. So far, we demonstrated the ability of stilbene-based compounds to selectively induce similar glutamate-mediated excitatory responses in wild type kainate receptors. Although, to be comparable to caged glutamate compounds available in the market, stilbene-based PCLs must also demonstrate their differential activation capacity in complex tissue like brain slices.

**GluS2** performance in vitro demonstrated more bio-compatible characteristics and better photoisomerization properties compared to its former partner **GluS1**, for these reasons we decided to test **GluS2** potential on hippocampal organotypic slices of rat. As activation readout, organotypic slices were transiently expressing the genetically encoded calcium indicator GCaMP6s and as morphology marker the red fluorescent indicator dsRed2 (Figure S7a). The methods used to prepare hippocampal organotypic slices of rat are further explained in Appendix Protocol section.

First of all, we wanted to demonstrate, as done in HEK cells, the different activation capacity of *trans* and *cis* isomer of **GluS2**. Slices were imaged in a confocal microscope with a laser-rasting stimulation of the whole field of view. Baseline recording of neural activity do not show overactivation of neurons or cell death because of the procedure. During recording, slices are continuously perfused with physiological artificial cerebrospinal fluid (ACSF) bubbled with carbogen. Then, perfusion of *trans*-**GluS2** induced rapid calcium fluorescence increase as an indicator of glutamate receptor activation of all the neurons in the field of view (Figure S7b). Light stimulation in presence of trans-GluS2 at 405 nm and 514 nm did not induce any change in evoked calcium response more than slight photobleaching of GCaMP6s. On the other hand, *cis*-**GluS2** perfusion do not induce any change in calcium signal, indicating no activation of glutamate receptors (Figure S7c). After, in presence of *cis*-**GluS2** (30 µM) light stimulation at 405 nm followed by 514 nm light induces calcium signal increase comparable to *trans*-**GluS2** (30 µM) (Figure S7d). The delayed response observed at 514 nm may indicate a slower photoactivation due to low optimized light stimulation protocol (laser scanning at low intensity) or an indication that the wavelength used was incorrect. As observed in absorption spectra of **GluS2** (Figure S5), *trans* isomer absorption spectra could slightly be excited with 405 nm, but *cis* isomer optimal wavelength of excitation is far from it, around 330 nm. Morphology marker dsRed2 fluorescence do not change over the experiments, as an evidence that **GluS2** induces specific calcium mediated responses.

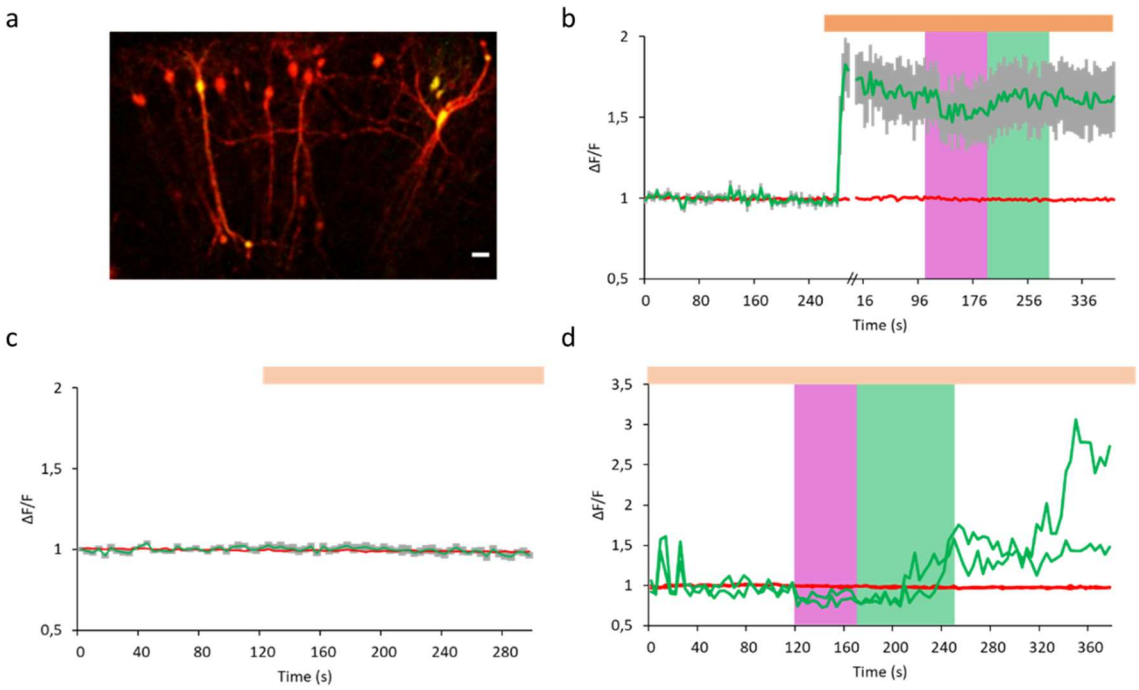


**Supplementary figure 7. $Ca^{2+}$ imaging responses in rat hippocampal organotypic slices**. a) Microphotograph of rat hippocampal slices transiently expressing GCaMP6s:dsRed2. Scale bar is 50 µm. b) Average responses of neurons after perfusion of *trans*-**GluS2** (30 µM, orange bar; n=8) and c) *cis*-**GluS2** (30 µM, light orange bar; n=20). GCaMP6s signal is showed as green trace and dsRed2 signal as red trace. Error bars are ±SEM. Time bar in b) is split to point the concatenation of two subsequent experiments. d) Real time traces of two neurons responding to light stimulation after *cis*-**GluS2** (30 µM, light orange bar) perfusion. Light stimulation was performed with whole field laser scanning at 405 nm (0.37 mW $\mu m^{-2}$) and 514 nm (0.35 mW $\mu m^{-2}$) at resolution of 256x256, with at a frame rate of 300 ms.

## REFERENCES


1. Ellis-Davies, G. C. R. Caged compounds: Photorelease technology for control of cellular chemistry and physiology. *Nat. Methods* **4**, 619–628 (2007).
2. Ando, H., Furuta, T., Tsien, R. Y. & Okamoto, H. Photo-mediated gene activation using caged RNA/DNA in zebrafish embryos. *Nat. Genet.* **28**, 317–325 (2001).
3. Wieboldt, R. *et al.* Photolabile precursors of glutamate: Synthesis, photochemical properties, and activation of glutamate receptors on a microsecond time scale. *Proc. Natl. Acad. Sci. U. S. A.* **91**, 8752–8756 (1994).
4. Matsuzaki, M. *et al.* Dendritic spine geometry is critical for AMPA receptor expression in hippocampal CA1 pyramidal neurons. *Nat. Neurosci.* **4**, 1086–1092 (2001).
5. Fedoryak, O. D., Sul, J. Y., Haydon, P. G. & Ellis-Davies, G. C. R. Synthesis of a caged glutamate for efficient one- and two-photon photorelease on living cells. *Chem. Commun.* 3664–3666 (2005). doi:10.1039/b504922a
6. Ellis-Davies, G. C. R., Matsuzaki, M., Paukert, M., Kasai, H. & Bergles, D. E. 4-Carboxymethoxy-5,7-dinitroindolinyl-glu: An improved caged glutamate for expeditious ultraviolet and two-photon photolysis in brain slices. *J. Neurosci.* **27**, 6601–6604 (2007).
7. Fino, E. *et al.* RuBi-Glutamate: Two-photon and visible-light photoactivation of neurons and dendritic spines. *Front. Neural Circuits* **3**, 1–9 (2009).
8. Olson, J. P. *et al.* Optically selective two-photon uncaging of glutamate at 900 nm. *J. Am. Chem. Soc.* **135**, 5954–5957 (2013).
9. Maier, W., Corrie, J. E. T., Papageorgiou, G., Laube, B. & Grewer, C. Comparative analysis of inhibitory effects of caged ligands for the NMDA receptor. *J. Neurosci. Methods* **142**, 1–9 (2005).
10. Volgraf, M. *et al.* Reversibly caged glutamate: a photochromic agonist of ionotropic glutamate receptors. *J. Am. Chem. Soc.* **129**, 260–1 (2007).
11. Pittolo, S. *et al.* Reversible silencing of endogenous receptors in intact brain tissue using 2-photon pharmacology. *Proc. Natl. Acad. Sci. U. S. A.* **116**, 13680–13689 (2019).
12. Ogasawara, S. & Maeda, M. Photoresponsive 5'-cap for the reversible photoregulation of gene expression. *Bioorganic Med. Chem. Lett.* **21**, 5457–5459 (2011).
13. Schmidt, D. *et al.* Axitinib: A Photoswitchable Approved Tyrosine Kinase Inhibitor. *ChemMedChem* **13**, 2415–2426 (2018).
14. Jones, B. J. *et al.* Potent prearranged positive allosteric modulators of the glucagon-like peptide-1 receptor. *ChemistryOpen* **6**, 501–505 (2017).
15. Paul, A. *et al.* Push-Pull Stilbene: Visible Light Activated Photoremovable Protecting Group for Alcohols and Carboxylic Acids with Fluorescence Reporting Employed for Drug Delivery. *Org. Lett.* **21**, 2968–2972 (2019).
16. Ito, Y., Kajita, T., Kunimoto, K. & Matsuura, T. Accelerated Photodimerization of Stilbenes in Methanol and Water. *J. Org. Chem.* **54**, 587–591 (1989).
17. Syamala, M. S. & Ramamurthy, V. Consequences of Hydrophobic Association in Photoreactions: Photodimerization of Stilbenes in Water. *J. Org. Chem.* **51**, 3712–3715 (1986).
18. Ellis-Davies, G. C. R. Two-Photon Uncaging of Glutamate. *Front. Synaptic Neurosci.* **10**, 1–13 (2019).

# CHAPTER 8| Synthetic photoswitchable neurotransmitters based on bridged azobenzenes

Gisela Cabré[a,‡], Aida Garrido-Charles[b,‡], Àngels González-Lafont[a,c], Widukind Moormann[d], Daniel Langbehn[d], David Egea[a], José M. Lluch[a,c], Rainer Herges[d], Ramon Alibés[a], Félix Busqué[a], Pau Gorostiza[b,e,f,*] and Jordi Hernando[a,*]

[a] Departament de Química, Universitat Autònoma de Barcelona (UAB), Cerdanyola del Vallès, Spain.
[b] Institut de Bioenginyeria de Catalunya (IBEC), Barcelona Institute of Science and Technology (BIST), Barcelona, Spain.
[c] Institut de Biotecnologia i Biomedicina (IBB), UAB, Cerdanyola del Vallès, Spain.
[d] Otto Diels-Institute of Organic Chemistry, Christian Albrechts University Kiel, Kiel, Germany.
[e] Institució Catalana de Recerca i Estudis Avançats (ICREA), Barcelona, Spain.
[f] Centro de Investigación Biomédica en Red en Bioingeniería, Biomateriales y Nanomedicina, Zaragoza, Spain.
*Supporting Information Placeholder*

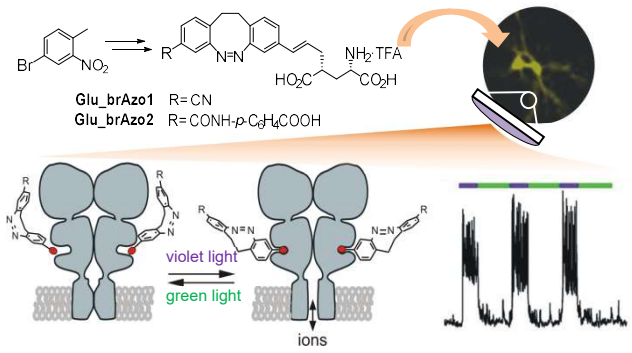


**ABSTRACT:** Photoswitchable neurotransmitters of ionotropic kainate receptors were synthesized by tethering a glutamate moiety to disubstituted C2-bridged azobenzenes, which were prepared through a novel methodology that allows access to diazocines with higher yields and chemical versatility. Because of the singular properties of these photochromes, photoisomerizable compounds were obtained that show larger thermal stability for their inert *cis* isomer while presenting tunable biological activity in the *trans* state. This enabled selective neuronal firing upon irradiation without background activity in the dark.

By enabling remote manipulation of neuronal signaling with light, optogenetics[1] and photopharmacology[2] have revolutionized neuroscience and neurobiology. Neural receptors responding to glutamate (GluRs), the primary excitatory neurotransmitter, are one of the major targets in these fields, since they regulate several key processes in the nervous system and are related to numerous diseases.[3] As such, a plethora of photopharmacological tools have been developed for lightgating GluRs,[4] among which photochromic ligands (PCLs)[5–12] are often preferred because they combine (a) the advantages of small-molecule, freely diffusing drugs with (b) the capacity for reversibly photoswitching their activity without byproduct generation nor modification of native receptors.[2,4] The major strategy employed to derive PCLs relies on introducing an azoaromatic photoswitch into the structure of well-known, biologically active ligands.[2,4] Upon *trans*−*cis* photoisomerization,[13] a geometrical change is induced in these compounds that alters their interaction with the receptor. Typically, the more extended configuration of the *trans* isomer favors such interaction, while affinity is reduced for the folded *cis* state due to steric effects (i.e., *trans*-active PCLs).[2,4] Because of the inherent photochemical properties of azoaromatic compounds,[13] this imposes a severe limitation to most PCLs developed to date for GluRs[5–11] (and other receptors[2] ): they are active in the dark, where they lie in the more stable *trans* state. Consequently, these compounds elicit strong tonic responses in the absence of illumination (e.g., when acting as receptor agonists), which drastically hampers their use. This is the case of **GluAzo** (Figure 1a), which is a *trans*-active, transstable partial agonist of ionotropic kainate receptors GluK1 and GluK2,[5,14,15] two of the principal GluRs mediating excitatory neurotransmission in the central nervous system.[3]

To overcome this obstacle while preserving the main design principles behind azo-based PCLs, bridged azobenzenes (brAzo) such as diazocines (C2 bridge, Figure 1b) could be used as photochromes, since they (a) should also favor transactive behavior by switching between extended *trans* and bent *cis* configurations but (b) exhibit *cis* thermal stability.[16–23] This combination of properties should therefore allow direct administration of the inert *cis* form of the PCL, which could then be selectively photoactivated. In addition, diazocines isomerize with visible light,[16–23] which is a further advantage with respect to common UV-responding azoaromatic compounds.[13] However, the limited synthetic accessibility and versatility of these photochromes have so far limited their application to the photocontrol of biological systems.[22,23b]

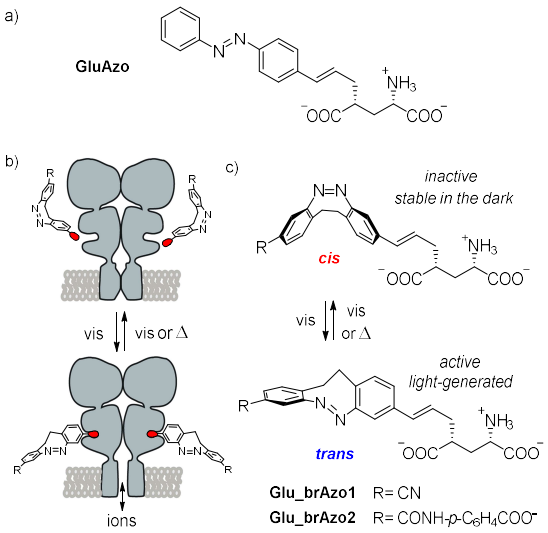


**Figure 1.** (a) Structure of **GluAzo**.[5] (b) Strategy proposed to prepare *trans*-active, *cis*-stable PCLs based on C2-bridged azobenzenes for the light-control of neuronal membrane receptors GluK1 and GluK2. (b) Photoisomerization of **Glu_brAzo1-2**.

Actually, their use in photopharmacology to modulate the activity of N-methyl-D-aspartate (NMDA) receptors and potassium ion channels has only been reported very recently,[24] for which a low-yield 4-monosubstituted diazocine previously described was employed.[23]

In this work we aim to apply this strategy to photocontrol GluK1 and GluK2, while broadening its scope by developing diazocine-based PCLs with larger yields and multiple functionalization sites to favor chemical versatility. To reach this goal our attention focused on 3,3′-disubstituted diazocines,[17,18,21] because very inefficient syntheses have been reported to date for 4,4′-disubstituted analogues (<1% yield[22]). On the basis of these photochromes and the structure of **GluAzo**,[5] we designed **Glu_brAzo2** as the first *trans*-active, *cis*-stable agonist of GluK1 and GluK2 by tethering a diazocine unit to a biologically active glutamate moiety through a vinyl linker (Figure 1c). In addition, we took advantage of the disubstitution pattern of the photochrome to introduce a lateral ionic, bulky group for (a) enhancing solubility in aqueous media and (b) further hindering the interaction of the *cis* isomer with the receptor by increasing the steric congestion around the glutamate moiety. The latter should boost the difference in activity between the two states of the PCL, a required feature given the moderate photoconversions of most functionalized diazocines.[17,18,20–23] To evaluate this effect, **Glu_brAzo1** lacking the additional bulky substituent was also synthesized (Figure 1c).

To validate our design principles, we conducted molecular docking simulations for the two isomers of **Glu_brAzo1-2** on kainate receptors. Our attention particularly focused on GluK2, since (a) it presents a narrower binding cavity that imposes larger steric constraints to ligands,[25] and (b) the crystallographic structure of its ligand-binding domain after complexation with *trans*-**GluAzo** is available.[15] Dockings were computed on this structure keeping the protein rigid, while the initial geometries of the PCLs were optimized at the B3LYP/6-31G(d) level. In all the cases, the best docking solutions placed the glutamate moiety of the ligands in a very similar position as with *trans*-**GluAzo**, [26] thus suggesting analogous interaction with the receptor via hydrogen bonds. However, clear differences were observed for the binding arrangement of each ligand (Figure 2 and Figure S1), which led to different complexation energies

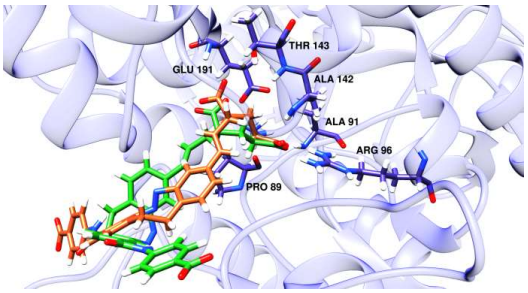


**Figure 2.** Best docking solutions for *trans*-**Glu_brAzo2** (orange) and *cis*-**Glu_brAzo2** (green) in GluK2. The protein residues interacting with the glutamate group of both ligands are also indicated. Oxygen, nitrogen and hydrogen atoms are depicted in red, blue and white, respectively.

(in Chemscore units[27]): 41.2, 37.0, 48.0, and 37.3 for *trans*-**Glu_brAzo1**, *cis*-**Glu_brAzo1**, *trans*-**Glu_brAzo2**, and *cis*-**Glu_brAzo2**, respectively. Importantly, these figures indicate larger affinity of the *trans* isomers of **Glu_brAzo1-2** to GluK2, thus preserving the targeted *trans*-active behavior of **GluAzo**. By contrast, they do not support our hypothesis that the introduction of an ionic, bulky group in **Glu_brAzo2** should decrease the binding efficiency of the *cis* isomer with respect to less hindered **Glu_brAzo1**. It must be noted, however, that this is compensated by the higher complexation energy calculated for *trans*-**Glu_brAzo2** relative to *trans*-**Glu_brAzo1**, which arises from the additional attractive hydrogen bonding and lipophilic interactions formed between its bulky group and the receptor. Therefore, an enhanced contrast in biological activity is indeed to be expected between the two states of **Glu_brAzo2**, as originally designed.

On the basis of our experience in the synthesis of C2- bridged azobenzenes[16–21] and light-responsive glutamate ligands,[28–30] we devised a linear sequence to prepare **Glu_brAzo1-2** by Heck coupling reaction between their constituting units: a 3,3′-disubstituted diazocine and previously reported, protected glutamate derivative 1[29] (Scheme 1). The preparation of the photochromic unit started from commercially available 4-bromo-2-nitrotoluene, 3, which was subjected to deprotonation with

potassium tert-butoxide and further oxidation with bromine to afford dinitro derivative 4.

**Scheme 1. Synthesis of Glu_brAzo1 and Glu_brAzo2**

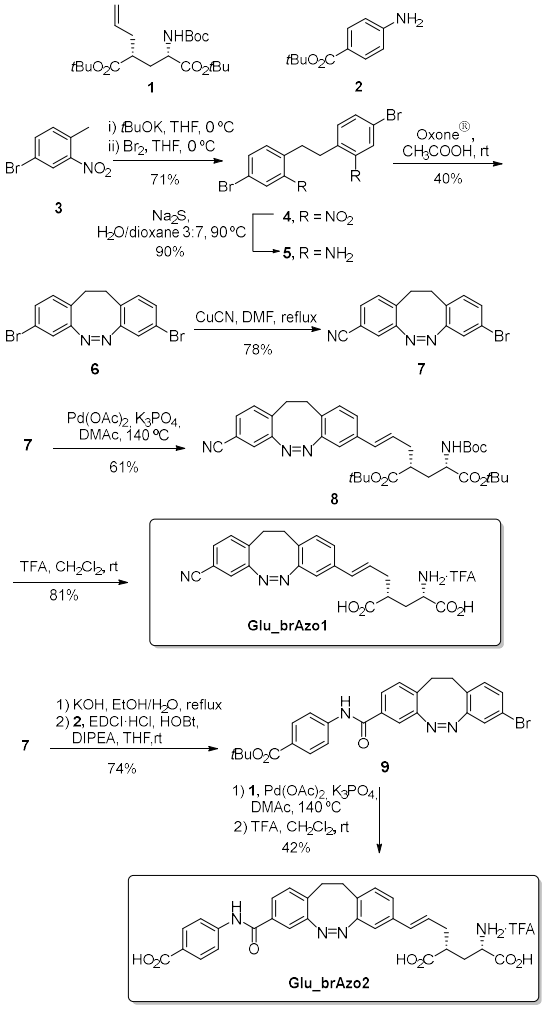


When attempting common reductive ring-closing conditions on this intermediate that had been previously reported for the synthesis of diazocines (e.g., Zn, Ba(OH)2),[16–21] formation of the desired bridged azobenzene was only observed with very low yields (<14%). This prompted us to develop a new methodology for the azocyclization process, for which we explored the Mills coupling reaction. With this aim, we first reduced the nitro groups of 4 using sodium sulfide,[31] which delivered diamine 5 in 90% yield. Then, the oxidative coupling of 5 was undertaken in the presence of Oxone[32] in glacial acetic acid[33] at room temperature for 1 h, which nicely furnished dibromosubstituted diazocine 6 in good yield (40%). According to this result, Oxone-mediated oxidation of one of the aniline moieties to provide the corresponding nitrosoarene followed by condensation with the other, unaltered aniline emerges as a novel one-pot synthesis of diazocines with reproducible yields. Azobenzene 6 was next monocyanated under standard Rosenmund−von Braun conditions[34] to obtain common asymmetric diazocine 7 in 78% yield (based on recovered 6). This compound was directly coupled to glutamate 1 under palladium catalysis, for which proper selection of the base and the solvent was found to be fundamental. After several tests, the reaction was performed with K3PO4 and N,N-dimethylacetamide[35] at 140 °C under argon in the presence of 0.1 mol % Pd(OAc)2, which delivered 8 in 61% yield. Finally, acid removal of the protecting groups gave the target compound **Glu_brAzo1** as its monotrifluoroacetate salt in good yield. For **Glu_brAzo2**, intermediate 7 was hydrolyzed in basic medium to give the corresponding acid, which was then tethered to previously prepared amine 2 using carbodiimide coupling reagent EDCl·HCl along with HOBt to afford 9 in 74% yield for the two steps. The Heck reaction of this compound with 1 under the aforementioned conditions and subsequent removal of the protecting groups finally delivered the target PCL. It must be noted that, despite its larger structural complexity, **Glu_brAzo2** was obtained with an overall yield that is ca. 2- to 10-fold larger than those recently reported for diazocine-based PCLs,[24] thus paving the way for the general application of this strategy in photopharmacology.

By comparison with previous data reported for diazocines,[16–21] NMR and UV−vis absorption analysis confirmed the formation of the *cis* isomer of **Glu_brAzo1-2** due to their larger stability. In addition, upon irradiation of their n−π* absorption band with violet light (λabs,max ∼ 395 nm, λexc = 405 nm), spectral changes were observed indicative of *cis*−*trans* isomerization (Figure 3a and Figures S2−S4). This is the case of the new red-shifted

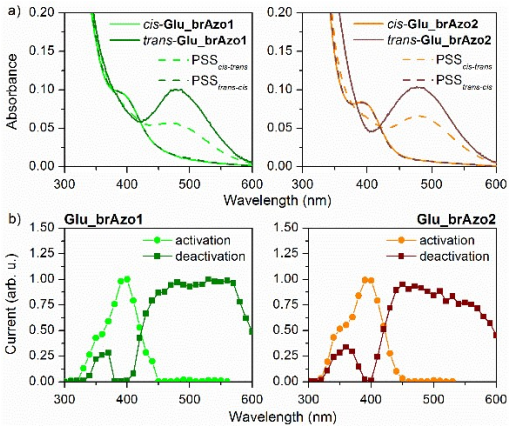


Figure 3. (a) Absorption spectra of both isomers of **Glu_brAzo1** and **Glu_brAzo2** in PBS:DMSO 1:1, as well as of the PSS mixtures obtained under *cis*−*trans* (λexc = 405 nm) and *trans*−*cis* (λexc = 532 nm) photoisomerization. (b) Activation and deactivation spectra of GluK2 in HEK293 cells after perfusion of **Glu_brAzo1** or **Glu_brAzo2** and irradiation to induce *cis*−*trans* (for activation) and *trans*−*cis* (for deactivation) photoisomerization.

absorption band found at λabs,max ~ 480 nm, which is distinctive of the *trans* isomer of diazocines[16–18,20–23] and allowed the isomerization process to be reverted by green light illumination (λexc = 532 nm, Figure 3a and Figures S2, S3, and S5). Further characterization of **Glu_brAzo1-2** revealed that they undergo *cis*−*trans* photoisomerization with moderate quantum yields (Φ*cis*−*trans* ~ 0.1) and efficiencies in aqueous media (Table S1), which resulted in photostationary state mixtures (PSS *cis*−*trans*) containing 47% and 60% of their trans isomer, respectively. By contrast, *trans*−*cis* photoconversion proceeded quantitatively with high quantum yields (Φ*trans*−*cis* ~ 0.9), thus ensuring fast lightinduced recovery of *cis*-**Glu_brAzo1-2** (Table S1) and repetitive photoswitching without degradation (Figure S6). Back-isomerization of the *trans* state of these compounds was also found to occur in the dark, though at a much longer time scale (t1/2 ~ 4 h at 298 K in aqueous media, Figure S7 and Table S1).

To assess the capacity of **Glu_brAzo1-2** to light-gate GluRs, whole-cell voltage clamp recordings were conducted on HEK293 cells expressing GluK1 or GluK2, whose activation causes channel opening and ion flux across the membrane (Figure 1b).[3,5] After perfusion of **Glu_brAzo1-2**, clear changes in the currents evoked in these cells were observed upon irradiation, which were consistent with the different absorption properties of their *cis* and *trans* isomers (Figure 3b and Figures S8−S10). In particular, maximal inward currents arising from receptor activation were measured at λexc = 390−400 nm (i.e., when inducing *cis*−*trans* photoisomerization of the PCLs). Minimal signals due to receptor deactivation were instead detected in the dark (i.e., for *cis*-**Glu_brAzo1-2**) and at λexc > 450 nm (i.e., upon *trans*−*cis* photoisomerization). As predicted by our molecular docking calculations, preferential interaction between the glutamate agonist ligand and GluK1/GluK2 was therefore observed for the trans state of **Glu_brAzo1-2,** which allowed light-induced manipulation of these receptors.

The *trans*-active behavior of **Glu_brAzo1-2** was further demonstrated when measuring their dose−response curves with GluK1 and GluK2 in the dark and at λexc = 390 (10−300 μM, Figure S11). In all the cases, larger inward current signals were retrieved for the PSS *cis*−*trans* mixture generated upon irradiation of the initial *cis* isomer, though with (a) low-tomoderate photoinduced modulation (ca. 10−35% current increase with respect to the dark) and (b) maximal values that were only about 20−40% of those evoked by free glutamate at 300 μM. Three main factors should account for these results: incomplete photoconversion into the active *trans* isomer, as observed in solution (<60%, Table S1); ; limited modification of the glutamate-binding site affinity upon *cis*−*trans* isomerization; and the steric effects imparted by the appended diazocine group with respect to free glutamate even in its less hindered *trans* configuration, which are of especial importance for GluK2 interaction because of its narrower ligand-binding cavity.[25] Actually, the latter accounts for the lower inward current signals with higher light-induced selectivity obtained for this receptor. However, it did not prevent **Glu_brAzo2** that bears a bulkier terminal group from (a) showing higher activity (ca. 2-fold increase with respect to **Glu_brAzo1** for GluK2), as anticipated by our molecular docking simulations, which (b) is further modulated upon photoisomerization, as pursued in our initial design.

**Glu_brAzo1-2** were finally tested as photoswitchable neurotransmitters in hippocampal neurons where GluK2 is highly expressed.[36] Because of their *trans*-active, *cis*-stable behavior, physiological behavior was not altered upon perfusion of **Glu_brAzo1-2** in the dark, a clear advantage over most PCLs reported for GluRs to date such as **GluAzo**. [5–11] Neuronal firing was instead selectively induced upon *cis*−*trans* photoisomerization of **Glu_brAzo2** at relatively low concentrations (30 μM, Figure 4a−c) and weak light intensities (22.0 and 47.4 μW mm$^{-2}$ at λexc = 390 and 530 nm, respectively). As a result, sequential and sustained trains of action potentials could be triggered with **Glu_brAzo2** by consecutively switching between violet and green light illumination, even at low irradiation powers and high excitation frequencies (up to 1 Hz, Figure 4c). Interestingly, this photoinduced behavior was inhibited by addition of DNQX,[37] a well-known antagonist of kainate and AMPA GluRs (Figure 4d), which further demonstrates that the efficient

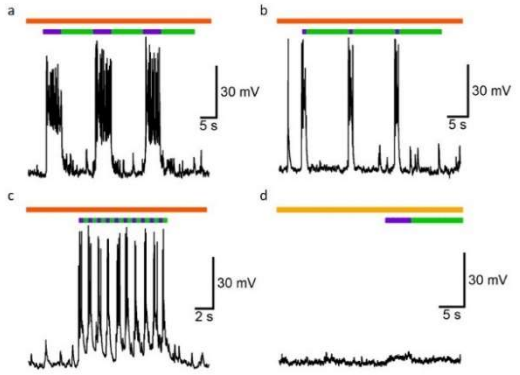


**Figure 4.** Whole-cell current clamp recordings of rat hippocampal neurons in culture after perfusion of **Glu_brAzo2** (30 μM) and irradiation at $\lambda_{exc}$ = 390 (purple) and 530 nm (green). Successful neuron activation was observed with 390 nm light pulses of (a) 5 s, (b) 1s, and (c) 0.5 s (1 Hz stimulation), while it was inhibited upon perfusion of DNQX (10 μM). Neurons were current clamped at -60 mV and, to truly report on their GluK2-mediated gating and connectivity, no Concanavalin A was used to prevent receptor desensitization after activation.

photoactivation of hippocampal neurons accomplished with **Glu_brAzo2** arose from its light-dependent interaction with those glutamate receptors. Noticeably, this clean physiological effect was achieved despite the limited activity modulation measured upon **Glu_brAzo2** photoisomerization in GluK2-expressing HEK293 cells (ca. 20% at 30 μM concentration), while it could not be reproduced with the slightly less efficient **Glu_brAzo1** agonist (Figure S12). We ascribe this situation to the well-known nonlinear behavior of neuronal signaling, since ligand interaction with a minimum fraction of glutamate receptors is needed to overcome the depolarization threshold required to initiate an action potential.[5] In our case, such a threshold was only surpassed with *trans*-**Glu_brAzo2**, probably due to its larger affinity for GluK2, as suggested by our measurements in cultured cells.

In conclusion, we demonstrated in this work the potential of C2-bridged azobenzenes for the preparation of azo-based photochromic ligands capable of light-controlling neural receptors, which preserve the larger activity typically observed for their *trans* state while ensuring larger stability for the inert *cis* isomer. By introducing a novel synthetic methodology for the preparation of 3,3′-disubstituted diazocines based on an Oxone-mediated intramolecular azocyclization reaction, the desired ligands could be obtained with higher yields and larger versatility, thus enabling fine-tuning of their light-dependent biological response. As a proof of concept, this strategy was applied to the preparation of new photoswitchable neurotransmitters for the light-induced operation of kainate glutamate receptors, with which we achieved selective neural firing upon irradiation without background activity in the dark.

## ASSOCIATED CONTENT

### Supporting Information

The Supporting Information is available free of charge on the ACS Publications website.
General methods and materials, synthetic procedures, and additional computational, photochemical and electrophysiological data (PDF)

## AUTHOR INFORMATION


### Corresponding Author

* pau@icrea.cat (P.G.), jordi.hernando@uab.cat (J.H.)

### Author Contributions

‡These authors contributed equally.


### Notes

The authors declare no competing financial interests.

## ACKNOWLEDGMENT


We acknowledge financial support from MINECO/FEDER (projects CTQ2015-65439-R, CTQ2016-80066-R, CTQ2016-75363-R and CTQ2017-83745-P), AGAUR/Generalitat de Catalunya (CERCA Programme and projects 2017-SGR-00465 and 2017-SGR-1442), Human Brain Project WAVESCALES projects, Fundaluce foundation, and Deutsche Forschungsgemeinschaft (SFB677). G. C. acknowledges the Generalitat de Catalunya for her pre-doctoral FI grant. A. G.-C. was supported by fellowship BES-2014-068169.


## REFERENCES


() (a) Deisseroth, K. *Nat. Methods* **2011**, *8*, 26-29. (b) Deisseroth, K. *Nat. Neurosci.* **2015**, *18*, 1213-1225.

(2) (a) Gorostiza, P; Isacoff, E. Y. *Science* **2008**, *322*, 395-399. (b) Fehrentz, T.; Schonberger, M.; Trauner, D. *Angew. Chem., Int. Ed.* **2011**, *50*, 12156−12182. (c) Kramer, R. H.; Mourot, A.; Adesnik, H. *Nat. Neurosci.* **2013**, *16*, 816−823. (d) Velema, W. A.; Szymanski, W.; Feringa, B. L. *J. Am. Chem. Soc.* **2014**, *136*, 2178−2191. (e) Berlin, S.; Isacoff, E. Y. *EMBO Rep.* **2017**, *18*, 677-692. (f) Hüll, K.; Morstein, J.; Trauner, D. *Chem. Rev.* **2018**, *118*, 10710-10747.

(3) (a) Traynelis, S. F.; Wollmuth, L. P.; McBain, C. J.; Menniti, F. S.; Vance, K. M.; Ogden, K. K.; Hansen, K. B.; Yuan, H.; Myers, S. J.; Dingledine, R. *Pharmacol. Rev.* **2010**, *62*, 405–496. (b) Niswender, C. M.; Conn, P. J. *Annu. Rev. Pharmacol. Toxicol.* **2010**, *50*, 295–322. (c) Bowie, D. *CNS Neurol Disord Drug Targets* **2008**, *7*, 129–143.

(4) Reiner, A.; Levitz, J.; Isacoff, E. Y. *Curr. Opin. Pharmacol*. **2015**, *20*, 135-143.

(5) Volgraf, M.; Gorostiza, P.; Szobota, S.; Helix, M. R.; Isacoff, E. Y.; Trauner, D. *J. Am. Chem. Soc.* **2007**, *129*, 260-261.

(6) Stawski, P.; Sumser, M.; Trauner, D. *Angew. Chem. Int. Ed.* **2012**, *51*, 5748-5751.

(7) Pittolo, S.; Gómez-Santacana, X.; Eckelt, K.; Rovira, X.; Dalton, J.; Goudet, C.; Pin, J. P.; Llobet, A.; Giraldo, J.; Llebaria, A.; Gorostiza, P. *Nat. Chem. Biol.* **2014**, *10*, 813-815.

(8) Rovira, X.; Trapero, A.; Pittolo, S.; Zussy, C.; Faucherre, A.; Jopling, C.; Giraldo, J.; Pin, J.-P.; Gorostiza, P.; Goudet, C.; Llebaria, A. *Cell Chem. Biol.* **2016**, *23*, 929−934.

(9) Barber, D. M.; Liu, S. A.; Gottschling, K.; Sumser, M.; Hollmann, M.; Trauner, D. *Chem. Sci.* **2017**, *8*, 611–615.

(0) Gómez-Santacana, X.; Pittolo, S.; Rovira, X.; Lopez, M.; Zussy, C.; Dalton, J. A. R.; Faucherre, A.; Jopling, C.; Pin, J.-P.; Ciruela, F.; Goudet, C.; Giraldo, J.; Gorostiza, P.; Llebaria, A. *ACS Cent. Sci.* **2017**, *3*, 81-91.

(1) Hartrampf, F. W. W.; Barber, D. M.; Gottshcling, K.; Leippe, P.; Hollmann, M.; Trauner, D. *Tetrahedron* **2017**, *73*, 4905-4912.

(2) Laprell, L.; Repak, E.; Franckevicius, V.; Hartrampf, F.; Terhag, J.; Hollmann, M.; Sumser, M.; Rebola, N.; DiGregorio, D. A.; Trauner, D. *Nat. Commun*. **2015**, *6*, *8076*.

(3) Bandara, H. M. D.; Burdette, S. C. *Chem. Soc. Rev.* **2012**, *41*, 1809-1825.

(4) Abrams, Z. R.; Warrier, A.; Trauner, D.; Zhang, X. *Front. Neural Circuits* **2010**, *4*, 13.

(5) Reiter, A.; Skerra, A.; Trauner, D.; Schiefner, A. *Biochemistry* **2013**, *52*, 8972-8974.

(6) Siewertsen, R.; Neumann, H.; Buchheim-Stehn, B.; Herges, R.; Nather, C.; Renth, F.; Temps, F. *J. Am. Chem. Soc.* **2009**, *131*, 15594−15595.

(7) Sell, H.; Nather, C.; Herges, R. *Beilstein J. Org. Chem.* **2013**, *9*, 1−7.

(8) Tellkamp, T.; Shen, J.; Okamoto, Y.; Herges, R. *Eur. J. Org. Chem.* **2014**, *2014*, 5456−5461.

(9) Hammerich, M.; Schütt, C.; Stahler, C.; Lentes, P.; Rohricht, F.; Höppner, R.; Herges, R. *J. Am. Chem. Soc.* **2016**, *138*, 13111−13114.

(20) Moormann, W.; Langbehn, D.; Herges, R. *Synthesis* **2017**, *49*, 3471-3475.

(2) Moormann, W.; Langbehn, D.; Herges, R. *Beilstein J. Org. Chem.* **2019**, *16*, 727-732.

(22) Samanta, S.; Qin, C. G.; Lough, A. J.; Woolley, G. A. *Angew. Chem. Int. Ed.* **2012**, *51*, 6452−6455.

(23) (a) Joshi, D. K.; Mitchell, M. J.; Bruce, D.; Lough, A. J.; Yan, H. *Tetrahedron* **2012**, *68*, 8670-8676. (b) Eljabu, F.; Dhruval, J.; Yan, H. *Bioorg. Med. Chem. Lett.* **2015**, *25*, 5594-5596; (c) Jun, M.; Joshi, D. K.; Yalagala, R. S.; Vanloon, J.; Simionescu, R.; Lough, A. J.; Gordon, H. L.; Yan, H. *ChemistrySelect* **2018**, *3*, 2697−2701.

(24) Thapaliya, E. R.; Zhao, J.; Ellis-Davies, G. C. R. *ACS Chem. Neurosci.* **2019**, 10.1021/acschemneuro.8b00734.

(25) Mayer, M. L. *Neuron*, **2005**, *45*, 539-552.

(26) Guo, Y.; Wolter, T.; Kubar, T.; Sumser, M.; Trauner, D.; Elstner, M. *PLoS One* **2015**, *10*, e0135399.

(27) Eldridge, M. D.; Murray, C. W.; Auton, T. R.; Paolini, G. V.; Mee, R. P. *J. Comput.-Aided Mol. Des.* **1997**, *11*, 425–445..

(28) Izquierdo-Serra, M.; Gascón-Moya, M.; Hirtz, J. J.; Pittolo, S.; Poskanzer, K. E.; Ferrer, È.; Alibés, R.; Busqué, F.; Yuste, R.; Hernando, J.; Gorostiza, P. *J. Am. Chem. Soc.* **2014**, *136*, 8693-8701.

(29) Gascón-Moya, M.; Pejoan, A.; Izquierdo-Serra, M.; Pittolo, S.; Cabré, G.; Hernando, J.; Alibés, R.; Gorostiza, P.; Busqué, F. *J. Org. Chem.* **2015**, *80*, 9915-9925.

(30) Cabré, G.; Garrido-Charles, A.; Moreno, M.; Bosch, M.; Porta-de-la-Riva, M.; Krieg, M.; Gascón-Moya, M.; Camarero, N.; Gelabert, R.; Lluch, J. M.; Busqué, F.; Hernando, J.; Gorostiza, P.; Alibés, R. *Nat. Commun.* **2019**, *10*, 907.

(31) Mourot, A.; Kienzler, M. A.; Banghart, M. R.; Fehrentz, T.; Huber, F. M. E.; Stein, M.; Kramer, R. H.; Trauner, D. *ACS Chem. Neurosci.* **2011**, *2*, 536–543.

(32) Yu, B. C.; Shirai Y.; Tour, J. M. *Tetrahedron*, **2006**, *62*, 10303-10310.

(33) Davey, H. H.; Lee R. D.; Marks, T. J. *J. Org. Chem.* **1999**, *64*, 4976-4979.

(34) Friedman, L.; Shechter, H. *J. Org. Chem.* **1961**, *26*, 2522-2524.

(35) Yao, Q.; Kinney, E. P.; Yang, Z. *J. Org. Chem.* **2003**, *68*, 7528-7531.

(36) Carta, M.; Fièvre, S.; Gorlewicz, A.; Mulle, C. *Eur. J. Neurosci.* **2014**, *39*, 1835-1844.

(37) Honore, T.; Davies, S. N.; Drejer, J.; Fletcher, E. J.; Jacobsen, P.; Lodge, D.; Nielsen, F. E. Science 1988, 241, 701-703.

**Supporting information**
**Computational, photochemical and biological supplementary methods**

***Molecular docking calculations:*** Docking calculations were performed with GOLD5.6.3[3] program on the rigid crystallographic structure of GluK2 Ligand Binding Domain retrieved from the Protein Data Bank (PDB code: 4H8I).[4] H++ web-server[5] was used to add missing hydrogen atoms to the protein pdb file and to determine the protonation states of ionizable residues at pH = 7.0. All co-crystallized ligands, and water molecules were removed. The structures of *trans*-**Glu_brAzo1** and *cis*-**Glu_brAzo1** were built with standard bond lengths and angles using Gaussview[6] and UCSF Chimera[7] codes. Those structures were further minimized using Quantum Mechanics at the B3LYP/6-31G(d) level with the Gaussian09 package.[8] The *trans*-**Glu_brAzo2** and *cis*-**Glu_brAzo2** initial structures were built from the coordinates of *trans*-**Glu_brAzo1** and *cis*-**Glu_brAzo1** QM minima, respectively, by replacing the cyano substituent by the bulky -CONH-*p*-C6H4COOH group, and the corresponding QM minima were also located. The four minimized compounds and the protein were further prepared for docking by assigning GOLD atom types to all the atoms by means of Hermes (GOLD 3D Visualizer).

To ensure a complete exploration of the conformational space of the four ligands in the binding site of the protein, the maximum efficiency of the genetic algorithm was selected in the docking setup. All the parameters of the genetic algorithm were set to the default values of the program and partial flexibility was assigned to the ligands. The binding site of the receptor was defined as all atoms within 15 Å of a conveniently specified central point (given by its X, Y, Z coordinates). 100 binding solutions for each ligand were generated. The Chemscore fitness function[9] was selected to estimate the binding affinities of the four ligands. The obtained poses were ranked based on those affinity docking scores (kJ/mol) and the best solution for each ligand was selected.

***Photochemical characterization of Glu_brAzo1 and Glu_brAzo2:*** All spectroscopic and photochemical experiments were carried out in HPLC- or spectroscopy-quality solvents. Steady-state UV-vis absorption measurements were recorded on a HP 8453 spectrophotometer with temperature control. The

UV-vis absorption spectra of *trans*-**Glu_brAzo1** and *trans*-**Glu_brAzo2** in PBS:DMSO 1:1 was estimated from the absorption spectra of as-synthesized *cis*-**Glu_brAzo1** and *cis*-**Glu_brAzo2** and of a well-known mixture of their *cis* and *trans* isomers, the composition of which was measured by $^{1}$H NMR in DMSO-$d_6$. Isomerization quantum yields were determined relative to 1,2-bis(5-chloro-2-methyl-3-thienyl)perfluorocyclopentene in hexane ($\Phi_{\text{ring opening}}$ = 0.13[10]). Different excitation sources were used in the photochemical experiments depending on the spectral requirements: a cw DPSS laser ($\lambda_{exc}$ = 405 nm, SciTec) for *cis-trans* photoisomerization, and the second harmonic of a ns-pulsed Nd:YAG laser ($\lambda_{exc}$ = 532 nm, Brilliant, Quantel) for *trans-cis* photoisomerization.

***Cell line and transfection:*** HEK293 tsA201 cell line (SV40-transformed, Human Embryonic Kidney 293 cells) was maintained at 37 ºC in a 5% $CO_2$ humid incubator with Dulbecco's Modified Eagle Medium/Nutrient Mixture F-12 media (DMEM) (1:1, Invitrogen) supplemented with 10% Fetal Bovine Serum (FBS) and 1% Penicillin/Streptomycin. Cells transiently expressed the receptor subunit GluK2 or GluK1(Q)-2b(GGAA). The expression plasmid for GluK2 was kindly provided by Ehud Y. Isacoff (University of California). GluK2 was subcloned into EcoRI site of the pCDNA3.1 expression vector. To obtain the GluK2-eGFP pCDNA3 construct, a fragment spanning the C-terminal domain of GluK2 and eGFP was amplified by PCR using AfeI/XbaI flanked primers and subcloned into GluK2-pCDNA3 plasmid by replacing the former AfeI/XbaI cassette. GluK1(Q)-2b(GGAA) was kindly provided by G. Swanson (Northwestern University, Feinberg School of Medicine), with the endoplasmic reticulum retention motif of the carboxy-terminal mutated to increase surface expression.[11] DNA–X-tremGENE 9 Transfection Reagent (Roche) mix was used following manufacturer's instructions with a Reagent:DNA ratio of 3:1. GluK1(Q)-2b-GGAA plasmid was co-transfected with peGFP with a Transfection Reagent:GluK1:eGPF ratio of 3:1:0.1.

The mix was incubated for 20 min at room temperature, meanwhile cells were detached and freshly plated into a 12-mulltiwell plate at a density of 3 × 105 cells before the DNA-Transfection Reagent mix was added dropwise into each well. Experiments were performed after 48–72 h, and the day before the experiment

cells were plated at low density on 16-mm coverslips (Fisher Scientific) treated with collagen(Sigma-Aldrich) to allow cell adhesion.

***Electrophysiology:*** Whole-cell voltage-clamp recordings were done using an EPC-10 amplifier and data at 10 kHz was acquired with amplifier's software Patch Master (HEKA). Bath solution was composed of (in mM): 140 NaCl, 1 $MgCl_2$, 2.5 KCl, 10 HEPES, 2.5 $CaCl_2$ and 10–20 glucose to fix osmolarity to 310 $mOsm \cdot kg^{-1}$, while pH 7.42 was adjusted with NaOH. Borosilicate glass pipettes were pulled with a typical resistance of 4–6 MΩ for HEK293 cells. Pipette solution contained (in mM): 120 cesium methanosulfonate, 10 TEA-Cl, 5 $MgCl_2$, 3 $Na_2ATP$, 1 $Na_2GTP$, 20 HEPES, 0.5 EGTA; osmolarity was 290 $mOsm \cdot kg^{-1}$ and pH 7.2 was adjusted with CsOH.

Before starting the recording, cells were incubated 10 min with 0.3 mg $mL^{-1}$ Concanavalin A (Sigma) —to block GluK1 and GluK2 desensitization— on an ES based on $NMDG^+$ (to avoid depolarization due to open GluRs, in mM): 110 $NMDG^+$, 2.5 KCl, 1 $MgCl_2$, 10 HEPES, 10–20 glucose to fix osmolarity to 300 $mOsm \cdot kg^{-1}$, while pH 7.4 was adjusted with HCl. Before placing the coverslip to the recording chamber, cells were washed again with bath solution.

Light stimulation was done by illumination of the entire focused field using a Polychrome V monochromator (TILL Photonics) connected through the back port of an IX71 inverted microscope (Olympus) with a XLUMPLFLN 20XW x20/1 water immersion objective (Olympus). For automatically controlling wavelength, the monochromator was connected to the EPC-10 amplifier via Photochromic Manual Control (TILL Photonics) and controlled with the photometry module of Patch Master. Light power density measured with a Newport 1916-C light meter after the objective was 22.0 $\mu W\ mm^{-2}$ for 380 nm, 45.9 $\mu W\ mm^{-2}$ for 460 nm and 47.4 $\mu W\ mm^{-2}$ for 500 nm.

One-photon action spectrum characterization was done during voltage-clamp recordings applying a train of 1 s light-pulses at different wavelengths (for the whole action spectrum, we ranged wavelengths from 300 to 600 nm, with 10 nm steps) with 5 s delay between pulses in which light was switched to 530 nm to *trans-cis* back-isomerize for activation spectrum, and to 390nm for deactivation spectrum.

***Rat hippocampal neural primary culture.*** All procedures were conducted in accordance with the European guidelines for animal care and use in research, and were approved by the Animal Experimentation Ethics Committee at the University of Barcelona (Spain). Low-density primary hippocampal cultures were prepared from newborn P0-P3 pups from Sprague Dawley rat and maintained in cell culture for 1-2 weeks in coverslips coated with poly-L-lysine (Sigma-Aldrich), as previously described.[12-14].

Cells were cultured with complete medium (Neurobasal A, B-27 5%, GlutaMax (0.5x), glucose 15mM, penicillin (5 U ml−1) and streptomycin (5 µg ml−1)). Within 48-72 h an anti-mitotic treatment with AraC 5 µM is done to avoid fibroblast and astrocyte proliferation. Half of the medium in each well was changed every 3-4 days.

***Electrophysiology recording conditions for rat hippocampal neurons*:** Voltage and current-clamp recordings under whole-cell configuration were done using an EPC-10 amplifier and data at 10 kHz was acquired with amplifier's software Patch Master (HEKA). Bath solution was composed of (in mM): 140 NaCl, 2 MgCl, 2.5 KCl, 10 HEPES, 0.2 $CaCl_2$ and 10–20 mM glucose to fix osmolarity to 310 mOsm·kg–1, pH 7.42 adjusted with NaOH. Borosilicate glass pipettes were pulled with a typical resistance of 6–8 MΩ for neurons. Pipette solution contained (in mM): 130 KCl, 5 $MgCl_2$, 3 $Na_2ATP$, 1 $Na_2GTP$, 20 HEPES, 0.5 EGTA. Osmolarity is adjusted at 289 mOsm·kg–1 and pH 7.2 adjusted with KOH. During recordings, neurons were maintained at room temperature (r.t., 25-27 °C) in a continuous perfusion of bath solution.

***Data analysis and statistics:*** Amplitude of photocurrents were analyzed using IgorPro (Wavemetrics). Displayed whole-cell current traces have been filtered using the infinite impulse response digital filter from IgorPro (low-pass filter with cutoff of 50 Hz). The drift in current observed during light spectra recordings was corrected where appropriate with the IgorPro (WaveMetrics) software using a custom-made macro for drift correction.

**Figure S1. Molecular docking simulations**

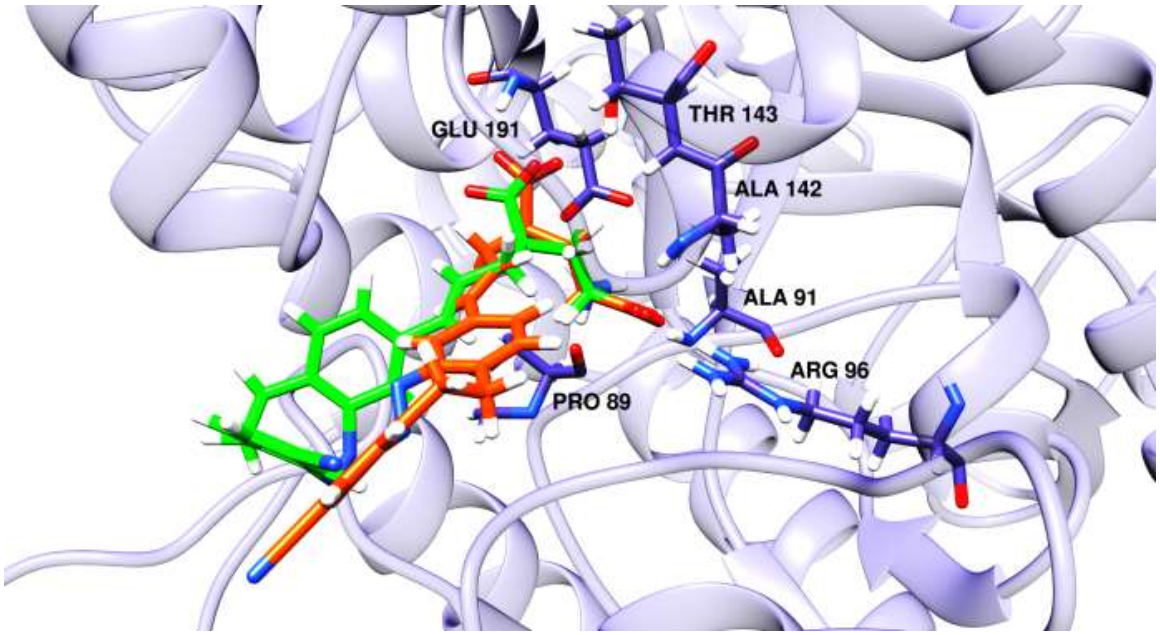


**Figure S1.** Best docking solutions for *trans*-**Glu_brAzo1** (orange) and *cis*-**Glu_brAzo1** (green) in GluK2. The protein residues interacting with the glutamate groups are also indicated. Oxygen, nitrogen and hydrogen atoms are depicted in red, blue and white, respectively.

**Figures S2-S7 and Table S1. Photoisomerization of Glu_brAzo1 and Glu_brAzo2**

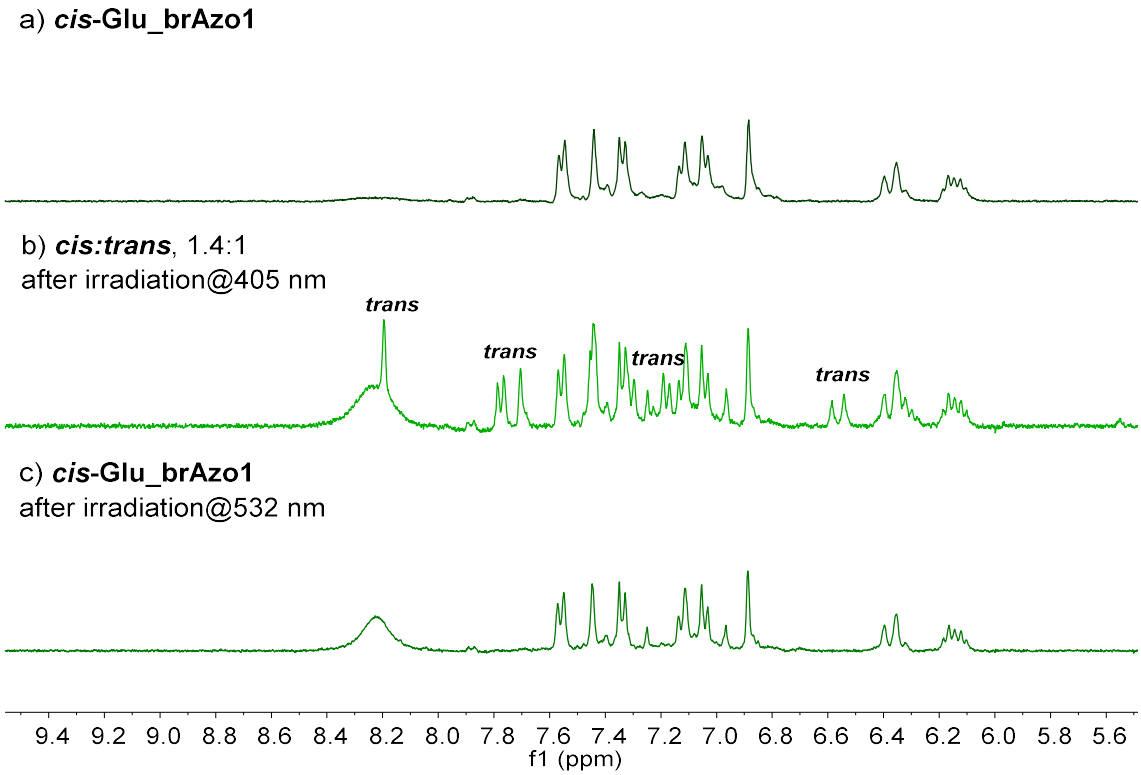


**Figure S2.** Low-field region of the $^{1}$H NMR spectra (360 MHz, DMSO-$d_6$) of **Glu_brAzo1**: (a) freshly prepared (*cis* isomer); (b) after irradiation at $\lambda_{exc}$ = 405 nm (power = 280 mW) for 3 h (*cis*:*trans* 1.4:1 mixture); (c) after irradiation of (b) at $\lambda_{exc}$ = 532 nm (power = 100 mW) for 3 h (*cis* isomer).

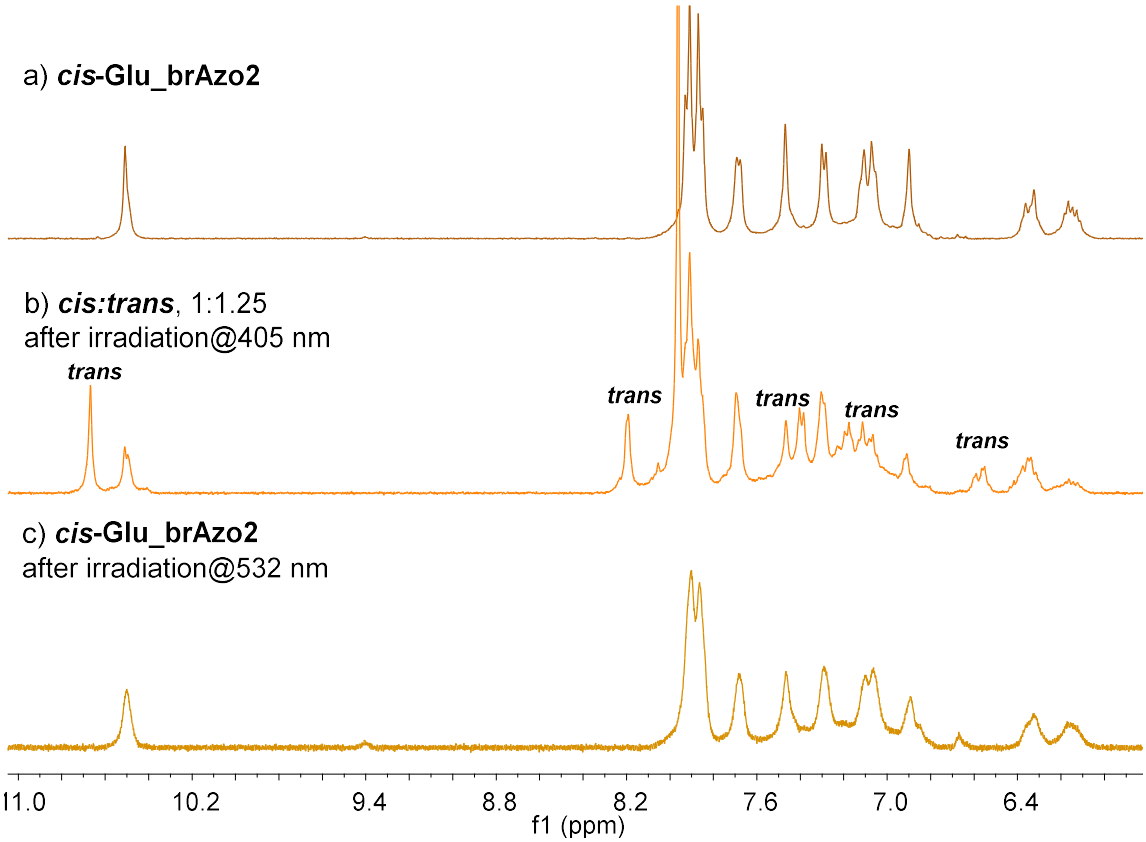


**Figure S3.** Low-field region of the $^{1}$H NMR spectra (400 MHz, DMSO-$d_6$) of **Glu_brAzo2**: (a) freshly prepared (*cis* isomer); (b) after irradiation at $\lambda_{exc}$ = 405 nm (power = 280 mW) for 3 h (*cis*:*trans* 1:1.25 mixture); (c) after irradiation of (b) at $\lambda_{exc}$ = 532 nm (power = 100 mW) for 3 h (*cis* isomer).

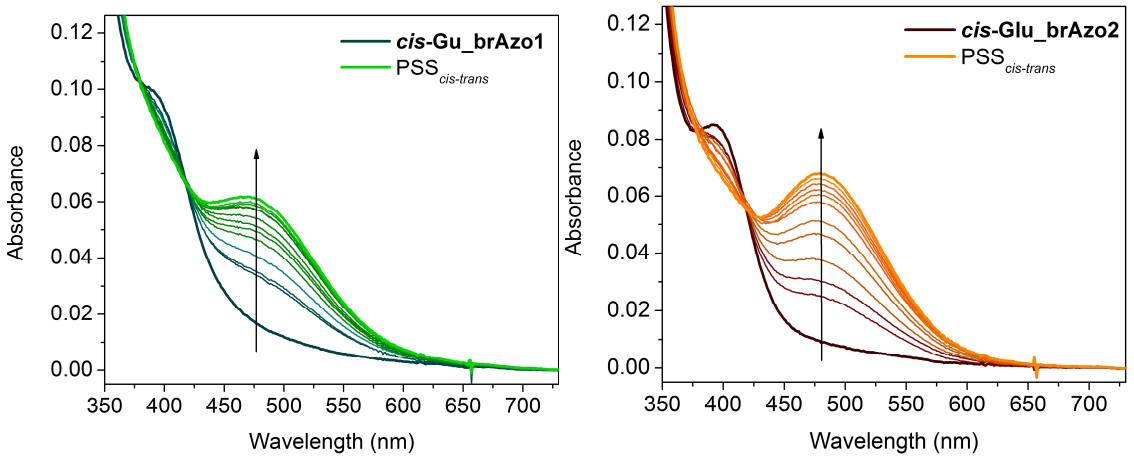


**Figure S4.** Absorption spectra of **Glu_brAzo1** and **Glu_brAzo2** in PBS:DMSO 1:1 upon irradiation of their *cis* isomer at $\lambda_{exc}$ = 405 nm (power = 88 mW).

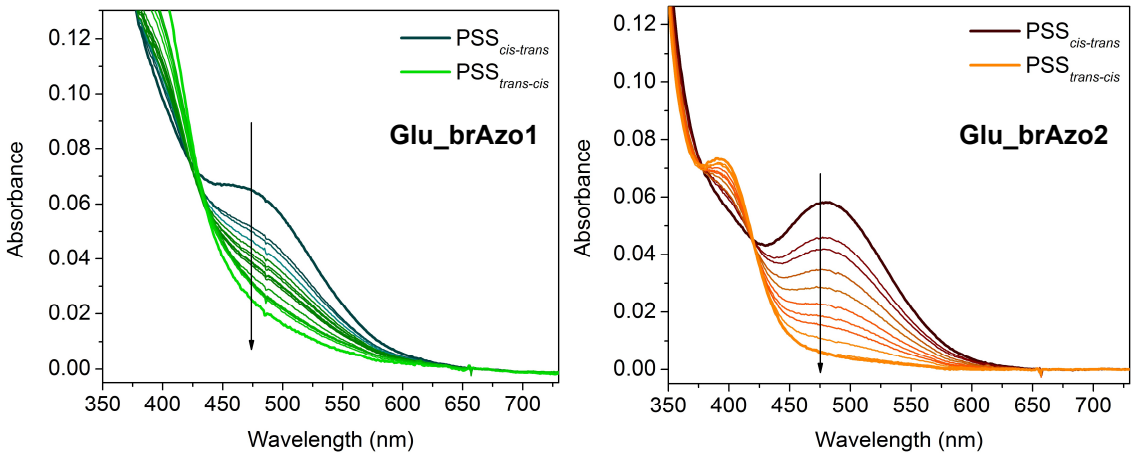


**Figure S5.** Absorption spectra of **Glu_brAzo1** and **Glu_brAzo2** in PBS:DMSO 1:1 upon irradiation at $\lambda_{exc}$ = 532 nm (power = 10 mW) of the *cis-trans* photostationary mixture previously prepared at $\lambda_{exc}$ = 405 nm.

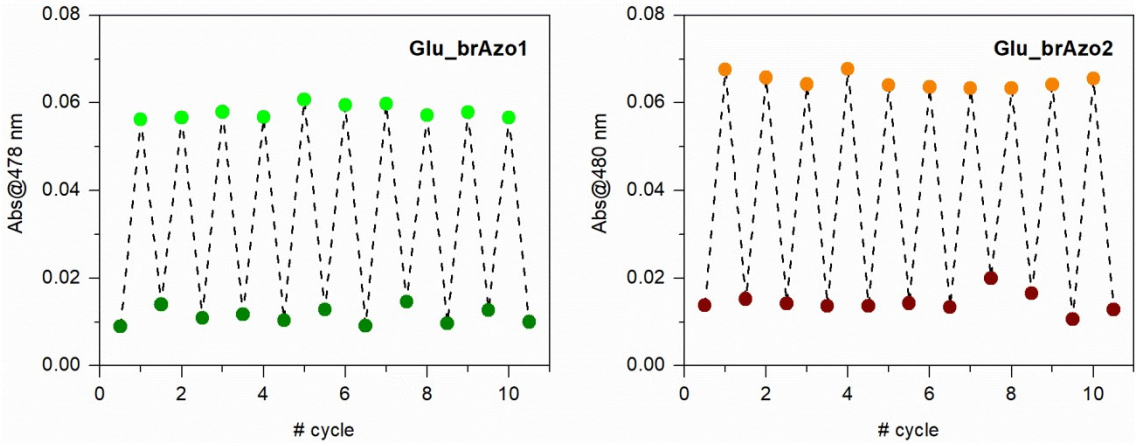


**Figure S6.** Variation of the absorption at 395 and 478 nm of **Glu_brAzo1** and **Glu_brAzo2** in PBS:DMSO 1:1 upon consecutive cycles of *cis-trans* ($\lambda_{exc}$ = 405 nm, 280 mW) and *trans-cis* photoisomerization ($\lambda_{exc}$ = 532 nm, power = 230 mW).

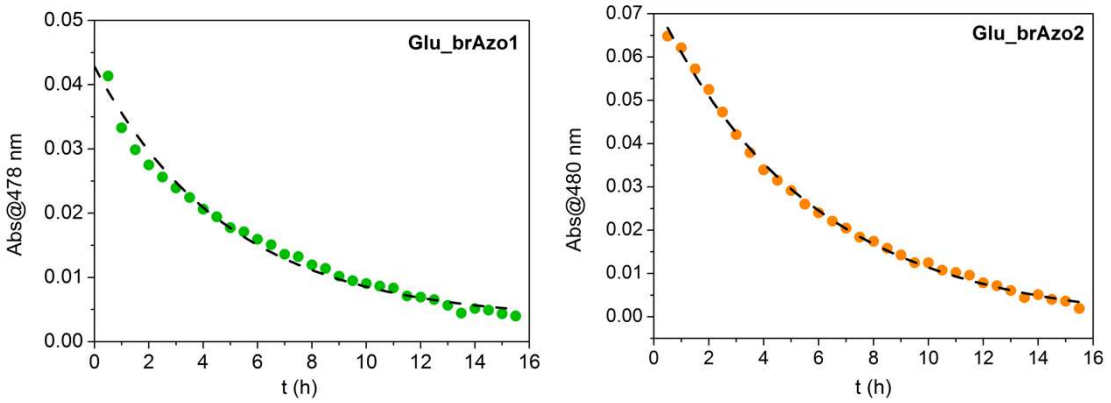


**Figure S7.** Variation of the absorption at $\lambda_{abs,max}^{trans}$ of the *cis-trans* photostationary state mixture of **Glu_brAzo1** and **Glu_brAzo2** in the dark at 25ºC in PBS:DMSO 1:1. At these conditions, thermal *trans-cis* back-isomerization takes place, thus restoring the initial concentration of the *cis* state of the ligands. Points correspond to the experimental data, while lines were obtained from monoexponential fits.

**Table S1.** Photochemical properties of **Glu_brAzo1** and **Glu_brAzo2** in PBS:DMSO 1:1.

| | $\lambda^{cis}_{abs,max}$ [a] (nm) | $\lambda^{trans}_{abs,max}$ [a] (nm) | $\Phi_{cis\text{-}trans}$ | $\Phi_{trans\text{-}cis}$ | %*trans* PSS$_{cis\text{-}trans}$ | %*cis* PSS$_{trans\text{-}cis}$ | $\tau_{trans}$ (h) [b] |
|---|---|---|---|---|---|---|---|
| **Glu_brAzo1** | 392 | 478 | 0.11 | 0.89 | 47 | 100 | 6.8 |
| **Glu_brAzo2** | 395 | 480 | 0.13 | 0.86 | 60 | 100 | 5.6 |

[a] Data for the n-π* band. [b] $t_{1/2}$ = 4.7 and 3.9 h, respectively.

**Figures S8-S11. Photomodulation of GluK1 and GluK2 in HEK293 cells using Glu_brAzo1 and Glu_brAzo2**

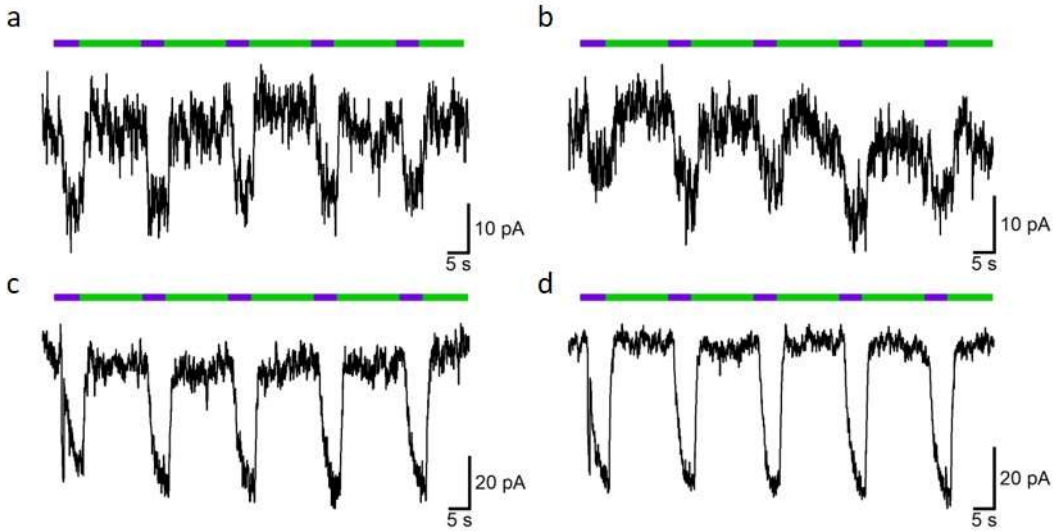


**Figure S8.** Light-dependent inward currents measured for HEK293 cells expressing GluK1 and GluK2. (a-b) HEK293 cells transfected with GluK1 and perfused with (a) *cis*-**Glu_brAzo1** (100 μM), and (b) *cis*-**Glu_brAzo2** (100 μM). (c-d) HEK293 cells transfected with GluK2 and perfused with (c) *cis*-**Glu_brAzo1** (100 μM), and (d) *cis*-**Glu_brAzo2** (100 μM). Light pulses at $\lambda_{exc}$ = 390 nm (purple bars) were employed to induce *cis-trans* photoisomerization, which in all the cases resulted in larger electrophysiological currents (i.e. receptor activation and channel opening). Irradiation at $\lambda_{exc}$ = 530 nm (green bars) was used to trigger *trans-cis* back-isomerization and recover the initial signal (i.e. receptor deactivation and channel closing).

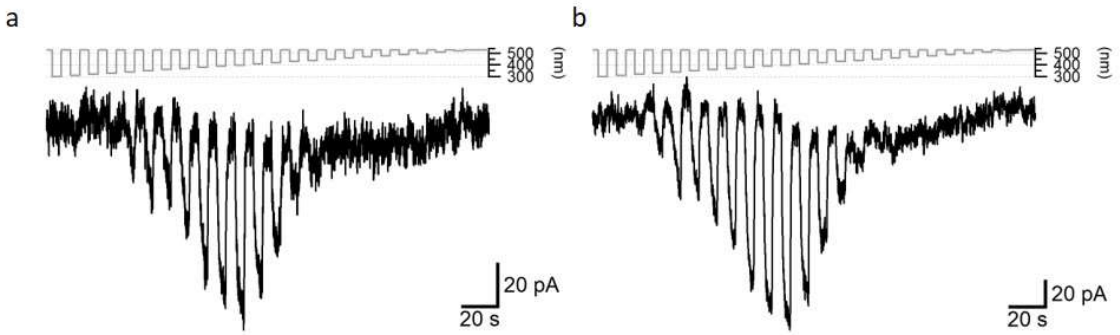


**Figure S9.** Activation spectra of (a) **Glu_brAzo1** (100 μM) and (b) **Glu_brAzo2** (100 μM) in HEK293 cells transfected with GluK2. Wavelength excitation to

promote *cis-trans* photoisomerization and receptor activation ranges from 300 nm to 530 nm. In all the cases, *trans-cis* back-isomerization was achieved with pulses at $\lambda_{exc}$ = 530 nm.

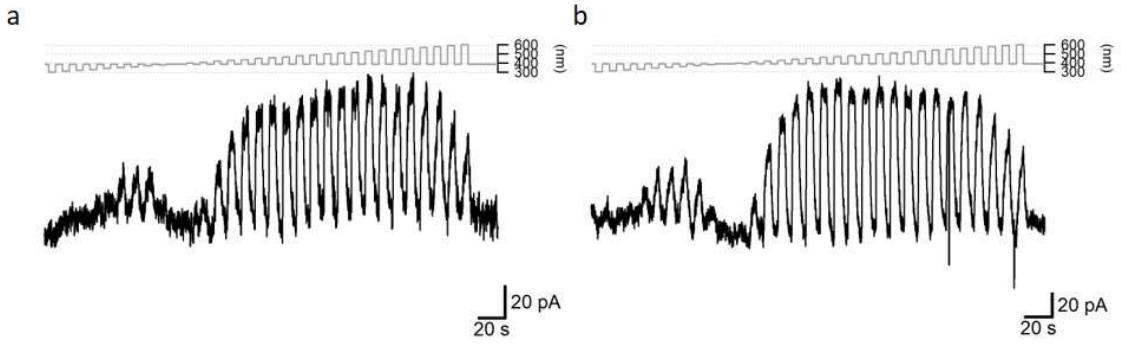


**Figure S10.** Deactivation spectra of (a) **Glu_brAzo1** (100 µM) and (b) **Glu_brAzo2** (100 µM) in HEK293 cells transfected with GluK2. Wavelength excitation to promote *trans-cis* photoisomerization and receptor deactivation ranges from 300 nm to 600 nm. In all the cases, *cis-trans* isomerization was previously conducted with pulses at $\lambda_{exc}$ = 390 nm.

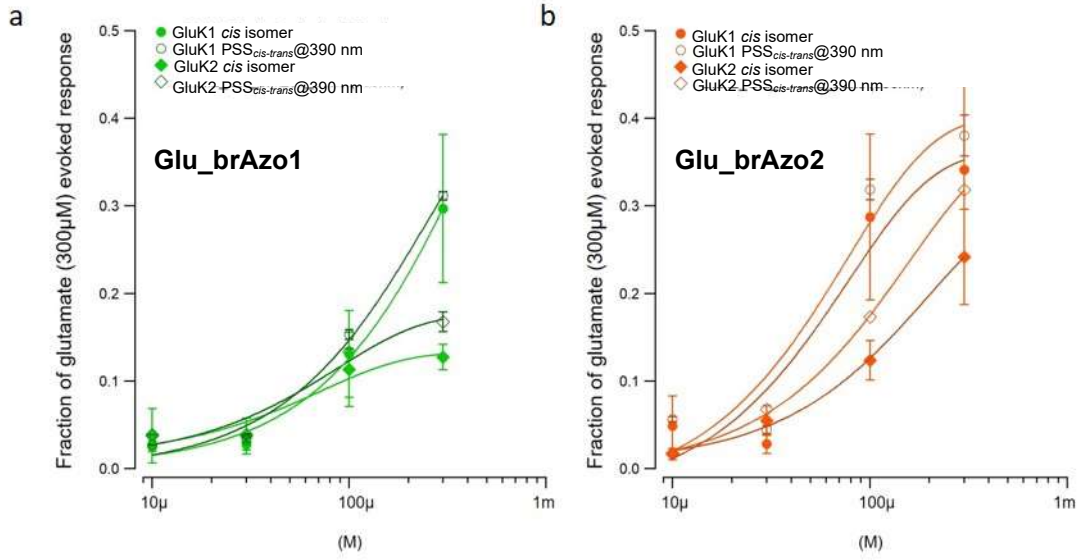


**Figure S11.** Dose-response curves of (a) **Glu_brAzo1** and (b) **Glu_brAzo2** in HEK293 cells transfected with GluK1 and GluK2. Measurements were conducted from 10 to 300 µM for their *cis* isomer and the *trans-cis* mixture obtained at $\lambda_{exc}$ = 390 ($PSS_{cis-trans}$@390 nm).

**Figures S12. Photoactivation of rat hippocampal neurons using Glu_brAzo1 and Glu_brAzo2**

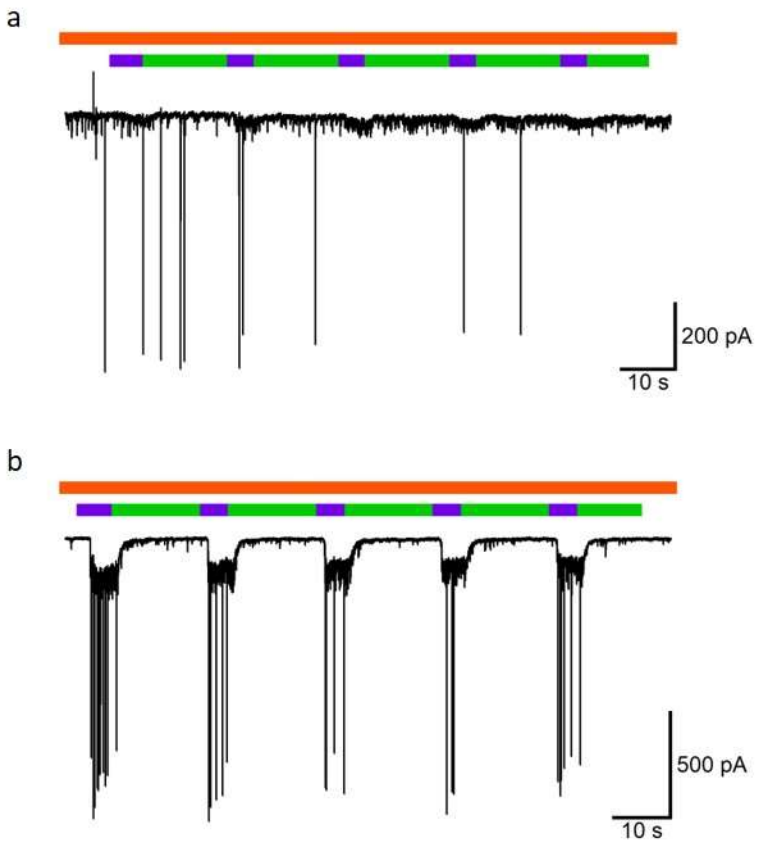


**Figure S12.** Whole-cell voltage clamp recording of rat hippocampal neurons in culture. Perfusion of 30 μM of (a) **Glu_brAzo1** and (b) **Glu_brAzo2**. Light activation is induced by pulses at $\lambda_{exc}$ = 390 and 530 nm (purple and green bars, respectively).

## References


[1] Gascón-Moya, M.; Pejoan, A.; Izquierdo-Serra, M.; Pittolo, S.; Cabré, G.; Hernando, J: Alibés, R.; Gorostiza, P.; Busqué, F. *J. Org. Chem.* **2015**, *80*, 9915-9925.

[2] Venkatachalam, T. K.; Huang, H.; Yu, G.; Uckun, F. M. *Synth. Commun.* **2004**, *34*, 1489-1497.

[3] Verdonk, M. L.; Cole, J. C.; Hartshorn, M. J.; Murray, C. W.; Taylor, R. D. *Proteins Struct. Funct. Biogenet.* **2003**, *52*, 609–623.

[4] Reiter, A.; Skerra, A.; Trauner, D.; Schiefner, A. *Biochemistry* **2013**, *52*, 8972-8974.

[5] Anandakrishnan, R.; Aguilar, B.; Onufriev, A. V. *Nucleic Acids Res.* **2012**, *40*, 537-541.

[6] GaussView, Version 6, Dennington, R.; Keith, T. A.; Millam, J. M. Semichem Inc., Shawnee Mission, KS, **2016**.

[7] Pettersen E. F.; Goddard, T. D.; Huang, C. C.; Couch, G. S.; Greenblatt, D. M.; Meng, E. C.; Ferrin, T. E. *J. Comput. Chem.* **2004**, *25*, 1605-1612.

[8] Gaussian 09, Revision C.01, Frisch, M. J.; Trucks, G. W.; Sch-legel, H. B.; Scuseria, G. E.; Robb, M. A.; et al. Gaussian, Inc., Wallingford CT, **2009**.

[9] Eldridge, M. D.; Murray, C. W.; Auton, T. R.; Paolini, G. V.; Mee, R. P. *J. Comput.-Aided Mol. Des.* **1997**, *11*, 425–445.

[10] Higashiguchi, K., Matsuda, K., Asano, Y.; Murakami, A.; Nakamura, S.; Irie, M. *Eur. J. Org. Chem*. **2005**, 91-97.

[11] Ren, Z.; Riley, N. J.; Needleman, L. A.; Sanders, J. M.; Swanson, G. T.; Marshall, J. *J. Biol. Chem*. **2003,** 278, 52700–52709.

[12] Halliwell, R. F.; Peters, J. A.; Lambert, J. J. *Br. J. Pharmacol.* **1989**, *96*, 480-494.

[13] Beaudoin, G. M.; Lee, S. H.; Singh, D.; Yuan, Y.; Ng, Y. G.; Reichardt, L. F.; Arikkath, J. *Nat. Protoc.* **2012**, *7*, 1741-1754.

[14] Kaech, S.; Banker; G. *Nat. Protoc.* **2006**, *1*, 2406-2415.

## CHAPTER 9 | CONCLUSIONS

The main conclusions obtained from this thesis are:

- The modular structure of "Photoswitchable tethered ligands" (PTLs) displays great versatility regarding both the reactive group (which can be made cysteine-selective, widely reactive, and photolabile) and the photoisomerizable group (which allows blue-shifted absorption, rapid relaxation, two-photon absorption, and FRET photosensitization).
- The introduction of an NHS ester reactive group enables to covalently attach PTLs to endogenous glutamate receptors. Since the conjugation is enhanced by targeting the ligand to its binding site, these new PTLs are called "Targeted Covalent Photoswitches" (TCPs).
- Characterization of the first generation of TCPs activated with UV light (e.g. TCP9) in overexpressed ionotropic glutamate receptor subtypes demonstrates their ability to conjugate to wildtype GluK1 and GluA1 receptors and photocontrol their activity.
- The long-term photocontrol obtained with TCP9 does not require genetic modifications. These properties make TCP9 a unique molecular tool to functionally track endogenous receptors during plasticity processes such as LTD; or to study neural connectivity.
- TCP9 allows photocontrolling neural activity in vivo in *Xenopus* tadpoles, from entire neurons to single synapses.
- Introduction of a photolabile group in PTLs allows to spatially constrain their conjugation to endogenous receptors of hippocampal neurons using patterns of illumination.
- Electronic asymmetric modifications in the vicinity of the azobenzene unit of TCPs shift their spectrum (activation achieved with visible light) and decrease their thermal relaxation time.
- Two TCPs activated with blue light (B-TCP) have been developed. B-TCPa is able to photoswitch heterologously expressed GluK1 receptors and B-TCPc photoswitches GluA1 and GluA2 receptors.
- Both B-TCPa and B-TCPc can photosensitize endogenous receptors in primary cultures of hippocampal neurons. B-TCPc displays an optimal behavior, enabling spatiotemporal photocontrol of neural activity that is reversible, fast, long-lasting, and pharmacologically selective.
- B-TCPc also enables to photocontrol neural activity of adult gerbil cochlea in vivo. These results demonstrate for the first time a drug-based approach to photoswitch spiral ganglion neurons, and constitute an important step towards the development of novel optical cochlear implants that do not require (opto)genetic modifications.
- Modifications of the azobenzene unit of PTLs can be rationally designed to optimize two-photon (2P) responses without altering other important optical properties. This allows to photostimulate neurons in vivo using highly penetrating infrared light and high spatial resolution in the axial direction that is characteristic of 2P.
- The action spectrum of a photoisomerizable molecule can be adjusted using light-harvesting fluorophores covalently conjugated to the vicinity of the photoswitch. This novel method expands the strategies to customize photopharmacological and optogenetic tools without mutagenesis or new chemical synthesis.

- Neural activity can be controlled with photochromic ligands (PCLs) based on stilbenes and bridged azobenzenes, which offer several advantages compared to classic azobenzene PCLs. Bridged azobenzenes have reversed thermal stability, the high activity of their *trans* state is preserved while ensuring larger stability for the inert *cis* isomer, and in consequence their molecular activity is also reverted. This allows controlling neural firing with light without background activity in the dark. Besides, stilbenes allow for the non-destructive irreversible activation of the PCL, avoiding the generation of photo-uncaging by-products.
- Overall, a comprehensive exploration of the different functionalities of photoswitches (pharmacological ligand, photoswitch, reactive moiety) has been performed, leading to the desired properties and to the demonstration of several new applications in intact brain tissue and in different animal models (worms, tadpoles, and gerbils).

## CHAPTER 10 | RESUM: Control òptic de receptors endògens i excitabilitat cel·lular amb llum

### Capítol 1: Introducció

La manipulació externa de la fisiologia cel·lular s'ha realitzat generalment mitjançant l'administració de fàrmacs, tant amb finalitats en el camp de la recerca bàsica com per finalitats terapèutiques. Tot i així, la farmacologia clàssica presenta alguns desavantatges com ara el baix control espacial i temporal de l'acció farmacològica, causa sovint de possibles efectes secundaris no desitjats. El desenvolupament d'eines regulades per la llum ha transformat la manipulació de la fisiologia cel·lular, dirigides especialment en el control de l'activitat neuronal.

L'optogenètica convencional i la fotofarmacologia requereixen de la sobre-expressió mitjançant teràpia gènica de proteïnes sensibles a la llum o receptors mutants, la qual sovint altera la fisiologia cel·lular. El desenvolupament de nous fàrmacs fotocommutables (medicaments regulats per la llum) ofereix una alternativa en el control per llum de receptors endògens evitant així qualsevol manipulació genètica.

Terapèuticament, l'administració d'un fàrmac fotocommutable en combinació amb patrons d'il·luminació definits en l'espai i el temps proporcionaria un nou grau de control i regulació de l'acció dels fàrmacs, independentment dels inputs naturals i sense interferir en altres processos cel·lulars.

Avui en dia, hi ha dos tipus de fotocommutadors disponibles: lligands fotocròmics difusibles (PCLs) i lligands units fotocommutables (PTLs) (Kienzler and Isacoff, 2017). Els PTLs son molècules tri-modulars estructurades en reactiu-commutador-lligand. El lligand pot ser un agonista, un antagonista o un bloquejador que es pot unir de manera reversible al centre d'unió de lligands o a un lloc per al control al·lostèric d'una proteïna.

La conjugació selectiva dels fotocommutadors es basa en l'ancoratge mitjançant la part reactiva a prop del lloc d'unió del lligand, ja sigui en un aminoàcid introduït o natiu. La conjugació en receptors no mutats només s'ha demostrat en (Bartels, Wassermann and Erlanger, 1971; Izquierdo-Serra *et al.*, 2016). El centre fotocommutador acostuma a estar format per un azobenzé (H Satzger, S Spörlein, C Root, J Wachtveitl, W Zinth, 2003), el qual conté un enllaç fotoisomeritzable les propietats de les quals (longitud, geometria i moment dipolar) es modifiquen amb la llum. Entre els exemples de receptors modificats amb PTLs hi ha SPARK, una modificació del canal de potassi depenent de voltatge "Shaker" que s'ha utilitzat per silenciar les neurones (Banghart M, Borges K, Isacoff E, Trauner D, 2004). Una altra estratègia va ser la modificació del domini d'unió a lligand del receptor de glutamat tipus kainat 2 (GluK2) per tal que PTLs de la família dels MAG (Maleimida-azobenzé-glutamat) es puguin fixar al receptor mitjançant una cisteïna introduïda en la posició 439. Aquest tipus de receptors de glutamat regulats per llum es van passar a anomenar LiGluR(Volgraf *et al.*, 2006). L'ús de LiGluR s'ha utilitzat per despolaritzar la membrana cel·lular i induir l'activació neuronal(Szobota *et al.*, 2007). Més recentment, fotocommutadors derivats del MAG s'han demostrat sensibles en la foto-activació per 2 fotons(Izquierdo-Serra *et al.*, 2014; Carroll *et al.*, 2015) com a noves eines en aplicacions in vivo(G. Cabré *et al.*, 2019).

Posteriorment, l'estudi de les seqüències gèniques d'altres tipus de receptors i la introducció de mutacions puntuals ha resultat en l'ampliació d'una llibreria de receptors activables per

llum(Hüll, Morstein and Trauner, 2018; Paoletti, Ellis-Davies and Mourot, 2019): LinAChR pel control de receptors d'acetilcolina (Tochitsky *et al.*, 2012); LiGABARs (Lin *et al.*, 2014); LimGluRs (Levitz *et al.*, 2013); LiGluNs, on segons el tipus de mutació s'observa un efecte agonista o antagonista en receptors NMDARs (Berlin *et al.*, 2016).
Anteriorment, els fàrmacs fotocommutables s'han demostrat útils com a eines útils en diferents àrees de la neurobiologia: el disseny d'un nou analgèsic per controlar la nocicepció i suprimir la sensació del dolor d'una manera més selectiva que els anestèsics locals habituals(Mourot, Tochitsky and Kramer, 2013); com a nova teràpia per restablir la pèrdua de visió en pacients cecs degut a una degeneració de la retina(Polosukhina *et al.*, 2012); i fins i tot com a moduladors dels patrons de comportament en animals(Kokel *et al.*, 2013; Pittolo *et al.*, 2014).
La fotofarmacologia permet l'estimulació directa de l'activitat neuronal enllaçant estimulació amb registre de l'activitat en sinapsis individuals, neurones senceres, circuits funcionals i estructures anatòmiques, evitant distorsions associades a l'expressió proteica exògena.
Aquest treball vol demostrar que sempre hi ha marge per millorar, per exemple, en el disseny de nous PTLs per a controlar receptors endògens no modificats; noves estratègies per la modificació de la longitud d'ona d'activació en el rang visible o infraroig de l'espectre de llum; millorar el control espacial i temporal a nivell sub-cel·lular; o conferir major sensibilitat d'excitació d'una molècula per llum infraroja polsada a dos fotons per tal de millorar-ne la penetració en teixits per futures aplicacions *in vivo*.

## *Objectius*

L'objectiu principal d'aquesta tesis és l'obtenció de nous lligands fotocommutables per la fotosensibilització de receptors neuronals endògens sense necessitat de modificacions genètiques i així controlar òpticament l'activitat neuronal.

En trets generals, la tesi s'estructura en tres parts principals:

**Part I: Modificacions de la part reactiva de lligands units fotocommutables (PTLs):**

**Capítol 2**: es desenvolupen els següents objectius:

- Controlar amb llum receptors de glutamat endògens no modificats genèticament a través de la conjugació química de "Fotocommutadors covalents dirigits" (TCPs).
- Induir mitjançant llum l'activació neuronal en cultius organotípics d'hipocamp a nivell d'un grup de neurones, una única neurona o una única espina.
- Aplicar els PTLs dissenyats per fotocontrolar l'activitat neuronal in vivo i modificar el procés de regeneració nerviosa en un model in vivo en capgrossos de *Xenopus*.

**Capítol 3**: es centra en el següent objectiu:

- A través de la introducció de grups foto-làbils demostrar el potencial control espacio-temporal a nivell de conjugació que confereix la llum.

**Part II: Modificacions de les propietats òtiques de lligands units fotocommutables (PTLs):**

**Capítol 4**: es desenvolupen els següents objectius:

- Disseny i caracterització de derivats dels TCPs activables en el rang visible de llum i funcionals a elevades freqüències. Descripció de les propietats òptiques, farmacològiques i respostes funcionals en receptors endògens in vitro.
- Aplicació per la foto-activació de receptors natius de les neurones que conformen el nervi auditiu. En un model animal es mesura la resposta auditiva evocada per la conjugació química dels TCPs i se'n caracteritza el seu rendiment i possible potencial.

**Capítol 5**: es centra en el següent objectiu:

- Desenvolupament racional de fotocommutadors per optimitzar-ne la seva sensibilitat a l'activació per dos fotons.

**Capítol 6**: es centra en el següent objectiu:

- Desenvolupament d'una estratègia de conjugació de fluoròfors que funcionen com a col·lectors de llum, els quals mitjançant FRET transfereixen la seva energia al cromòfor (fotocommutador), modificant-ne les característiques espectrals.

**Part III. Modificacions de les propietats òptiques de lligands fotocròmics solubles (PCLs):**

**Capítol 7**: es centra en el següent objectiu:

- Disseny i caracterització de PCLs per a l'activació irreversible però no foto-destructiva de la molècula original degut a la substitució de l'azobenzé per un estilbé. S'evita així la creació de foto-productes.

**Capítol 8**: es centra en el següent objectiu:

- Disseny i caracterització de PCLs amb propietats òtiques invertides en introduir azobenzens cíclics en els fotocommutadors.

## Part I: Modificacions de la part reactiva de lligands units fotocommutables (PTLs):
## Capítol 2 | Lligands units fotocommutables dirigits a receptors endògens de glutamat permeten el control funcional amb llum de sinapsis i neurones úniques *in vivo*

La primera generació de lligands units fotocommutables (PTLs) esta formada per la família dels MAG (Maleimida-azobenzé-glutamat). La maleimida és la part reactiva responsable de la conjugació del MAG a una cisteïna genèticament introduïda en el domini d'unió a lligand del receptor de glutamat tipus kainat 2 (GluK2), donant lloc al receptor de glutamat activable per llum (LiGluR). La isomerització de l'azobenzé en ser excitat per llum ultravioleta o visible, permet el control òptic de l'obertura de canals iònics i en conseqüència l'activitat neuronal(Paoletti, Ellis-Davies and Mourot, 2019).

La nova estratègia de síntesis química descrita en el nostre grup (Izquierdo-Serra *et al.*, 2016), té com a objectiu principal evitar la modificació genètica dels receptors ionotròpics de glutamat mitjançant la substitució de la maleimida del MAG per un grup altament reactiu. Degut a la promiscuïtat d'aquest nou grup electrofílic, es va dissenyar una estratègia on es divideix el compost en dos parts principals: "cap" (lligand-commutador) i "cua" (part reactiva connectada

a connectors de diferent longitud). Dins d'una llibreria de compostos obtinguts per la combinació sistemàtica d'ambdós precursors, es van obtenir els compostos TCP9 i TCP10. Tots dos compostos finals van demostrar ser capaços d'evocar les millors fotorespostes en ser isomeritzats de *trans* a *cis* repetidament mitjançant polsos alternats de llum (380 i 500 nm). La seva caracterització complerta es pot trobar en (Izquierdo-Serra *et al.*, 2016).

Posteriorment, es va testar el potencial del compost TCP9 en la fotosensibilització de receptors endògens en neurones d'hipocamp en cultiu no modificades (**Capítol 2**). Simplement incubant el compost TCP9 en els cultius neuronals, som capaços de controlar de manera robusta i reversible la generació de potencials d'acció amb gran resolució temporal (Figura 1). Tal i com ja s'havia descrit, TCP9 és actiu en la seva conformació *cis* obtinguda quan s'ilumina amb llum UV (~380 nm). L'isòmer *cis* és estable tèrmicament (~80 min) i actua com a ple agonista. També en demostrem l'absència de foto-fatiga com a indicador de la seva foto-estabilitat un cop conjugat. Les fotorespostes registrades son dependents de la intensitat de llum, de manera que augmentat la intensitat aconseguim respostes majors i més ràpides (Figura S2). La caracterització farmacològica del compost TCP9 en neurones hipocampals ens indica que el TCP9 no influencia els receptors del tipus NMDA, ja que no s'observa cap efecte en presencia del seu angagonista selectiu AP5. D'altra banda, la perfusió de l'antagonista de receptors AMPA i Kainat (NBQX) redueix significativament les fotorespostes induïdes per TCP9 (Figura S1a). El model de conjugació suggerit es basa en un procés de conjugació per afinitat. Igualment hem confirmat en neurones d'hipocamp que la conjugació ve dirigida per l'afinitat que té el lligand pel domini d'unió en el receptor (Figura S1b).Comparant els dominis d'unió a lligand dels receptors GluK1 i AMPA podem dir que son força similars ja que tenen una sequencia gènica molt conservada. Això explicaria perquè el TCP9 és capaç de conjugar-se i foto-activar de la mateixa manera els receptors GluK1 com GluA1 (Figura S3).

Aquests resultats també van ser confirmats mitjançant imatge de calci en cultius organotípics d'hipocamp en els quals sobre-expressem el sensor de calci GCaMP6s i el marcador morfològic dsRed2 (Figura 2). En incubar TCP9, podem foto-induir respostes, registrades com a increments intracel·lulars de calci, estimulant amb llum violeta (405 nm) totes les neurones en el camp de visió, una única neurona, o fins i tot una única espina sinàptica (Figures 2 i 5). L'efecte fotosensibilitzador del TCP9 es manté en estable en el temps (Figura 2e) i només pot ser revertit per l'efecte d'antagonistes de receptors tipus AMPA i Kainat (NBQX o CNQX) (Figura 3). El control estable de la funció dels receptors AMPA a través del TCP9 en els cultius organotípics d'hipocamp, permet el seguiment funcional dels receptors AMPA endògens en processos de plasticitat sinàptica com és el LTD ("depressió a llarg termini"). (Figura 4)

Tal i com s'ha demostrat, el compost TCP9 es capaç de fotosensibilitzar receptors endògens de neurones dissociades i en teixits en cultiu. Fet que ens condueix a provar les capacitats de TCP9 en el control neuronal en un model in vivo. En aquest cas, es va escollir el model animal de capgròs de *Xenopus* per la seva facilitat de manipulació i per tenir la pell transparent, ambdós trets que permeten el seguiment de l'activitat neuronal a traves del registre d'imatge de calci per microscòpia òptica i alhora l'estimulació lumínica dels fotocommutadors.

Per tal d'assegurar la capacitat de TCP9 de poder conjugar-se en receptors d'origen amfibi, es van incubar talls aguts de cervell de capgrossos de *Xenopus tropicalis* amb TCP9. Per tal de registrar l'activitat neuronal, el teixit prèviament va ser incubat amb l'indicador químic de calci OGB1-AM. Tal com s'havia observat anteriorment, TCP9 indueix l'activació dels receptors neuronals d'igual manera que el neurotransmissor endogen glutamat (Figura S4). Seguidament,

el registre de l'activitat neuronal in vivo induïda per TCP9 no va ser possible mitjançant la injecció d'indicadors químics de calci, tal i com es descriu en (Dunfield and Haas, 2010). Per tal de millorar el marcatge de neurones amb sensors de calci, es va implementar en el laboratori la tècnica d'electroporació in vivo en larves de *Xenopus* apressa al laboratori de la Dra Christine Holt (Cambridge, UK)(Falk *et al.*, 2007; Wong and Holt, 2018). El nostre objectiu era modificar la seva tècnica d'electroporació in vivo per tal de registrar l'activitat neuronal en la regió del bulb olfactiu (Per més detalls consultar Appendix protocols). Curiosament, aquesta regió del telencèfal dels *Xenopus* és l'única zona descrita en la s'hi poden trobar neurones espinoses(Huang *et al.*, 2015). Per tal d'electroporar aquest tipus de neurones, la barreja de DNA s'injecta en la línia mitja a l'interior del ventricle. Exemples de neurones espinoses electroporades amb marcadors morfològics (mGFP) o indicadors genètics de calci (GCaMP6s:mRFP) es poden veure en la Figura 7 i en la secció Appendix protocols.
Després d'optimitzar el mètode d'electroporació de les neurones del bulb olfactiu (Figura 6), es van poder registrar respostes induïdes amb llum en larves incubades amb TCP9. La resolució que obtenim mitjançant l'electroporació de neurones aïllades ens permet registrar l'activació neuronal induïda pel TCP9 a nivell d'una única cèl·lula o, fins i tot, una única espina (Figures 6 i 7). Fins on arriba el nostre coneixement, aquesta és la primera vegada que es demostra l'ús de fotocommutadors de receptors endògens en el control in vivo aquests nivells de resolució espacial i temporal.

*Aplicació d'activadors neuronals (TCP9) per influenciar en la regeneració nerviosa*
El demostrat control de l'activitat neuronal que ens permet l'aplicació del fotocommutador TCP9, ens dirigeix a provar el seu potencial en altres àmbits com ara la regeneració nerviosa. Amb la col·laboració del grup del Dr Artur Llobet (UB) es va dissenyar un model experimental in vivo amb una línia transgènica de *Xenopus tropicalis* en la qual es pogués fer un seguiment exhaustiu de la regeneració nerviosa. La nostra hipòtesis en aquest cas era que un augment de l'activitat neuronal induïda per la fotoactivació del TCP9 influiria en la reconnexió en un nervi degenerat. El model transgènic de Xenopus utilitzat en aquest cas es caracteritza per la sobre-expressió de la proteïna fluorescent verda (GFP) en connexió amb la proteïna tubulina. D'aquesta manera, tots els nervis de les larves presenten una fluorescència verda estable. Després de procedir a l'escissió del nervi olfactiu dret, es va injectar el TCP9 a nivell del bulb olfactiu i les larves es van sotmetre a dos tipus de patrons d'iluminació constants: (1) estimulació alternada a 380 i 500 nm a la freqüència d'1 Hz; (2) estimulació a 375 nm durant 10 segons cada 2 min. El procés de regeneració va ser estudiat amb fotografies diàries de fluorescència i la quantificació ratiomètrica del gruix del nervi degenerat respecte el nervi intacte en el mateix capgròs. En el cas de les larves control la regeneració es complerta en 4 dies, però en el grup tractat amb TCP9 en combinació amb el patró d'il·luminació (1) la regeneració s'endarrereix un dia. Els capgrossos tractats amb TCP9 en combinació amb el patró (2) no van presentar diferències significatives en el procés de regeneració nerviosa (Figura S6).
Està descrit que la regeneració nerviosa en amfibis es un procés estretament controlat depenent de l'activitat sensorial(Kikuta *et al.*, 2015; Terni *et al.*, 2017). En alterar l'activació neuronal en el bulb olfactiu a través de la foto-activació del TCP9, estem alhora alterant tota l'homeòstasi del procés regeneratiu. Una possible explicació del retard observat en els capgrossos tractats amb el patró d'il·luminació (1) pot ser que el TCP9 es dirigeix als receptors inotròpics de glutamat (AMPA o Kainat) presents en les cèl·lules externes (amb ramificacions en forma de plomall,

"external tufted cells") de la capa granular del bulb olfactiu. La sobre-activació d'aquest tipus cel·lular inhibeix l'activitat espontània i l'activitat induïda per olors que normalment es tradueix a les cèl·lules mitrals o cèl·lules en plomall(Tatti *et al.*, 2014). Tot i així, l'administració del TCP9 i la seva conjugació no estan específicament dirigides a un únic tipus cel·lular en el bulb olfactiu i per tant, amb l'aproximació experimental actual, només podem concloure que una correcta senyalització aferent i homeòstasi en el circuit neuronal és essencial per a un correcte procés de regeneració nerviosa.

**Capítol 3 | Introducció de grups foto-làbils pel control espacio-temporal en la conjugació de lligands units fotocommutables (PTLs)**

La llum ens ofereix el control espacial i temporal de proteïnes mitjançant molècules fotocommutables. No obstant, aquesta propietat també pot ser explotada a nivell de la conjugació de lligands units fotocommutables. En el capítol 3 es presenta el disseny d'un PTL en el qual podem controlar mitjançant patrons de llum la conjugació. En comptes de reaccionar directament amb cisteïnes (MAG) o lisines (TCP), es va modificar químicament la part reactiva del TCP9 per introduir-hi un grup foto-làbil que només permet l'ancoratge del TCP9 al receptor en el moment i lloc en el qual s'il·lumina. Prèviament, els grups foto-làbils com les benzofenones, aril azides i diazirines han estat utilitzades per al control de l'alliberació de neurotransmissors, identificació de receptors i els seus llocs d'unió, caracteritzar la funció sinàptica i monitorar el tràfic de receptors en temps real(Chambers *et al.*, 2004; Mortensen *et al.*, 2014).

En el nostre cas, utilitzem connectors "*crosslinkers"* heterobifuncionals que contenen un grup amino-reactiu (N-hidroxisuccinimida ester, NHS) i un anell foto-activable (Figura 1). La reacció foto-làbil té com a resultat l'alliberament del grup NHS que pot formar enllaços covalent amb qualsevol aminoàcid del domini d'unió a lligand dels receptors endògens de glutamat (Figura 2). Tal i com es descriu en (Izquierdo-Serra *et al.*, 2016) i en el Capítol 2.

La funcionalitat del nou TCP9 foto-làbil va ser experimentalment estudiada in vitro en cultius primaris de neurones d'hipocamp mitjançant registres electrofisiologics per Patch-clamp. Les neurones van ser incubades amb TCP9 foto-làbil i exposades a la il·luminació continua a 350 nm. Després de diversos rentats amb solució fisiològica, es va procedir a fer els registres electrofisiologics de les neurones. El potencial de membrana es va establir en tots els casos a -60 mV. L'estimulació lumínica amb polsos de llum UV indueixen potencials d'acció que poden ser silenciats amb polsos de llum visible (verda) (Figura 3). Les neurones incubades amb TCP9 foto-làbil però sense rebre el protocol d'il·luminació òptim o amb el grup foto-làbil ja foto-degradat no presenten fotorespostes evocades per llum UV (Figura 4 i 5).

Com a conclusió podem dir que en el Capítol 3 demostrem la capacitat de foto-induir la conjugació de PTLs en diferents poblacions neuronals mitjançant la il·luminació controlada de llum UV. Aquests resultats obren noves possibilitats a projectes, per exemple in vivo, en els quals es busca el control espacial i temporal de la conjugació de PTLs en una regió especifica o en un grup neuronal dins un circuit, de manera que es pugui controlar la seva activitat sense afectar el sistema sencer.

**Part II: Modificacions de les propietats òtiques de lligands units fotocommutables (PTLs):**

## Capítol 4 | Estimulació foto-farmacològica a elevades freqüències dels receptors AMPA endògens en neurones de la còclea

La primera generació de lligands units fotocommutables capaços de fotosensibilitzar receptors glutamatèrgics endògens presenta un inconvenient principal, son activables amb llum ultra violeta. S'ha demostrat que la llum UV pot ser perjudicial per les cèl·lules, a més presenta una baixa capacitat de penetració en teixits, fet que en limita l'ús en certs models in vivo. D'altra banda, l'estabilitat tèrmica en foscor fa que es necessiti una segona longitud d'ona d'il·luminació per tal de revertir l'efecte de l'isòmer *cis*. En el Capítol 4 busquem derivats del TCP que siguin activables en el rang visible de llum i que tinguin un temps de relaxació curt, de manera que només sigui necessària una longitud d'ona per controlar-ne l'activitat.

Seguint la mateixa estratègia de síntesis química que en la primera generació de TCPs, es van sintetitzar dos nous "caps" foto-activables amb llum blava per tal de combinar-los amb diferents "cues" (Figura 2). En primer lloc, els "caps" blaus es van provar com a lligands solubles en cèl·lules que sobre-expressaven el receptor GluK1 (Figura S1). D'aquí, es va seleccionar el "cap-2" degut a una millor capacitat de foto-activació. Seguidament, la funcionalitat dels PTLs obtinguts de la combinació entre el "cap-2" i les diferents "cues" es va examinar en cultius primaris de neurones d'hipocamp, on tots els receptors de glutamat són presents. La primera combinació de "cap-2" amb "cua-1" dóna com a resultat el compost B-TCPa. Aquest, és capaç de conjugar-se als receptors endògens de les neurones induint una despolarització constitutiva que només pot ser revertida mitjançant llum blava (~460 nm) (Figura S2). El nivell de despolarització causat per B-TCPa no es suficient per induir la generació constant de potencials d'acció, tot i que sembla hiperpolaritzar la neurona quan aquesta es troba en mode de "corrent clampejada". La segona combinació de "cap-2" amb "cua-2" busca revertir l'efecte d'activació constitutiva del B-TCPa a través d'una cua més rígida, de manera que el lligand quedi fora del lloc d'unió del lligand i només hi pugui interaccionar quan es troba en la seva conformació plegada (cis). No obstant, el compost generat B-TCPb no es capaç d'induir foto-respostes (Figura S3). El següent pas a seguir va ser la combinació del "cap-2" amb una "cua-3" més llarga, en l'intent que el lligand quedés fora de l'abast del lloc d'unió al lligand quan el fotocommutador es trobés en la conformació trans. Així, el compost B-TCPc es capaç d'evocar corrents internes mesurables que generen suficient despolarització per provocar potencials d'acció quan aquest es isomeritzat de *trans* a *cis* amb llum blava a diferents freqüències d'estimulació (Figura 3). Les fotorespostes registrades en neurones van ser farmacològicament caracteritzades. Els resultats obtinguts indiquen que B-TCPc no afecta als receptors tipus NMDA, però es conjuga en receptors tipus AMPA o Kainat (Figura 4a). La foto-activació dels receptors homomèrics GluA1 i GluA2 sobre-expressats en línies cel·lular confirma els resultats (Figura 4b i 4c). Per últim, la combinació del "cap-2" amb una "cua-4" més llarga no mostra corrents controlades per llum en neurones (Figura S4). Una possible explicació és que la "cua-4", massa llarga, deixa fora de l'abast al lligand fins i tot en la conformació plegada *cis*, de manera que B-TCPd es incapaç d'activar el receptor.
El comportament idoni que presenta el compost B-TCPc in vitro ens fa pensar que és un bon candidat per fotosensibilitzar processos sinàptics ultra ràpids en els quals hi estiguin implicats els receptors de glutamat tipus AMPA. Un exemple es la sinapsis formada per les cèl·lules

ciliades i les neurones ganglionars de la còclea (Figura 1 i S6). Amb la col·laboració del grup del Dr Tobias Moser, es va testar la capacitat de B-TCPc en la fotosensibilització de les neurones de la còclea en jerbus adults (8 a 12 setmanes) no modificats genèticament. L'activitat de les neurones ganglionars de la còclea es registrada mitjançant un elèctrode situat a l'entrada de la finestra circular(Batrel *et al.*, 2017). Així, s'obtenen registres de l'activació sincronitzada de les neurones ganglionars evocada per l'estimulació sonora o per llum (Figura 5 i S12). L'aplicació directa de B-TCPc en combinació amb polsos de llum (473 nm) a través d'una fibra òptica situada en la finestra circular és suficient per induir la generació de potencials d'acció sincronitzats en les neurones ganglionars. Les respostes evocades per la llum es caracteritzen per l'amplitud, mesurada com la diferència entre el primer pic negatiu (N1) i el pic positiu (P1)(Bourien *et al.*, 2014); i la latència, definida com el retard entre l'inici del pols de llum i el pic N1. Analitzant la dependència a la intensitat podem dir que el llindar mesurable es situa a partir de 10 mW, l'amplitud màxima registrada és de 30.87 ± 2 µV (Figura 6d-e) i la latència disminueix de 1.67 ± 0.08 a 1.50 ± 0.06 ms (Figura 6f). La duració òptima de l'estímul lumínic es troba entre 60 i 100 µs (Figura 6g-h) i variacions en la freqüència d'estimulació indiquen que les respostes son mesurables fins a 4 KHz (Figura 6j-k).

En el Capítol 4 presentem per primera vegada l'ús de lligands units fotocommutables en el control dels receptors endògens de les neurones ganglionars de la còclea. Els resultats obtinguts indiquen que B-TCPc té rendiments comparables a les millors eines optogenètiques aplicades en el camp (Keppeler *et al.*, 2018; Mager *et al.*, 2018; Wrobel *et al.*, 2018): (1) relaxació tèrmica de l'isòmer *cis* a l'isòmer *trans* ultra ràpida, en el rang de mil·lisegons; (2) la longitud d'ona d'activació es troba en el rang de llum visible; (3) no s'observa foto-adaptació al llarg del temps d'estimulació de la llum.

No obstant això, cal destacar la necessitat de preservar la integritat del terminal post-sinàptic per la correcta fotosensibilització mitjançant B-TCPc. D'aquesta forma, l'aplicació fotofarmacològica en condicions de pèrdua d'audició es veu limitada en condicions de sordesa originades per l'acció d'antibiòtics aminoglicòsids (Figura S9) o altres causes de degeneració sinàptica com la sordesa relacionada amb l'edat. Malgrat tot, encara hi ha esperança en l'ús de fàrmacs fotocommutables en condicions de pèrdua d'audició degudes per mutacions en els canals de calci (Figura S10) (Pangrsic, Singer and Koschak, 2018) o causades per tractaments antitumorals (Wake *et al.*, 1994).

## Capítol 5 | Disseny racional de fotocommutadors azobenzènics per l'excitació neuronal eficient a dos fotons

Prèviament, els mètodes descrit per la síntesis de PTLs sensibles a l'activació per dos fotons han resultat en la síntesis de molècules desplaçades cap a longituds d'ona vermelles però de relaxació tèrmica ràpida(Kienzler *et al.*, 2013; Izquierdo-Serra *et al.*, 2014). Aquest tipus de compostos presenten una eficàcia millorada respecte als fotocommutadors on l'azobenzé no conté substituents asimètrics. Tot i així, tots ells estan lluny de proporcionar un 100% de fiabilitat en la generació de potencials d'acció per l'activació a dos fotons. En el Capítol 5(G. Cabré *et al.*, 2019), el nostre objectiu és el disseny de derivats del MAG optimitzats per absorbir a dos fotons canviant-ne el seu espectre d'activació però sense modificar les seves característiques foto-dinàmiques: temps de relaxació lent i bi-estabilitat d'activació entre 380 nm (*trans* → *cis*) i 500 nm (*cis* → *trans*) (Figura 3).

En aquest treball, amb la col·laboració del Departament de Química Orgànica de la Universitat Autònoma de Barcelona, es descriuen dos nous derivats del MAG amb diferent sensibilitat a dos fotons depenent del grau d'efecte "push-pull" que impliquen els diferents substituents al voltant de l'azobenzé (Figura 1 i 2). Els resultats obtinguts concorden amb el disseny teòric que prediu que com més electronegatiu sigui el substituent, major serà l'efecte "push-pull" en la molècula, i per tant major serà la sensibilitat a dos fotons. L'activació per dos fotons comporta una major precisió espacio-temporal i un augment de la capacitat de penetració de la llum en el teixit. Tot i així, aquestes molècules conserven el control dual amb dos longituds d'ona diferenciades.

Després d'una caracterització bàsica mitjançant imatge de calci en línies cel·lulars transfectades (Figura 3d, 4 i 5), el compost es va testar en cultius organotípics d'hipocamp per tal de comparar-ne l'eficàcia amb el MAG original (Figura 6). En aquest cas, $MAG^{slow}_{2P\_F}$ indueix més eficientment respostes evocades de calci mitjançant la foto-estimulació a dos fotons que el MAG original.

A més a més, es va investigar la capacitat de $MAG^{slow}_{2P\_F}$ per fotosensibilitzar i controlar in vivo l'activació de neurones dels cucs *Caenorhabditis elegans* mitjançant l'excitació a dos fotons (Figura 7). La morfologia i funció de les 302 neurones que es troben en els cucs *C.elegans* esta descrita en detall i permet per exemple que puguem investigar l'efecte fotofarmagologic en circuits sensorials i motors senzills. El receptor LiGluR fusionat a la proteïna fluorescent vermella (mCherry) i l'indicador genètic de calci GCaMP6s es van co-expressar en les neurones receptores del tacte (TRNs) (Figura 7a-b). De les sis neurones TRNs descrites que formen el camp receptor a la part anterior-posterior i d'esquerra a dreta, ens vam centrar en el parell de neurones PLML/R de la cua del nematode. De la mateixa manera que altres neurones en el sistema nerviós, els parells de neurones TRNs poden ser selectivament estimulats en la part anterior i posterior de l'animal amb patrons de llum. No obstant, l'activació unilateral és més difícil i suposa un obstacle per la foto-manipulació de la seva activitat per mètodes optogenètics(Stirman *et al.*, 2011). Aquest fet és especialment rellevant quan les neurones es troben superposades en el mateix eix òptic o estan molt empaquetades com en el cap. En aquests casos, l'excitació a dos fotons confereix un avantatge únic comparat amb l'excitació simple a un fotó, la qual presenta una selectivitat en el pla axial de 10 µm (Prakash *et al.*, 2012). Després d'administrar $MAG^{slow}_{2P\_F}$ en un animal viu (detallat en la secció de mètodes de l'article), l'activitat neuronal va ser registrada per imatge de calci en les neurones TRNs posterior (PLM) que expressaven el receptor LiGluR-mCherry i l'indicador GCaMP6s a través d'un microscopi confocal. Clarament s'observen respostes foto-induides per l'excitació a dos fotons en tots aquells animals que també responen a l'excitació per llum a un fotó. Mentre que els animals control tractats amb el vehicle només presenten una reducció parcial de la fluorescència deguda al "bleaching" dels indicadors mCherry i GCaMP6s (Figura 7c-d). En cap cas es van observar signes de toxicitat deguts a la injecció dels compostos durant el període de recuperació i d'imatge. Així concloem que el disseny racional de les propietats dels fotocommutadors excitables a dos fotons també poden ser utilitzades per foto-manipular l'activitat neuronal d'una única neurona amb gran eficàcia i selectivitat.

El Capítol 5 reprodueix el següent article:

*Cabré G, Garrido-Charles A, Moreno M, et al. Rationally designed azobenzene photoswitches for efficient two-photon neuronal excitation. Nat Commun. 2019;10(1). doi:10.1038/s41467-019-08796-9*

## Capítol 6 | Enginyeria de proteïnes col·lectores de llum per optogenètica i optofarmacologia

L'ampliació i la modificació espectral de la resposta d'eines optogenètiques i fotofarmacològiques és necessària per desenvolupar tot el seu potencial en el control de l'activitat biològica amb llum. Per tal d'assolir aquest objectiu evitant la tediosa tasca del disseny de noves modificacions genètiques(Klapoetke *et al.*, 2014) o químiques dels fotocommutadors(Paoletti, Ellis-Davies and Mourot, 2019), en aquest capítol proposem una nova estratègia inspirada a partir de la maquinària col·lectora de llum dels sistemes fotosintètics (Figura 1).

Decorant els voltants de la unitat fotoisomeritzable dels sistemes amb fotosensibilitzadors moleculars, millorem i desplacem espectralment els senyals evocats per llum per la proteïna sensible a llum "Channelrhodopsin-2" (ChR2) i pel receptor de glutamat regulat per llum (LiGluR), com a models d'eines optogenètiques i fotofarmacològiques. La nostra aproximació es basa en la superposició espectral d'activació de la ChR2(Nagel *et al.*, 2005) i l'activació del receptor LiGluR conjugat amb el fotocommutador $MAG_{2P}$(Izquierdo-Serra *et al.*, 2014) o $MAG_{2P\_long}$, tots en el rang de llum visible blava, amb l'espectre d'emissió del fluòrofor Alexa Fluor 350 (Figura 2b). La longitud d'ona d'excitació de l'Alexa Fluor 350 es troba a 350 nm, lluny de la longitud d'ona d'activació de ChR2 i LiGluR-$MAG_{2P}$, de manera que l'efecte fotosensibilitzador és més evident. Diferències significatives es poden observar en l'efecte fotosensibilitzador de l'Alexa Fluor 350 comparant l'activitat de ChR2 (Figura 3) o del LiGluR (Figura 4). Mitjançant estudis comparatius de la seqüencia i estructura de ChR2 i el LBD del receptor LiGluR, s'observen clares diferències a nivell del nombre de lisines susceptibles a ser fotosensibilitzades que explicarien les diferencies funcionals registrades en presencia del mateix fotosensibilitzador (Figura S3). En el cas d'utilitzar fluoròfors que no presenten superposició espectral entre la seva emissió i l'absorció dels fotocommutadors, com és el cas de Texas Red, no s'observa cap efecte fotosensibilitzador (Figura S6).

A partir dels experiments realitzats i de simulacions teòriques, concloem que la sensibilitat a la llum d'aquestes i altres proteïnes fotosensibles pot ser modificada diversos ordres de magnitud utilitzant fotosensibilitzadors químics. A més, introduïm una metodologia única per a la conjugació ortogonal de fotosensibilitzadors i fotocommutadors en la millora del rendiment de les eines optogenètiques i fotofarmacològiques actuals.

**Part III. Modificacions de les propietats òptiques de lligands fotocròmics solubles (PCLs):**

La fotofarmacologia clàssica va començar amb la modificació de petites molècules per sensibilitzar-les a l'activació per llum i així millorar la seva especificitat i disminuir-ne els efectes adversos que poguessin causar. Una de les estratègies utilitzades és la protecció de fàrmacs

actius amb un grup foto-làbil que en ser irradiat allibera el compost actiu i altres productes secundaris (especialment neurotransmissors(Wieboldt *et al.*, 1994)). Una altra estratègia va sorgir de la introducció d'un fotocommutador que pogués canviar reversiblement la seva conformació i així es pogués controlar l'activació del fàrmac bi-direccionalment amb llum. Aquests fàrmacs sensibles a llum van passar a ser anomenats lligands fotocròmics solubles (PCLs), els quals es poden considerar una nova generació de lligands foto-amagats no-destructius. La seva principal limitació és que la diferència d'activitat entre tots dos isòmers típicament és 10 vegades menor i l'isòmer actiu acostuma a ser el que és tèrmicament més estable. Per tal de revertir aquest inconvenients en el Capítol 7 i 8 es presenten dues estratègies diferents basades en la substitució del cromòfor azobenzè per l'estilbé o per azobenzens cíclics i les seves aplicacions en el control de l'activitat neuronal amb llum.

**Capítol 7 | Activació dels receptors iGluR regulada per llum mitjançant lligands no-foto-destructius basats en el cromòfor estilbé**

La primera estratègia emprada es basa en la substitució de l'azobenzè per un estilbé per donar lloc a un fotocommutador similar al GluAzo(Volgraf *et al.*, 2007) en el qual es busca augmentar l'estabilitat tèrmica de l'isòmer *cis* i evitar la fotoisomerització de *trans* a *cis* (Figura S1 i S2). D'aquesta manera, l'activació foto-induïda del fotocommutador GluS2 és irreversible, amb un 100% d'eficiència i sense generar cap foto-producte secundari.

Els primer fotocommutadors amb estilbens sintetitzats es van testar per induir la foto-activació del receptor GluK1. No obstant, l'eficàcia del compost GluS1 es veu limitada per la seva baixa solubilitat en medis polars (aigua)(Figura 2 i S3). Per tant, es va procedir a introduir químicament un àcid carboxílic en el seu extrem més apolar per tal d'augmentar la seva solubilitat en aigua i millorar alhora la fotoisomerització.

Per demostrar funcionalment la diferent acció de tots dos isòmers del segon fotocommutador estilbé GluS2 es van dur a terme registres electrofisiològics en línies cel·lulars transfectades amb el receptor de glutamat tipus GluK2 (Figura 3). L'activació mitjançant la perfusió en el medi de glutamat lliure demostra el correcte funcionament dels canals homomèrics formats per GluK2(Traynelis *et al.*, 2010). Tot seguit, la perfusió de *trans*-GluS2, evoca corrents despolaritzants similars a les evocades pel glutamat lliure. En canvi, la perfusió de *cis*-GluS2 no provoca cap canvi mesurable a nivell del potencial de membrana, com a resultat de l'absència d'activació del receptor per part de *cis*-GluS2. En el moment en que s'irradia amb llum UV (~365 nm), *cis*-GluS2 fotoisomeritza a *trans*-GluS2 i es capaç d'induir corrents iòniques internes (despolarització cel·lular) com a conseqüència de l'activació del receptor GluK2.

Resultats preliminars en cultius organotípics d'hipocamp en els quals es sobre-expressa l'indicador de calci GCaMP6s combinat amb l'indicador morfològic dsRed2, mostren que ambdós isòmers *cis*- i *trans*-GluS2 tenen efectes diferenciats en la manipulació de l'activitat neuronal (Figura S7).

En aquest treball demostrem per primera vegada la capacitat dels fotocommutadors basats en estilbé pel control específic de respostes excitadores en receptors endògens de glutamat. Els resultats obtinguts in vitro concorden amb el disseny químic i la caracterització fotoquímica dels

compost obtinguts. És remarcable el fet que en aquest treball s'ha posat de manifest que les condicions biològiques no sempre coincideixen amb les condicions òptimes "en cubeta". Finalment, es demostra que el disseny químic es pot adaptar per resoldre problemes biològics reals de manera eficient.

**Capítol 8 | Neurotransmissors sintètics fotocommutables basat en azobenzens cíclics**

La segona estratègia utilitzada és la substitució de l'azobenzè per un azobenzè cíclic(Hammerich *et al.*, 2016). Els azobenzens cíclics es caracteritzen per tenir un isòmer *cis* més estable tèrmicament, el qual normalment és l'isòmer inactiu. El nostre objectiu en aquest treball és demostrar que l'administració de l'isòmer *cis* dels PCLs Glu_brAzo1 i Glu_brAzo2 no afecta a l'activitat de receptors neuronals endògens. De manera que només seran foto-activats selectiva i reversiblement quan siguin estimulats amb llum, un altre avantatge més respecte dels azobenzens clàssics activats amb llum violeta com el GluAzo(Volgraf *et al.*, 2007).

Per valorar la capacitat de Glu_brAzo1 i Glu_brAzo2 per regular amb llum els receptors iGluR, es van dur a terme registres electrofisiològics de l'activitat induïda en línies cel·lular que sobre-expressessin els receptors GluK1 o GluK2 (Figura 3b, S8-S11). Després de l'aplicació i posterior irradiació de Glu_brAzo1 i Glu_brAzo2, es va registrar un increment en les corrents evocades per l'isòmer trans. No es van detectar canvis mesurables en foscor o a longituds d'ona d'excitació > 450 nm (fotoisomerització *trans*-*cis*). En canvi, l'amplitud màxima de corrent registrada es troba en les longituds d'excitació 390- 400 nm (fotoisomerització *cis*-*trans*).

L'activació selectiva mitjançant l'siòmer *trans* dels compostos Glu_brAzo1 i Glu_brAzo2 es demostra també mitjançant corbes de dosis-resposta en cèl·lules sobre-expressant els receptors GluK1 o GluK2, en foscor i a longitud d'excitació 390 nm (10 - 300 µM) (Figura S11). En tots els casos, majors respostes van ser registrades per l'activitat induïda de l'isòmer *trans*, encara que (1) la manipulació de l'activitat foto-induïda es entre moderada i baixa (del 10 al 35 % d'increment respecte la condició en foscor); i (2) els valors màxims registrats representen només el 20-40 % del total de resposta evocada per glutamat. Principalment tres factors poden explicar aquests resultats: fotoisomerització incompleta de *cis* a *trans*, tal i com s'observa en solució (< 60%); variacions menors de l'afinitat pel lloc d'unió a lligand entre els isòmers *cis* i *trans*; efectes estèrics del grup azobenzè cíclic en la seva configuració *trans* són d'especial importància en la interacció amb el receptor GluK2 ja que presenta una cavitat d'unió a lligand més estreta(Mayer, 2005). De fet, el darrer punt explica els menors senyals amb major selectivitat induïda per llum obtinguts per aquest receptor. No obstant, no evita que el grup terminal més voluminós de Glu_brAzo2 produeixi majors corrents (2 vegades més respecte Glu_brAzo1). Provablement aquest fet es deu a una millor solubilitat en aigua i/o a interaccions addicionals estables amb la cavitat d'unió a lligand del receptor GluK2.

Finalment, Glu_brAzo1 i Glu_brAzo2 es van provar com a neurotransmissors fotocommutables en cultius de neurones d'hipocamp, on el receptor GluK2 s'expressa en abundància (Figura 4 i S12). Cap tractament addicional es va fer en les neurones i simplement es van registrar les corrents induïdes per llum en un corrent de membrana mantingut a -60 mV. Degut al comportament *trans*-actiu, *cis*-estable, no s'observen canvis biològics (despolarització) quan es perfon Glu_brAzo1 o Glu_brAzo2 sense estimulació lumínica, un clar avantatge respecte la

majoria de PCLs descrits fins ara. La generació de potencials d'acció, en canvi, pot ser induïda específicament mitjançant la isomerització *cis-trans* de Glu_brAzo2, però no de Glu_brAzo1, a concentracions (30 μM) i intensitats de llum (22.0 μW $mm^{-2}$ per 380 nm i 47.4 μW $mm^{-2}$ per 500 nm) relativament baixes.

Com a resultat, es generen potencials d'acció seqüencials i mantinguts mitjançant la fotoisomerització de Glu_brAzo2 a través de l'isomerització consecutiva entre llum violeta i verda. Aquest comportament es silenciat per l'aplicació de DNQX, un conegut antagonista de receptors de kainat i AMPA (Figura 4d). Basant-nos en aquests resultats i en les condicions experimentals emprades, atribuïm les fotorespostes registrades en neurones d'hipocamp a una major interacció de Glu_brAzo2 amb el receptor GluK2, resultat clarament sorprenent si es té en compte el caràcter d'agonista parcial del compost i la limitada modulació amb llum obtinguda prèviament en línies cel·lulars. Malgrat això, es demostra el comportament no lineal de la senyalització neuronal, ja que només es requereix la interacció de l'agonista amb una petita fracció dels receptors GluRs per tal de superar el llindar de despolarització necessari per generar un potencial d'acció.

El Capítol 8 reprodueix el següent article:

*Cabré G, Garrido-Charles A, González-Lafonta À, et al. Synthetic photoswitchable neurotransmitters based on bridged azobenzenes. Org Lett. 2019. doi:10.1021/acs.orglett.9b01222*

## Capítol 9 | Conclusions

Les principals conclusions obtingudes a partir d'aquest treball són :

- L'estructura modular dels lligands units fotocommutables (PTLs) ofereix una gran versatilitat en: (1) la modificació de la part reactiva (incloent reaccions selectives per cisteïnes, reaccions més permissives, i funcionalitat de grups foto-làbils); i (2) la modificació del grup fotocommutable (incloent canvis espectrals i de relaxació tèrmica, augment de la sensibilitat a l'excitació per dos fotons i capacitat de ser fotosensibilitzats amb col·lectors químics de llum).
- La unió covalent de PTLs és possible en receptors de glutamat endògens mitjançant la substitució del grup reactiu maleimida pel grup NHS ester. Aquest nou subtipus de PTLs l'hem anomenat "Fotocommutadors covalents dirigits" (TCPs).
- La caracterització de la primera generació de TCPs activables per llum UV en línies cel·lulars demostra la seva capacitat de conjugació en els receptors GluK1 i GluA1 no modificats genèticament.
- El fotocontrol que ens permet el TCP9 no requereix de modificacions genètiques, fet que el fa idoni en aproximacions experimentals on es vulgui fer el seguiment funcional de receptors endògens in situ (per exemple en processos de plasticitat sinàptica) i experiments in vivo. En particular, s'ha provat la capacitat de TCP9 de foto-modular la regeneració nerviosa en un model de capgrossos de Xenopus.
- Les millores en termes de marcatge i resolució aconseguides gracies a la tècnica

d'electroporació in vivo, ens han permès demostrar la capacitat de TCP9 en la fotomodulació de l'activitat neuronal en capgrossos de Xenopus in vivo, a temps real, fins a un nivell de precisió d'una única sinapsis.

- La introducció d'un grup foto-làbil demostra la capacitat de controlar espacialment amb patrons de llum la conjugació dels TCPs en receptors endògens presents en neurones d'hipocamp.
- Les modificacions químiques electrònicament asimètriques en el centre azobenzènic del TCP, tenen com a resultat un canvi espectral (activables amb llum visible) i una disminució del temps de relaxació tèrmic.
- Els fotocommutadors resultants de la combinació d'una llibreria de "cues" indiquen que B-TCPa es conjuga a GluK1 i B-TCPc es conjuga als receptors GluA1 i GluA2.
- La incubació d'ambdós compostos en cultius primaris de neurones d'hipocamp comporta la fotosensibilització dels receptors endògens. Sobre el comportament òptim de B-TCPc podem dir que: B-TCPc permet el control temporal i espacial de l'activació neuronal; l'efecte obtingut es reversible i mantingut en el temps; les fotorespostes obtingudes són farmacològicament selectives.
- D'altra banda, s'ha demostrat la capacitat de B-TCPc per al ràpid foto-control de l'activitat neuronal dels receptors endògens en la còclea de jerbus. Aquesta representa la primera estratègia de fotosensibilització fotofarmacològica com alternativa a les modificacions optogenètiques en el disseny d'implants òptics en la còclea.
- Presentem una estratègia racional per al disseny químic d'azobenzens optimitzats per ser excitats a dos fotons sense alterar-ne altres característiques òptiques i foto-dinàmiques. Així, aconseguim augmentar la resolució espacial necessària per la foto-estimulació amb dos fotons in vivo.
- Descrivim un mètode innovador per la modificació espectral de fotocommutadors mitjançant col·lectors de llum (fluoròfors químics) com ampliació de les tècniques per la foto-modulació de molècules o proteïnes que anteriorment només s'havia aconseguit mitjançant mutagènesis o nova síntesis química.
- L'ús d'altres cromòfors no conjugables als receptors (PCLs) ha demostrat també la seva utilitat per controlar l'activació de neurones d'hipocamp. Els PCLs presentats ofereixen diferents avantatges en comparació amb l'azobenzè clàssic: en un primer cas, l'ús d'azobenzens cíclics reverteix l'estabilitat i en conseqüència l'activitat de la molècula; i per altra banda, els estilbens permeten l'activació irreversible però no foto-destructiva de la molècula original, evitant així la creació de foto-productes.
- Hem realitzat una exploració exhaustiva de les diferents funcionalitats biològiques de diferents fotocommutadors (modificacions farmacològiques, cròmiques i reactives), hem obtingut amb èxit les propietats desitjades, i hem demostrat diverses aplicacions noves en teixit cerebral intacte i en diferents models animals (capgrossos, cucs i jerbus).

## ACKNOWLEDGMENTS

M'agradaria començar agraint les beques del *Ministerio de Ciencia, Innovación y Universidades del Govierno de España* per ajudar en el finançament del meu doctorat amb la beca BES-2014-068169 i la possibilitat que em van donar amb dos beques de mobilitat. A més a més, el finançament que fa possible el funcionament dia a dia del nostre laboratori i dels nostres projectes: ERANET SynBio MODULIGHTOR project, Human Brain Project WAVESCALES projects, La Marató TV3, THERALIGHT (ERC-PoC) i Fundaluce and Ramón Areces foundations.

A nivell personal voldria agrair al Pau l'oportunitat que m'ha donat de poder agafar el meu "càmping kit" i poder anar a molts laboratoris i aprendre moltes tècniques noves i, tot i que normalment els nostres instruments son "pals i pedres", he après que aquest son els que millor ens funcionen i mai ens han fallat.

Moltes gracies a la Mercè per dipositar en mi tot el seu coneixement en un temps rècord i així donar-me la possibilitat d'entusiasmar-me pels projectes de fotofarmacologia que després em van portar a fer un doctorat que mai hagués pensat capaç de fer.

Gracies també a tota la gent del Lab 5312 que em va acollir i que ara ja fa temps que no hi son: Natalia, Santi, Ari, Silvia... el vostre suport ha estat sempre molt important. I a la Nuri, que sempre hi ha estat i pateix les anades i vingudes de molta gent i es converteix en un pilar per tots nosaltres al laboratori, sense tu no seria el mateix.

Gràcies Miquel per transmetrem tot el teu coneixement i estima per la ciència, entre moltes d'altres històries. A la Rosalba, por amenizar siempre la hora de comer con las mil y una peripecias que le pasan en la vida. Gracias Clara por venir y compartir conmigo los dolores de cabeza que puede causar el patch y por ayudarnos en todos los proyectos que te hemos propuesto. Alex, la persona amb menys memòria que he conegut però que sempre em recorda la importància dels bons controls. I el seu segon a bord que ara ja vola tot sol, Pablo, per inclourem per un temps en el *zebrafish team*.

A l'Anna, per compartir els patiments del doctorat i múltiples discussions sobre quin és el català *correcte*. Als seus innumerables estudiants que sempre l'han perseguit i li han donat molta vida al 5312, i que com la Nerea s'han convertit en nous bons amics. I a les noves incorporacions del lab, Galyna y Ricardo, espero que disfrutéis vuestro paso por el lab tanto como lo he hecho yo.

Al grup de químics, els que primer em van introduir i em van fer entendre una mica millor el món de les provetes: Antoni Bautista, Anna Trapero i Amadeu Llebaria; i als que han continuat amb mi durant tot aquest procés i m'han parlat de les meravelles de la *bella Italia*: Carlo, Fabio, Davia i Rossella; i els estudiants de màster (majoritàriament també italians) que van venir a veure una mica de biologia, Francesco y Claudio.

Aquesta tesi tampoc hagués sigut possible sense la col·laboració incondicional del grup de químics de la UAB. Agrair a la Gisela, que amb unes forces de química sintètica imparables i la seva empenta va fer tirar endavant més d'un projecte que semblava impossible i s'ha convertit en una biòloga més del grup. Al Jordi, Ramón i Felix, que amb les seves idees, discussions i bon rotllo han fet molt més que una simple col·laboració.

Agrair la gran col·laboració amb el grup de l'Artur Llobet i la Beatrice, que primer em van introduir al món dels amfibis de mans de l'Helena i després ens han ajudat sempre, tant a nivell tècnic com d'idees, fins poder posar a punt una tècnica que es convertirà en tot un referent per tots nosaltres al lab.

Finalment agrair a tots els laboratoris de la 4a planta per les mil i una vegades que hi hem anat a demanar gel sec o altres mil històries i de fer possible any rere any les millors *Mojitades*.

I am also grateful to all the labs that hosted me during my PhD:

Mi primera aventurilla en el laboratorio del dr Pedro de la Villa en la Universidad de Alcalá de Henares, aunque breve y buena, no dio los resultados que esperábamos.

Dr Christine Holt, for hosting me at University of Cambridge (UK) from September to December 2017 and letting me learn from Hovy that it is easier to see it with your eyes than trying to reproduce a protocol from a methods paper.

La ayuda del dr Eduardo Soriano y su equipo por dejarnos ocupar su laboratorio con tubos, botellas y carritos rodantes.

The collaboration with Dr Krieg lab and specially with the expert hands of Montse during the summer of 2018, that made possible closing one project and to open more others.

And finally, I am grateful to Dr Tobias Moser, for hosting me at the Institute for Auditory Neuroscience and InnerEarLab in Göttingen (Germany) in June 2018 and March and April 2019. This last collaboration started from 2 min conversation and seemed one of the craziest. Even in the worst-case scenario, with the huge effort of Antoine, it became one of the most fruitful and amazing experiences of my life.

Agrair els mesos que vaig passar a l'estabulari de Bellvitge com a becaria i tota la gent magnifica que allí vaig conèixer. A tota la família IBEC que dia a dia ens facilita la nostra vida administrativa. I especialment als membres del servei de microscòpia de l'IRB Anna Lladó, Lidia Badia, Sebastien Tosi i Julien Colombelli, per ajudar-nos a donar forma a algunes de les nostres idees més esbojarrades.

Agraeixo també a tots aquells que durant aquests anys m'heu anat ajudant i aconsellant per aconseguir que aquest projecte hagi arribat a bon terme.

Immensament agraeixo el suport incondicional de la meva família. Espero que us sentiu més orgullosos que no pas tristos ja que la raó per la que no ens veiem tant com voldríem per mi ha sigut un repte apassionant. Cela inclut également toi Adren, je ressens tous mes hauts et mes bas, mes allées et venues et je vous remercie pour votre patience infinie.

Tampoc pot faltar el meu "Consell de sàvies" que m'han acompanyat al llarg de tota la vida, Carme, Alba, Ares i Gemma, perquè encara que faci mesos que no ens veiem per natres és com si el temps no hagués canviat res. I al meu amic i conseller Toni, s'ha de fer mes llimonada a la vida!

## REFERENCES


Agez, M. *et al.* (2017) 'Molecular architecture of potassium chloride co-transporter KCC2', *Scientific Reports*, 7(1), pp. 1–14. doi: 10.1038/s41598-017-15739-1.

Banghart M, Borges K, Isacoff E, Trauner D, K. R. (2004) 'Light-activated ion channels for remote control of neuronal firing', *Nature neuroscience*, 7, pp. 1381–1386. Available at: http://www.ncbi.nlm.nih.gov/pubmed/15558062.

Banghart, M. R. *et al.* (2009) 'Photochromic blockers of voltage-gated potassium channels.', *Angewandte Chemie (International ed. in English)*, 48(48), pp. 9097–101. doi: 10.1002/anie.200904504.

Bartels, E., Wassermann, N. H. and Erlanger, B. F. (1971) 'Photochromic activators of the acetylcholine receptor.', *Proceedings of the National Academy of Sciences of the United States of America*, 68(8), pp. 1820–3. Available at: http://www.pubmedcentral.nih.gov/articlerender.fcgi?artid=389300&tool=pmcentrez&rendertype=abstract.

Batrel, C. *et al.* (2017) 'Mass potentials recorded at the round window enable the detection of low spontaneous rate fibers in gerbil auditory nerve', *PLoS ONE*. doi: 10.1371/journal.pone.0169890.

Bautista-Barrufet, A., Izquierdo-Serra, M. and Gorostiza, P. (2014) 'Novel Approaches for Single Molecule Activation and Detection', in Benfenati, F., Di Babrizio, E., and V., T. (eds) *Advances in Atom and Single Molecule Machines,*. Springer-Verlag Berlin Heidelberg, pp. XII, 219 p. 73 illus., 26 illus. in color. doi: 10.1007/978-3-662-43367-6.

Bean, B. P. (2007) 'The action potential in mammalian central neurons', *Nature Reviews Neuroscience*, 8(6), pp. 451–465. doi: 10.1038/nrn2148.

Berger, S. I. and Iyengar, R. (2011) 'Role of systems pharmacology in understanding drug adverse events', *Wiley Interdisciplinary Reviews: Systems Biology and Medicine*, 3(2), pp. 129–135. doi: 10.1002/wsbm.114.

Berlin, S. *et al.* (2016) 'A family of photoswitchable NMDA receptors', *eLife*, pp. 1–29. doi: 10.7554/eLife.12040.

Boldog, E. *et al.* (2018) 'Transcriptomic and morphophysiological evidence for a specialized human cortical GABAergic cell type', *Nature Neuroscience*. Springer US, 21(9), pp. 1185–1195. doi: 10.1038/s41593-018-0205-2.

Bosch, M. *et al.* (2014) 'Structural and molecular remodeling of dendritic spine substructures during long-term potentiation', *Neuron*, 86(12), pp. 3279–3288. doi: 10.1016/j.neuron.2014.03.021.

Bourien, J. *et al.* (2014) 'Contribution of auditory nerve fibers to compound action potential of the auditory nerve', *Journal of Neurophysiology*, 112(5), pp. 1025–1039. doi: 10.1152/jn.00738.2013.

Braubach, O. *et al.* (2018) 'Sparsened neuronal activity in an optogenetically activated olfactory glomerulus', *Scientific Reports*, 8(1), pp. 1–17. doi: 10.1038/s41598-018-33021-w.

Broichhagen, J. *et al.* (2015) 'Orthogonal optical control of a G protein-coupled receptor with a SNAP-tethered photochromic ligand', *ACS Central Science*, 1(7), pp. 383–393. doi: 10.1021/acscentsci.5b00260.

Browne, L. E. *et al.* (2014) 'Optical control of trimeric P2X receptors and acid-sensing ion channels', *Proceedings of the National Academy of Sciences of the United States of America*, 111(1), pp. 521–526. doi: 10.1073/pnas.1318582111.

Cabré, G. *et al.* (2019) 'Rationally designed azobenzene photoswitches for efficient two-photon neuronal excitation', *Nature Communications*, 10(1). doi: 10.1038/s41467-019-08796-9.

Cabré, Gisela *et al.* (2019) 'Synthetic photoswitchable neurotransmitters based on bridged azobenzenes', *Organic Letters*. doi: 10.1021/acs.orglett.9b01222.

Callaway, E. M. and Katzt, L. C. (1993) 'Photostimulation using caged glutamate reveals functional circuitry in living brain slices', *Proceedings of the National Academy of Sciences*, 90, pp. 7661–7665.

Carroll, E. C. *et al.* (2015) 'Two-photon brightness of azobenzene photoswitches designed for glutamate receptor optogenetics.', *Proceedings of the National Academy of Sciences of the United States of America*, 112(7),

pp. E776-85. doi: 10.1073/pnas.1416942112.

Casey, D. (1997) 'The relationship of pharmacology to side effects', *J Clin Psychiatry*, 58, pp. 55–62.

Castillo, P. E., Malenka, R. C. and Nicoll, R. A. (1997) 'Kainate receptors mediate a slow postsynaptic current in hippocampal CA3 neurons', *Nature*, 388, pp. 182–186.

Chambers, J. J. *et al.* (2004) 'Photochemically knocking out glutamate receptors in vivo', *Journal of the American Chemical Society*, 126(43), pp. 13886–13887. doi: 10.1021/ja048331p.

Choquet, D. and Triller, A. (2013) 'The dynamic synapse', *Neuron*. Elsevier Inc., 80(3), pp. 691–703. doi: 10.1016/j.neuron.2013.10.013.

Dana, H. *et al.* (2016) 'Sensitive red protein calcium indicators for imaging neural activity.', *eLife*, 5, p. e12727. doi: 10.7554/eLife.12727.

Deisseroth, K. and Hegemann, P. (2017) 'The form and function of channelrhodopsin', *Science*, 357(6356). doi: 10.1126/science.aan5544.

Donthamsetti, P. C. *et al.* (2017) 'Optical Control of Dopamine Receptors Using a Photoswitchable Tethered Inverse Agonist', *Journal of the American Chemical Society*, 139, pp. 18522–1853. doi: 10.1021/jacs.7b07659.

Donthamsetti, P. C. *et al.* (2019) 'Genetically-targeted optical control of an endogenous G protein-coupled receptor', *Journal of the American Chemical Society*. doi: 10.1021/jacs.9b02895.

Dunfield, D. and Haas, K. (2010) 'In vivo single-cell excitability probing of neuronal ensembles in the intact and awake developing Xenopus brain.', *Nature protocols*. Nature Publishing Group, 5(5), pp. 841–848. doi: 10.1038/nprot.2010.10.

Ellis-Davies, G. C. R. (2007) 'Caged compounds: Photorelease technology for control of cellular chemistry and physiology', *Nature Methods*, 4(8), pp. 619–628. doi: 10.1038/nmeth1072.

Ellis-Davies, G. C. R. (2019) 'Two-Photon Uncaging of Glutamate', *Frontiers in Synaptic Neuroscience*, 10(January), pp. 1–13. doi: 10.3389/fnsyn.2018.00048.

Falk, J. *et al.* (2007) 'Electroporation of cDNA/Morpholinos to targeted areas of embryonic CNS in Xenopus.', *BMC developmental biology*, 7, p. 107. doi: 10.1186/1471-213X-7-107.

Förster, D. *et al.* (2017) 'An optogenetic toolbox for unbiased discovery of functionally connected cells in neural circuits', *Nature Communications*. Springer US, 8(1), p. 116. doi: 10.1038/s41467-017-00160-z.

Frerking, M., Malenka, R. C. and Nicoll, R. A. (1998) 'Synaptic activation of kai- nate receptors on hippocampal interneurons', *Nature Neuroscience*, 1, pp. 479–486.

Gereau, R. W. I. and Swanson, G. T. (eds) (2008) *The Glutamate Receptors*. Totowa, NJ.: Humana Press.

Gomila, A. M. J. *et al.* (2019) 'Photocontrol of endogenous glycine receptors in vivo', *bioRxiv. The prepint server for biology*, pp. 1–20.

Gong, Y. *et al.* (2015) 'High-speed recording of neural spikes in awake mice and flies with a fluorescent voltage sensor', *Science*, 350(6266), pp. 1361–1366. doi: 10.1126/science.aab0810.

H Satzger, S Spörlein, C Root, J Wachtveitl, W Zinth, P. G. (2003) 'Fluorescence spectra of trans- and cisazobenzene- emission from the Franck-Condon state', *Chemical Physics Letters*, 372(1–2), pp. 216–223. Available at: http://www.sciencedirect.com/science/article/pii/S0009261403003646.

Haas, K., Li, J. and Cline, H. T. (2006) 'AMPA receptors regulate experience-dependent dendritic arbor growth in vivo.', *Proceedings of the National Academy of Sciences of the United States of America*, 103(32), pp. 12127–31. doi: 10.1073/pnas.0602670103.

Habermacher, C. *et al.* (2016) 'Photo-switchable tweezers illuminate pore-opening motions of an ATP-gated P2X ion channel', *eLife*, 5(JANUARY2016), pp. 1–22. doi: 10.7554/eLife.11050.

Hammerich, M. *et al.* (2016) 'Heterodiazocines: Synthesis and Photochromic Properties, Trans to Cis Switching within the Bio-optical Window', *Journal of the American Chemical Society*, 138(40), pp. 13111–13114. doi: 10.1021/jacs.6b05846.

Henley, J. M. (2003) 'Proteins interactions implicated in AMPA receptor trafficking: A clear destination and an improving route map', *Neuroscience Research*, 45(3), pp. 243–254. doi:

10.1016/S0168-0102(02)00229-8.

Herguedas, B. *et al.* (2019) 'Architecture of the heteromeric GluA1/2 AMPA receptor in complex with the auxiliary subunit TARP γ8', *Science*, p. eaav9011. doi: 10.1126/science.aav9011.

Huang, Y.-B. *et al.* (2015) 'In Vivo Study of Dynamics and Stability of Dendritic Spines on Olfactory Bulb Interneurons in Xenopus laevis Tadpoles.', *PloS one*, 10(10), p. e0140752. doi: 10.1371/journal.pone.0140752.

Hüll, K., Morstein, J. and Trauner, D. (2018) 'In Vivo Photopharmacology', *Chemical Reviews*, 118(21), pp. 10710–10747. doi: 10.1021/acs.chemrev.8b00037.

Iyer, S. M. *et al.* (2016) 'Optogenetic and chemogenetic strategies for sustained inhibition of pain', *Scientific Reports*. Nature Publishing Group, 6(July), pp. 1–10. doi: 10.1038/srep30570.

Izquierdo-Serra, M. *et al.* (2014) 'Two-photon neuronal and astrocytic stimulation with azobenzene-based photoswitches.', *Journal of the American Chemical Society*, 136(24), pp. 8693–701. doi: 10.1021/ja5026326.

Izquierdo-Serra, M. *et al.* (2016) 'Optical control of endogenous receptors and cellular excitability using targeted covalent photoswitches', *Nature Communications*, 7, p. 12221. doi: 10.1038/ncomms12221.

Kandel, Eric R., Schwartz, James H., Jessell, T. M. (ed.) (2000) *Principles of Neural Science*. 4th edn. New York: McGraw-Hill.

Keppeler, D. *et al.* (2018) 'Ultrafast optogenetic stimulation of the auditory pathway by targeting-optimized Chronos', *The EMBO Journal*, 37(24), p. e99649. doi: 10.15252/embj.201899649.

Kidd, F. L. and Isaac, J. T. R. (1999) 'Developmental and activity dependent regulation of ionotropic glutamate receptors at synapses.', *Nature*, 400, pp. 569–573. doi: 10.1100/tsw.2002.74.

Kienzler, M. A. *et al.* (2013) 'A red-shifted, fast-relaxing azobenzene photoswitch for visible light control of an ionotropic glutamate receptor', *Journal of the American Chemical Society*, 135(47), pp. 17683–17686. doi: 10.1021/ja408104w.

Kienzler, M. A. and Isacoff, E. Y. (2017) 'Precise modulation of neuronal activity with synthetic photoswitchable ligands', *Current Opinion in Neurobiology*. Elsevier Ltd. doi: 10.1016/j.conb.2017.05.021.

Kikuta, S. *et al.* (2015) 'Sensory Deprivation Disrupts Homeostatic Regeneration of Newly Generated Olfactory Sensory Neurons after Injury in Adult Mice', *Journal of Neuroscience*, 35(6), pp. 2657–2673. doi: 10.1523/JNEUROSCI.2484-14.2015.

Klapoetke, N. C. *et al.* (2014) 'Independent optical excitation of distinct neural populations.', *Nature methods*, 11(3), pp. 338–46. doi: 10.1038/nmeth.2836.

Ko, S. *et al.* (2005) 'Altered Behavioral Responses to Noxious Stimuli and Fear in Glutamate Receptor 5 ( GluR5 ) - or GluR6-Deficient Mice', 25(4), pp. 977–984. doi: 10.1523/JNEUROSCI.4059-04.2005.

Kokel, D. *et al.* (2013) 'Photochemical activation of TRPA1 channels in neurons and animals.', *Nature chemical biology*. Nature Publishing Group, 9(4), pp. 257–63. doi: 10.1038/nchembio.1183.

Kost, L. A. *et al.* (2019) 'Red Fluorescent Genetically Encoded Voltage Indicators with Millisecond Responsiveness', *Sensors*, 19(13), p. 2982. doi: 10.3390/s19132982.

Lemoine, D. *et al.* (2013) 'Optical control of an ion channel gate', *Proceedings of the National Academy of Sciences*, 110(51), pp. 20813–20818. doi: 10.1073/pnas.1318715110.

Lerma, J. and Marques, J. M. (2013) 'Kainate receptors in health and disease', *Neuron*. Elsevier Inc., 80(2), pp. 292–311. doi: 10.1016/j.neuron.2013.09.045.

Levitz, J. *et al.* (2013) 'Optical control of metabotropic glutamate receptors', *Nature Neuroscience*. Nature Publishing Group, 16(4), pp. 507–516. doi: 10.1038/nn.3346.

Lin, J. Y. (2010) 'A user's guide to channelrhodopsin variants: Features, limitations and future developments', *Experimental Physiology*, 96(1), pp. 19–25. doi: 10.1113/expphysiol.2009.051961.

Lin, W. C. *et al.* (2014) 'Engineering a light-regulated GABA A receptor for optical control of neural inhibition', *ACS Chemical Biology*, 9(7), pp. 1414–1419. doi: 10.1021/cb500167u.

Mager, T. *et al.* (2018) 'High frequency neural spiking and auditory signaling by ultrafast red-

shifted optogenetics', *Nature Communications*. Springer US, 9(1), p. 1750. doi: 10.1038/s41467-018-04146-3.

Maier, W. *et al.* (2005) 'Comparative analysis of inhibitory effects of caged ligands for the NMDA receptor', *Journal of Neuroscience Methods*, 142(1), pp. 1–9. doi: 10.1016/j.jneumeth.2004.07.006.

Maleeva, G. *et al.* (2019) 'A photoswitchable GABA receptor channel blocker', *British Journal of Pharmacology*, 176(15), pp. 2661–2677. doi: 10.1111/bph.14689.

Matera, C. *et al.* (2018) 'Photoswitchable Antimetabolite for Targeted Photoactivated Chemotherapy', *Journal of the American Chemical Society*, 140(46), pp. 15764–15773. doi: 10.1021/jacs.8b08249.

Mayer, M. L. (2005) 'Crystal Structures of the GluR5 and GluR6 Ligand Binding Cores : Molecular Mechanisms Underlying Kainate Receptor Selectivity', *Neuron*, 45, pp. 539–552. doi: 10.1016/j.neuron.2005.01.031.

Meyerson, J. R. *et al.* (2014) 'Structural mechanism of glutamate receptor activation and desensitization', *Nature*, 514. doi: 10.1038/nature13603.

Meyerson, J. R. *et al.* (2016) 'Structural basis of kainate subtype glutamate receptor desensitization', *Nature*. Nature Publishing Group, pp. 1–16. doi: 10.1038/nature19352.

Mortensen, M. *et al.* (2014) 'Photo-antagonism of the GABAA receptor.', *Nature communications*, 5, p. 4454. doi: 10.1038/ncomms5454.

Mourot, A. *et al.* (2012) 'Rapid optical control of nociception with an ion-channel photoswitch', *Nature Methods*, 9(4), pp. 396–402. doi: 10.1038/nmeth.1897.

Mourot, A., Tochitsky, I. and Kramer, R. H. (2013) 'Light at the end of the channel: optical manipulation of intrinsic neuronal excitability with chemical photoswitches.', *Frontiers in molecular neuroscience*, 6(March), p. 5. doi: 10.3389/fnmol.2013.00005.

Nagel, G. *et al.* (2005) 'Light activation of Channelrhodopsin-2 in excitable cells of caenorhabditis elegans triggers rapid behavioral responses', *Current Biology*, 15(24), pp. 2279–2284. doi: 10.1016/j.cub.2005.11.032.

Nagy, J. I., Pereda, A. E. and Rash, J. E. (2018) 'Electrical synapses in mammalian CNS: Past eras, present focus and future directions', *Biochimica et Biophysica Acta - Biomembranes*. Elsevier B.V., 1860(1), pp. 102–123. doi: 10.1016/j.bbamem.2017.05.019.

Olson, J. P. *et al.* (2013) 'Optically selective two-photon uncaging of glutamate at 900 nm', *Journal of the American Chemical Society*, 135(16), pp. 5954–5957. doi: 10.1021/ja4019379.

Pangrsic, T., Singer, J. H. and Koschak, A. (2018) 'Voltage-gated calcium channels: Key players in sensory coding in the retina and the inner ear', *Physiological Reviews*, 98(4), pp. 2063–2096. doi: 10.1152/physrev.00030.2017.

Paoletti, P., Bellone, C. and Zhou, Q. (2013) 'NMDA receptor subunit diversity: impact on receptor properties, synaptic plasticity and disease', *Nature Reviews Neuroscience*. Nature Publishing Group, 14, pp. 383–400. doi: 10.1038/nrn3504.

Paoletti, P., Ellis-Davies, G. C. R. and Mourot, A. (2019) 'Optical control of neuronal ion channels and receptors', *Nature Reviews Neuroscience*. Springer US. doi: 10.1038/s41583-019-0197-2.

Park, Y. *et al.* (2006) 'Long-term depression of kainate receptor-mediated synaptic transmission', *Neuron*, 49(1), pp. 95–106. doi: 10.1016/j.neuron.2005.11.035.

Partin, K. *et al.* (1993) 'Selective modulation of desensitization at AMPA versus kainate receptors by cyclothiazide and concanavalin A.', *Neuron*, 11, pp. 1069–1082.

Petrovic, M. M. *et al.* (2017) 'Metabotropic action of postsynaptic kainate receptors triggers hippocampal long-term potentiation', *Nature Neuroscience*, 20(4). doi: 10.1038/nn.4505.

Pittolo, S. *et al.* (2014) 'An allosteric modulator to control endogenous G protein-coupled receptors with light.', *Nature chemical biology*, 10(10), pp. 813–5. doi: 10.1038/nchembio.1612.

Polosukhina, A. *et al.* (2012) 'Photochemical Restoration of Visual Responses in Blind Mice', *Neuron*, 75(2), pp. 271–282. doi: 10.1016/j.neuron.2012.05.022.

Prakash, R. *et al.* (2012) 'Two-photon optogenetic toolbox for fast inhibition, excitation and bistable modulation', *Nature Methods*, 9(12), pp. 1171–1179. doi: 10.1038/nmeth.2215.

Reiner, A. and Isacoff, E. Y. (2014) 'Tethered ligands reveal glutamate receptor desensitization depends on subunit occupancy', *Nature Chemical Biology*. Nature Publishing Group, (february), pp. 1–10. doi: 10.1038/nchembio.1458.

Riefolo, F. *et al.* (2019) 'Optical Control of Cardiac Function with a Photoswitchable Muscarinic Agonist', *Journal of the American Chemical Society*, p. jacs.9b03505. doi: 10.1021/jacs.9b03505.

Robert, A. and Howe, J. R. (2003) 'How AMPA receptor desensitization depends on receptor occupancy.', *The Journal of neuroscience : the official journal of the Society for Neuroscience*, 23(3), pp. 847–58. doi: 23/3/847 [pii].

Rovira, X. *et al.* (2016) 'OptoGluNAM4.1, a Photoswitchable Allosteric Antagonist for Real-Time Control of mGlu4 Receptor Activity', *Cell Chemical Biology*, 23(8), pp. 929–934. doi: 10.1016/j.chembiol.2016.06.013.

Shepherd, G. M. G. (2012) 'Circuit Mapping by Ultraviolet Uncaging of Glutamate', *Cold Spring Harbor Protocols*, pp. 998–1005. doi: 10.1101/pdb.prot070664.

Soto, D. *et al.* (2019) 'L-Serine dietary supplementation is associated with clinical improvement of loss-of-function GRIN2B - related pediatric encephalopathy', *Science Signaling*, 12, pp. 1–16.

Sterling, P. and Matthews, G. (2005) 'Structure and function of ribbon synapses', *Trends in Neurosciences*, 28(1), pp. 20–29. doi: 10.1016/j.tins.2004.11.009.

Stirman, J. N. *et al.* (2011) 'Real-time multimodal optical control of neurons and muscles in freely behaving Caenorhabditis elegans', *Nature Methods*, 8(2), pp. 153–158. doi: 10.1038/nmeth.1555.

Szobota, S. *et al.* (2007) 'Remote control of neuronal activity with a light-gated glutamate receptor.', *Neuron*, 54(4), pp. 535–45. doi: 10.1016/j.neuron.2007.05.010.

Tatti, R. *et al.* (2014) 'A population of glomerular glutamatergic neurons controls sensory information transfer in the mouse olfactory bulb', *Nature Communications*, 5. doi: 10.1038/ncomms4791.

Terni, B. *et al.* (2017) 'Tight temporal coupling between synaptic rewiring of olfactory glomeruli and the emergence of odor-guided behavior in Xenopus tadpoles', *Journal of Comparative Neurology*, 525(17), pp. 3769–3783. doi: 10.1002/cne.24303.

Thapaliya, E. R., Zhao, J. and Ellis-Davies, G. C. R. (2019) 'Locked-Azobenzene: Testing the Scope of a Unique Photoswitchable Scaffold for Cell Physiology', *ACS Chemical Neuroscience*, p. acschemneuro.8b00734. doi: 10.1021/acschemneuro.8b00734.

Tochitsky, Ivan; Kramer, R. H. (2015) 'Optopharmacological tools for restoring visual function in degenerative retinal diseases', *Current opinion in neurobiology*, pp. 74–78. doi: 10.1007/978-1-4615-5933-7.

Tochitsky, I. *et al.* (2012) 'Optochemical control of genetically engineered neuronal nicotinic acetylcholine receptors', *Nature Chemistry*. Nature Publishing Group, 4(2), pp. 105–111. doi: 10.1038/nchem.1234.

Trads, J. B. *et al.* (2019) 'Sign Inversion in Photopharmacology: Incorporation of Cyclic Azobenzenes in Photoswitchable Potassium Channel Blockers and Openers', *Angewandte Chemie - International Edition*. doi: 10.1002/anie.201905790.

Traynelis, S. F. *et al.* (2010) 'Glutamate Receptor Ion Channels : Structure , Regulation , and Function', *Pharmacological Reviews*, 62(3), pp. 405–496. doi: 10.1124/pr.109.002451.405.

Tsukada, Y. and Mori, I. (2015) 'Optogenetics in Caenorhabditis elegans', in Yawo, H., Kandori, H., and Koizumi, A. (eds) *Optogenetics: Light-Sensing Proteins and Their Applications*. Tokyo: Springer Japan, pp. 213–226. doi: 10.1007/978-4-431-55516-2_14.

Twomey, E. C. *et al.* (2017) 'Channel opening and gating mechanism in AMPA-subtype glutamate receptors', *Nature*. Nature Publishing Group, 549(7670), pp. 60–65. doi: 10.1038/nature23479.

Twomey, E. C. and Sobolevsky, A. I. (2018) 'Structural Mechanisms of Gating in Ionotropic Glutamate Receptors', *Biochemistry*, 57(3), pp. 267–276. doi: 10.1021/acs.biochem.7b00891.

Vignes, M. *et al.* (1998) 'The GluR5 subtype of kainate receptor regulates excitatory synaptic transmission in areas CA1 and CA3 of the rat hippocampus', *Neuropharmacology*, (37), pp. 1269–1277.

Volgraf, M. *et al.* (2006) 'Allosteric control of an ionotropic glutamate receptor with an optical switch.', *Nature chemical biology*, 2(1), pp. 47–52. doi: 10.1038/nchembio756.

Volgraf, M. *et al.* (2007) 'Reversibly caged glutamate: a photochromic agonist of ionotropic glutamate receptors.', *Journal of the American Chemical Society*, 129(2), pp. 260–1. doi: 10.1021/ja067269o.

Wake, M. *et al.* (1994) 'Selective Inner Hair Cell Ototoxicity Induced by Carboplatin', *Laringoscope*, 104, pp. 488–493.

Weston, M. C. *et al.* (2006) 'Interdomain Interactions in AMPA and Kainate Receptors Regulate Affinity for Glutamate', *The Journal of neuroscience*, 26(29), pp. 7650–7658. doi: 10.1523/JNEUROSCI.1519-06.2006.

Wieboldt, R. *et al.* (1994) 'Photolabile precursors of glutamate: Synthesis, photochemical properties, and activation of glutamate receptors on a microsecond time scale', *Proceedings of the National Academy of Sciences of the United States of America*, 91(19), pp. 8752–8756. doi: 10.1073/pnas.91.19.8752.

Wong, H. H.-W. and Holt, C. E. (2018) 'Targeted electroporation in the CNS in Xenopus embryos', in Vleminckx, K. (ed.) *Xenopus. Methods in Molecular Biology*. New York, NY, pp. 119–130.

Wrobel, C. *et al.* (2018) 'Optogenetic stimulation of cochlear neurons activates the auditory pathway and restores auditory-driven behavior in deaf adult gerbils', *Science Translational Medicine*, 10(449). doi: 10.1126/scitranslmed.aao0540.

Xu, N. (2013) 'On the concept of resting potential - Pumping ratio of the Na +/K+ pump and concentration ratios of potassium ions outside and inside the cell to sodium ions inside and outside the cell', *Journal of Membrane Biology*, 246(1), pp. 75–90. doi: 10.1007/s00232-012-9507-6.

Yang, W. and Yuste, R. (2017) 'In vivo imaging of neural activity', *Nature Methods*, 14(4), pp. 349–359. doi: 10.1038/nmeth.4230.

Yue, L. *et al.* (2016) 'Retinal stimulation strategies to restore vision: Fundamentals and systems', *Progress in Retinal and Eye Research*. Elsevier Ltd. doi: 10.1016/j.preteyeres.2016.05.002.

Zhang, F. *et al.* (2011) 'The microbial opsin family of optogenetic tools', *Cell*, 147(7), pp. 1446–1457. doi: 10.1016/j.cell.2011.12.004.

Zhao, Y. *et al.* (2019) 'Architecture and subunit arrangement of native AMPA receptors elucidated by cryo-EM', *Science*, p. eaaw8250. doi: 10.1126/science.aaw8250.

Zhu, S. and Gouaux, E. (2017) 'Structure and symmetry inform gating principles of ionotropic glutamate receptors', *Neuropharmacology*. Elsevier Ltd, 112, pp. 11–15. doi: 10.1016/j.neuropharm.2016.08.034.

## APPENDICES

### 1. PROTOCOLS

#### Rat organotypic hippocampal slice culture and gene transfection

All procedures were conducted in accordance with the European guidelines for animal care and use in research, and were approved by the Animal Experimentation Ethics Committee at the University of Barcelona (Spain). Hippocampal organotypic slice cultures were prepared from postnatal day 6-7 rats as described (Okamoto et al. 2004). Slices were cultured at 35 ºC on interface membranes (Millipore) and fed with MEM media containing 20% horse serum, 27 mM D-glucose, 6 mM NaHCO3, 2 mM CaCl2, 2 mM MgSO4, 30 mM HEPES, 0.01 % ascorbic acid and 1 µg/ml insulin. pH was adjusted to 7.3 and osmolality to 300-320 mOsm $kg^{-1}$. Slices were biolistically transfected (BioRad) after 5-7 DIV with GCaMP6s (Addgene) under CMV promoter and dsRed2 under CAG promoter as described (Bosch et al. 2014, 2017).

#### Nerve regeneration animal model of Xenopus embryos

In collaboration with Dr Artur Llobet (IDIBELL and UB) we developed a procedure to study the process of nerve regeneration and to test TCPs for neuronal pacemaking. Transgenic Xenopus tropicalis tadpoles from stages from 45 to 50 are anesthetized with Tricaine 0.02% and right olfactory nerve is cut. After one day for recovery, TCPs are delivered in the right olfactory bulb by micro-bolus injection (Dunfield and Hass 2010). The control animals are injected with the vehicle with the same conditions as TCP-treated group. Both groups are kept at the same conditions of illumination. The regenerative process is controlled everyday with fluorescent photos of the nerves for 8 days. In each photo we take the uncut nerve as a control. From the cut nerve we average the thickness of the nerve in three points from the placode to the olfactory bulb. Finally, we ratio the average of the cut and the uncut in each day. Values near 1 indicate a complete regeneration of the nerve.

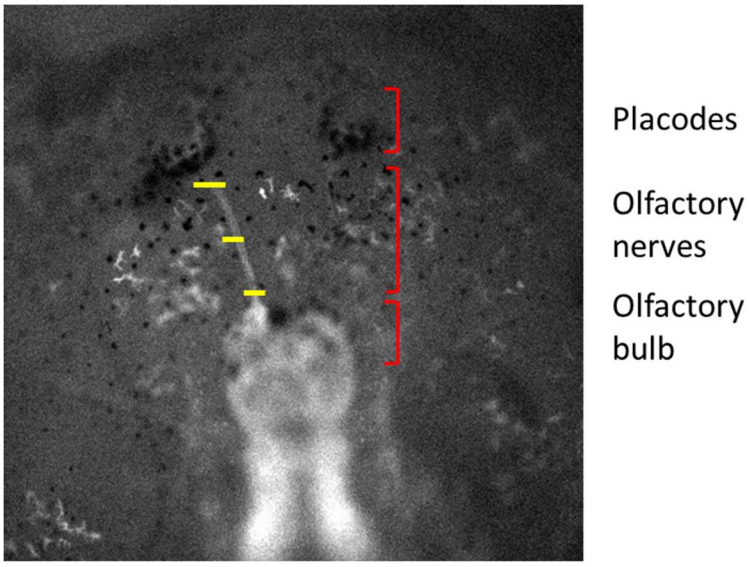


**Figure 1**. Transgenic NBT *Xenopus tropicalis* embryos expressing GFP fused to tubulin beta 2B class IIb. Left olfactory nerve is kept intact as a control. Right olfactory nerve is degenerated after surgical incision. Yellow lines indicate the three quantification points for analysis.

**Electroporation of *Xenopus* embryos**

This protocol was adapted from (Wong and Holt 2018) to electroporate Xenopus tropicalis tadpoles at stage 28-43 (Nieuwkoop and Faber 1994). Supplementary information can be found in (Falk et al. 2007).

MATERIALS

Electroporation chamber

- Sylgard dish: Mix the base and curing agents from the Sylgard 184 Silicone Elastomer Kit in a 10:1 ratio. Pour the mixture into a 35 mm dish with the negative model of the electroporation chamber to create a 0.8 cm layer of silicone elastomer at the bottom. Leave the Sylgard to polymerize at room temperature for 24 h.
- Design for Stage 24–32 embryos of *X. tropicalis*: A "T" shape chamber with a length (L) of 2.5 mm × width (W) of 1 mm × depth (D) of 1 mm in the longitudinal channel, and 2 mm (L) × 0.5 mm (W) × 0.25 mm (D) in the transverse channel (Figure 2).
- No. 15A surgical scalpel blade.
- 27 G Needle.
- Fine forceps (#5).

Solutions

- 10× Modified Barth's saline (MBS)

| Reagent | Final concentration (mM) | Quantity (g) for 1L ddH2O |
|---|---|---|
| NaCl | 880 | 51.43 |
| KCl | 10 | 0.74 |
| $NaHCO_3$ | 24 | 2.016 |
| HEPES | 100 | 23.8 |
| $MgSO_4$ | 8.2 | 0.984 |
| $Ca(NO_3)_2$ | 3.3 | 0.5412 |
| $CaCl_2$ | 4.1 | 0.451 |

Mix and adjust to pH 7.6 with NaOH. Filter and store at 4 °C.

- Electroporation solution: prepare 1× MBS (50ml) with 0.4 mg/ml of tricaine methanesulfonate (MS-222, Sigma) and 1% PSF (100 U/ml penicillin, 100 µg/ ml streptomycin and 0.25 µg/ml fungizone; Gibco). Mix and adjust pH 7.6 with NaOH.
- Rearing solution: make 0.1× MBS (500ml) from 10x MBS stock solution.
- Injection mixture: Final concentration of DNA solution can range from 1–2 µg/µl. Fast green was added to the mixture to track correct injection. To electroporate simultaneously two plasmids proportions are 2:1 for functional marker or protein of interest and morphological fluorescent marker, respectively.

Brain exposure:

- Sylgard dish.

- 0.1 mm and bended 0.2 mm insect pins.
- Insect pin holders.

Electroporation setup

- Pressurized microinjector with adjustable pulse duration and pressure (PicospritzerPicospritzer III - Intracellular Microinjection Dispense Systems).
- Standard 1 mm outer diameter (OD) glass capillary holder.
- Pull long and sharp capillaries 1 mm OD borosilicate glass capillary with 0.78 mm internal diameter (ID). Filled capillaries will be manually opened with fine forceps under the microscope.
- Electroporator with square wave pulse generation capability (TSS20 Ovodyne Electroporator, Micro control instruments).
- Adjustatrode twin electrode holder.
- Electrodes: platinum electrode are the most stable and resistant, however insulated silver 40mm x 0.8mm wire electrode with offset pole (Micro control instruments) can also be used. General characteristics of the electrodes are:
- A 2.5 cm unmodified segment of wire (0.5 mm diameter) for insertion into the electrode adaptor. (2) A 4 cm insulated segment to allow a convenient working distance. (3) A 6 mm flattened electrode tip bent with a 45° angle.
- Micromanipulators for glass capillary holder and electrode adaptor (Narishige).
- Steering glass rod with rounded end or round end forceps.
- Stereo microscope with light source.

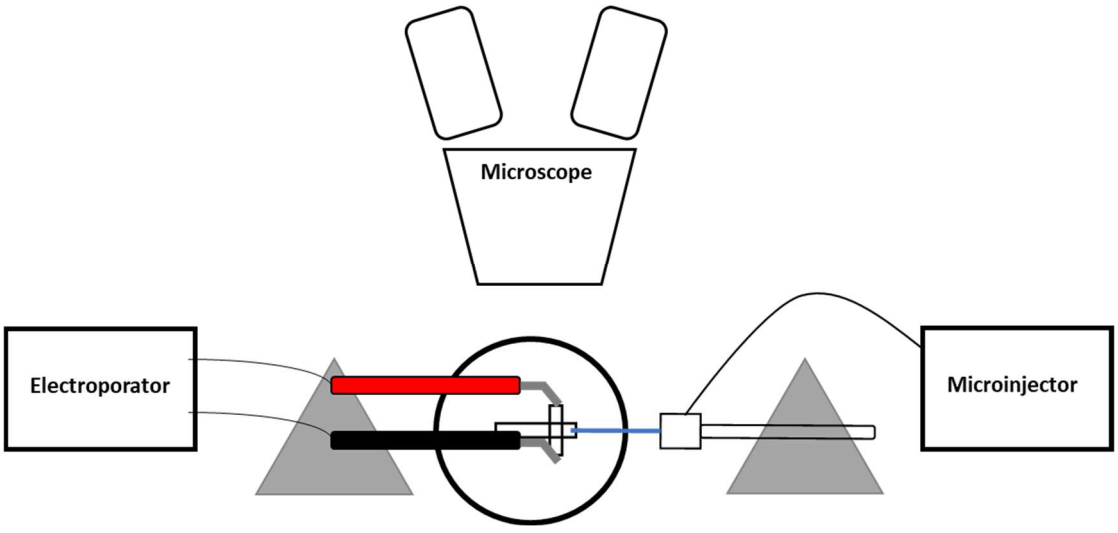


**Figure 2.** Schematic representation of the electroporation setup for retina and olfactory bulb electroporation. Micromanipulators (represented with gray triangles) for electrode adaptor and capillary holder are arranged in a straight horizontal line.

METHODS

- **Preparation**

1. Properly clean remaining vitelline membrane of the embryos with fine forceps or carefully rinsing with 0.1x MBS.
2. Transfer the embryos to a clean dish filled with 0.1× MBS.
3. Prepare the injection mixture.
4. Clean the electrodes and electroporation chamber with 70% ethanol and rinse with 1× MBS.
5. Place electrode adaptor and capillary holder micromanipulators one in front the other to place and secure electrodes at the two crossing ends of the electroporation chamber (Figure 2).
6. Attach the cables of the electrode adaptor to the electroporator to determine polarity. Since DNA is a negatively charged mixture, it will be repealed by the cathode (negative electrode, black wire connection).
7. Set the electroporator parameters: voltage, number of pulses, duration, and intervals of electric pulses. Generally, 18 V, 8× 50 ms pulses with 1 s intervals is used(Falk et al. 2007).
8. Transfer electroporation solution to cover the chamber channels and remove any trapped air bubbles with the steering rod. It is recommended to check proper function of the electroporation protocol prior to place embryos in the chamber. When current is correctly passing through electrodes in presence of electroporation solution bubbles come out from the electrodes.
9. Set the pressure output of the microinjector to 50 pound-forces per square inch (psi) for retina electroporation or 20 psi for brain electroporation.
10. Back-fill glass capillary with injection mixture and attach it to the capillary holder.
11. Break the capillary tip with fine forceps to obtain an angle at the tip. Adjust the pulse duration of the microinjector to deliver 5 nl of injection mixture per pulse.
12. Anesthetize the embryos in electroporation solution.

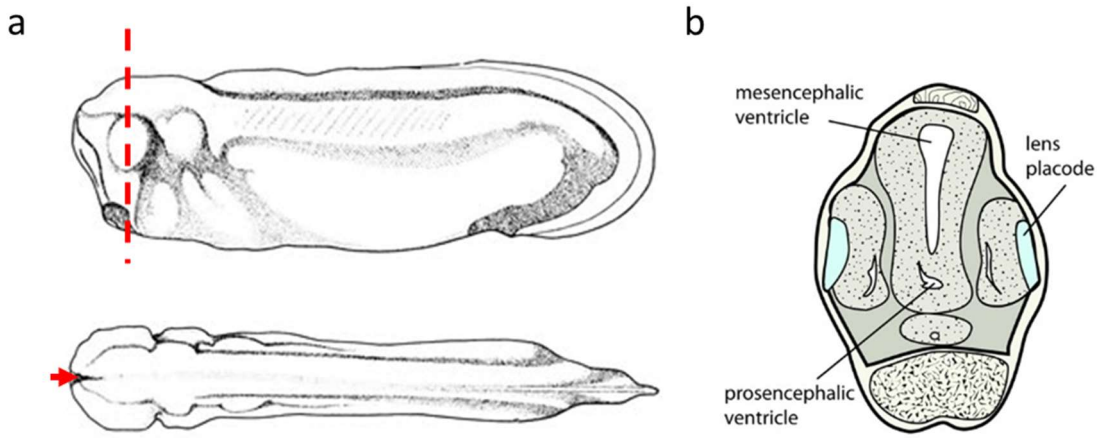


**Figure 3.** Digitized images and developmental data from (Nieuwkoop and Faber 1994) to show anatomical features of *Xenopus laevis* embryos at stage 28. Red arrow indicates the correct position to inject in the ventricle. Dashed red line indicates coronal plane representation in b. b) Adapted from (Gonzalez-fernandez, Dann, and Garlipp 2011).

- **Targeted retina electroporation**

1. Transfer an anesthetized embryo with a drop of electroporation solution to the electroporation chamber.

2. With the help of the steering rod, position the embryos in the channels such that the dorsal side is facing up and the retina primordia/lens placode are between the electrodes in the transverse channel (Figure 3).
3. Leave only sufficient volume of electroporation solution to cover the embryo in the channels and remove the excess.
4. Position and insert the capillary into the retina of interest.
5. Trigger of electroporation pulses let a small window of time to deliver 1–8 injection pulses into the retina. Immediately after, withdraw the capillary away from the retina to let the electric pulses pass through the embryos.
6. Use a plastic Pasteur pipette to gently pipette rearing solution up and down near the chamber channels in order to flush the embryo out.
7. Transfer the embryo to a clean dish filled with rearing solution for recovery.
8. Remove bubbles, mucus, and debris from the chamber channels by rinsing with electroporation buffer using a plastic Pasteur pipette.
9. Check to see if capillary is clogged before starting the subsequent round.

**Examples of electroporated dorsal retinal ganglion neurons**

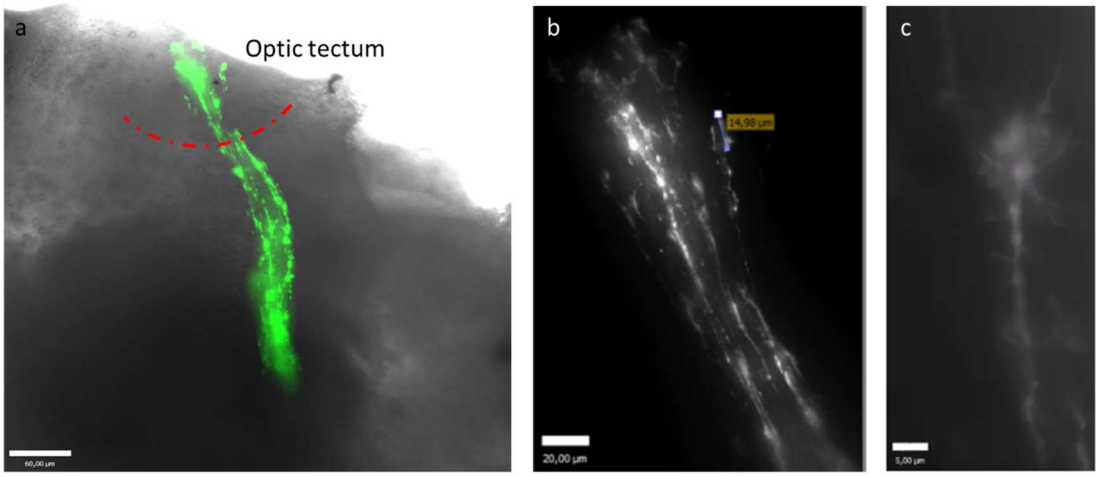


**Figure 4.** Electroporation of RGCs of the right eye with membrane targeted GFP (mGFP) at stage 28. a) Anatomical study of axon arbor from RGCs reaching the optic tectum at stage 41-43. Scale bar 60 µm. b) In vivo time lapse of axon arbor growing. Acquisition rate 300 ms during 30 min. Scale bar 20 µm. c) Single growth cone time lapse imaging. Acquisition rate 200 ms during 10 min. Scale bar 5 µm.

- **Targeted olfactory bulb electroporation**

1. Transfer an anesthetized embryo with a drop of electroporation solution to the electroporation chamber.
2. With the help of the steering rod, position the embryos in the channels such that the dorsal side is facing up and the olfactory bulb primordia are between the electrodes in the transverse channel (Figure 2).
3. Leave only sufficient volume of electroporation solution to cover the embryo in the channels and remove the excess.

4. Position and insert the capillary in the midline of the olfactory bulb to target the ventricle (depicted with a red arrow in Figure 3).
5. Trigger of electroporation pulses let a small window of time to deliver 1–8 injection pulses into the ventricle. Immediately after, withdraw the capillary away to let the electric pulses pass through the embryos. Correct injection can be observed by the staining of fast green inside the cavities of the ventricles.
6. Use a plastic Pasteur pipette to gently pipette rearing solution up and down near the chamber channels in order to flush the embryo out.
7. Transfer the embryo to a clean dish filled with rearing solution for recovery.
8. Remove bubbles, mucus, and debris from the chamber channels by rinsing with electroporation buffer using a plastic Pasteur pipette.
9. Check to see if capillary is clogged before starting the subsequent round.

**Examples of electroporated spiny neurons of the olfactory bulb**

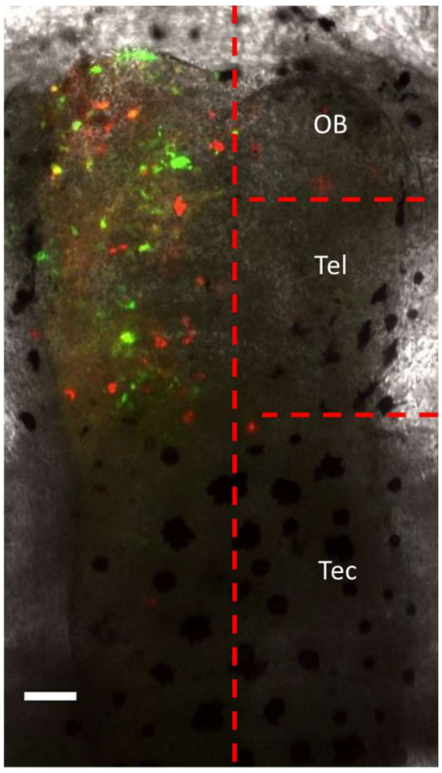


**Figure 5.** Microphotograph of electroporated embryo with GCaMP6s:mRFP (2:1) at st. 28 in one single hemisphere. Image was taken at st.41-42. Scale bar is 50 µm. OB, olfactory bulb; Tel, telencephalon; Tec, tectum.

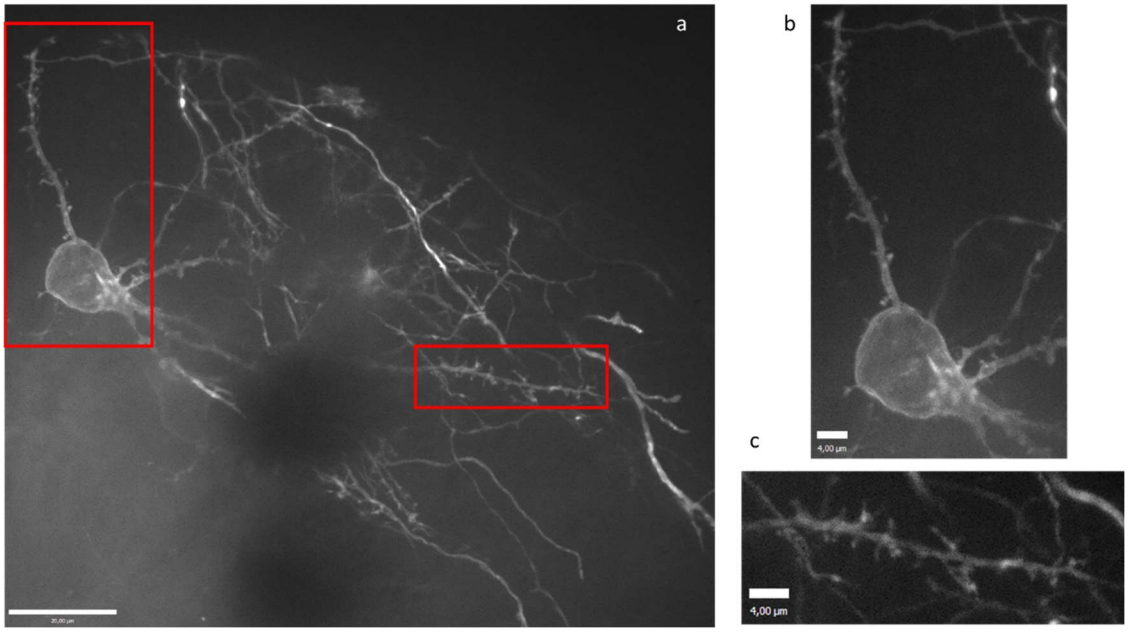


**Figure 6.** Morphology of spiny neurons confirms a correct electroporation to target granular cells from the olfactory bulb. a) mGFP electroporation of spiny neuron in the olfactory bulb. Scale bar 20µm. b-c) Magnification of the red squared zones in a. Scale bar 4µm.

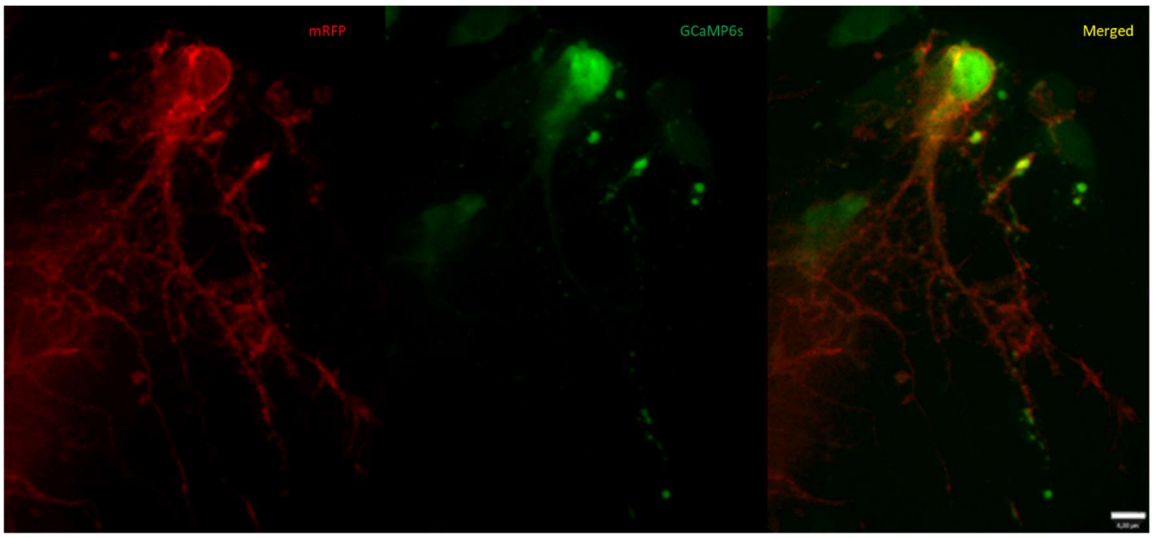


**Figure 7**. Co-electroporation of GCaMP6s:mRFP (2:1) in a granular spiny neuron of the olfactory bulb. Scale bar 6µm.

**Publicacions en revistes d'impacte (JCR) o que tinguin una evaluació prèvia (peer review)**

Gisela Cabré[*], Aida Garrido-Charles[*], Miquel Moreno, Miquel Bosch, Montserrat Porta-de-la-Riva, Michael Krieg, Marta Gascón-Moya, Núria Camarero, Ricard Gelabert, José M. Lluch, Félix Busqué, Jordi Hernando, Pau Gorostiza and Ramon Alibés. "Rationally designed azobenzene photoswitches for efficient two-photon neuronal excitation". Nat. Commun., 2019, 10, Article 907.

(*) Equivalent contribution. In particular, Aida Garrido performed all physiological experiments in vitro (including cell and brain slice cultures, transfection, electrophysiology, activity imaging, and two-photon excitation) and activity imaging and two-photon excitation in worms. Gisela Cabré and Miquel Moreno performed compound synthesis and characterization and participated in physiological experiments. Montserrat Porta performed genetic manipulation and screening of worms. The project was a collaboration between the laboratories of Pau Gorostiza and Ramon Alibés.

Impact factor 2017: 12.353

Subject Category: MULTIDISCIPLINARY SCIENCES

Ranking: 3/64

Quartile: Q1 / Decile: D1

Gisela Cabré[*], Aida Garrido-Charles[*], Àngels González-Lafont, Widukind Moormann, Daniel Langbehn, David Egea, José M. Lluch, Rainer Herges, Ramon Alibés, Félix Busqué, Pau Gorostiza and Jordi Hernando. "Synthetic photoswitchable neurotransmitters based on bridged azobenzenes". *Org. Lett.* (2019).

(*) Equivalent contribution. In particular, Aida Garrido performed all physiological experiments in vitro (including cell cultures, transfection, electrophysiology, activity imaging, and data analysis). Gisela Cabré performed compound synthesis and characterization and participated in physiological experiments. The project was a collaboration between the laboratories of Pau Gorostiza and Jordi Hernando.

Impact factor 2017: 6.492

Subject Category: CHEMISTRY, ORGANIC

Ranking: 3/57

Quartile: Q1

**Other publications:**

Izquierdo-Serra, M., Bautista-Barrufet, A., Trapero, A., Garrido-Charles, A., Díaz-Tahoces, A., Camarero, N., … Gorostiza, P. (2016). Optical control of endogenous receptors and cellular excitability using targeted covalent photoswitches. Nature Communications, 7,

12221. http://doi.org/10.1038/ncomms12221

Riefolo F, MATERA C, Garrido-Charles A, et al. Optical Control of Cardiac Function with a Photoswitchable Muscarinic Agonist. J Am Chem Soc. 2019:jacs.9b03505. doi:10.1021/jacs.9b03505

**Articles in preparation:**

Aida Garrido-Charles, et al. Nanoengineered light-harvested proteins for optogenetics and photopharmacology

Aida Garrido-Charles, et al. Photoswitching the activity of intact neurons from individual spines to in vivo.

Aida Garrido-Charles, et al. High frequency optopharmacologic stimulation of endogenous AMPA receptors of cochlear neurons

Aida Garrido-Charles, et al. Photocontrol of neuronal receptor activity with stilbene derivatives of glutamate.